WAVE SPEEDS IN GAS HYDRATE AND SEDIMENTS CONTAINING GAS HYDRATE: A LABORATORY AND MODELING STUDY

A DISSERTATION
SUBMITTED TO THE DEPARTMENT OF GEOPHYSICS
AND THE COMMITTEE ON GRADUATE STUDIES
OF STANFORD UNIVERSITY
IN PARTIAL FULFILLMENT OF THE REQUIREMENTS
FOR THE DEGREE OF
DOCTOR OF PHILOSOPHY

Michael B. Helgerud
April 2001

I certify that I have read this dissertation and that in my opinion it is fully adequate, in scope and quality, as a dissertation for the degree of Doctor of Philosophy.

Amos Nur, Principal Advisor

I certify that I have read this dissertation and that in my opinion it is fully adequate, in scope and quality, as a dissertation for the degree of Doctor of Philosophy.

Stephen H. Kirby

I certify that I have read this dissertation and that in my opinion it is fully adequate, in scope and quality, as a dissertation for the degree of Doctor of Philosophy.

Gary Mavko

I certify that I have read this dissertation and that in my opinion it is fully adequate, in scope and quality, as a dissertation for the degree of Doctor of Philosophy.

Jack Dvorkin

Approved for the University Committee on Graduate Studies:

Abstract

Natural gas hydrates are nonstoichiometric crystalline solids comprised of a hydrogen-bonded water lattice and entrapped “guest” molecules. Gas hydrate with methane as the guest species is stable at the pressure and temperature conditions present in the sediments beneath most of the worlds continental margins and deep inland seas and also in arctic sediments below the permafrost layer. Enormous amounts of methane are believed to be trapped in nature by hydrates, both in the hydrate crystal structure itself and also in sediments beneath hydrate deposits as free gas. This large reservoir of methane may be a future energy resource and may play a significant role in global climate change. The formation or melting of gas hydrate also has a strong effect on sub-sea slope stability. Unfortunately, all distribution and hydrate-related methane estimates are very inexact because accurate estimates of the amount of methane hydrate in situ are not currently available on a regional or site specific basis. A remote sensing technique which can accurately assess the amount and distribution of hydrate in natural deposits is needed to improve these distribution and hydrate-related methane estimates.

The best technique for remotely probing sediments several hundred meters below the surface or beneath deep bodies of water is seismic reflection profiling. Interpreting seismic data to deduce the amount of gas hydrate in place requires a relation between the hydrate fraction in the sediments and the elastic properties of the hydrate-sediment composite. Unfortunately, very little is known about the elastic properties of gas hydrate and sediment-hydrate composites. In Chapter 2 of this thesis, I review the measurements available in the literature and discuss a published method for theoretically estimating compressional wave speed in pure gas hydrate, extending it to the estimation of shear wave speeds as well.

To address the lack of elastic property measurements in the literature, I began a series

of experiments on propane hydrate formed in the laboratory by bubbling gas through water and water saturated sand in a clear walled pressure vessel. These experiments are described in Chapter 3. The goal was to observe the hydrate formation process in detail so that I could better understand why there were so few published wave speed measurements for gas hydrate. After analyzing the initial experiments, I would proceed to measure compressional and shear wave speeds in pure propane hydrate and in sediments containing propane hydrate. Propane was chosen as the hydrating gas because the pressure conditions were less stringent, making a glass walled pressure vessel practical. The glass walled pressure vessel made it possible to directly observe the gas hydrate formation process and all the propane hydrate experiments were videotaped.

The propane hydrate experiments were very successful at demonstrating why there are so few elastic property measurements published in the literature. The reason is that it is relatively easy to make gas hydrate in the laboratory, but it is nearly impossible to create well characterized, pure samples by bubbling gas through water, the traditional way of making samples. It is very difficult to drive the reaction to completion. As a result, unreacted water and/or gas generally remain in the pressure vessel. Additionally, the hydrate that is formed is seldom dense but rather a collection of spherical shells. In Chapter 3, I summarize the observations made during the propane hydrate experiments and describe the results from one experiment in which compressional wave speed was measured through a glass bead pack containing propane hydrate.

With the results from the experiments described in Chapter 3, it was clear that a different method for making gas hydrate in the lab would have to be pursued if any meaningful wave speed measurements were to be made. A research group from the USGS in Menlo Park, CA and Lawrence Livermore National Laboratory had recently published a method for making methane hydrate from ice instead of liquid water (see Chapter 4). In this method, single crystal ice made from triply distilled water is ground and sieved to extract the $180-250\mu$m diameter fraction. The granulated ice is then placed in a steel pressure vessel which is transferred to a temperature bath and pressurized with methane gas. The methane hydrate is formed by heating the temperature bath to approximately 17°C. As the sample temperature passes through the melting point of ice, the methane and ice react to form methane hydrate instead of liquid water. The formation process is proven and repeatable and leads to very

well characterized porous samples of polycrystalline methane hydrate.

After several meetings, a collaboration was initiated with the USGS in Menlo Park and Lawrence Livermore National Laboratory to measure compressional and shear wave speeds in methane hydrate samples made at the USGS in Menlo Park. A pressure vessel with hydraulic compaction and wave speed measurement capabilities was designed and built. This apparatus was used to study polycrystalline ice and polycrystalline methane hydrate samples. Those experiments are the subjects of Chapters 4 and 5.

Chapter 4 describes the apparatus and initial experiments performed on ice and methane hydrate. The results matched literature values for ice and showed that the apparatus could be used to successfully measure compressional and shear wave speeds simultaneously in both ice and methane hydrate. The results also showed that compressional and shear wave speeds were measurably different between methane hydrate and ice, that porous polycrystalline methane hydrate was much more resistant to compaction than porous polycrystalline ice Ih, and that bonds formed between ice grains or methane hydrate grains when active compaction of the porous samples was not occurring.

Chapter 5 describes the modifications made to the system and procedure that made it possible to measure the variations with uniaxial pressure and temperature of compressional and shear wave speed in compacted ice and compacted methane hydrate samples. The results showed that shear wave speed in both ice Ih and methane hydrate decreased with increasing confining pressure. This property had been reported previously for ice Ih, but no previous data for methane hydrate were available for comparison. In the subset of the studied confining pressures and temperatures where both ice Ih and methane hydrate were stable, compressional wave speed was greater in ice Ih and shear wave speed was greater in methane hydrate. As a result, the dynamic Poisson's ratio was smaller in methane hydrate than in ice. Using calculated densities for ice Ih and methane hydrate, the wave speeds were converted to isotropic, dynamic elastic moduli. The results showed that compressional wave and bulk moduli are greater in ice Ih, and shear modulus is greater in methane hydrate. The results presented in Chapter 5 appear to be the first ever reported measurements of compressional and shear wave speed in methane hydrate as a function of temperature (–15 to 15°C) and pressure (4,000 to 9,000 psi uniaxial pressure).

The methane hydrate elastic moduli values reported in Chapter 5 are used in Chapter 6

to model the effect methane hydrate would have on wave speeds in sediments. Three elastic effective medium models are presented which place the methane hydrate in the sediment as a pore fluid component, a load-bearing sediment frame component (i.e., a sediment grain) or as an elastic cement at grain contacts. The cementation model is appropriate only for high porosity (36 to 40%) granular sediments (i.e., sands) but the other two models are appropriate for both sands and clay-rich ocean bottom sediments. Two models for the wave speed effects of free gas in the pore space are also presented. Free gas is often trapped in the sediments directly beneath gas hydrate deposits.

First, the models are applied to theoretical sediments to demonstrate the location dependent effect on compressional wave speed of placing methane hydrate (or methane gas) in the pore space. The models are then used to analyze data from hydrate bearing onshore sands in the Arctic (Northwest Eileen State Well #2) and hydrate-bearing, high porosity, clay-rich ocean bottom sediments from offshore of the Southeastern United States (ODP site 995). The modeling results show that methane hydrate does not act as a grain contact cement at Northwest Eileen State Well #2, but there is not enough independent data to choose between the pore fluid and sediment frame component models. The amount of data available at ODP site 995 makes it possible to conclude from the modeling that methane hydrate acts as a sediment frame component at site 995 and that it comprises about 2 to 4% of the sediment (by volume) from 200 to 450 mbsf with peak concentrations of 8 to 9% at some depths. The results also suggest that a large volume of methane gas may be trapped in the sediments beneath the gas hydrate containing interval at site 995.

Acknowledgements

First and foremost I want to thank my wife, Ruth, who helped me endure the tough days and celebrate the good ones. Without her, I never could have finished. I also want to thank my parents, Bruce and Judy, for their support, encouragement and love.

Additionally, I want to thank my advisor, Dr. Amos Nur, for introducing me to the topic of gas hydrates and allowing me to pursue a thesis based on them. I also want to thank Jack Dvorkin, who helped me push this thesis to completion and without whom the theoretical analyses presented herein would not have been possible.

I'd like to thank Keith Kvenvolden, Tom Lorenson, Lynn Orr and Peter Brewer for stimulating discussions about gas hydrates and occasional help and encouragement along the way.

I need to thank the guys in the Physics shop at Stanford University, Paul and Ezio formerly of the Petroleum Engineering department and Ben at the USGS in Menlo Park, CA. Their skill at the craft of metal work and machining turned two dimensional drawings into functioning, three-dimensional laboratory tools. Without them, ideas could not have become reality.

Finally, I want to thank Bill Waite for all his work and long hours in the lab. Without his positive attitude and skill at making things work, this thesis would have been vastly different. I also especially need to thank Steve Kirby, Laura Stern, Sue Circone and John Pinkston at the USGS in Menlo Park and Bill Durham at Lawrence Livermore National Laboratory for letting Bill Waite and myself be part of their ongoing gas hydrate research project. Steve Kirby and John Pinkston designed the pressure vessel and Steve Kirby and Laura Stern devised the synthesis method for forming methane gas hydrate described in Chapters 4 and 5. Manika Prasad of Stanford University helped with the initial design of

the transducers described in Chapter 4.

This thesis is dedicated to my wife Ruth and our daughters Erica and Jessica.

Contents

List of Tables

List of Figures

Chapter 1

Introduction

Clathrate hydrates of natural gases, commonly referred to as gas hydrates, are nonstoichiometric crystalline solids stable at temperatures above the freezing point of water. Gas hydrates are comprised of a hydrogen-bonded water lattice and entrapped "guest" molecules. The guest molecules are trapped in the polyhedral void spaces created by the water crystal structure. For a compilation of the current state of the art in gas hydrate thermodynamics and kinetics research see Sloan (1998). A more geologically focused discussion can be found in the review papers of Kvenvolden(1993a; 1993b). This thesis reports on new laboratory and modeling results for elastic wave speeds in gas hydrate and sediments containing gas hydrate.

1.1 Background

Gas hydrates were first reported by H. Davy (1811) when he described the formation of a solid by cooling mixtures of chlorine gas and water in the laboratory. For the next century gas hydrate research focused on identifying the compounds that formed clathrate hydrates and discerning their ratio of water to guest. This research showed that considerable amounts of the guest molecule could be stored in the gas hydrate crystal structure. However, until the early part of this century, gas hydrates were treated mostly as laboratory curiosities of indeterminate crystal structure and stoichiometry.

The discovery in the 1930s that oil and gas pipelines could be plugged by the formation

of gas hydrate (Hammerschmidt, 1934) led to a considerable amount of research on the physical structure of gas hydrates and their thermodynamic properties. This research was greatly aided by the invention of modern analytical tools such as x-ray diffraction, nuclear magnetic resonance and various forms of spectroscopy and revealed that gas hydrates were in fact a family of non-stoichiometric crystalline solids which trapped molecules in cages within the water crystal lattice.

Gas hydrate was first hypothesized to occur in nature in the late 1960s and the first samples were recovered in the early 1970s (discussed in Sloan, 1998). Samples have now been recovered from a number of wells drilled offshore on continental margins and beneath deep inland seas (Booth et al., 1996). Samples have also been recovered onshore from wells drilled in the Arctic (Bily and Dick, 1974; Uchida et al., 1998).

Additional evidence for the presence of gas hydrate in nature comes from a common marine seismic event called a bottom simulating reflector (BSR). A BSR is a seismic event of reverse polarity which parallels the seafloor and cross cuts lithostratigraphic events. It is now generally accepted that gas hydrate related BSRs are caused by gas accumulating beneath sediments hydraulically sealed by gas hydrate. Some BSRs can be created by other geologic phenomena such as the depth and temperature controlled diagenetic transition from Opal A to Opal CT (Lonsdale, 1990) and gas hydrates have been found with no associated BSR (von Huene and Aubouin et al., 1985), but many BSRs have been positively correlated with gas hydrate deposits in the earth. The worldwide distribution (Figure 1.1) of BSRs and recovered gas hydrate samples (predominantly methane gas hydrate), suggest that gas hydrates and associated free gas may comprise a huge methane reservoir in the shallow geosphere (Kvenvolden, 1993c).

1.2 Gas Hydrate Geoscience Research Areas

Recognition of the wide spread distribution of gas hydrate in nature has spurred geoscience research in three main areas: alternative energy source, climate change and sea floor stability. Additional areas of research not covered here but also of interest are the inhibition of gas hydrate formation in oil and gas pipelines (Sloan, 1998), the formation of air hydrates in the earth's icecaps (Miller, 1969), and the occurrence of gas hydrate on other objects

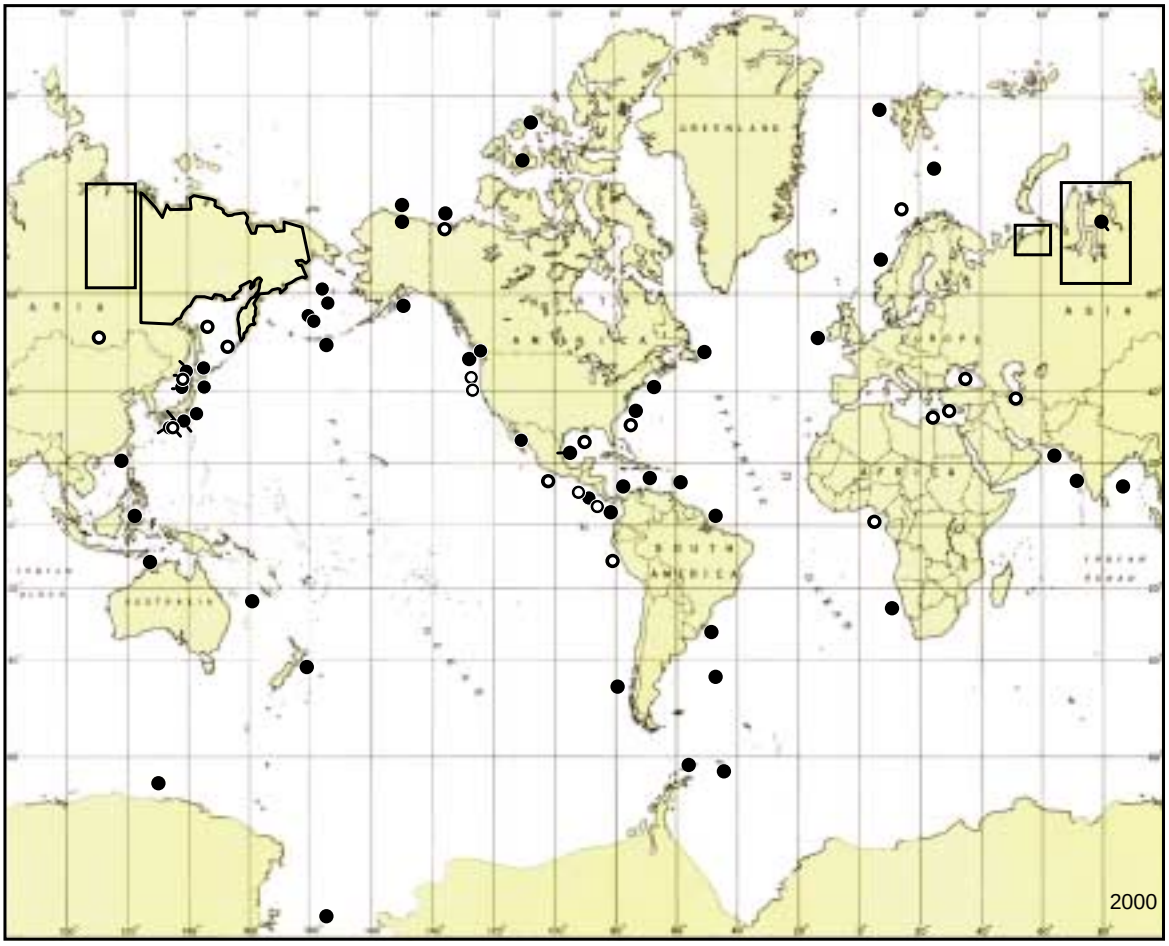

Figure 1.1: Worldwide distribution of natural gas hydrate deposits. Open circles signify locations where gas hydrate samples have been recovered from the subsurface. Filled circles represent locations where gas hydrate is inferred to be present based on the presence of a BSR. Boxed areas represent regions with a high potential for gas hydrate. Map and data courtesy K. Kvenvolden, pers. comm.

in the solar system such as comets and the planets and moons of the outer solar system (Consolmagno, 1983).

Historical estimates of the amount of methane stored in terrestrial gas hydrates vary by several orders of magnitude, but recent independent estimates have begun to converge to a value of $\sim 700,000$ Tcf at standard temperature and pressure (STP). This amount is twice the methane equivalent of all known coal, oil and natural gas deposits in the world (Kvenvolden, 1993c). Gas hydrates are believed to be the second largest reservoir of carbon in the shallow geosphere behind only dispersed organic carbon (kerogen and bitumen). If these estimates are correct, gas hydrates may represent a significant source of energy in the next century. However, many questions related to the in situ disassociation and production of gas hydrates remain to be answered before this potential can be realized. Japan and India are two nations particularly interested in this aspect of gas hydrate research. Both have large energy needs but inadequate conventional hydrocarbon resources. The Japanese drilled a gas hydrate production research well in the Nankai Trough in 1999. The only nation believed to have produced natural gas from gas hydrates is Russia, where it is possible that gas was produced from gas hydrates beneath permafrost at the Messoyakh field in Siberia.

The size of the gas hydrate related methane reservoir has also stimulated interest in the climatic effects of methane hydrate formation and disassociation. Methane is a highly efficient greenhouse gas (Shine et al., 1990). Extensive gas hydrate deposits potentially represent a complicated feedback mechanism for natural climate control (MacDonald, 1990; Kvenvolden, 1993a). Recent research has suggested that much of the methane released from gas hydrates should be absorbed by the ocean, and global climate modeling suggests the effects of methane release from gas hydrates are smaller than those associated with the burning of fossil fuels and the parameters governing climate sensitivity (Harvey and Huang, 1995). Still, Dickens et al. (1995; 1997) have shown that the carbon isotopic shift associated with the latest Paleocene thermal maximum could plausibly be explained by a massive release of the light molecular weight carbon stored in methane hydrates. The effect of gas hydrates on climate remains an open question.

The distribution of gas hydrate deposits also suggests that gas hydrates could represent a significant geohazard. Gas hydrates displace fluid from the pore space. Therefore, the

presence of gas hydrate potentially modifies the shear strength and other mechanical properties of the sediment in which it forms (McIver, 1982), making it more rigid than it would otherwise be. However, the pressure and temperature requirements for gas hydrate stability (Chapter 2) place a limit on the depth to which gas hydrates are stable in the subsurface. As sediments are added at the sea floor, gas hydrates are eventually buried deeply enough that they begin to disassociate from the heat supplied by the Earth. Thus, what was once an anomalously strong sedimentary section now becomes anomalously weak. This weak layer provides a potential glide plane for an underwater land slide. A number of authors have reported submarine land slides correlated with the location of gas hydrate zones (Carpenter, 1981; Bugge et al., 1988; Popenoe et al., 1993; Kayen and Lee, 1993; Field and Barber, 1993; Paull et al., 1996). As offshore hydrocarbon exploration moves into deeper and deeper water, the geotechnical properties of sediments containing gas hydrate will become more and more important. The presence of gas hydrate in the sediments at a drillsite may strongly impact engineering decisions about well bore stability, subsea emplacements and platform design.

1.3 Defining the Problem

The methane resource estimates which drive much of the recent interest in gas hydrates are highly speculative because of the difficulty in determining the amount of gas hydrate present in the subsurface. Currently, reliable technology does not exist for extracting intact gas hydrate samples from wells. The process of drilling disturbs the stability of the material and transporting the hydrate-bearing core sample to the surface removes the gas hydrate from its pressure and temperature stability field. Work is being done to address these problems with some success (Dickens et al., 1997; Uchida et al., 1998), but gas hydrate deposits can cover large areas (many thousands of square km) and are very heterogeneous. Spot sampling by drilling will never be able to completely characterize natural gas hydrate concentrations and distributions. Instead a remote sensing technique is needed which can survey large volumes of the subsurface, even beneath a few kilometers of water. The remote sensing technique that offers the best resolution is controlled-source seismology. But in order to interpret seismic data for gas hydrate concentration or to use them for

extending the ground truth obtained at wells to entire deposits, the elastic properties of sediments containing gas hydrate must be understood. Unfortunately, very little is known about the elastic properties of gas hydrate and sediments containing gas hydrate. This problem was highlighted in a recent report on the recommended directions for future gas hydrate research (Sloan et al., 1999)

To address this gap in knowledge about gas hydrates, I have conducted laboratory experiments to measure the compressional and shear wave speeds through pure gas hydrate and compressional wave speeds through granular materials containing gas hydrate. Additionally, I have modeled gas hydrate-sediment systems based on real-world well log and vertical seismic profile (VSP) data. The results described in the following chapters show that compressional and shear wave speeds through pure gas hydrate can be successfully and reliably measured in the laboratory and that elastic modeling of sediments containing gas hydrate can be used to quantify the presence of gas hydrate and to infer its location in the pore space.

1.4 Description of Chapters

The following is a short summary of the contents of each chapter in this thesis.

Chapter 1 presents a brief background discussion of what gas hydrates are and why they have generated such interest in the last few years. It discusses the need for more information related to the elastic properties of gas hydrates and sediments containing gas hydrate.

Chapter 2 provides a synopsis of the crystallographic information about gas hydrates and describes the thermodynamic conditions necessary for their formation. A summary of all published laboratory measurements and theoretical predictions of compressional and shear wave speeds in pure gas hydrate is also provided, along with a summary of all laboratory wave speed measurements on gas hydrate-sediment composites.

Chapter 3 describes experiments performed on propane hydrate formed in a clear-walled pressure vessel by bubbling gas through water and water saturated sediments. It describes the complications associated with this method of forming gas hydrate in the laboratory and comes to the conclusion that samples formed in this manner are unsuitable for

physical property measurements.

Chapter 4 describes compressional and shear wave speed measurements made on compacted polycrystalline ice samples and compacted polycrystalline methane hydrate samples formed by reacting methane gas with granulated ice.

Chapter 5 describes modifications made to the apparatus and procedures described in Chapter 4 that made it possible to measure compressional and shear wave speeds in compacted ice and compacted methane hydrate samples as functions of temperature and uniaxial pressure. These results represent the first ever reported measurements of compressional and shear wave speed in methane hydrate as functions of temperature and pressure. The wave speed results are used to calculate isotropic, dynamic, elastic moduli for the polycrystalline ice and polycrystalline methane hydrate samples.

Chapter 6 details physics-based elastic effective medium models for gas hydrate-sediment composites and uses them to analyze data acquired at Northwest Eileen State Well #2, drilled on the north slope of Alaska and at ODP site 995 (Blake-Bahama Ridge), located off the coast of the southeastern United States.

1.5 References

Booth, J. S., M. M. Rowe and K. M. Fischer, 1996, Offshore gas hydrate sample database with an overview and preliminary analysis, U.S. Geol. Surv. Open-File Report **96-272**, 17pp.

Bily, C. and J. W. L. Dick, 1974, Naturally occurring gas hydrates in the MacKenzie Delta, N.W.T. Bulletin of Canadian Petroleum Geology, **22**, 340–352.

Bugge, T., R. H. Belderson, N.H. Kenyon, 1988, The Storegga Slide, Philosophical Transactions of the Royal Society of London, **A325**, 357–388.

Carpenter, G., 1981, Coincident sediment slump/clathrate complexes on the US Atlantic continental slope, Geo-Marine Letters, **1**, 29–32.

Consolmagno, G., 1983, Ice-rich moons and the physical-properties of ice, Journal of Physical Chemistry, **87**, 4204–4208.

Davy, H., 1811, The Bakerian Lecture: On some of the combinations of oxymuriatic gas and oxygene, and on the chemical relations of these principles, to inflammable bodies, Philosophical Transactions of the Royal Society of London, **101**, 1–35.

Dickens, G. R., J. R. O'Neil, D. K. Rea, R. M. Owen, 1995, Dissociation of oceanic methane hydrate as a cause of the carbon isotope excursion at the end of the Paleocene, Paleoceanography, **10**, 965–971.

Dickens, G. R., M. M. Castillo, J. C. G. Walker, 1997, Blast of gas in the latest Paleocene: simulating first-order effects of massive dissociation of oceanic methane hydrate, Geology, **25**, 259–262.

Dickens, G. R., C. K. Paull and P. Wallace, 1997, Direct measurement of in situ methane quantities in a large gas-hydrate reservoir, Nature, **385**, 427–428.

Field, M. E. and J. H. Barber Jr., 1993, A submarine landslide associated with shallow seafloor gas and gas hydrates off Northern California, in Schwab, W. C. et al., eds., Submarine Landslides: Selective studies in the U.S. Exclusive Economic Zone, U.S.G.S. Bulletin **2002**, 151–157.

Harvey, L. D. D and Z. Huang, 1995, Evaluation of the potential impact of methane clathrate destabilization on future global warming, Journal of Geophysical Research–Atmospheres, **100**, 2905–2926.

Hammerschmidt, E. G., 1934, Formation of gas hydrates in natural gas transmission lines, Industrial Engineering Chemistry, **26**, 851–855.

Kayen, R. E. and H. J. Lee, 1993, Slope Stability in Regions of Sea-Floor Gas Hydrate: Beaufort Sea Continental Slope, in Schwab, W. C. et al., eds., Submarine Landslides: Selective studies in the U.S. Exclusive Economic Zone, U.S.G.S. Bulletin **2002**, 97–103.

Kvenvolden, K. A., 1993a, Gas Hydrates-Geological Perspective and Global Change, Reviews of Geophysics, **31**, 173-187.

Kvenvolden, K. A., 1993b, A Primer on Gas Hydrates, in The Future of Energy Gases - U.S.G.S. Professional Paper **1570**, 279–291.

Kvenvolden, K. A., 1993c, Gas Hydrates as a Potential Energy Resource-A Review of Their Methane Content, in The Future of Energy Gases - U.S.G.S. Professional Paper **1570**, 555–561.

Lonsdale, M. J., 1990, The Relationship between silica diagenesis, methane, and seismic reflections on the South Orkney Microcontinent, Proceedings of the ODP, Scientific Results, **113**, 27–37.

MacDonald, G. T., 1990, Role of methane clathrates in past and future climates, Climatic Change, **16**, 247–281.

McIver, R. D., 1982, Role of naturally occurring gas hydrates in sediment transport, AAPG Bulletin, **66**, 789–792.

Miller, S. L., 1969, Clathrate hydrates of air in Antarctic ice, Science, **165**, 489–490.

Paull, C. K., W. J.Buelow, W. Ussler III and W. S. Borowski, 1996, Increased continental-margin slumping frequency during sea-level lowstands above gas hydrate-bearing sediments, Geology, **24**, 143–146.

Popenoe, P., E. A. Schmuck and W. P. Dillon, 1993, The Cape Fear Landslide: slope failure associated with salt diapirism and gas hydrate decomposition, in Schwab, W. C. et al., eds., Submarine Landslides: Selective studies in the U.S. Exclusive Economic Zone, U.S.G.S. Bulletin **2002**, 41–68.

Shine, K. P., R. G. Derwent, D. J. Wuebbles and J.J. Morcrette, 1990, Radiative forcing of climate, in Climate Change, the IPCC Scientific Assessment, ed. J. T. Houghton, G. J. Jenkins, and J. J. Ephraums, 41–68.

Sloan, E. D., Jr., 1998, Clathrate hydrates of natural gases, 2nd Ed., Marcel Dekker, New York, 705pp.

Sloan, E. D., P. G. Brewer, C. K. Paull, T. S. Collett, W. P. Dillon, W. S. Holbrook, K. A. Kvenvolden, 1999, Future of gas hydrate research, EOS, Transactions, American Geophysical Union, **80**, 247.

Uchida, T., S. Dallimore, M. Nixon, and J. Mikami, 1998, Occurrences of gas hydrates obtained from the JAPEX/JNOC/GSC Mallik 2L-38 research well, Proceedings of the International Symposium on Methane Hydrates: Resources in the Near Future?, 371–378.

von Huene, R., J. Aubouin, et al., 1985, Initial Reports of the DSDP, **84**, U.S. Govt. Printing Office, Washington.

Chapter 2

Gas Hydrate Properties

2.1 Introduction

In this chapter I present the relevant crystallographic and thermodynamic data for gas hydrates. This will be done by providing a basic primer on the crystallographic properties of naturally occurring gas hydrate structures and the pressure and temperature conditions required for their formation. Once these basic properties of the material have been described, I will turn to a summary of available theoretical estimates and laboratory measurements of compressional and shear wave speeds through gas hydrate and laboratory measurements of compressional and shear wave speeds in sediments containing gas hydrate.

2.2 Crystal Structure

Gas hydrates formed from natural gases occur in one of three crystallographic lattice types: body centered cubic (Structure I), diamond cubic (Structure II) and hexagonal (Structure H). Structures I and II have been known for many years. Structure H was identified for the first time just a decade ago. The basis for all three gas hydrate crystal lattices is a tetrahedral arrangement of water molecules held together by hydrogen bonds. The tetrahedral arrangement of water molecules in gas hydrate is very similar to the tetrahedral arrangement of water molecules in standard water ice Ih. The bond lengths differ by only about 1% and the angles between oxygen atoms differ by less than 4° (Sloan, 1998). The difference

comes from how the water tetrahedra are arranged. The gas hydrate crystal lattice is comprised of a series of polyhedral cages whereas ice is a collection of non-planar "puckered" hexagonal rings. As a result, gas hydrate has the ability to trap guest molecules within its crystal lattice. This in turn changes the thermodynamic conditions necessary for its formation and allows gas hydrate to form at temperatures above the freezing point of water provided a sufficient supply of the guest molecules is available to fill some of the cages and help stabilize the structure.

Structure H (sH) differs markedly in its crystallographic details from structures I and II. Structure H was only recently identified and as such is a less extensively studied form of natural gas hydrate. sH requires a particularly large guest molecule to be present in conjunction with smaller molecules for stability. In this thesis, only gas hydrates of structure I (sI) and structure II (sII) have been studied. A research program looking at the elastic properties of sH would be an excellent topic for future study, but will not be included here. The following summary of sI and sII gas hydrate crystal properties and thermodynamic stability conditions is based on the review of Sloan (1998) and references contained therein.

2.2.1 Structure I

All of the natural gas hydrate crystal structures can be represented as a collection of polyhedral cages formed by hydrogen bonded water molecules. In the literature, the polyhedra are usually referred to in the manner suggested by Jeffrey (1984), namely, $n_i{}^{m_i}$, where n_i represents the number of edges of face type i and m_i is the number of faces of type i. Under this system, a dodecahedron would be labeled 5^{12} because it is comprised of 12 pentagonal faces. Structure I is comprised of two kinds of polyhedra, 5^{12} and $5^{12}6^2$. Structure I is an example of vertex linking between the 5^{12} cavities in three dimensions. The spaces left over are the $5^{12}6^2$ cages. The 5^{12} cage is essentially spherical with a radius of 3.95Å. The $5^{12}6^2$ cage is shaped like a slightly oblate spheroid. Its radius varies by as much as 14.4% (see Table 2.1).

The unit cell of sI gas hydrate is cubic, approximately 12Å to a side, and contains six of the $5^{12}6^2$ and two of the 5^{12} cages, for a total of eight potential guest sites per unit cell. This gives a potential molar gas density of 7690 mol/m^3. The molar density of an ideal gas at STP (0°C, 1 atm) is only 44.6 mol/m^3. Therefore, sI gas hydrate formation is potentially

Table 2.1: Gas Hydrate Cage Properties

Gas Hydrate Structure	sI		sII	
Polyhedral Cage Type	5^{12}	$5^{12}6^2$	5^{12}	$5^{12}6^4$
Cages/Unit Cell	2	6	16	8
Avg. Cage Radius[a], Å	3.95	4.33	3.91	4.73
Variation in Radius, %	3.4	14.4	5.5	1.73

[a] Average distance from center of cage to oxygen atoms
(Table modified from Sloan (1998, p. 33))

equivalent to a 172 fold compression of the gas. For an ideal gas, this compression is achieved at 172 atmospheres which is the hydrostatic pressure of a 1780 m column of water of density 1000 kg/m^3. The compression in forming gas hydrate is significantly less than the compression achieved during gas liquefaction.

Each crystallographic unit cell in sI gas hydrate contains 46 water molecules and 8 cages, giving a maximum possible guest to water ratio of $1 : 5\frac{3}{4}$ if all the cages are filled. Equivalently, one could say that sI gas hydrate is at least 85.2 mol percent water. However, it is not thermodynamically possible to fill all the cages, so sI gas hydrate is invariably more than 85 mol percent water and the effective ideal gas compression factor is always less than 172.

The density of sI gas hydrate depends on the mass of the guest species and the degree of cage occupancy. However, the lower limit for density can be calculated from the molar mass of water (18 g/mol) and the unit cell dimension for sI gas hydrate (12 Å), giving an empty cage density of 0.80 g/cm^3. For comparison, the density of ice Ih is approximately 0.92 g/cm^3.

Hooke's law for a general, anisotropic linear elastic solid (in Einstein's notation) is (Mavko et al., 1998)

$$\sigma_{ij} = c_{ijkl}\varepsilon_{kl}, \tag{2.1}$$

where σ_{ij} is the stress tensor, ε_{kl} is the strain tensor and c_{ijkl} is the elastic stiffness tensor which relates stress to strain in the material. Tensor symmetry and energy constraints reduce the number of independent c_{ijkl} from 81 to 21. Because of this, it is common to

rewrite the anisotropic form of Hooke's law as

$$\sigma_I = c_{IJ}\varepsilon_J, \tag{2.2}$$

where the six independent components of the stress and strain tensors have been rewritten as 6-element column vectors:

$$\sigma = \begin{bmatrix} \sigma_1{=}\sigma_{11} \\ \sigma_2{=}\sigma_{22} \\ \sigma_3{=}\sigma_{33} \\ \sigma_4{=}\sigma_{23} \\ \sigma_5{=}\sigma_{13} \\ \sigma_6{=}\sigma_{12} \end{bmatrix} \quad \text{and} \quad \varepsilon = \begin{bmatrix} \varepsilon_1{=}\varepsilon_{11} \\ \varepsilon_2{=}\varepsilon_{22} \\ \varepsilon_3{=}\varepsilon_{33} \\ \varepsilon_4{=}2\varepsilon_{23} \\ \varepsilon_5{=}2\varepsilon_{13} \\ \varepsilon_6{=}2\varepsilon_{12} \end{bmatrix}, \tag{2.3}$$

and the four subscripts ($ijkl$) of the compliance tensor have been reduced to two (IJ), using the following convention:

$ij(kl)$	$I(J)$
11	1
22	2
33	3
$23, 32$	4
$13, 31$	5
$12, 21$	6

(2.4)

As a result, the compliance tensor (c_{ijkl}) can be written as a 6×6 matrix (c_{IJ}).

In sI gas hydrate, the 5^{12} cages are arranged in a body centered cubic lattice, placing it in the crystallographic space group Pm3n (Sloan, 1998). The stiffness matrix c_{IJ} for this and all other materials with cubic symmetry (Nye, 1985) is

$$(c_{IJ}) = \begin{pmatrix} c_{11} & c_{12} & c_{12} & \cdot & \cdot & \cdot \\ c_{12} & c_{11} & c_{12} & \cdot & \cdot & \cdot \\ c_{12} & c_{12} & c_{11} & \cdot & \cdot & \cdot \\ \cdot & \cdot & \cdot & c_{44} & \cdot & \cdot \\ \cdot & \cdot & \cdot & \cdot & c_{44} & \cdot \\ \cdot & \cdot & \cdot & \cdot & \cdot & c_{44} \end{pmatrix}. \tag{2.5}$$

From (2.5) we see that there are three independent constants in the stiffness matrix c_{IJ} as opposed to two in isotropic materials. Therefore, the elastic properties of individual crystals of sI gas hydrate are anisotropic with cubic symmetry.

2.2.2 Structure II

Structure II gas hydrate is also a collection of two differently sized polyhedral cages. As in sI, the smallest cage is 5^{12}, but in sII they are connected by sharing faces in three dimensions. The remaining spaces are the $5^{12}6^4$ cages which are arranged in a diamond lattice. The 5^{12} cage is slightly smaller than in sI, with a radius of 3.91Å. The $5^{12}6^4$ cage is reportedly the most spherical of the three, with a radius of 4.73Å (see Table 2.1).

The unit cell of sII is also cubic, but larger than in sI. It is approximately 17.3Å to a side. The unit cell contains 16 of the 5^{12} and 8 of the $5^{12}6^4$ cages, for a total of 24 potential guest sites per unit cell. This gives a potential molar density of 7700 mol/m^3 which represents a compression factor of approximately 173 times over an ideal gas at STP. However, as with sI, this is an unachievable theoretical upper limit.

Each unit cell in sII gas hydrate contains 136 molecules of water, giving an empty cage density of 0.79 g/cm^3. If all 24 cages in sII gas hydrate are occupied, the guest to water ratio becomes $1 : 5\frac{2}{3}$ and the gas hydrate is 85 mol percent water.

Structure II gas hydrate belongs to space group Fd3m (Sloan, 1998). Because of its cubic symmetry, the stiffness matrix (c_{IJ}) for sII is also given by (2.5), although the values of the three independent constants need not be (and probably are not) the same as for sI.

2.3 Thermodynamic Equilibrium Conditions

The pressure and temperature conditions required to form gas hydrate depend strongly on the guest molecules available to fill the cages of the gas hydrate crystal. Similarly, the gas hydrate crystal structure is completely determined by the size of the molecules present to fit in the cages. The cage radii listed in Table 2.1 represent the average distance from the center of the cage to the oxygen atoms in the water molecules that comprise the crystal lattice. This is an overestimation of the space available for the guest. Sloan (1998) suggests that a better estimate is the difference between the average van der Waals radius of the water

Table 2.2: Guest Molecule/Cage[a] Diameter Ratios

Guest Molecule	Guest Diameter (Å)	Guest/Cage Diameter Ratio sI 5^{12}	sI $5^{12}6^2$	sII 5^{12}	sII $5^{12}6^4$
He	2.28	0.447	0.389	0.454	0.342
H_2	2.72	0.533	0.464	0.542	0.408
Ne	2.97	0.582	0.507	0.592	0.446
Ar	3.80	0.745	0.648	0.757†	0.571†
Kr	4.00	0.784	0.683	0.797†	0.601†
N_2	4.10	0.804	0.700	0.817†	0.616†
O_2	4.20	0.824	0.717	0.837†	0.631†
CH_4	4.36	0.855†	0.744†	0.868	0.655
Xe	4.58	0.898†	0.782†	0.912	0.687
H_2S	4.58	0.898†	0.782†	0.912	0.687
CO_2	5.12	1.00	0.834†	1.02	0.769
C_2H_6	5.5	1.08	0.939†	1.10	0.826
C_3H_8	6.28	1.23	1.07	1.25	0.943†
i-C_4H_{10}	6.5	1.27	1.11	1.29	0.976†
n-C_4H_{10}	7.1	1.39	1.21	1.41	1.07

†Cage occupied by molecule

[a]Cage diameters calculated from Table 2.1 minus twice the water van der Waals radius ($2 \cdot 1.4$Å)

(Table modified from Sloan, 1998, p. 47)

molecule (1.4Å) and the cage radii listed in Table 2.1. This gives diameters of 5.10Å and 5.86Å, in the 5^{12} and $5^{12}6^2$ cages of sI, and 5.02Å and 6.66Å in the 5^{12} and $5^{12}6^4$ cages of sII, respectively. The ratios of some gas molecular diameters to these recalculated cage diameters are shown in Table 2.2. In this table, cage occupation by a guest molecule is denoted with a superscripted dagger (†). Note that if the ratio is greater than or equal to one, the guest molecule does not occupy that cage.

Table 2.2 contains a number of interesting features characteristic of gas hydrate formation. First, if a gas hydrate guest is found to occupy the small cage, it also enters the large cage. But it is also possible for a gas hydrate structure to be stabilized if only the large cages are filled, as with ethane in sI and propane and isobutane in sII. Second, note that molecules between 3.8 and 4.2Å in diameter form sII even though the size difference

between the 5^{12} cages in sI and sII is apparently insignificant and the $5^{12}6^4$ cage in sII is larger than the $5^{12}6^2$ cage in sI. This is thought to occur because these guests are too small to stabilize the large cage and the density of small cages is larger in sII (Sloan, 1998). And finally, note that molecules smaller than 3Å do not stabilize any of the cages whereas molecules larger than 6.6Å do not fit into any of the cages in sI or sII (molecules up to 9Å can fit in sH). This information is summarized graphically in Figure 2.1

As shown in Table 2.2, guest molecules take up a significant fraction of available cage volume. As a result, the guest's translational freedom is fairly limited. However, NMR spectroscopy and dielectric relaxation measurements by Davidson et al. (1977; 1984) have shown that there is little or no barrier to guest molecule rotation within the cages. This implies there is little interaction between guest and water lattice. The lattice essentially acts as a physical restraint. In support of this, von Stackelberg and Jahns (1954) found no evidence of lattice distortion by any guest. *This implies that placing guest molecules into the cages does not affect the elastic properties of the material, which are governed by the crystal lattice properties, but rather changes only the density*.

However, there is some evidence that this simple interpretation may be incorrect. Holder et al. (1994) recently argued that guest induced lattice deformations two orders of magnitude less than the cell dimension do occur and that they have a profound effect on thermodynamic parameters. Additionally, the amount of heat it takes to disassociate gas hydrates with only the large cages occupied is considerably higher than for gas hydrates with both cages occupied and the thermal conductivity of gas hydrates is anomalously low when compared to ice (Sloan, 1998). Tse and White (1988) and Tse et al., (1997) have explained these anomalous gas hydrate heat transport properties as being due to a resonance between the motions of water molecules in the crystal lattice and the guest molecules.

In summary, to first order, guest molecules are relatively free to move and rotate within their cages, but evidence is mounting that they do interact with the water molecules in the lattice. This interaction may affect the elastic properties of the material.

Complete coverage of the thermodynamics of gas hydrate formation is beyond the scope of this thesis. There is a general statistical thermodynamic theory for gas hydrates, advanced by van der Waals and Platteeuw (1959) and revised incrementally since then. It

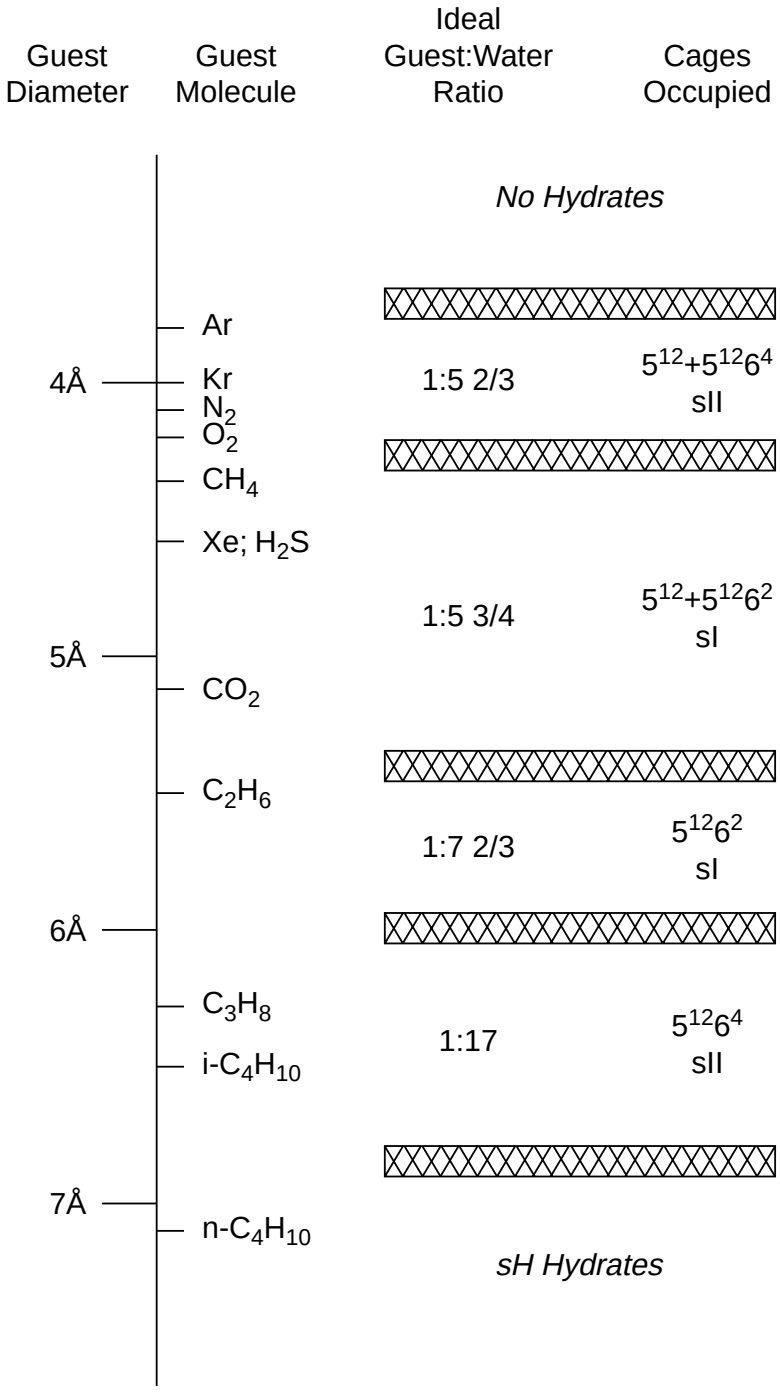

Figure 2.1: Graphical representation of how molecule size determines whether sI or sII gas hydrate is formed. Cross-hatched areas represent the approximate boundary between filling both cages or one cage within a structure, or between the formation of sI or sII (or no structure or sH). Figure modified from Sloan (1998).

is reportedly very accurate at predicting the conditions necessary for gas hydrate formation, cage occupancy rates and the effects of mixing different gases. I refer the reader to Sloan (1998) for an extensive discussion of this theory and gas hydrate thermodynamics and kinetics in general.

In this thesis, I focus exclusively on the thermodynamic stability requirements for methane and propane hydrate, the types formed in the experiments reported in this thesis. Methane and propane hydrate are examples of sI and sII gas hydrate, respectively.

2.3.1 Structure I – Methane Hydrate

Many molecules form sI gas hydrate. From a geoscience perspective, the most relevant is methane because most recovered natural gas hydrate samples have been sI hydrates with methane comprising more than 90% of the guest molecules. The methane in these samples is predominantly microbially derived. Methane and other gas hydrate forming hydrocarbon gases are also produced when elevated temperatures and pressures act on carbon-rich sediments. These are the same processes that produce oil. If these hydrocarbon gases migrate to shallow depths in the sediment, where temperatures are much lower, they can also form gas hydrates. Thermally derived hydrocarbon gases have been found in gas hydrate samples recovered from the Gulf of Mexico (Brooks et al., 1984) and the Caspian Sea (Ginsburg et al., 1992). However, the larger molecular size of the heavier hydrocarbon gases usually leads to the formation of sII (discussed below) or sH.

As mentioned above, the van der Waals and Platteeuw model accurately predicts the macroscopic pressure and temperature conditions necessary for gas hydrate formation for a number of gases and their combinations. However, when possible, it is better to have actual measurements. Figure 2.2 shows the pressure and temperature stability field for methane gas hydrate as determined from experiments.

Figure 2.3 shows the number of moles of methane gas in one cubic meter as a function of pressure and temperature based on the modified equation of state for methane presented by Sychev et al. (1987). The labeled contour is the theoretical maximum number of moles of methane stored in one cubic meter of methane hydrate. From this plot, one can see that for pressures less than about 10-15 MPa, gas hydrate formation potentially represents a compression of the methane relative to the free gas phase. At higher pressures, the free gas

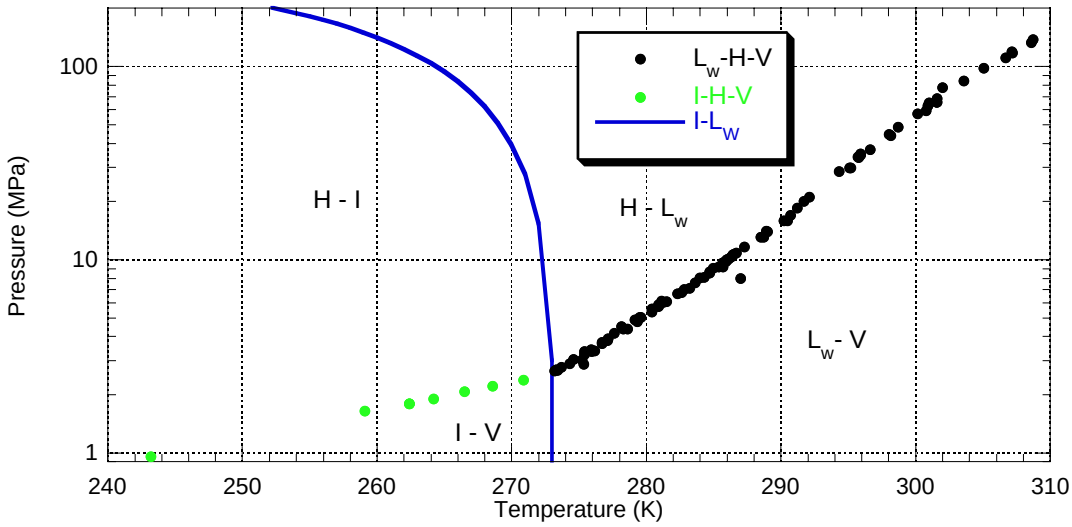

Figure 2.2: Methane hydrate pressure and temperature stability field. Each point represents an equilibrium temperature and pressure measurement for the given phase combination (H = Gas Hydrate, I=Ice Ih, L_W = Liquid Water, V = Methane Gas). The I-L_W line is from W.B. Durham (pers. comm., 1999), measured on a pure water system. Measurements on Xenon gas hydrate and ice (Aaldijk, 1971) suggest the presence of gas hydrate does not affect the melting curve of ice Ih, provided the hydrate guest molecule is not highly soluble in water. Methane hydrate data are from the compilation by Sloan (1998) and the recent measurements of Nakano et al. (1999).

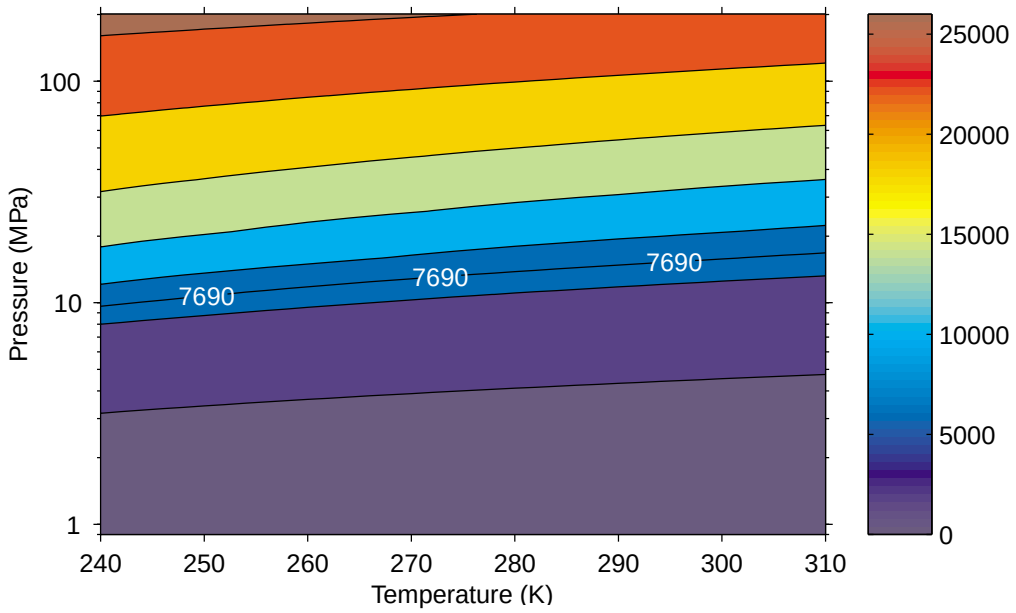

Figure 2.3: Moles of methane gas in a cubic meter volume as a function of pressure and temperature, calculated after Sychev et al. (1987). The labeled contour (7690) is the theoretical maximum molar density of methane in methane hydrate. Comparing to Figure 2.2, we see that at many pressures and temperatures, methane in the gas phase is more compressed than methane in the hydrate phase.

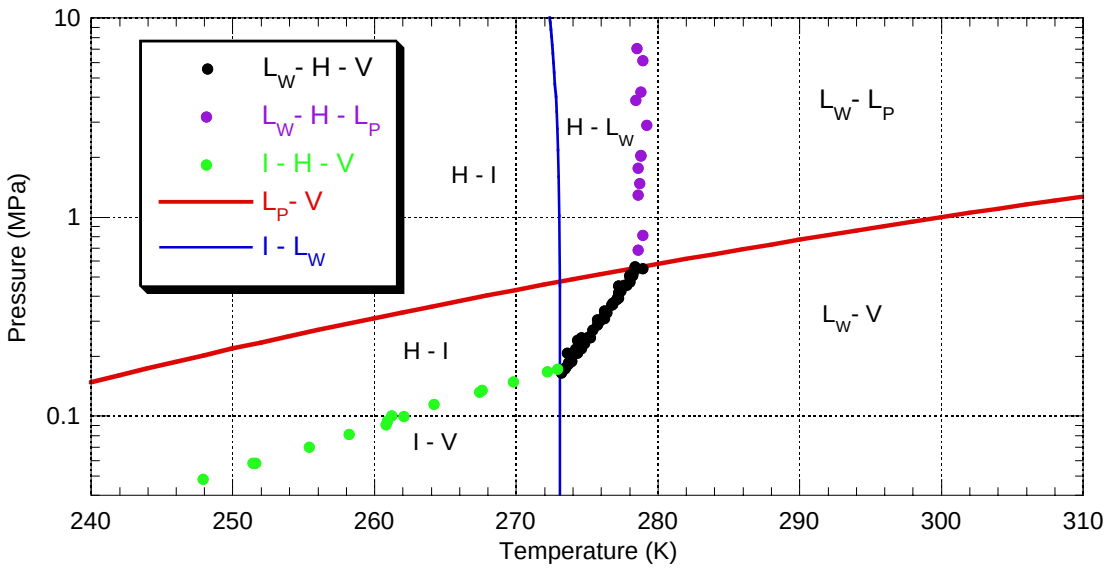

Figure 2.4: Propane hydrate pressure and temperature stability field. Each point represents an equilibrium temperature and pressure measurement for the given phase combination (H = Gas Hydrate, I=Ice Ih, L_W = Liquid Water, L_P = Liquid Propane, V = Propane Gas). The I-L_W line is from W.B. Durham (pers. comm., 1999), measured on a pure water system. Measurements on Xenon gas hydrate and ice (Aaldijk, 1971) suggest the presence of gas hydrate does not affect the melting curve of ice Ih, provided the hydrate guest molecule is not highly soluble in water. The L_P -V curve is from Sychev et al. (1987) for a pure propane system. Propane hydrate data are from the compilation by Sloan (1998).

phase actually stores more gas molecules per cubic meter. 10-15 MPa is equivalent to a water depth of 1.0 to 1.5 km, assuming a water density of 1000 kg/m^3.

2.3.2 Structure II – Propane Hydrate

I chose propane gas hydrate for study in this thesis because the pressure conditions necessary for its formation are very modest, as can be seen in Figure 2.4. These pressure conditions make it possible to use a clear-walled pressure vessel for gas hydrate formation. As a result, I was able to record several hours of video footage of propane hydrate being formed by bubbling propane gas through water and water saturated sediments. The observations made during these experiments are discussed in Chapter 3.

Propane hydrate is a somewhat unusual gas hydrate because the guest molecule occupies only the $5^{12}6^4$ cage of sII. Consequently, the maximum possible gas molar density is 2600 mol/m^3, equivalent to a gas compression factor of 57 compared to an ideal gas at STP.

2.4 Gas Hydrate Wave Speed Data

There are very few published papers which describe theoretical estimates or laboratory measurements of elastic wave speeds in gas hydrate or sediments containing gas hydrate. There is also a great deal of confusion in the literature about the few elastic wave speed and moduli measurements that have been made. For example, some data compilation papers attribute measurements to the wrong gas hydrate crystal structure and sometimes the values within data tables are not self-consistent. In this section I describe and analyze the published models and laboratory measurements of elastic wave speeds in gas hydrate.

2.4.1 Wave Speeds in Pure Gas Hydrate – Models

There are only two published papers which propose theories for estimating the speed of compressional waves through bulk samples of gas hydrate. The first (Whalley, 1980), starts from the premise that ice Ih and gas hydrate are similar materials and should have similar properties. The paper estimates the compressional wave speed ratio between gas hydrates and ice by estimating some of the thermophysical properties of gas hydrate to be equal to ice and some slightly different. Although not noted in the original paper, the assumptions and analysis can also be used to estimate shear wave speeds. Below, I develop this extension of the theory.

The second paper (Shpakov et al., 1998), applies a rigorous mechanics-based approach to estimating the moduli of sI methane hydrate. The authors apply a lattice dynamics method using the quasiharmonic approximation. They calculate several elastic properties (dynamic, adiabatic and isothermal moduli) and theoretically explore the stability of the sI crystal structure. Their model predicts that at 260K methane gas hydrate, with all cages occupied, should have a compressional wave speed of 2.49 km/sec. This is well below the measured values available prior to this thesis, (3.4-3.6 km/sec) and the values reported in this thesis (Chapters 4 and 5). In contrast, Whalley's method produces estimates which come quite close to the few available laboratory measurements. Therefore, this section will concentrate on an in-depth discussion of Whalley's method.

Whalley (1980) was the first to develop a theoretical technique for estimating the speed

of compressional waves through sI and sII gas hydrate. He made his estimate by comparing the thermophysical properties of gas hydrate to those of water ice Ih. Unfortunately, there are some factual and computational errors in his paper and some of the derivations are not completely explained. Additionally, some of his assumptions about gas hydrate properties have been proven inaccurate by subsequent laboratory measurements. Therefore, I will rederive Whalley's fundamental equation and reevaluate it using today's best available laboratory data for the relevant properties of ice Ih and gas hydrate.

Whalley estimates the compressional wave speed in gas hydrate by comparing its thermophysical properties to those of ice Ih. For the thought experiment that motivates the derivation we compare equal volumes of ice Ih and sI or sII gas hydrate. Each block of material is fully dense (i.e., zero porosity) and comprised of randomly oriented (anisotropic) constituent crystals, each much smaller than the wavelength of the compressional wave used to probe the sample. Therefore, each block can be considered a homogenous, isotropic, linear elastic effective medium.

Applying Elastic Identities

In a homogenous, isotropic, linear elastic medium, the square of the compressional wave speed (V_P) can be written as

$$V_P^2 = \frac{K + \frac{4}{3}G}{\rho}. \tag{2.6}$$

where K is adiabatic bulk modulus, G is adiabatic shear modulus and ρ is density. The elastic identities

$$G = 3K\left(\frac{1-2\nu}{2+2\nu}\right) \tag{2.7}$$

and

$$K = \frac{1}{\kappa} \tag{2.8}$$

allow us to rewrite Equation 2.6 as

$$V_P^2 = \frac{3}{\kappa} \cdot \frac{1}{\rho} \cdot \frac{1-\nu}{1+\nu}, \tag{2.9}$$

where ν is Poisson's ratio and κ is adiabatic compressibility. In Equation 2.9, we concentrate on κ. The adiabatic compressibility of sI and sII gas hydrate is unknown, so we apply

the thermodynamic relationship (Wallace, 1998)

$$\kappa = \kappa_T \left(1 - \frac{\alpha^2 TV}{\kappa_T C_P}\right), \tag{2.10}$$

to obtain,

$$V_P^2 = \frac{3}{\kappa_T} \cdot \frac{1}{\rho} \cdot \frac{1-\nu}{1+\nu} \cdot \frac{1}{1-\frac{\alpha^2 TV}{\kappa_T C_P}} \tag{2.11}$$

where κ_T is isothermal compressibility, α is volume thermal expansivity, T is temperature, V is *molar* volume and C_P is *molar* heat capacity at constant pressure. This transformation clearly adds algebraic complexity and new physical properties to Equation 2.9, but all the properties in Equation 2.11 have been measured for ice Ih. In 1980, Whalley was forced to make assumptions about most of these properties for gas hydrate, but in the intervening 20 years many have also been measured for both sI and sII gas hydrate. The exception is isothermal compressibility. Whalley's method for estimating the ratio between the isothermal compressibility of ice and gas hydrate (see below) is the key to his method for predicting the speed of sound in gas hydrate.

Here I must point out the importance of the word *molar* used in relation to volume and heat capacity in this derivation. The question must be asked, how do you define molar for a nonstoichiometric material such as gas hydrate? I have chosen the convention that whenever the word molar is used, it refers to moles of water molecules in the hydrate or ice. With this choice, a molar volume always refers to the same absolute volume (at a given temperature and pressure), regardless of the relative number of guests present in the gas hydrate. It is important to keep this distinction in mind because much of the sparse literature covering gas hydrate heat capacity measurements is reported relative to one mole of the guest species. Therefore a multiplicative factor must be applied to many reported heat capacity measurements in order to use them in this wave speed estimation technique.

Note that Equation 2.11 is written as a simple product of factors. It is valid for any homogenous, isotropic, linear elastic material. Therefore, we can apply Equation 2.11 to our hypothetical, polycrystalline gas hydrate and ice samples. The square root of the ratio

of the two resultant equations gives,

$$\frac{V_{P_h}}{V_{P_i}} = \sqrt{\frac{\kappa_{T_i}}{\kappa_{T_h}} \cdot \frac{\rho_i}{\rho_h} \cdot \frac{1-\nu_h}{1-\nu_i} \cdot \frac{1+\nu_i}{1+\nu_h} \cdot \frac{1-\frac{\alpha_i^2 T V_i}{\kappa_{T_i} C_{P_i}}}{1-\frac{\alpha_h^2 T V_h}{\kappa_{T_h} C_{P_h}}}}, \tag{2.12}$$

where the subscripts *h* and *i* refer to gas hydrate and ice, respectively. In Equation 2.12 we see that the ratio of compressional wave speed in gas hydrate and ice Ih can be written as the square root of the product of a number of ratios of other measured or estimable thermophysical properties.

Estimating the Isothermal Compressibility

The first factor in Equation 2.12 is the the most difficult to calculate. Isothermal compressibility (κ_T) could be directly measured by applying a hydrostatic pressure change (ΔP) to our hypothetical volume of polycrystalline ice Ih or gas hydrate and measuring the resultant relative volume change ($\Delta V/V$):

$$\Delta P = -\frac{1}{\kappa_T} \frac{\Delta V}{V}\bigg|_T. \tag{2.13}$$

The sign convention in Equation 2.13 has been chosen such that compressive stresses are positive. Solving Equation 2.13 for $\frac{1}{\kappa_T}$ and applying infinitesimally small pressure changes gives,

$$\frac{1}{\kappa_T} = -V \frac{\mathrm{d}P}{\mathrm{d}V}\bigg|_T. \tag{2.14}$$

However, we do not know *a priori* how the volumes of ice Ih or gas hydrate will vary as a function of hydrostatic pressure (at constant temperature), so we must make some assumptions and calculate $\frac{1}{\kappa_T}$ from theoretical considerations. As Whalley (1980) showed, we can do this by expressing the pressure as a function of the Helmholtz free energy.

Helmholtz free energy (A) is defined as

$$A = E - TS, \tag{2.15}$$

where E is the total energy of the ensemble, T is temperature and S is entropy. The total differential of A is

$$\mathrm{d}A = \mathrm{d}E - T\mathrm{d}S - S\mathrm{d}T. \tag{2.16}$$

From classical statistical thermodynamics (Mandl, 1988), it can be shown that

$$\mathrm{d}E = T\mathrm{d}S - P\mathrm{d}V, \tag{2.17}$$

and therefore,

$$\mathrm{d}A = -P\mathrm{d}V - S\mathrm{d}T. \tag{2.18}$$

For an isothermal process, $\mathrm{d}T = 0$ and we have

$$\mathrm{d}A|_T = -P\mathrm{d}V|_T\,. \tag{2.19}$$

Solving for P gives

$$P = -\left.\frac{\mathrm{d}A}{\mathrm{d}V}\right|_T. \tag{2.20}$$

Substituting this isothermal definition for P into Equation 2.14 yields

$$\frac{1}{\kappa_T} = V\left.\frac{\mathrm{d}^2A}{\mathrm{d}V^2}\right|_T. \tag{2.21}$$

Equation 2.21 represents an improvement because $\left.\frac{\mathrm{d}^2A}{\mathrm{d}V^2}\right|_T$ can be analytically expressed in terms of known and assumed quantities by making the hypothetical isothermal measurement at absolute zero (i.e., T = 0 K).

For an isothermal process at T=0 K, Equation 2.15 becomes

$$A = E. \tag{2.22}$$

E is the total energy which is defined as $E = K_E + U$, where K_E is kinetic energy and U is potential energy. At absolute zero we assume there is no thermal motion of the molecules, so $K_E = 0$ and $E = U$. This assumption ignores the zero point energy of the water (and guest) molecules, which should be small (Wallace, 1998). Therefore, at absolute zero in an isothermal process, the Helmholtz free energy of a system is equal to the total potential energy of the system,

$$A = U. \tag{2.23}$$

We can calculate the potential energy of our ice and gas hydrate blocks at absolute zero using the following method suggested by Whalley (1980). Since we know the atomic crystallographic arrangement for ice Ih and sI and sII gas hydrate, we know the number

of water molecules in any given volume of fully dense ice or gas hydrate. We also know the water molecules in ice and gas hydrate are bound together by hydrogen bonds and the hydrogen atoms in each water molecule are attached to their respective oxygen atoms by covalent bonds. Therefore, the distance between water molecules (or more appropriately between oxygen atoms) is the sum of the hydrogen and covalent bond lengths. If we imagine the ice and gas hydrate crystals as collections of water molecules (or oxygen atoms) connected by springs, we can assume that volume changes arising from small changes in hydrostatic pressure can be expressed through a change in the length (compression or extension) of the springs connecting the water molecules. In this approach, there exists an equilibrium bond length between water molecules that corresponds to a minimum in the potential energy function for the crystal. Near this minimum, the potential energy curve can be approximated as a parabola. A Hookian force law produces parabolic potential energy curves; therefore, we will assume that for small deviations from equilibrium, the potential energy for each bond connecting two water molecules can be calculated from the definition of potential energy (Ohanian, 1989) as

$$U = -\int_0^{\varepsilon} F(x)dx = \frac{1}{2}k\varepsilon^2, \tag{2.24}$$

where F(x) is the Hooke's law force (F(x)=-kx), k is the effective nearest neighbor spring constant and ε is the difference between the instantaneous water to water bond length (r) and the equilibrium bond length (r_o):

$$\varepsilon = r - r_o. \tag{2.25}$$

This formulation of potential energy neglects non-nearest neighbor water interactions and guest lattice interactions in gas hydrate. To make the Hookian approximation as accurate as possible, we require $|\varepsilon| << r_o$. The potential energy for the change of length in one water to water bond then becomes

$$U = \frac{1}{2}k(r - r_o)^2. \tag{2.26}$$

The two hydrogen atoms in each water molecule share a hydrogen bond with two neighboring water molecules. Therefore, the total change in potential energy that arises from a change of hydrostatic pressure applied to a system of N water molecules can be expressed

as:

$$U = \frac{1}{2}\sum_{i=1}^{2N} k_i (r_i - r_{o_i})^2. \tag{2.27}$$

Note that N is different for ice and sI and sII gas hydrate. If we assume that all the k_i (and r_i and r_{o_i}) are approximately the same, we can rewrite Equation 2.27 as

$$U = Nk(r - r_o)^2, \tag{2.28}$$

where k, r and r_o are representative "average" values for the effective bond spring constant, instantaneous bond length and equilibrium bond length, respectively. k and r_o are constants (at a given temperature); N varies with the volume of the initial system; and r varies as the volume changes due to applied hydrostatic stress.

Wallace (1998) (p. 392) asserts that, given a potential energy function depending on the nearest neighbor molecular distance r and the assumption that $V \propto r^3$,

$$V\frac{\mathrm{d}U}{\mathrm{d}V} = \frac{1}{3}r\frac{\mathrm{d}U}{\mathrm{d}r} \tag{2.29}$$

$$V^2\frac{\mathrm{d}^2U}{\mathrm{d}V^2} = \frac{1}{9}\left[r^2\frac{\mathrm{d}^2U}{\mathrm{d}r^2} - 2r\frac{\mathrm{d}U}{\mathrm{d}r}\right]. \tag{2.30}$$

Applying Equation 2.30 to our derived expression for U(r), Equation 2.28, we obtain

$$V^2\frac{\mathrm{d}^2U}{\mathrm{d}V^2} = -\frac{2}{9}Nk[r(r-2r_o)]. \tag{2.31}$$

But $r = r_o + \varepsilon$ where $\varepsilon \ll r_o$. Therefore

$$\begin{aligned} V^2\frac{\mathrm{d}^2U}{\mathrm{d}V^2} &= -\frac{2}{9}Nk[(r_o+\varepsilon)(r_o+\varepsilon-2r_o)] \\ &= -\frac{2}{9}Nk[-r_o^2+\varepsilon^2] \\ &\approx \frac{2}{9}Nkr_o^2. \end{aligned} \tag{2.32}$$

Dividing both sides by V gives,

$$V\frac{\mathrm{d}^2U}{\mathrm{d}V^2} = \frac{2}{9}\tilde{N}kr_o^2, \tag{2.33}$$

where $\tilde{N} = \frac{N}{V}$ is the number of water molecules per unit volume. Combining this result with Equation 2.21 we find that

$$\kappa_T = \frac{9}{2}\frac{1}{\tilde{N}kr_o^2}. \tag{2.34}$$

Therefore the first factor on the right hand side of Equation 2.12 can be expressed as

$$\frac{\kappa_{T_i}}{\kappa_{T_h}} = \frac{\tilde{N}_h k_h r_h^2}{\tilde{N}_i k_i r_i^2}, \tag{2.35}$$

where, for notational clarity, I have removed the subscript from the equilibrium bond symbol (i.e., r_o is written as r to reduce the use of double subscripts). Bertie et al. (1967; 1974; 1978) have measured the far infrared spectrum of ice and sI and sII gas hydrates. The similarity of these spectra implies that the harmonic force constant, k, is similar between ice Ih and sI and sII gas hydrate (Whalley, 1980). Therefore, in the absence of directly measured values for k, we assume that $\frac{k_i}{k_h} \approx 1$ and we have that at absolute zero,

$$\frac{\kappa_{T_i}}{\kappa_{T_h}} = \frac{\tilde{N}_h r_h^2}{\tilde{N}_i r_i^2}. \tag{2.36}$$

Equation 2.36 is a very important result and may in fact be the most important contribution from Whalley's original paper. It shows that the ratio of isothermal compressibilities in ice (i) and gas hydrate (h) can be approximated by the product of the water molecule number density ratio ($\tilde{N}_h/\tilde{N}_i$) and the square of the ratio of the average equilibrium bond lengths in the ice and gas hydrate crystal lattices (r_h^2/r_i^2).

Inconsistencies in Whalley (1980)

In his original paper, Whalley (citing Davidson, 1973) asserted that crystallographic data gave N_h/N_i equal to 0.880 and 0.872, for sI and sII gas hydrate, respectively, and that the ratio of equilibrium bond lengths was 1.022. Therefore, we would expect that

$$sI : \frac{\kappa_{T_i}}{\kappa_{T_h}} = 0.880 \cdot (1.022)^2 = 0.919 \tag{2.37}$$

$$sII : \frac{\kappa_{T_i}}{\kappa_{T_h}} = 0.872 \cdot (1.022)^2 = 0.911 \tag{2.38}$$

However, Whalley reports values of 1.135 and 1.162 for $\kappa_{T_h}/\kappa_{T_i}$ in sI and sII, respectively. These are equivalent to values of 0.881 and 0.861 for $\kappa_{T_i}/\kappa_{T_h}$. Even if we assume that "the ratio of equilibrium bond lengths" in Whalley (1980) referred to the ratio of the squares of the equilibrium bond lengths, we only obtain $\kappa_{T_i}/\kappa_{T_h} = 0.899$ and 0.891 for sI and sII, respectively. This is a significant discrepancy, and it is not easily resolved. The most

likely explanation is some combination of typographical errors because Whalley's results, as published, are not internally consistent. Dividing his calculated $\kappa_{T_i}/\kappa_{T_h}$ by his stated N_h/N_i does not give the same value for r_h^2/r_i^2 for sI and sII gas hydrate and neither of the resulting estimates for r_h^2/r_i^2 is equal to $1.022^n, n = \frac{1}{2}, 1, 2$. Furthermore, Davidson (1973) (p.133) states, "The O- -O bond lengths [in gas hydrates] on average exceed those in hexagonal ice (2.76 Å) by only 1% and are comparable to those in most of the other forms of ice." This would imply $r_h/r_i \approx 1.01$ (or $r_h^2/r_i^2 \approx 1.0201$) not 1.022 as Whalley states. Since there appears to be no obvious resolution to the internal discrepancies within Whalley's original paper, I recalculate the isothermal compressibility ratio below, beginning with the number density ratios.

Recalculating the Isothermal Compressibility Ratio

First let me note that Whalley's number density ratio refers to the number of hydrogen atoms (or equivalently hydrogen bonds) per unit volume, while $\tilde{N}$ used in this derivation refers to water molecules per unit volume. Since $\tilde{N}_h$ and $\tilde{N}_i$ appear only in ratios, this is not the cause of any discrepancy between the results. The factor of two relating the number of hydrogen atoms to water molecules cancels.

The unit cell of sI gas hydrate contains 46 water molecules in a cubic unit cell of dimension a_I. sII has 136 water molecules in a cubic unit cell of dimension a_{II}. The values of a_I and a_{II} vary with guest molecule type, temperature and pressure and potentially with occupation number as well. Values of 12.0Å and 17.3Å are cited as representative for sI and sII at 273K by Sloan (1998) (p. 60), but no reference pressure is given. Ice Ih, on the other hand, has 4 water molecules in a quadrilateral unit cell whose volume is given by $a_i^2 c_i \frac{\sqrt{3}}{2}$ where a_i and c_i are the crystallographic axes of the hexagonal crystal and $\frac{\sqrt{3}}{2} = \sin 60^\circ$. Therefore, we can write,

$$\frac{\tilde{N}_I}{\tilde{N}_i} = \frac{46/V_I}{4/V_i} = \frac{23}{2}\frac{\frac{\sqrt{3}}{2}a_i^2 c_i}{a_I^3}, \tag{2.39}$$

$$\frac{\tilde{N}_{II}}{\tilde{N}_i} = \frac{136/V_{II}}{4/V_i} = 34\frac{\frac{\sqrt{3}}{2}a_i^2 c_i}{a_{II}^3}, \tag{2.40}$$

where $\tilde{N}_I$ and $\tilde{N}_{II}$ are the water molecule number densities and V_I and V_{II} are the unit cell

volumes in sI and sII, respectively. The subscript *i* refers to ice Ih.

Röttger et al. (1994) recently made precise measurements of a_i and c_i for ice Ih in the temperature range from 10 to 265 K, at atmospheric pressure. They supply an empirical fit to the ice unit cell volume (in Å^3) as a function of temperature. However, their reported coefficients lack sufficient significant figures to reproduce the data. The correct fit parameters are (Kuhs, 1999, pers. comm.),

$$\begin{aligned} V_i(T) = 128.2147 - 1.3152 \times 10^{-6} \cdot T^3 + 2.4837 \times 10^{-8} \cdot T^4 + \\ -1.6064 \times 10^{-10} \cdot T^5 + 4.6097 \times 10^{-13} \cdot T^6 + \\ -4.9661 \times 10^{-16} \cdot T^7. \end{aligned} \tag{2.41}$$

Shpakov et al. (1998), reported measurements of a_I for sI methane gas hydrate in the temperature range 80-210 K, also at atmospheric pressure. The empirical fit they supply for their data (in Å) is given by

$$a_I(T) = 11.80 + 5.39 \times 10^{-5} \cdot T + 1.78 \times 10^{-6} \cdot T^2. \tag{2.42}$$

Tse (1987) published measurements of a_{II} for sII THF hydrate from 20-250 K. His empirical fit to the data (in Å) is given by

$$a_{II}(T) = 17.130 + 2.429 \times 10^{-4} \cdot T + 2.013 \times 10^{-}6 \cdot T^2 - 1.009 \times 10^{-9} \cdot T^3. \tag{2.43}$$

All three groups made their measurements using X-ray powder diffraction. The cubic unit cell volumes (V_I and V_{II}) are easily calculated from the reported values of a_I and a_{II} as functions of temperature. The resulting values for $\tilde{N}_I/\tilde{N}_i$ and $\tilde{N}_{II}/\tilde{N}_i$ using Equations 2.41, 2.42 and 2.43 evaluated at T=0 K are:

$$\frac{\tilde{N}_I}{\tilde{N}_i} = 0.897 \tag{2.44}$$

$$\frac{\tilde{N}_{II}}{\tilde{N}_i} = 0.867 \tag{2.45}$$

These ratios will vary depending on the true values of a_I and a_{II} for a given guest. It is not clear if the ratio will remain the same as pressure is applied. In the absence of any data, we will assume this ratio is valid for all guests and applied pressures at T=0 K. This

result should be compared to Whalley's stated values of 0.880 and 0.872 for sI and sII, respectively.

Next we calculate the ratios r_I^2/r_i^2 and r_{II}^2/r_i^2. We can determine r_i from the lattice parameter measurements of Röttger et al. (1994) using the relationship (Hobbs, 1974) (p.21)

$$r_i = \frac{1}{2}\sqrt[3]{\frac{V_i}{(1+\sin 19^\circ 28')\sin^2 54^\circ 44' \sin 60^\circ}}. \tag{2.46}$$

From Equation 2.46 and $V_i = 128.2147\text{Å}^3$ at T=0 K (Equation 2.41) we obtain $r_i = 2.751$Å (and $r_i = 2.768$Å at 273.15K). Equation 2.46 assumes perfect tetrahedral coordination between the water molecules. This implies that $c/a = 1.633$ (Hobbs, 1974). However the data from Röttger et al. (1994) give $c/a = 1.6280$. Therefore the use of Equation 2.46 introduces some error into r_i, but it is assumed to be small and will be neglected.

A similar geometry based formula for the cubic structure of gas hydrate is not available in the literature. It is clear, however, that Equation 2.46 has the form $V_i = C_i r_i^3$ (i.e., $V_i \propto r_i^3$) where C_i is a geometry dependent constant. Therefore, given V_I and V_{II} (from a_I and a_{II}) we can estimate C_I and C_{II} if r_I and r_{II} are known at any temperature. Davidson's (1973) Table II gives $r_I = 2.793$ Å and $r_{II} = 2.790$ Å, with no temperature attributed. The original sources show the sI measurements (McMullan and Jeffrey, 1965) were made on ethylene oxide hydrate at $\sim -30^\circ$C (~ 243 K) and the sII measurements (Mak and McMullan, 1965) on a double hydrate of tetrahydrofuran and hydrogen sulfide at -20 to -25°C (~ 250.5 K). Therefore, the values of the geometry based constants C_I and C_{II} are 77.70 and 238.5, respectively, and we calculate that at T=0 K,

$$r_I = \sqrt[3]{\frac{V_I}{C_I}} = 2.765\,\text{Å}, \tag{2.47}$$

$$r_{II} = \sqrt[3]{\frac{V_{II}}{C_{II}}} = 2.762\,\text{Å}. \tag{2.48}$$

This theoretical result is in agreement with recent measurements by Tulk et al. (1998) of r_{II} in THF hydrate at 10 K (2.727–2.810 Å with a maximum likelihood value of 2.766 Å). Combining these results for r_I and r_{II} at 0 K with the result for r_i at 0 K calculated above, we have

$$\frac{r_I^2}{r_i^2} = 1.010, \tag{2.49}$$

$$\frac{r_{II}^2}{r_i^2} = 1.008. \tag{2.50}$$

Combining 2.49 (2.50) with 2.44 (2.45) we obtain,

$$\frac{\kappa_{T_i}}{\kappa_{T_I}} = 0.906 \tag{2.51}$$

$$\frac{\kappa_{T_i}}{\kappa_{T_{II}}} = 0.874. \tag{2.52}$$

This result should be compared to Whalley's estimates of $\kappa_{T_i}/\kappa_{T_I} = 1/1.135 = 0.881$ and $\kappa_{T_i}/\kappa_{T_{II}} = 1/1.162 = 0.861$.

These derived ratios for $\kappa_{T_i}/\kappa_{T_h}$ depend on assumptions valid only at T = 0 K. However, the premise of the entire method is that two materials as similar as ice and gas hydrate (both sI and sII), will have very similar properties. Therefore, as Whalley (1980) did, we will assume that this ratio is approximately correct for all temperatures from 0 K to the melting point of ice Ih.

Calculating Density Ratio

The second factor in Equation 2.12 is the ratio of ice density to gas hydrate density. The density of ice (ρ_i) can be calculated from the unit cell volumes (V_i) reported by Röttger et al. (1994) and the molecular mass of water ($m_{H_2O} = 2.9915 \times 10^{-26}$ kg) using

$$\rho_i = \frac{4 \cdot m_{H_2O}}{V_i(T)}, \tag{2.53}$$

where V_i is given as a function of temperature in Equation 2.41. The density of gas hydrate depends on the mass of the molecules in the cages and the percentage of cages that are filled. The general formulas are,

$$\rho_I = \frac{46 \cdot m_{H_2O} + 2 \cdot x_s \cdot m_s + 6 \cdot x_l \cdot m_l}{a_I^3(T)}, \tag{2.54}$$

$$\rho_{II} = \frac{136 \cdot m_{H_2O} + 16 \cdot x_s \cdot m_s + 8 \cdot x_l \cdot m_l}{a_{II}^3(T)}, \tag{2.55}$$

where x_s (x_l) is the fraction of small (large) cages filled in each structure and m_s (m_l) is the mass of the guest in the small (large) cages. a_I and a_{II} are given as functions of

temperature in Equations 2.42 and 2.43, respectively. Clearly ρ_I and ρ_{II} vary as a function of cage filling percentage and guest mass. All three densities also vary with temperature. The variation of ρ_i/ρ_I and ρ_i/ρ_{II} with temperature for sI methane hydrate and sII propane hydrate, respectively, is shown in Figures 2.5 and 2.6. The curves in each figure represent 0%, 70% and 100% cage occupancy rates. Note that in the case of propane hydrate, percent occupancy rate refers to only the large cages because the propane molecule does not fit in the smaller cage (see Table 2.2).

Calculating Poisson's Ratio Factors

The third and fourth factors in Equation 2.12 are functions of Poisson's ratio (ν). In his original paper, Whalley (1980) set $\nu_i = 0.33$ and assumed $\nu_I = \nu_{II} = \nu_i$ reasoning that Poisson's ratio varies little between dissimilar materials, so between ice and gas hydrate, the differences should be minimal. In this thesis, I set $\nu_i = 0.33 \pm 0.01$, consistent with measurements by Gagnon et al. (1988) and the measurements reported in Chapter 5. Kiefte et al. (1985) measured bulk (K) and shear (G) moduli of 8.5 GPa and 3.5 GPa, respectively, in THF hydrate at 0° C. Poisson's ratio can be calculated from these values using (Mavko et al., 1998)

$$\nu = \frac{\frac{3}{2}K - G}{3K + G}, \tag{2.56}$$

giving $\nu_{II} = 0.32$. In Chapter 5, I present compressional and shear wave speed measurements that give $\nu_I = 0.32$ in methane hydrate. These appear to be the only valid reported measurements of Poisson's ratio in gas hydrate. Kiefte et al.'s measurement is at only a single temperature, but the results presented in Chapter 5 show that Poisson's ratio does not vary significantly with temperature from -15 to 15°C in sI methane hydrate. Therefore, I will assume that Poisson's ratio is a constant versus temperature in ice and sI and sII gas hydrate and that $\nu_I = \nu_{II} = 0.32 \pm 0.01$. The products of factors three and four then become

$$\frac{1-\nu_I}{1-\nu_i}\,\frac{1+\nu_i}{1+\nu_I} = \frac{1-\nu_{II}}{1-\nu_i}\,\frac{1+\nu_i}{1+\nu_{II}} = 1.02 \pm 0.02. \tag{2.57}$$

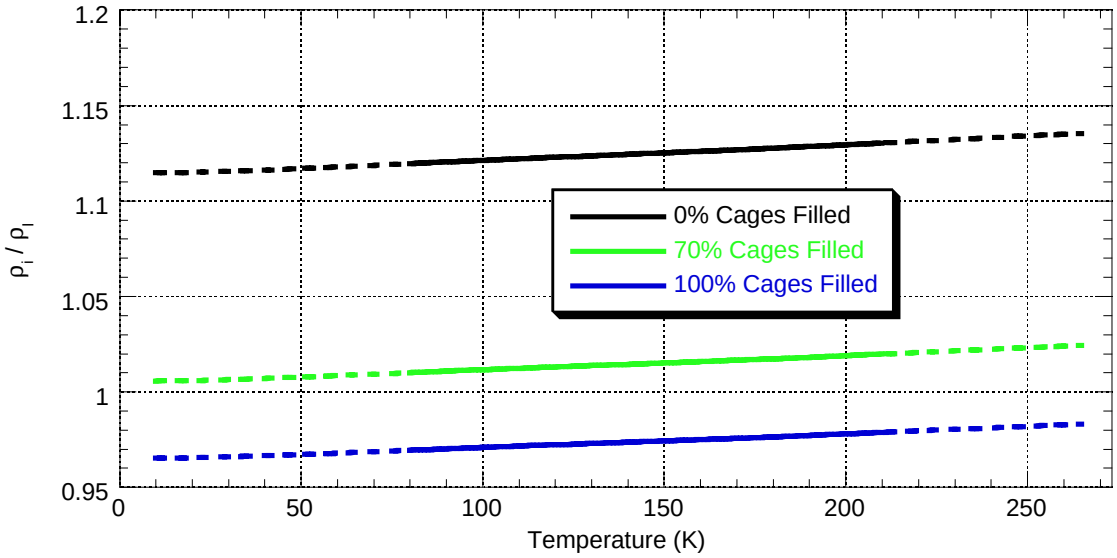

Figure 2.5: Ratio of ice Ih density and sI gas hydrate density versus temperature for methane hydrate. Curves represent ratios for 0%, 70% and 100% cage occupancy in the methane hydrate. Solid lines signify the temperature interval where fits to unit cell volume measurements are available for both ice and gas hydrate (Equations 2.41 and 2.42). Dashed lines signify temperatures where gas hydrate data has been extrapolated for comparison with available ice data.

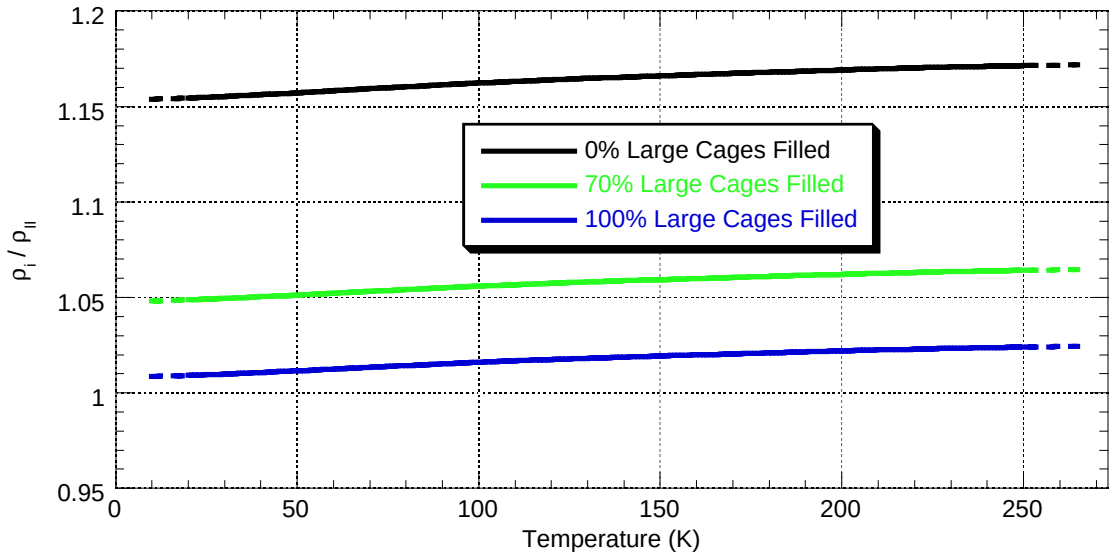

Figure 2.6: Ratio of ice Ih density and sII gas hydrate density versus temperature for propane hydrate. Curves represent ratios for 0%, 70% and 100% large cage occupancy in the propane hydrate. Solid lines signify the temperature interval where fits to unit cell volume measurements are available for both ice and gas hydrate (Equations 2.41 and 2.43). Dashed lines signify temperatures where gas hydrate data has been extrapolated for comparison with available ice data. Note that the y-axis scale is the same as for Figure 2.5.

Calculating Final Factor in Equation 2.12

The final factor in Equation 2.12 depends on volume thermal expansivity (α), temperature (T in K), molar volume (V), isothermal compressibility (κ_T) and molar heat capacity at constant pressure (C_p). I will discuss the values of each one of these properties in ice and gas hydrate.

Volume Thermal Expansivity

Volume thermal expansivity (α) is defined as

$$\alpha = \frac{1}{V}\frac{\mathrm{d}V}{\mathrm{d}T}\bigg|_P, \tag{2.58}$$

where V is volume and T is temperature. Given $V(T)$, Equation 2.58 can be used to calculate volume thermal expansivity directly. Since α is obtained from the derivative of a function, the error in this property can be large, as evidenced by the relatively large range of values for α_i shown in the compilation by Touloukian (1977). To calculate α_i, α_I and α_{II}, I use V_i (Equation 2.41) as determined from Röttger et al. (1994) and V_I and V_{II} as determined from the a_I (Equation 2.42) and a_{II} (Equation 2.43) given by Shpakov et al. (1998) and Tse (1987), respectively. This does not account for differences in lattice dimension caused by the particular guest found in the gas hydrate or by variations in cage occupancy rate. Those differences are probably less than the error in the calculation itself, estimated to be around 7-10% (Touloukian et al., 1977; Tse, 1987). The calculated variation of thermal expansivity with temperature for ice Ih and sI and sII gas hydrate is shown in Figure 2.7

Molar Volume

Since this is a theoretical estimate of compressional wave speed in gas hydrate, I assume that temperature (T) is known exactly. The molar volumes of ice (V_i) and sI and sII gas hydrate (V_I and V_{II}, respectively) are calculated as functions of temperature by multiplying the appropriate unit cell volume (V_{cell}) by the ratio of Avogadro's number ($A_N = 6.02214199 \times 10^{23}$) to the number of water molecules in the unit cell (N_{cell}),

$$V = V_{cell} \cdot \frac{A_N}{N_{cell}}. \tag{2.59}$$

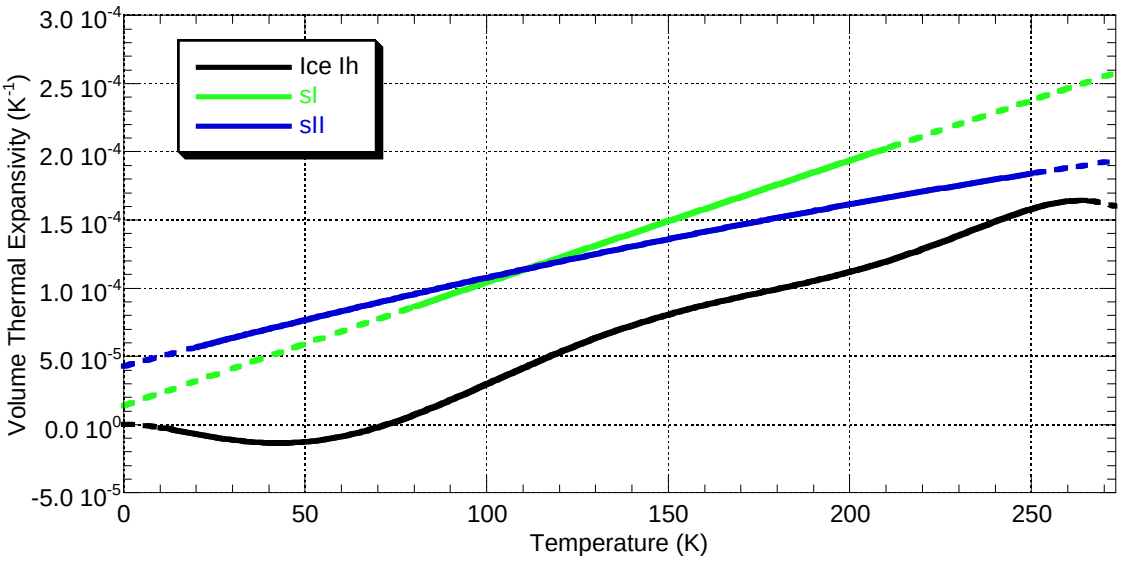

Figure 2.7: Volume thermal expansivity of ice and sI and sII gas hydrate versus temperature. Volume thermal expansivity is calculated from the temperature derivatives of the respective unit cell volumes (see text). Solid lines signify the temperature interval where fits to unit cell volume measurements are available. Dashed lines signify temperatures where the fits have been extrapolated.

The unit cell volume for ice is given as a function of temperature by Equation 2.41. The unit cell volumes for sI and sII gas hydrate are given as functions of temperature by cubing the unit cell dimensions a_I and a_{II} given in Equations 2.42 and 2.43 for sI and sII, respectively. The variation of these molar volumes with temperature is shown in Figure 2.8.

Isothermal Compressibility

There are very few published measurements of isothermal compressibility in ice (κ_{T_i}) and measurements of isothermal compressibility in gas hydrate (κ_{T_h}) have not yet been published. The published values for κ_{T_i} come from Bridgman (1912), Richards and Speyers (1914), Bridgman's personal communication cited in Richards and Speyers (1914), and Gow and Williamson (1972). The Bridgman data do not match the others or measurements of κ_S. Because of the lack of data, I have used an estimate of κ_{T_i} as a function of temperature (T) provided by S. Kirby (pers. comm., 1999) which is consistent with available isothermal and adiabatic measurements,

$$\kappa_{T_i} = \frac{1000}{1.0820 \times 10^4 - 2.6934 \cdot T - 2.1632 \times 10^{-2} \cdot T^2}. \tag{2.60}$$

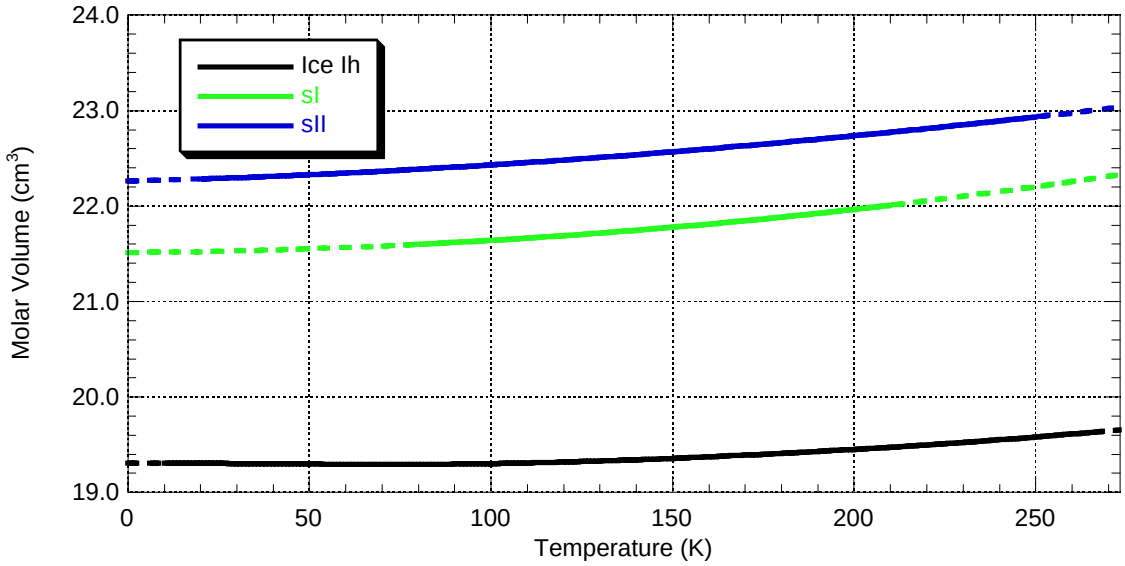

Figure 2.8: Molar volume of ice Ih and sI and sII gas hydrate versus temperature. Solid lines signify the temperature interval where fits to unit cell volume measurements are available. Dashed lines signify temperatures where the fits have been extrapolated. As throughout this text, *molar* refers to a mole of water molecules.

In Equation 2.60, T is in K and κ_{T_i} is in GPa^{-1}. The result of evaluating Equation 2.60 from 0 to 273 K and the measurements of Richards and Speyers (1914) and Gow and Williamson (1972) are shown in Figure 2.9. κ_{T_I} and $\kappa_{T_{II}}$ are calculated from κ_{T_i} by dividing κ_{T_i} by the previously determined (and assumed constant for all T) ratio of isothermal compressibilities in ice and gas hydrate (Equations 2.51 and 2.52).

Heat Capacity at Constant Pressure

There are a small but significant number of heat capacity measurements made on gas hydrate (Handa et al., 1984; White and MacLean, 1985; Handa, 1986a; Handa, 1986b; Handa, 1988; Rueff et al., 1988; Yamamuro et al., 1988; Yamamuro et al., 1990). Handa et al. (1984) also reported heat capacity measurements on polycrystalline ice samples. When discussing molar heat capacities for clathrate hydrates, it is very important to be clear and consistent about what "molar" refers to. As stated above, in this thesis, "per mol" always refers to a mole of water molecules. This is an important distinction because results are often reported as per mol of guest. Heat capacity at constant pressure (C_P) data are available for Xe (Handa, 1986a), CH_4 (Handa, 1986b), C_2H_6 (Handa, 1986b) and ethylene oxide

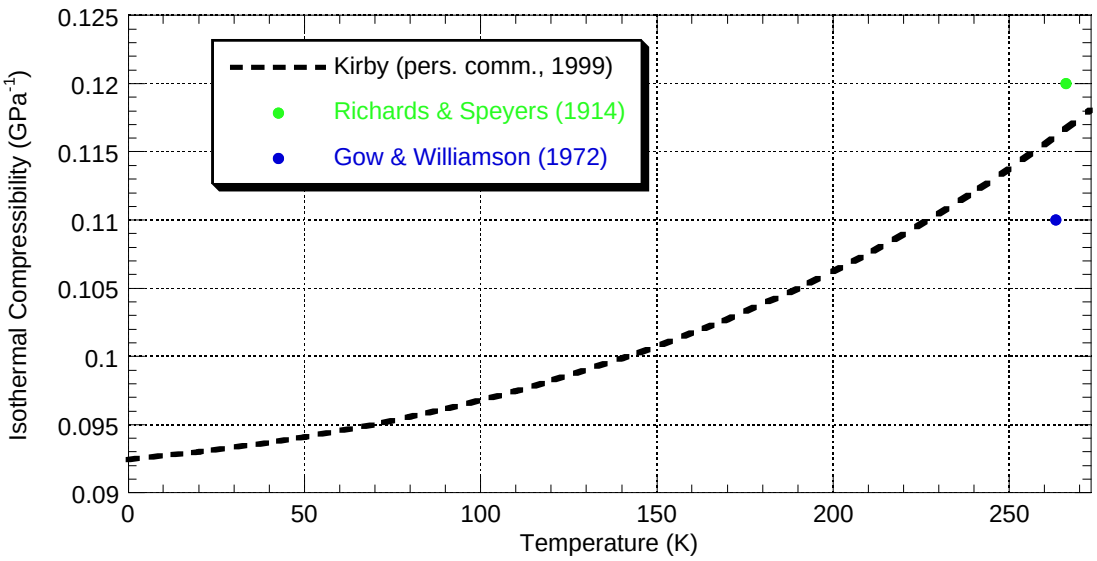

Figure 2.9: Isothermal compressibility of ice Ih versus temperature. The two points represent direct measurements of ice Ih isothermal compressibility. The dashed curve is an estimate of isothermal compressibility based on measurements of ice Ih adiabatic compressibility.

(Yamamuro et al., 1990) sI gas hydrate and THF (Handa et al., 1984), Kr (Handa, 1986a), C_3H_8 (Handa, 1986b) and Ar (Yamamuro et al., 1988) sII gas hydrate. The empirical fits for heat capacity measurements made on ice Ih, sI methane hydrate and sII propane hydrate supplied by Handa et al., (1984) and Handa (1986b) are in the form of cubic polynomials,

$$C_P = A_0 + A_1 \cdot T + A_2 \cdot T^2 + A_3 \cdot T^3. \tag{2.61}$$

The fitting parameters A_0 through A_3 are given in Table 2.3, along with the standard deviations of the fitting equations. The fitting parameters were determined from data acquired between 85 and 270 K for ice Ih and methane hydrate and between 85 and 265 K for propane hydrate. The resulting fit-based estimates for the heat capacities of ice Ih, sI methane hydrate and sII propane hydrate as functions of temperature are shown in Figure 2.10.

The heat capacity (per mol of water) of gas hydrate is higher than that of ice for all temperatures and guest species where data are available. This is due to the contribution of the guest to the gas hydrate's heat capacity. The range of reported heat capacity values for sI or sII gas hydrate at any temperature from 85-270 K is approximately $\pm$ 2-3 J mol^{-1} K^{-1}. For gas hydrates formed from guest species where heat capacity has not yet been

Table 2.3: Gas Hydrate Heat Capacity Curve Fitting Parameters

		Fitting Parameters[a,b]				Standard
Composition	Structure	A_0	A_1	A_2	A_3	Deviation
H_2O	Ice Ih	-0.1593	0.01348	-4.0000×10^{-5}	7.7912×10^{-8}	0.006[b]
$CH_4 \cdot 6.00H_2O$	sI	6.6	1.4538	-3.640×10^{-3}	6.312×10^{-6}	0.8
$C_3H_8 \cdot 17.0H_2O$	sII	−37.6	4.8606	-1.625×10^{-2}	3.291×10^{-5}	1.9

[a]Fit equations give molar heat capacity in units of J K^{-1} mol^{-1} Guest. To convert results to mol^{-1} H_2O, divide fit parameters by n in the composition formula Guest·nH_2O

[b]Handa et al., (1984) report ice Ih C_P in units of J K^{-1} g^{-1}. To convert to J K^{-1} mol^{-1} H_2O, multiply by the molar mass (18.015 g mol^{-1} H_2O) of Ice Ih.

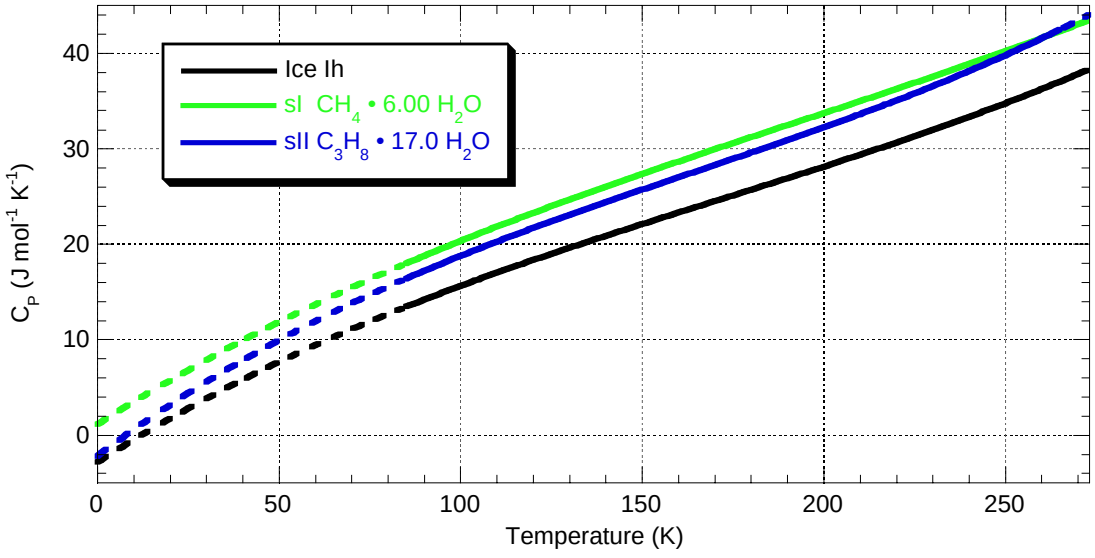

Figure 2.10: Molar heat capacity at constant pressure versus temperature for ice Ih, sI methane hydrate and sII propane hydrate. Curves are from published empirical fits to measured data. Dashed lines signify temperatures where the fits have been extrapolated. *Molar* refers to a mole of water molecules.

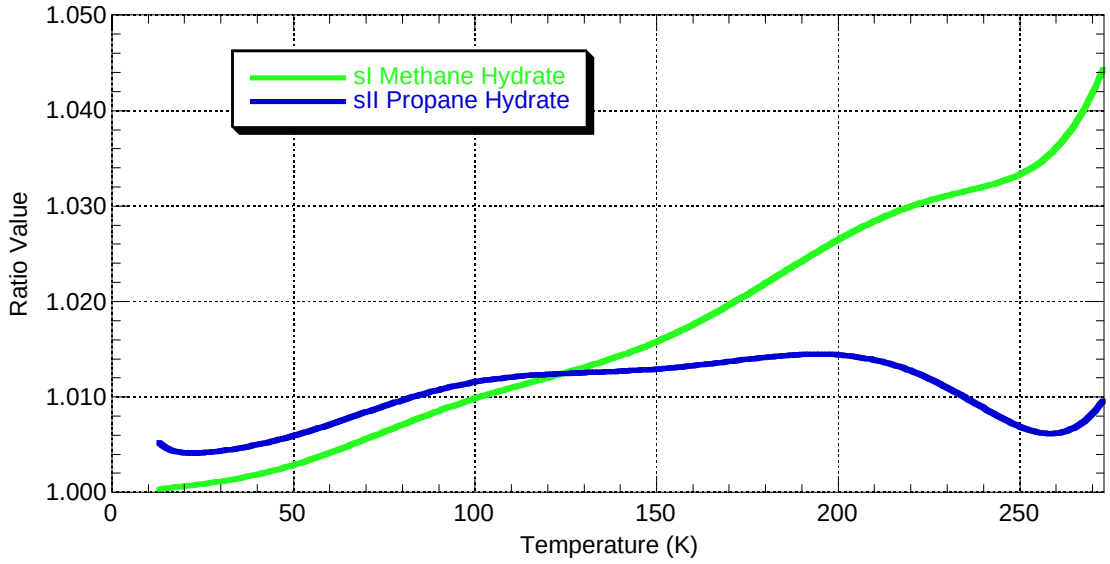

Figure 2.11: $\left(1-\alpha_i^2 TV_i/\kappa_{T_i}C_{P_i}\right)/\left(1-\alpha_h^2 TV_h/\kappa_{T_h}C_{P_h}\right)$ evaluated for ice Ih and sI methane hydrate and ice Ih and sII propane hydrate as a function of temperature. Subscript *i* refers to ice Ih. Subscript *h* refers to gas hydrate. Curves stop at 13 K because C_{P_i} extrapolation is negative for T$<$ 13 K (see Figure 2.10).

measured, a curve fit to the available data would probably be accurate to within $\pm$ 5 J mol^{-1} K^{-1} or less.

Figure 2.11 shows the resulting estimates for the final factor in Equation 2.12 for sI methane hydrate and sII propane hydrate. Note that these estimates will vary slightly with relative cage occupancy rates because of changes in heat capacity, volume thermal expansivity and molar volume that are attributable to the guest. These changes should be small for realistic cage occupancy rates ($\sim$ 70-100%).

Calculating Compressional Wave Speed Ratio

Combining all the factors calculated above, the result for Equation 2.12 for sI methane hydrate with 70% and 100% cage occupancy rates is shown as a function of temperature in Figure 2.12. The result for sII propane hydrate with 70% and 100% of the large cages occupied is given in Figure 2.13. At 273 K, the ratio for sI methane hydrate with 100% of the cages filled is 0.976. This should be compared to Whalley's original estimate of 0.939. At 273 K, the ratio for sII propane hydrate with 100% of the large cages filled is 0.961, compared to Whalley's original prediction of 0.945. The prediction for sI methane

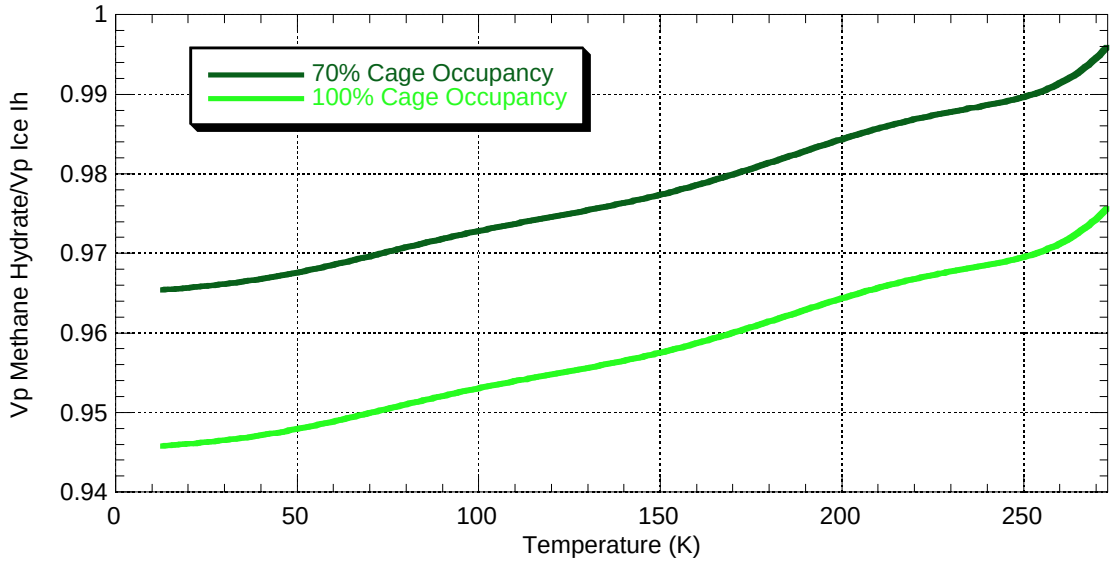

Figure 2.12: Compressional wave speed ratio for sI methane hydrate and ice Ih versus temperature. The two curves represent the results obtained by assuming 70% or 100% cage occupancy, respectively. The decrease in ratio value in going from 70% to 100% cage occupancy is due solely to the increase in gas hydrate density that occurs with the increased cage occupancy rate. The curves stop at 13 K because the C_{P_i} extrapolation is negative for T$<$ 13 K (see Figure 2.10).

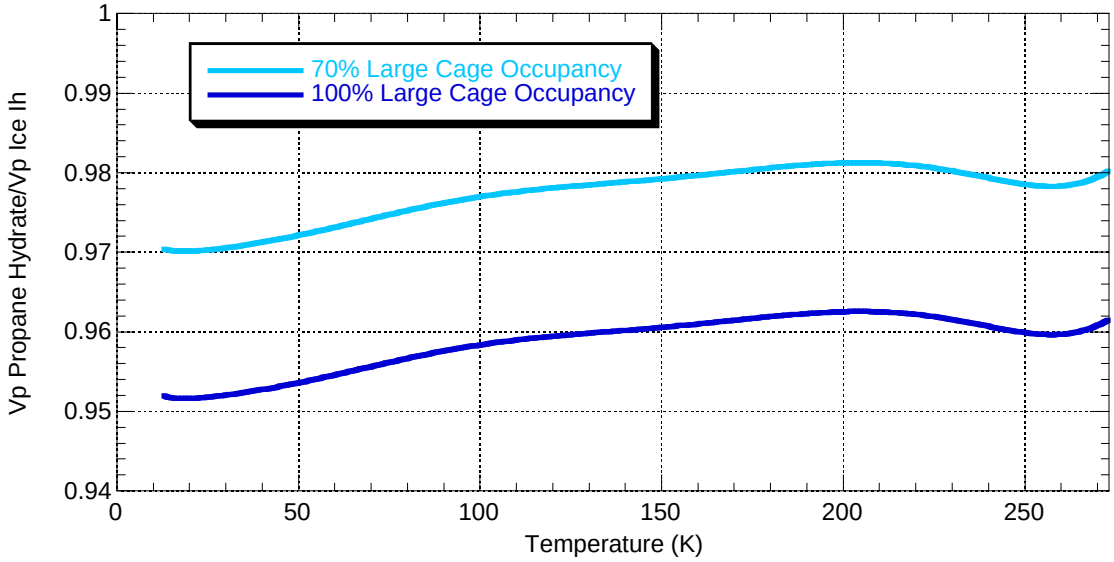

Figure 2.13: Compressional wave speed ratio for sII propane hydrate and ice Ih versus temperature. The two curves represent the results obtained by assuming 70% or 100% large cage occupancy, respectively. The decrease in ratio value in going from 70% to 100% large cage occupancy is due solely to the increase in gas hydrate density that occurs with the increased large cage occupancy rate. The curves stop at 13 K because the C_{P_i} extrapolation is negative for T$<$ 13 K (see Figure 2.10).

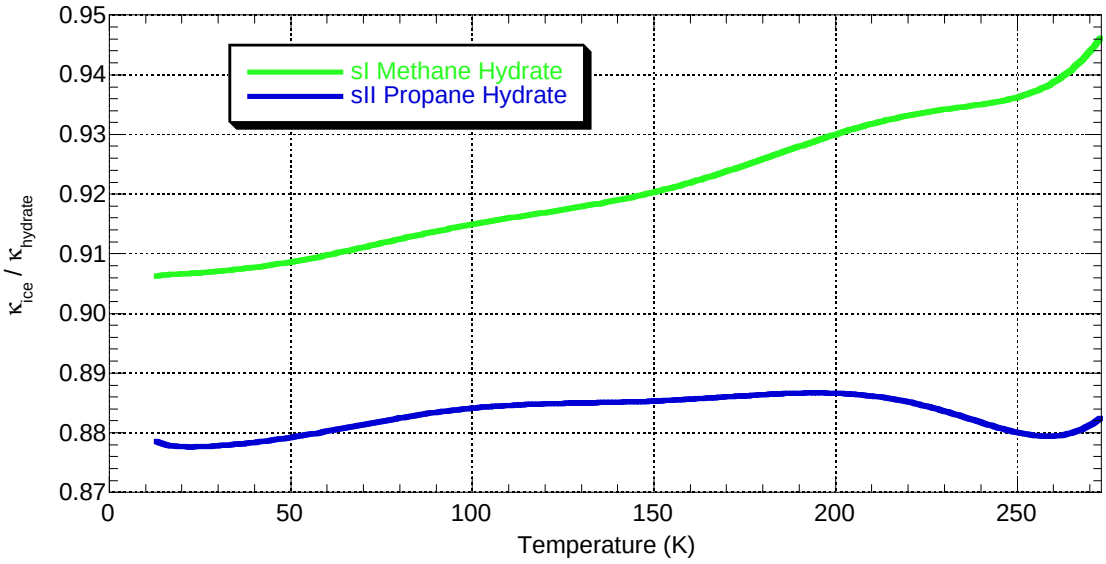

Figure 2.14: Adiabatic compressibility ratio for ice Ih and methane hydrate and ice Ih and propane hydrate versus temperature. The curves stop at 13 K because the C_{P_i} extrapolation is negative for T< 13 K (see Figure 2.10).

hydrate varies more with temperature than the prediction for sII propane hydrate. This is due to the difference in behavior of the final factor in Equation 2.12, as can be seen in Figure 2.11. The variation in this factor between sI and sII is caused by differences in thermal expansivity versus temperature (see Figure 2.7).

It is interesting to note that the product of the first and last factors in Equation 2.12 is the ratio of adiabatic compressibility in ice and gas hydrate. This product is plotted versus temperature for sI methane hydrate and sII propane hydrate in Figure 2.14. The first factor in Equation 2.12 is assumed to be constant versus temperature, so the predicted variations of adiabatic compressibility ratio between ice and sI and sII gas hydrate shown in Figure 2.14 are entirely attributable to the variation with temperature of the final factor in Equation 2.12 (see Figure 2.11).

Extending the Method to Shear Wave Speeds

The methodology described by Whalley (1980) for estimating the ratio of compressional wave speeds in gas hydrate and ice can also be applied to estimating the ratio of shear wave speeds in gas hydrate and ice. In a homogeneous, isotropic linear elastic medium,

the square of the shear wave speed (V_S) is given in terms of the shear modulus (G) and density (ρ) by

$$V_S^2 = \frac{G}{\rho}. \tag{2.62}$$

Applying Equations 2.7, 2.8 and 2.10 to Equation 2.62 gives,

$$V_S^2 = \frac{3}{\kappa_T} \cdot \frac{1}{\rho} \cdot \frac{\frac{1}{2}-\nu}{1+\nu} \cdot \frac{1}{1-\frac{\alpha^2 TV}{\kappa_T C_P}}. \tag{2.63}$$

Equation 2.63 can be used to calculate V_{S_h}/V_{S_i} in the same fashion that Equation 2.11 was used to calculate V_{P_h}/V_{P_i} above, giving

$$\frac{V_{S_h}}{V_{S_i}} = \sqrt{\frac{\kappa_{T_i}}{\kappa_{T_h}} \cdot \frac{\rho_i}{\rho_h} \cdot \frac{\frac{1}{2}-\nu_h}{\frac{1}{2}-\nu_i} \cdot \frac{1+\nu_i}{1+\nu_h} \cdot \frac{1-\frac{\alpha_i^2 TV_i}{\kappa_{T_i} C_{P_i}}}{1-\frac{\alpha_h^2 TV_h}{\kappa_{T_h} C_{P_h}}}}. \tag{2.64}$$

Alternatively, we can observe that Equations 2.11 and 2.63 differ only in the Poisson's ratio factor and express V_{S_h} in terms of V_{P_h} as

$$V_{S_h} = V_{P_h} \sqrt{\frac{\frac{1}{2}-\nu_h}{1-\nu_h}}. \tag{2.65}$$

(Note that Equation 2.65 can also be derived from the relationship $\nu = \frac{1}{2}\frac{(V_P/V_S)^2-2}{(V_P/V_S)^2-1}$.) Therefore Whalley's method can be used to estimate both the compressional and shear wave speeds in isotropic, linear elastic polycrystalline gas hydrate samples. The predictions for shear wave speed ratios between sI methane hydrate (70% and 100% cage occupancy) and ice and sII propane hydrate (70% and 100% large cage occupancy) and ice are shown in Figures 2.15 and 2.16, respectively.

Uncertainty in Wave Speed Ratio Estimates

Uncertainty in the estimates of V_{P_h}/V_{P_i} and V_{S_h}/V_{S_i} can be calculated from the general propagation of uncertainty formula

$$\Delta F = \sqrt{\sum_{i=1}^{n} \left(\frac{\partial F}{\partial x_i}\Delta x_i\right)^2}, \tag{2.66}$$

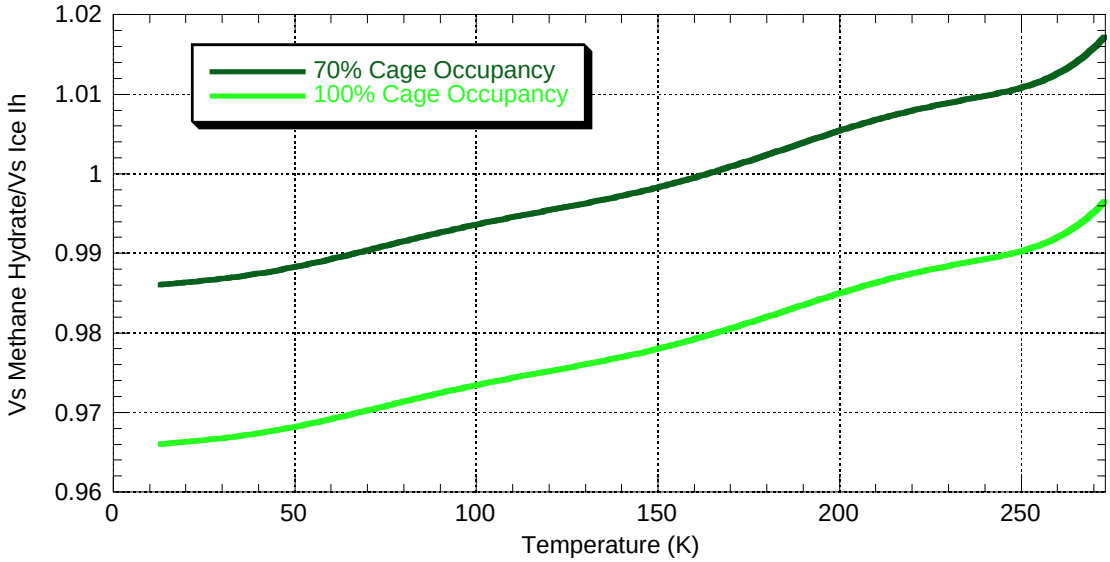

Figure 2.15: Shear wave speed ratio for sI methane hydrate and ice Ih vs temperature. The two curves represent the results obtained by assuming 70% or 100% cage occupancy, respectively. The decrease in ratio value in going from 70% to 100% cage occupancy is due solely to the increase in gas hydrate density that occurs with the increased cage occupancy rate. The curves stop at 13 K because the C_{P_i} extrapolation is negative for T$<$ 13 K (see Figure 2.10).

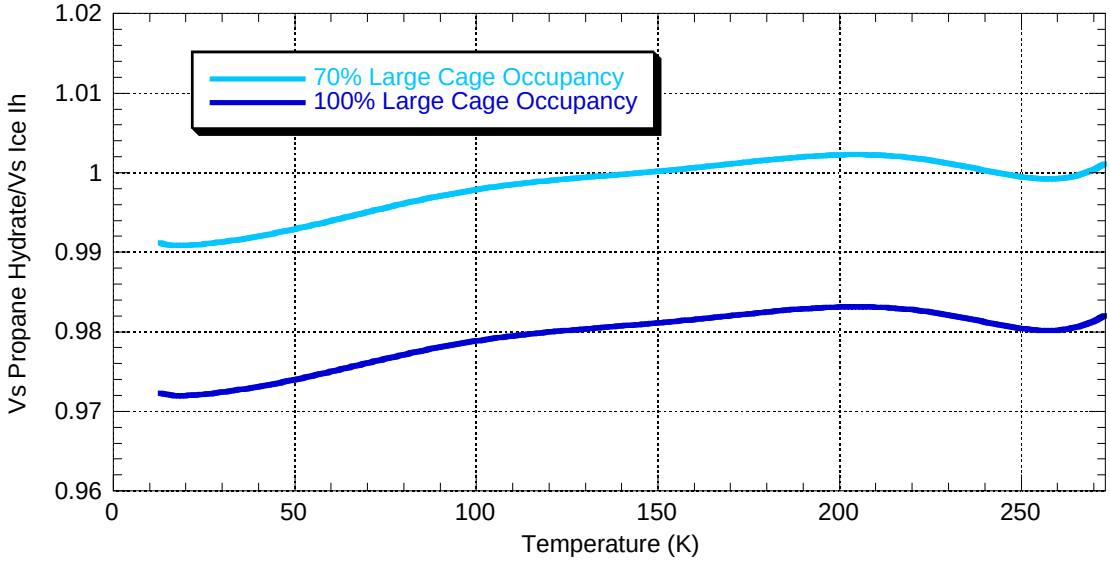

Figure 2.16: Shear wave speed ratio for sII propane hydrate and ice Ih vs temperature. The two curves represent the results obtained by assuming 70% or 100% large cage occupancy, respectively. The decrease in ratio value in going from 70% to 100% large cage occupancy is due solely to the increase in gas hydrate density that occurs with the increased large cage occupancy rate. The curves stop at 13 K because the C_{P_i} extrapolation is negative for T$<$ 13 K (see Figure 2.10).

Table 2.4: Wave Speed Ratio Error Functions and Physical Property Uncertainty Estimates

x	$\frac{\partial F}{\partial x_i}$	$\frac{\partial F}{\partial x_h}$	Δx_{ice}	Δx_{sI}	Δx_{sII}
κ_T	$\frac{1}{2\kappa_{T_i}} \quad \frac{1}{1-\frac{\alpha_i^2 T V_i}{C_{P_i}\kappa_{T_i}}}$	$-\frac{1}{2\kappa_{T_h}} \quad \frac{1}{1-\frac{\alpha_h^2 T V_h}{C_{P_h}\kappa_{T_h}}}$	$\approx 0.05 \cdot \kappa_{T_i}$	$\approx 0.1 \cdot \kappa_{T_{sI}}$	$\approx 0.1 \cdot \kappa_{T_{sII}}$
ρ	$\frac{1}{2\rho_i}$	$-\frac{1}{2\rho_h}$	$< 0.001 \cdot \rho_i$	$\approx 0.01 \cdot \rho_{sI}$	$\approx 0.01 \cdot \rho_{sII}$
$\nu_{(P)}$	$\frac{1}{1-\nu_i^2}$	$-\frac{1}{1-\nu_h^2}$	≈ 0.01	≈ 0.01	≈ 0.01
$\nu_{(S)}$	$\frac{3}{4} \quad \frac{1}{\frac{1}{2}-\nu_i} \quad \frac{1}{1+\nu_i}$	$-\frac{3}{4} \quad \frac{1}{\frac{1}{2}-\nu_h} \quad \frac{1}{1+\nu_h}$	≈ 0.01	≈ 0.01	≈ 0.01
α	$\frac{1}{\alpha_i} \quad \frac{1}{1-\frac{C_{P_i}\kappa_{T_i}}{\alpha_i^2 T V_i}}$	$-\frac{1}{\alpha_h} \quad \frac{1}{1-\frac{C_{P_h}\kappa_{T_h}}{\alpha_h^2 T V_h}}$	$\approx 0.1 \cdot \alpha_i$	$\approx 0.1 \cdot \alpha_{sI}$	$\approx 0.1 \cdot \alpha_{sII}$
V	$\frac{1}{2V_i} \quad \frac{1}{1-\frac{C_{P_i}\kappa_{T_i}}{\alpha_i^2 T V_i}}$	$-\frac{1}{2V_h} \quad \frac{1}{1-\frac{C_{P_h}\kappa_{T_h}}{\alpha_h^2 T V_h}}$	$< 0.001 \cdot V_i$	$\approx 0.01 \cdot V_{sI}$	$\approx 0.01 \cdot V_{sII}$
C_P	$-\frac{1}{2C_{P_i}} \quad \frac{1}{1-\frac{C_{P_i}\kappa_{T_i}}{\alpha_i^2 T V_i}}$	$\frac{1}{2C_{P_h}} \quad \frac{1}{1-\frac{C_{P_h}\kappa_{T_h}}{\alpha_h^2 T V_h}}$	0.1 J/mol K	0.1 J/mol K	0.1 J/mol K

where F is the function being evaluated (in this case V_{P_h}/V_{P_i} or V_{S_h}/V_{S_i}), x_i is the ith variable of the function F and Δx_i is the uncertainty in the value of the ith variable. For both V_{P_h}/V_{P_i} and V_{S_h}/V_{S_i} it can be shown that each partial derivative $\frac{\partial F}{\partial x_i}$ can be written as $F \cdot g_i(x_1, x_2, \cdots, x_n)$. In this special case, Equation 2.66 becomes

$$\frac{\Delta F}{F} = \sqrt{\sum_{i=1}^{n} \left(g_i(x_1, x_2, \cdots, x_n) \cdot \Delta x_i\right)^2}, \tag{2.67}$$

and the contribution for each variable x_i to the relative uncertainty $\frac{\Delta F}{F}$ can be directly calculated. Table 2.4 lists the functions $g_i(x_1, x_2, \cdots, x_n)$ needed to calculate the right-hand side of Equation 2.67 for V_{P_h}/V_{P_i} and V_{S_h}/V_{S_i}. Using the error estimates for each variable as given in Table 2.4, the relative uncertainty in V_{P_h}/V_{P_i} for sI methane hydrate and

sII propane hydrate is approximately 6%. This should be compared to Whalley's (unsupported) assertion that the method is accurate to within 0.5% (Whalley, 1980). The relative uncertainty in V_{S_h}/V_{S_i} for sI methane hydrate and sII propane hydrate is 7 to 8%.

2.4.2 Wave Speeds in Pure Gas Hydrate – Measurements

There are only a handful of published laboratory measurements of compressional and shear wave speeds through gas hydrate. The first to report compressional wave speeds were Stoll and Bryan (1979). They used the ultrasonic pulse-transmission technique to study propane gas hydrate. Whiffen et al. (1982) and Kiefte et al. (1985) reported compressional wave speeds and one shear wave speed determined from Brillouin spectroscopy, a technique based on measuring the (Doppler) frequency shift of laser light inelastically scattered from thermally induced elastic waves (i.e., density fluctuations) in a transparent medium. They studied eight different guest species, four of each structure type. Pandit and King (1982) reported ultrasonic pulse-transmission compressional and shear wave speed measurements on propane gas hydrate/ice mixtures. Bathe et al. (1984) reported compressional and shear wave speeds in sII THF hydrate as a function of temperature from 180 to 256 K using a pulse-echo overlap technique. Recently, Berge et al. (1999) reported compressional wave speed measurements on Freon-11 hydrate. These papers are discussed below in chronological order.

Stoll and Bryan (1979) summarized a series of measurements (Stoll et al., 1971; Stoll, 1974) made on the physical properties of propane and methane gas hydrate. Stoll and Bryan (1979) focused on the anomalous thermal conductivity of gas hydrate and the speed of sound through sands containing gas hydrate, but they also reported one compressional wave speed experiment on pure propane gas hydrate. The propane gas hydrate sample was formed by vigorously mixing water and liquid propane in a cylindrical acrylic pressure vessel. This process formed a propane gas hydrate slurry. The propane gas hydrate was then compacted within the pressure vessel and left undisturbed at constant temperature (2° C) and gas pressure ($\sim$ 70 psia) for several days. During this aging process, compressional wave speeds were measured using the ultrasonic pulse-transmission method through the diameter of the cylindrical sample. Over the course of several days, the sample changed from "fairly stiff 'slush' " to a "hard impenetrable mass," without changing volume. Stoll

and Bryan reported that the compressional wave speed increased from 1418 m/s to 2400 m/s in ten days. They concluded that the changes in wave speed without observable change in volume (or temperature or pressure) suggested "formation and growth of bonds between gas hydrate flakes, probably owing to diffusion of gas and/or water molecules" within the sample. Because of the way this sample was made (see Chapter 3), it probably contained pockets of unreacted water and propane. Therefore, Stoll and Bryan's (1979) reported compressional wave speeds should not be used for estimating the elastic properties of pure propane gas hydrate.

Whiffen et al. (1982) reported compressional wave speeds for methane and xenon gas hydrate determined from Brillouin spectroscopy measurements. Brillouin spectroscopy is a laser based technique that utilizes the frequency shift of light scattered inelastically from the ambient, thermally induced elastic waves in a transparent medium. The technique requires optical clarity so that light can enter the medium of interest and be scattered within. The formula used to measure the compressional wave speed is

$$V = \frac{\Omega\,\lambda_0}{2n\,\sin\frac{\alpha}{2}}, \tag{2.68}$$

where V is the phase velocity of the elastic wave in the medium, Ω is the frequency shift of the scattered light, λ_0 is the wavelength of the incident light, n is the index of refraction in the medium and α is the scattering angle. An ideal Brillouin spectrum from an anisotropic elastic material would include three doublets, one for compressional waves and two for perpendicularly polarized shear waves. The frequency shifts (or, equivalently, velocities) also depend on crystal orientation relative to the incident laser light. These Brillouin shifts can be accurately measured using Fabry-Perot interferometry. Sample sizes for this technique can be quite small, $< 1\text{mm}^3$.

Whiffen et al. (1982) made samples of methane and xenon sI gas hydrate by first forming single crystals of ice approximately 5 mm high in a 10 cm tall 1.5 mm I.D. (6.5 mm O.D.) quartz tube. They then raised the temperature to 0°C and pressurized the system with gas (5.0 MPa for methane and 0.3 MPa for xenon). Within a few hours, this procedure produced small (about 0.5 mm tall) samples of gas hydrate, which were allowed to age for approximately one day. The optical quality of the resultant xenon gas hydrate samples was

quite high but the methane samples were reportedly very cloudy. After formation the samples were cooled to -10°C and the Brillouin spectra were measured using an argon-ion laser and a triple pass Fabry-Perot interferometer located at a scattering angle (α) of 90°. The laser light passed through a highly polished quartz plug at the bottom of the sample tube, traveled through the ice and then was diffusely scattered at the ice/gas hydrate boundary. This diffuse scattering meant the laser light did not penetrate a significant distance into the sample. As a result, a number of steps were taken to filter out the unwanted scattered light and observations were carried out for several days in order to observe *any* of the Brillouin spectral peaks. *Only two spectra for methane gas hydrate were ever obtained from a total of five samples*.

Five samples of higher optical quality xenon gas hydrate yielded nine spectra with a longitudinal component. The high optical quality of the xenon samples made it possible to study the variation of the Brillouin spectrum with height in the sample. Particular attention was paid to the ice/gas hydrate interface. Whiffen et al. (1982) reported that a sharp reduction and eventual disappearance of the ice Brillouin spectrum occurred at the ice/gas hydrate boundary, and this event coincided with a maximum in the gas hydrate Brillouin spectrum. The decrease in signal strength above the interface is probably due to a lack of beam penetration into the gas hydrate portion of the sample, but may also be related to variations in cage occupancy rates with height in the sample. Observations reported from the xenon gas hydrate experiments suggested that prolonged exposure to the laser light caused local deterioration of the gas hydrate sample. These three factors, beam penetration, cage occupancy and sample degradation, were cited as the main causes of sample to sample variability (reported simply as a $\pm$ error) in their results.

Instead of reporting their results as an absolute compressional wave speed in gas hydrate, they report values for difference in frequency shift (Ω_{hi}) between gas hydrate and ice, estimated density, estimated index of refraction (which is calculated theoretically instead of measured) and the ratio of compressional wave speeds in gas hydrate and ice (V_{P_h}/V_{P_i}). The results for xenon gas hydrate at -10°C were 18.5$\pm$1.5%, 1.731 g/cm^3, 1.40 and 0.76, respectively. It is interesting to note the xenon gas hydrate sample which reportedly produced by far the strongest spectra, also yielded the greatest reported reduction in frequency, 20% compared to the ice peak. The results for methane gas hydrate, also at -10°C, were

9.4±2.0%, 0.915 g/cm^3, 1.35 and 0.88 respectively. The authors converted the compressional wave speed ratio between methane hydrate and ice to a compressional wave speed of 3400 m/s in methane hydrate based on an average compressional wave speed in ice determined from measurements by Gammon et al. (1980).

To convert the stated errors in frequency shift to errors in velocity estimate, note that

$$\frac{\Omega_i - \Omega_h}{\Omega_i} = \Delta\Omega_{hi} \tag{2.69}$$

where Ω_h is the Brillouin frequency shift in gas hydrate, Ω_i is the Brillouin frequency shift in ice and $\Delta\Omega_{hi}$ is the relative change in frequency shift for gas hydrate relative to ice. Solving Equation 2.69 for Ω_h, we obtain,

$$\Omega_h = (1 - \Delta\Omega_{hi})\,\Omega_i. \tag{2.70}$$

Substituting Equation 2.70 into Equation 2.68 we have

$$V_{P_h} = \frac{(1 - \Delta\Omega_{hi})\,\Omega_i\,\lambda_0}{2n\,\sin\frac{\alpha}{2}}. \tag{2.71}$$

If we assume that Ω_i, λ_0, n and α are known exactly, then Equation 2.66 gives the relative uncertainty in compressional wave speed as,

$$\frac{\Delta V_{P_h}}{V_{P_h}} = \frac{\Delta\Omega_{hi}}{1 - \Delta\Omega_{hi}}. \tag{2.72}$$

From Equation 2.72 we can calculate the relative uncertainty in the compressional wave speed estimates for methane and xenon hydrate as 2.2% and 1.8%, respectively. These values underestimate the uncertainty because Ω_i, λ_0, n and α are not known exactly. However, Whiffen et al. (1982) report that the largest uncertainty is in the measurement of the frequency shift, so this estimate should be very close to the total uncertainty.

In a follow up paper, **Kiefte et al. (1985)** extended the Brillouin wave speed measurements reported by Whiffen et al. (1982) to sI gas hydrates of hydrogen sulfide (H_2S) and sulfur dioxide (SO_2) and sII gas hydrates of propane (C_3H_8), tetrahydrofuran (THF), Freon-11 and sulfur hexafluoride (SF_6). They also included the previous measurements reported by Whiffen et al. (1982) for methane and xenon sI gas hydrate. Kiefte et al. (1985) followed the same general procedure as reported in Whiffen et al. (1982). Kiefte et al. estimate the

total probable error in their velocity determinations as $\sim 2\%$. In order to compare their experimental results to the theoretical predictions made by Whalley (1980), the authors assumed compressional wave speeds in ice of 3805, 3820 and 3830 m/s at 0, -5 and -10 $^{\circ}$C, respectively. They also truncated Whalley's wave speed ratio equation (Equation 2.12) to include only the first two factors. Kiefte et al.'s measurements are included in the summary table at the end of this section (see Table 2.5). Some general observations reported by Kiefte et al. are summarized below.

sI methane gas hydrate was reportedly the most difficult gas hydrate to make. Only two very weak spectra, the two reported by Whiffen et al. (1982), were ever obtained and "the methane gas hydrate results are by far the most uncertain...it is conceivable that no significant well-defined (focused) penetration of the laser into the [methane] hydrate was made."

The sI hydrogen sulfide hydrate sample was 4 mm long and reportedly had excellent optical qualities. They measured the Brillouin frequency shift as a function of height within the sample and found a change of 2% from bottom to top. This variation was attributed to an assumed change in cage occupancy. It was also assumed the cages were 100% full at the top of the sample. Brillouin spectral line width measurements were made on the hydrogen sulfide sample, and they indicated a spectral line width four times greater in H_2S hydrate than in ice. If correct, this would suggest greater acoustic attenuation in gas hydrate than in ice (Kiefte et al., 1985). Even though sample quality was high and the Brillouin spectra were strong, no transverse (i.e., shear wave) components were observed in the H_2S hydrate sample. The authors assert this is consistent with increased attenuation in gas hydrate compared to ice.

The sI sulfur dioxide hydrate sample was grown slightly differently from the general procedure. It was grown from a saturated aqueous solution. This process was "exceptionally slow" but produced a sample of reportedly excellent quality from which three spectra were obtained. Again, even though the spectra were strong and well defined for the longitudinal component, no transverse peaks were observed.

sI xenon hydrate was reportedly the easiest gas hydrate to create. For this study, they formed one new sample of xenon gas hydrate using a combination of a thin layer of frozen condensed water and controlled amounts of xenon gas and water vapor. This new (4 mm

tall) sample required approximately 4 weeks to become sufficiently clear to allow the passage of a laser beam. The results for this sample differed less than one percent from the previously reported xenon results.

Five spectra were obtained from two sII propane hydrate samples. The spectra for ice and propane gas hydrate were so similar that the ice had to be melted before propane gas hydrate spectra could be taken.

Six, high quality sII tetrahydrofuran (THF) hydrate samples were created from THF-water mixtures (THF is miscible in water). Two of the samples were large single crystals. One of these crystals was probed at a number of different orientations to the crystallographic axes, resulting in spectra very similar to ice Ih. Both longitudinal and transverse components were visible and a total of 43 independent measurements were made. Average longitudinal and transverse frequency shifts were measured for the five other samples. The transverse velocity shift relative to ice was 0.96. The high number and quality of measurements made it possible to determine the elastic constants $C_{11} = 14.1$ GPa, $C_{12} = 5.6$ GPa and $C_{44} = 3.0$ GPa. These values yield averaged estimates of bulk (K) and shear (G) moduli of 8.5 and 3.5 GPa, respectively (Kiefte et al., 1985; Nye, 1985). From these values, Poisson's ratio (ν) can be calculated from Equation 2.56, giving $\nu = 0.32$. THF hydrate was the only gas hydrate reported to contain transverse components in its Brillouin spectra.

sII Freon-11 gas hydrate made using the general technique was excessively cloudy. Useable samples were made by starting with a seed hydrate crystal made outside the measurement system. Even so, samples were of low quality and the relative error was large compared to the other gas hydrate types.

sII sulfur hexafluoride gas hydrate samples were made by repeatedly cycling ice and pressurized sulfur hexafluoride through the melting point of ice so that the sulfur hexafluoride would saturate the melt water. This process produced two, good quality samples.

Kiefte et al. (1985) also state, without citing actual measurements, that the variation of velocity with temperature is believed to be approximately the same as for ice, $\sim -0.7\%\,^{\circ}C^{-1}$. However, this reported value must be a typographical error. The correct value should be $\sim -0.07\%\,^{\circ}C^{-1}$, from their assumed values of V_P in ice of 3805 m/s at 0°C and 3830 m/s at -10°C (i.e., $\frac{\frac{3805-3830}{0-(-10)}}{3830} \approx -0.0007$). Additionally, they observe that the ratio V_{P_h}/V_{P_i} varies linearly with the mass of the guest, and they speculate that a linear regression to their data

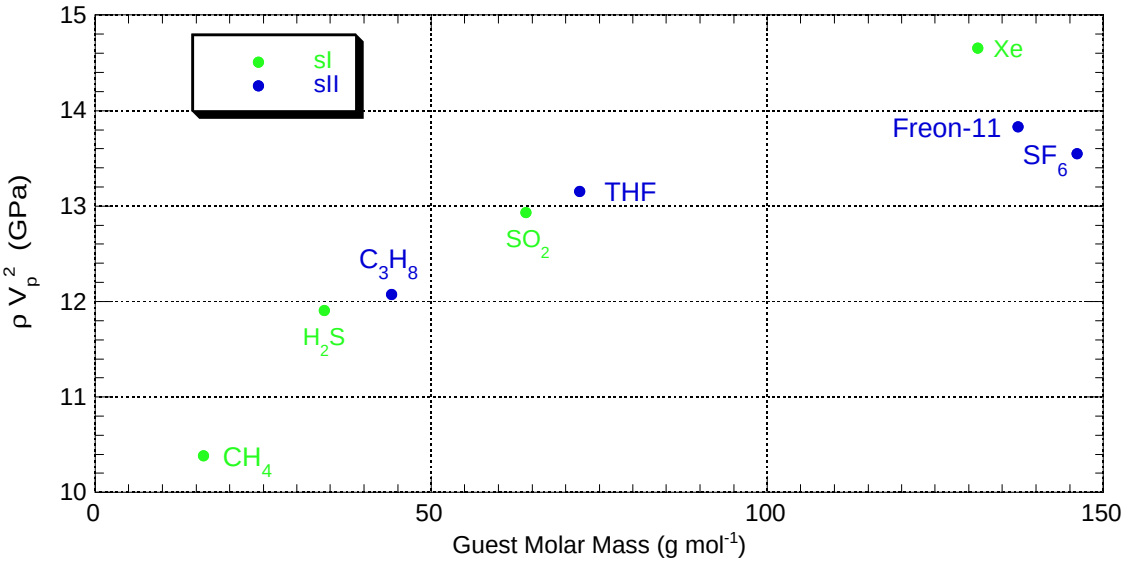

Figure 2.17: Compressional wave modulus (ρV_P^2) vs guest mass for sI and sII gas hydrate. ρV_P^2 calculated from Kiefte et al. (1985) compressional wave speed and density data. The variation of ρV_P^2 with guest mass implies the guest modifies the water crystal lattice in sI and sII gas hydrates, thereby changing the gas hydrates elastic properties.

could be used to infer compressional wave speed in other, as yet untested, gas hydrates. However, a much more relevant plot is ρV_P^2 versus guest mass. This plot tests to see if the compressional wave modulus ($\rho V_P^2 = M = K + \frac{4}{3}G$) is constant versus guest type (i.e., the guest does not modify the elastic properties of the frame), as was assumed by Whalley (1980) and many others. Figure 2.17 shows that this assumption is not strictly valid. However, the range of ρV_P^2 with guest mass is relatively small ($\sim \pm 20\%$ for sI and $\sim \pm 8\%$ for sII), suggesting Whalley's method may still produce reasonable compressional and shear wave speed estimates.

It should be pointed out here that the gas hydrate densities reported by Kiefte et al. (1985) were calculated, not measured. This leads to some uncertainty in the calculated value of ρV_P^2. Additionally, care should be taken when comparing the values for ρV_P^2 in the sI and sII hydrates in Figure 2.17. The sI gas hydrate formers studied by Kiefte et al. were all small enough to fit within both cages of sI, but the sII gas hydrate formers only occupied the large cages of sII. This difference may help account for the smaller variation of ρV_P^2 with respect to guest mass for the sII gas hydrates (i.e., fewer cages per unit volume filled causes less crystal lattice distortion in the sII gas hydrates).

Finally, Kiefte et al. (1985) compare their results to Whalley's predictions and the handful of measurements (see below) that were available at the time. They found that their compressional wave speed data range was less than predicted by Whalley's theory and suggested this could be due to Whalley's assumption that the interaction between guest and host lattice could essentially be ignored. They also found that their measurements did not agree with previously reported results on propane (Pandit and King, 1982) and THF (Bathe et al., 1984) hydrate. They attributed the differences to deficiencies in the previously reported work. This is probably the correct conclusion (see below).

Pandit and King (1982; 1983) reported results for compressional and shear wave speed measurements in propane gas hydrate. The samples were in fact mixtures of propane gas hydrate and ice. The samples were made in a cold room with temperature set at 2°C. Samples were made in a clear, plexiglas cylinder by repeatedly injecting liquified propane into distilled water and mixing vigorously. Each sample was then allowed to sit undisturbed for 24 hours, during which time it formed into a coherent mass. The temperature was then reduced to -18°C over the course of 12 hours. The pressure vessel was disassembled, the sample extracted and machined to produce flat ends. The sample was placed in the wave speed apparatus, double jacketed in rubber and wrapped with vinyl tape (to prevent contamination of the sample with hydraulic oil). The apparatus supplied both a hydrostatic confining pressure and a uniaxial load. Transducers in the wave speed apparatus were sequentially excited in compressional and shear wave mode. Velocities were determined from the time it took the waveform to travel the axial length of the sample. The center frequency of the waveforms was 820 kHz. The confining pressure was 0.35 MPa and the axial stress was binarily varied between 0.53 and 2.1 MPa. The temperature was ramped from -16.5 to 2.4 °C (allowing $\sim$ 24 hours to achieve thermal equilibrium at each temperature step) and the variation of compressional and shear wave speeds with temperature was determined. Results for two propane gas hydrate samples and one ice sample were reported. However, the results for the second gas hydrate sample are only partial because the temperature control system reportedly failed.

Pandit and King report they did not observe any change of wave speed with axial pressure, nor was there any significant wave speed variation with temperature up to 0°C. However, there was a significant drop in compressional wave speed as the sample passed through

0°C and the shear wave signal became essentially undetectable. The compressional wave speed reported for sample 1 (from Figure 9 Pandit and King, 1982) was $\sim$ 3.225 km/s below 0°C and 2.05 km/s above 0°C. The shear wave speed was $\sim$1.675 km/s below 0°C. Sample 2 yielded compressional wave speeds of about 3.075 km/s and shear wave speeds of approximately 1.75 km/s, both below 0°C. From these values and the measured sample densities they calculated bulk and shear moduli values of 5.8 and 2.3 GPa at -16.5°C and 5.6 and 2.4 GPa at -1.1°C, respectively. Applying the bulk and shear moduli results to Equation 2.56, we obtain poisson's ratio values of 0.32 at -16.5°C and 0.31 at -1.1°C, respectively.

The compressional and shear wave speeds through the ice sample were reported to increase from approximately 3.8 to 3.9 km/s and from 2.025 to 2.075 km/s respectively, in the temperature range -16 to -1°C. This is anomalous behavior and probably reflects sample shortening, not accounted for by Pandit and King who did not monitor their sample lengths during the experiments.

Unfortunately, there are a number of shortcomings in the work presented by Pandit and King (1982). The "gas hydrate" samples were actually mixtures of ice and propane gas hydrate. The authors estimate that the ice content in their Hydrate I sample was approximately 10-20% based on the volumetric ratio of propane to water in their sample formation vessel. They also did not check to see if there were any propane or water inclusions in their samples. However, a quick check of their stated densities shows that both propane gas hydrate samples were porous because the density of each sample (0.850 g/cm^3 and 0.750 g/cm^3, respectively) is much less than the density of either propane gas hydrate ($\sim$0.88 g/cm^3) or ice ($\sim$0.92 g/cm^3). They also make no mention of supplying propane pressure to the samples during the wave speed measurements. At the stated temperatures of measurement, propane gas hydrate is not stable at atmospheric pressure (see Figure 2.4). Therefore, some of the sample probably destabilized in the apparatus during the procedure. This destabilization, along with the melting of any ice present in the sample, would have caused a shortening of the sample. That the compressional wave speed dropped precipitously as the sample warmed through 0°C strongly suggests a significant amount of melting did occur. Unfortunately, this hypothesis cannot be rigorously tested because sample lengths were not measured during the experiment. Only after the sample was taken from -16 to +2°C and

back to -17°C and extracted was the length measured. The sample was found to be 0.69 mm shorter. Sample shortening is also a potential cause of the (anomalous) reported increase in compressional and shear wave speeds with increasing temperature for the ice sample.

The results presented by Pandit and King (1982; 1983) should only be used as a very rough estimate of the elastic properties of structure II propane gas hydrate. Unfortunately, because there are so few measurements of the elastic properties of gas hydrate, the values reported by Pandit and King have been repeated in a number of publications as the appropriate values for gas hydrate. Furthermore, the results of Pandit and King have often been cited as the correct values for structure I gas hydrate. The confusion appears to stem from the way Pandit and King refer to their samples, namely as Hydrate I and Hydrate II. They are referring to samples I and II, but the labels have apparently been misinterpreted as referring to structures I and II. This error means that imprecisely determined elastic properties for structure II propane gas hydrate are being extensively used for structure I gas hydrate. I hope that the results for sI methane hydrate presented in Chapter 5 of this thesis will eventually replace the erroneous Pandit and King values currently being quoted in many references.

Bathe et al. (1984) report on compressional and shear wave speed measurements made on tetrahydrofuran (THF) hydrate as a function of temperature from 183 to 256 K. The gas hydrate was formed from an aqueous solution of THF and distilled water (molar ratio 1:17, the ideal for 100% large cage occupancy in sII gas hydrate). THF hydrate was obtained by vigorously shaking the water/THF mixture while cooling the system through 0°C. The samples were made in 2 cm long cylindrical containers with caps, providing flat, parallel ends. Transducers were bonded to the samples and travel times through the sample were determined using a pulse-echo overlap technique. It appears that sample lengths were not directly measured throughout the experiment. Instead, a linear expansivity for THF hydrate was assumed (the same as for ice) and the corresponding length changes versus temperature were calculated. Bathe et al. apparently made no allowance for sample shortening due to applied axial pressure. It is also unclear whether they applied any confining pressure to the sample. No diagram of either the sample-forming chamber or wave speed measurement apparatus is provided. Bathe et al. measured the density of their sample prior to measuring wave speeds and obtained a value of 0.954 ± 0.002 g/cm^3. This is less than the theoretically

determined value of 0.979 g/cm^3 that would be expected for a fully dense sample with 100% large cage occupancy.

Bathe et al. report that compressional wave speed dropped from approximately 3.6 to 3.5 km/s as the temperature increased from 183 to 256 K and that shear wave speed increased from approximately 1.61 to 1.66 km/s over the same temperature range. From this data and their calculated variation of density with temperature, they conclude the adiabatic bulk modulus of THF hydrate decreased from 9.0 to 8.2 GPa as the temperature rose from 183 to 256 K and that Poisson's ratio dropped from 0.37 to 0.355. These results do not agree with those determined by Kiefte et al. (1985) for THF hydrate. There are many possible reasons for this discrepancy, including the poor quality shear wave signals reported by Bathe et al., and their erroneous assumption that the thermal expansion of ice and THF hydrate were equal. Because of these shortcomings, I consider the values provided by Kiefte et al. (1985) for THF hydrate to be more reliable than those provided by Bathe et al. (1984).

The only other data provided in the literature are recent measurements made by **Berge et al. (1999)** of compressional wave speed through Freon-11 gas hydrate. Samples were made at atmospheric pressure and 2°C by mixing water and Freon-11. As the material became viscous, active mixing stopped and the sample was allowed to "age" without disturbance. A layer of water was placed on top of the mixture to prevent any additional air from entering the sample and the material was left to harden overnight. Compressional wave speeds were measured along two paths through the diameter of the sample vertically separated by 60 mm using transducers with a 500 kHz center frequency. If the two measured wave speeds differed by a significant amount, that sample was rejected as inhomogeneous. Shear wave measurements were attempted, but sufficient signal quality reportedly could not be obtained through the pure gas hydrate samples. The fractional amount of gas hydrate in each sample was estimated after each experiment by flushing the sample with saline solution and measuring the conductivity of the water produced by melting the sample.

Using this procedure, Berge et al. (1999) report measuring a compressional wave speed of 1400 m/s in a sample with very low gas hydrate concentration and a compressional wave speed of 2500 m/s in a sample with 68% gas hydrate. They also show that the transition from 1400 to 2500 m/s takes place over several hours in an essentially two-step process, namely rapid increase in compressional wave speed after approximately 10 hours and then

asymptotic increase for the remainder. This strongly suggests the gas hydrate changes from a suspension to a (gas hydrate) grain supported material after approximately 10 hours. Berge et al. show that this behavior is relatively well modeled using the critical porosity model (Nur et al., 1998) with critical porosity 38%. Unfortunately, Berge et al., were never able to produce a non-porous sample of Freon-11 hydrate. Therefore, their data cannot be easily used to produce estimates of the elastic moduli of sII gas hydrate.

The wave speed measurements discussed in this section are summarized in Table 2.5. The publications of Whiffen et al. (1982) and Kiefte et al. (1985) stand out as the best available data on elastic wave speeds in gas hydrate. Unfortunately, their work still suffers from three deficiencies: (1) the methane gas hydrate data are highly suspect because of poor sample quality; (2) no shear wave speeds (except for sII THF hydrate) were determined; and (3) it is not entirely clear that the wave speeds they measured at ultra high frequency and short wavelengths are appropriate for macroscopic average properties at the well log or seismic scales. The pulse-transmission compressional and shear wave speed measurements presented in this thesis (Chapters 4 and 5) address these shortcomings for sI methane hydrate.

2.4.3 Wave Speeds in Sediments Containing Gas Hydrate

Similar to the situation for measurements of compressional and shear wave speeds in pure gas hydrate, there are very few published measurements of wave speeds in sediments containing gas hydrate. There is only one paper that describes an experiment where the amount of gas hydrate in the sediment sample was actually quantified. This section provides a survey of laboratory measurements described in the literature.

The publications of Stoll and co-workers (Stoll et al., 1971; Stoll, 1974; Stoll and Bryan, 1979) were the first to report laboratory measurements of compressional wave speeds in sediments containing gas hydrate. They reported measurements for compressional wave speed in water saturated Ottawa sand containing either methane or propane gas hydrate. Their work was motivated by anomalously high seismic interval velocities detected at the Blake Ridge, off the coast of the southeastern United States, at stratigraphic levels where highly gassy sediment was recovered from DSDP Leg 11 drill cores. The presence of gas in sediment is well known to cause a significant decrease in compressional

Table 2.5: Reported Wave Speed Measurements in Pure Gas Hydrate

Source	**Measurement Technique**	**Structure and Guest**	**Temp. (°C)**	**Vp (m/s)**	**Vs (m/s)**	**Density (kg/m^3)**
Stoll and Bryan, 1979	Pulse Transmission	sII, C_3H_8[a]	2	2400	NA	NA
Pandit and King, 1982	Pulse Transmission	sII, C_3H_8[a]	-16.5 to 2.4	3250 to 2050	1675 to NA	850
Bathe et al., 1984	Pulse-Echo Overlap	sII, THF	-90 to -17	3580 to 3510	1610 to 1660	954
Kiefte et al., 1985	Brillouin Spectroscopy	sI, CH_4[b]	-10	3369	NA	915
		sI, H_2S	-5	3355	NA	1058
		sI, SO_2	-5	3144	NA	1308
		sI, Xe[b]	-10	2910	NA	1731
		sII, C_3H_8	0	3698	NA	883
		sII, THF	0	3665	1890	979
		sII, Freon-11	0	3459	NA	1156
		sII, SF_6	-5	3390	NA	1179
Berge et al., 1999	Pulse Transmission	sII, Freon-11[a]	2	2500	NA	NA

[a] Sample either reported as porous or can be inferred porous from low V_P and/or density
[b] Kiefte et al. (1985) data supersede results in Whiffen et al. (1982) for CH_4 and Xe gas hydrate

wave speed. Additionally, an anomalous seismic event, referred to as a Bottom Simulating Reflector (BSR) was found at approximately the same depth in the section. The hypothesis of Stoll et al. (1971) was that this anomalously high velocity and unexplained seismic reflection were caused by increased compressional wave speed in the sediment due to the formation of gas hydrate. They performed experiments to test this theory and measure the physical properties of sands containing gas hydrate.

Stoll et al. (1971) and **Stoll (1974)** report on compressional wave speed measurements made on water saturated sands containing gas hydrate and free gas. They used commercial

grade methane gas that contained trace amounts ($\leq$ 3.6%) of carbon dioxide, nitrogen, ethane, propane, butane and heavier hydrocarbons. (Note that even trace amounts of certain gases can lead to the formation of sII gas hydrate, whereas pure methane gas hydrate forms sI gas hydrate.) Their samples were formed by bubbling gas through a water saturated sand column. They used rounded Ottawa sand that passed through a U.S. #20 standard sieve and was captured by a #30 sieve. The average grain size was $\sim$ 0.7 mm. The saturated sediment was confined between two porous platens that contained piezo-ceramic transducers. The platens were used to apply an axial confining pressure to the sand pack, but the actual applied pressure was not reported. The source transducer was pulsed 100 times/second and the delay time was measured using a calibrated delay circuit.

Stoll et al. (1971) report the results from two successful runs. In the first, distilled water was used and gas hydrate was formed by cooling the system to 3.3 °C, pressurizing the system to 1100 psia from the methane bottle and then slowly bleeding gas out through a valve in the top of the pressure vessel until the pressure reached 700 psia. This pressure reduction caused gas bubbles to travel through the sand pack and lasted approximately 15-20 minutes. This cycle was repeated 20 times over 9 hours. At 4.5°C and gas pressure 1000 psia, prior to the first pressure drop, a compressional wave speed of 1.83 km/s was observed. By the end of the 20th cycle, the compressional wave speed had reached 2.0 km/s. The first few bubbling cycles led to dramatic decreases in the amplitude and signal quality of the transmitted wave. By the end of the 20th cycle, the signal strength had returned, but the center frequency of the transmitted waveform was approximately 1/3 that of the signal transmitted prior to bubbling.

The second reported run used a different gas distribution system and sea water instead of distilled water. The temperature bath was held constant at 2.0 °C and the gas pressure was cycled from 1200 to 700-800 psia. During the first $\sim$20 cycles, the compressional wave speed increased from 1.85 to 1.97 km/s. At that point, a number of dramatic changes reportedly occurred in the waveform and the compressional wave speed jumped to 2.55 km/s. From that point on, the waveform reportedly remained stable and the compressional wave speed increased gradually to 2.69 km/s. **Stoll (1974)** recounts these experiments and adds that at least one run eventually reached a compressional wave speed greater than 2.7 km/s. After each run, the apparatus was quickly dismantled and Stoll (1974) reported the sand

was generally hard and coherent, closely resembling frozen, saturated sand.

Stoll and Bryan (1979) report compressional wave speed measurements from one pure propane gas hydrate sample (described above) and one propane gas hydrate in sand sample. The gas hydrate in sand sample was made by mixing sand, water and liquid propane in a pressure vessel and then compacting the resultant gas hydrate containing mixture to the volume originally occupied by the water saturated sand. The sample was left to sit undisturbed for several days. Stoll and Bryan reported the compressional wave speed increased from 1800 to 2260 m/s after 12 days. No changes in temperature, pressure or sample volume were observed during the "aging" of the sample. The authors concluded that this implied the creation and growth of bonds between gas hydrate flakes within the sample.

In the mid 1980s, **Pearson and co-workers (Pearson et al., 1983b; Pearson et al., 1984; Pearson et al., 1986)** reported results for compressional wave speed and electrical resistivity measurements in Berea sandstone, Austin chalk and Solenhofen limestone containing tetrahydrofuran (THF) hydrate. THF was used instead of a hydrocarbon gas because THF is miscible in water and forms gas hydrate at 4°C and room pressure. Their cylindrical samples were 2.5 cm in diameter and 4-5.5 cm long and were reportedly cored perpendicular to the bedding planes within the original rocks. The porosities of the sandstone, chalk and limestone samples were $\sim$20%, $\sim$30% and $<$ 1%, respectively. The samples were dried for 24 hours at 100°C in a vacuum oven to remove residual pore water. Samples were then transferred to another vacuum chamber, the water-THF mixture was added and the entire sample was placed in a high pressure system and exposed to 10 MPa of nitrogen gas. The water-THF mixture was prepared with varying amounts of salt (NaCl). Unfortunately, they used a molar ratio of 18:1 (water:THF). The ideal ratio is 17:1; therefore, their samples had an excess of water. The temperature of the system was controlled by a temperature bath and 24 hours were always allowed for the sample to come to thermal equilibrium before any measurements were made. The temperature was varied from a positive starting point (anywhere from 0 to 20°C) to -30°C. Wave speeds were measured using the "time-of-flight" technique. Waveforms were generated with 1 MHz center frequency LZT-5 transducers. Pearson et al. (1986) reported that errors in the arrival time delay measurement ranged from 5% (samples containing gas hydrate) to 10% (no gas hydrate). Length measurement errors were $<$ 1%. All measurements were conducted at atmospheric pressure with a small

axial load to maintain contact between the transducers and the sample.

Pearson and co-workers reported that compressional wave speed in Berea sandstone samples increased from ∼2.5 km/s, when water saturated, to ∼4.5 km/s, when THF hydrate saturated. The rate at which the increase occurred was dependent on the salinity of the pore water (greater salinity corresponded to more gradual compressional wave speed increase), but the maximum compressional wave speed did not. From plots of the data (Pearson et al., 1984), it appears that the compressional wave speed did not increase until the system passed through 0°C. This raises a question about the presence of ice in the samples tested. The authors report that the solid material formed in the experiments persisted until ∼ 4°C, "proving" it was gas hydrate. However, it seems likely the cores contained some water ice as well. (Reported NMR and resistivity measurements suggest brine might also have been present, even at -30° C.) Compressional wave speed through the Austin chalk samples increased from 1.4 to 5.0 km/s. The same behavior for wave-speed versus pore water salinity and temperature was reported for these samples as for Berea sandstone. The Solenhofen limestone samples showed no variations of compressional wave speed with temperature. This observation was attributed to the lack of porosity in the limestone samples.

Wittebolle and Sego (1985) reported measurements of compressional wave speed in sands containing Freon-12 hydrate. The samples were made from quartz sand that passed through U.S. Standard sieve #12 and were captured in a #20 sieve. Wet sand was compacted in a sample mold to a fixed density and then the pore space was pressurized with Freon-12 gas to 300 kPa. Next, the sample was cooled to 2°C and gas hydrate was reportedly observed forming in the pore spaces between the sand grains. At this temperature, Freon-12 condenses. When liquid Freon-12 was observed in the sample, the gas bottle was closed, and the excess liquid Freon-12 was vented. This caused mechanical agitation and Joule-Thompson cooling in the system. The venting caused more solid to form, some of which was probably water ice. The sample was then cooled to -25°C (converting any residual water to ice) and extracted from the mold. Some of the samples thusly made were reportedly placed in a triaxial test system and their resistance to deformation measured. As a quality control for these strength tests, the authors performed compressional wave speed measurements using transducers built into the triaxial apparatus. Because the wave speed measurements were not the focus of the project, the information on the actual wave-speed

measurements is minimal. However, they do show waveforms for measurements made at -1.7°C, 1.89°C and ∼5°C, clearly showing the amplitude and frequency content decreasing as temperature increases. The compressional wave speed at -1.7 °C was 3.55 km/s and decreased to 2.46 km/s at 1.89°C. The wave speed dropped to 1.9 km/s after all the gas hydrate had decomposed. Wittebolle and Sego report that the sample was 97% saturated. I assume that this was the original water saturation. They do not report gas hydrate saturation of the pore space. The change in wave speed as the sample warmed through 0°C strongly suggests that water ice was present in the sample.

Recently, **Berge et al. (1999)** reported measurements of compressional and shear wave speed versus gas hydrate saturation of the pore space for Freon-11 hydrate in sands. This is the only paper in the literature which reports pore space saturation values in conjunction with wave-speed measurements. The samples were made by adding dry sand to a pressure vessel, evacuating the system, saturating the sand with fresh water, injecting Freon-11 into the water saturated sand and then allowing the sample to sit for 1-4 days. Twelve different experiments were run, six with a grain size of 280μm and six with an average grain size of 100μm. Porosities were estimated from the difference between dry and saturated sample masses and the amount of Freon-11 was estimated from the volume of water ejected during the Freon injection process. After gas hydrate formation, brine of a known conductivity was flushed through the samples until the expelled brine had the same conductivity as the injected brine. P and S-wave speeds were measured using 500 kHz center frequency transducers located along two different horizontal planes through the sample a vertical distance 60 mm apart. The P-wave arrival times could be determined to within 0.1μs, but the S-wave arrival times were at best accurate to only 1 μs because of interference between ringing from the earlier P-wave arrival and the target shear wave. If the wave speeds measured at different locations within the sample differed substantially, the sample was rejected as too inhomogeneous. Gas hydrate saturation of the pore space was estimated by dissociating the gas hydrate phase and boiling off first the Freon-11 and then the water. The amounts of Freon and water that had been present in the sample were estimated from the mass change after each respective liquid was boiled off. The amount of salt present was determined by flushing the dried sample with deionized water and measuring the conductivity of the resulting fluid. From all these quantities, the gas hydrate saturation could be inferred with a

stated accuracy of approximately ± 0.05. This work illustrates the complexity of estimating gas hydrate saturation in laboratory samples made by injecting (or bubbling) a gas hydrate former into a water saturated sand pack.

Berge et al. (1999) reported that for the samples studied, the compressional wave speed varied from 1700 m/s at low gas hydrate content to 3810 m/s at a gas hydrate saturation of 52%. Shear wave speeds were undetectable for gas hydrate saturations below 35%. At $\sim$40% saturation, the shear wave speed was approximately 1500 m/s, increasing to $\sim$2200 m/s at 55% saturation. Samples with a gas hydrate saturation greater than 35% were hard and consolidated. One sample with 57% gas hydrate saturation reportedly resisted blows from a small sledge hammer! Berge et al. (1999) observed a significant shift in the wave speed versus saturation trend at $\sim$35% gas hydrate saturation of the pore space. This was the point where a shear wave became detectable and the P-wave speed increased substantially. They concluded that this was the approximate saturation of the pore space where the gas hydrate ceased being suspended in the fluid phase, and instead made mechanical contact between gas hydrate grains, and presumably with the sand grains as well. This paper is the only one in the literature which supplies laboratory measurements of gas hydrate saturation and wave speed on the same samples.

The papers by Stoll and co-workers were pioneering and proved the qualitative impact of gas hydrate formation on the elastic properties of water saturated sands. Many of the observations and comments found in their papers also apply to the work done for this thesis in forming propane gas hydrate by bubbling gas through water and water saturated sediments (Chapter 3). Unfortunately, their results are not useful for quantitative modeling because the amount of gas and gas hydrate in the pore space was never satisfactorily measured. As I discuss in Chapter 3, this is a fundamental problem of the "bubbling-gas-through-water" family of gas hydrate experiments. Additionally, the wave speed measurements reported by Stoll and co-workers were made on water saturated samples. The presence of water may have led to some pore fluid related velocity/frequency dispersion (Mavko et al., 1998). Therefore, it is not entirely clear how their results could be used to test models for interpreting seismic and well log data for gas hydrate content.

The measurements reported by Berge et al. (1999) provide the only possible laboratory data set for modeling the effect of gas hydrate formation on sediment elastic properties.

Unfortunately Berge et al. used an "exotic" gas hydrate forming agent, the accuracy of the saturation determination is not very high and the sample was water saturated, again leading to possible pore fluid related dispersion effects. Additionally, as with the other experiments presented in this section, sand was used as the sediment. Most naturally occurring gas hydrate deposits appear to be in clay rich ocean bottom sediments (Booth et al., 1996).

2.5 Conclusions

- Data on wave speeds in gas hydrate and sediment containing gas hydrate are sparse, especially for methane hydrate, the most commonly found gas hydrate in nature.
- Previously reported wave speed measurements in gas hydrate and sediments containing gas hydrate are not consistent from lab to lab.
- The above two conclusions call for a new series of measurements to be made on the elastic properties of gas hydrate and sediments containing gas hydrate.

2.6 References

Aaldijk, L., 1971, Monovariante gas hydraatevenwichten in het stelsel xenon-water, Ph.D. Thesis, Technische Hogeschool te Delft, 117 pp.

Bathe, M., S. Vagle, G. A. Saunders, and E. F. Lambson, 1984, Ultrasonic wave velocities in the structure II clathrate hydrate THF•17H_2O, Journal of Materials Science Letters, **3**, 904–906.

Berge, L. I., K. A. Jacobsen, and A. Solstad, 1999, Measured acoustic wave velocities of R11 (CCl_3F) hydrate samples with and without sand as a function of hydrate concentration, Journal of Geophysical Research, **104**, No. B7, 15,415–15,424.

Bertie J. E. and E. Whalley, 1967, Optical spectra of orientationally disordered crystals, II, Infrared spectrum of ice Ih and ice Ic from 360 to 50 cm^{-1}, Journal of Chemical Physics, **46**, 1271–1284.

Bertie J. E., F. E. Bates and D. K. Kendricksen, 1974, The far infrared spectra and x-ray powder diffraction patterns of the structure I hydrates of cyclopropane and ethylene oxide at 100K, Canadian Journal of Chemistry, **53**, 71–75.

Bertie, J. E., and S. M. Jacobs, 1978, Infrared spectra from 300 to 10 cm^{-1} of structure II clathrate hydrates at 4.3 K, Journal of Chemical Physics, **69**, 4105–4113.

Booth, J. S., M. M. Rowe and K. M. Fischer, 1996, Offshore Gas Hydrate Sample Database with an Overview and Preliminary Analysis, U.S. Geol. Surv. Open-File Report 96-272, 17pp.

Bridgman, P. W., 1912, Water in the liquid, and five solid forms under pressure, Proceedings of the American Academy of Sciences, **47**, 441–558.

Brooks, J. M., M. C. Kennicutt II, R. R. Fay and T. J. McDonald, 1984, Thermogenic Gas Hydrates in the Gulf of Mexico, Science, **255**, 409–411.

Dallimore, S. R., T. Uchida and T. S. Collett, eds., 1999, Scientific results from JAPEX/JNOC/GSC Mallik 2L-38 gas hydrate research well, Mackenzie Delta, Northwest Territories, Canada, GSC Bulletin 544, 403 pp.

Davidson, D. W., 1973, Clathrate hydrates, in Water–a comprehensive treatise, Vol. II, ed. F. Franks, p. 133.

Davidson, D. W., S. K. Garg, S. R. Gough, R. E. Hawkins and J. A. Ripmeester, 1977, Characterization of natural gas hydrates by nuclear magnetic resonance and dielectric relaxation, Canadian Journal of Chemistry, **55**, 3641–3650.

Davidson, D. W. and J. A. Ripmeester, 1984, NMR, NQR and dielectric properties of clathrates, in Inclusion Compounds, Vol 3, Physical Properties and Applications, J. L. Atwood, J. E. D. Davies and D. D. MacNichol, eds., Academic Press, London, 69–128.

Gagnon, R. E., H. Kiefte, M. J. Clouter and E. Whalley, 1988, Pressure dependence of the elastic constants of ice Ih to 2.8 kbar by Brillouin spectroscopy, Journal of Chemical Physics, **89**, 4522–4528.

Gammon, P. H., H. Kiefte and M. J. Clouter, 1980, Elastic constants of ice by Brillouin spectroscopy, Journal of Glaciology, **25**, 159–167.

Ginsburg G., R. A. Guseynov, A. A. Dadashev, G. A. Ivanova, S. A.Kazantsev, V. A. Soloviev, E. V. Telepnev, P. Ye. Askeri-Nasirov, A. A. Yesikov, V. I. Mal'tseva, Yu. G. Machirov and I. Yu. Shabayeva, Gas hydrates of the southern Caspian, International Geology Review, **43**, 765–782.

Gow, A. J. and T. C. Williamson, 1972, Linear compressibility of ice, Journal of Geophysical Research, **77**, 6348–6352.

Handa, Y. P., 1986a, Calorimetric determinations of the compositions, enthalpies of dissociation, and heat capacities in the range 85-270 K for clathrate hydrates of xenon and krypton, Journal of Chemical Thermodynamics, **18**, 891–902.

Handa, Y. P., 1986b, Compositions, enthalpies of dissociation, and heat capacities in the range 85 to 270 K for clathrate hydrates of methane, ethane, and propane, and enthalpy of dissociation of isobutane hydrate, as determined by a heat-flow calorimeter, Journal of Chemical Thermodynamics, **18**, 915-921.

Handa, Y. P., 1988, A calorimetric study of naturally occurring gas hydrates, Industrial Engineering and Chemistry Research, **27**, 872–874.

Handa, Y. P., R. E. Hawkins and J. J. Murray, 1984, Calibration and testing of a Tiam-Calvert heat-flow calorimeter – Enthalpies of fusion and heat capacities for ice and tetrahydrofuran hydrate in the range 85 to 270 K, Journal of Chemical Thermodynamics, **16**, 623–632.

Hobbs, P. V., 1974, Ice physics, Clarendon Press, Oxford, 837pp.

Holder G. D., S. Zele, R. Enick and C. LeBlond, 1994, Modeling Thermodynamics and Kinetics of Hydrate Formation, in first International Conference on Natural Gas Hydrates, Annals of the New York Academy of Sciences, eds. E. D. Sloan, J. Happel, M. A. Hnatow, **715**, 344 pp.

Jeffrey, G.A., 1984, Inclusion compounds, Vol. 1, eds. J.L. Kaplan, J.E.D. Davies, D.D. MacNichol, 135.

Kiefte, H., M. J. Clouter and R. E. Gagnon, 1985, Determination of acoustic velocities of clathrate hydrates by Brillouin spectroscopy, Journal of Physical Chemistry, **89**, 3103–3108.

Mak, T. C. W. and R. K. McMullan, 1965, Polyhedral clathrate hydrates. X. Structure of double hydrate of tetrahydrofuran and hydrogen sulfide, Journal of Chemical Physics, **42**, 2732–2737.

Mandl, F., 1988, Statistical physics, John Wiley & Sons Ltd., New York, 385pp.

Mavko, G, T. Mukerji and J. Dvorkin, 1998, The rock physics handbook, Cambridge University Press, Cambridge, 329pp.

McMullan, R. K. and G. A. Jeffrey, 1965, Polyhedral clathrate hydrates. IX. Structure of ethylene oxide hydrate, Journal of Chemical Physics, **42**, 2725–2732.

Nakano, S. M. Moritoki and K. Ohgaki, 1999, High-pressure phase equilibrium and raman microprobe spectroscopic studies on the methane hydrate system, Journal of Chemical Engineering Data, **44**, 254–257.

Nur, A., G. Mavko, J. Dvorkin, and D. Galmudi, 1998, Critical porosity: A key to relating physical properties to porosity in rocks, The Leading Edge, **17**, 357–362.

Nye, J. F., 1985, Physical properties of crystals – Their representations by tensors and matrices, 1985 ed., Oxford University Press, Inc., New York, 329 pp.

Ohanian, H. C., 1989, Physics, 2nd Ed. Expanded, W. W. Norton & Company, Inc., New York, 1148 pp.

Pandit, B. I., and M. S. King, 1982, Elastic wave propagation in propane gas hydrates, in Proceedings, Fourth Canadian Permafrost Conference Calgary, Alberta, 1981, 335–342.

Pandit, B. I., and M. S. King, 1983, Elastic wave velocities of propane gas hydrates, in Natural gas hydrates: properties, occurrence and recovery, ed. J. L. Cox, Butterworth, Boston, 49–61.

Paull, C. K., R. Matsumoto, P. J. Wallace, et al., 1996, Proceedings of the ODP, Initial Reports, **1**64: College Station, TX (Ocean Drilling Program), 623 pp.

Pearson, C., J. Murphy, P. Hallek, R. Hermes, and M. Mathews, 1983, Sonic and resistivity measurements on Berea sandstone containing tetrahydrofuran hydrates: a possible analog to natural gas hydrate deposits, in Proceedings, Fourth International Permafrost Conference, 973–978.

Pearson, C. F., J. R. Murphy, R. E. Hermes, and P. M. Halleck, 1984, Laboratory ultrasonic and resistivity measurements on sedimentary rocks containing tetrahydrofuran hydrates, Los Alamos National Laboratory Report LA-9972-MS, 67pp.

Pearson, C., J. Murphy, and R. Hermes, 1986, Acoustic and resistivity measurements on rock samples containing tetrahydrofuran hydrates: laboratory analogues to natural gas hydrate deposits, Journal of Geophysical Research, **91** No. B14, 14,132–14,138.

Rueff R. M., E. D. Sloan and V. F. Yesavage, 1988, Heat capacity and heat of dissociation of methane hydrates, AIChE Journal, **34**, 1468–1476.

Richards T. W. and C. L. Speyers, 1914, The compressibility of ice, Journal of the American Chemical Society, **36**, 491–494.

Röttger, K, A. Endriss, J. Ihringer, S. Doyle, W. F. Kuhs, 1994, Lattice constants and thermal expansion of H_2O and D_2O ice Ih between 10 and 265 K, Acta Crystallographica, **B50**, 644–648.

Shpakov, V. P., J. S. Tse, C. A. Tulk, B. Kvamme, and V. R. Belosludov, 1998, Elastic moduli calculation and instability in structure I methane clathrate hydrate, Chemical Physics Letters, **282**, 107–114.

Sloan, E. D., Jr., 1998, Clathrate hydrates of natural gases, 2nd Ed., Marcel Dekker, New York, 705pp.

Stoll, R. D., J. Ewing, and G. M. Bryan, 1971, Anomalous wave velocities in sediments containing gas hydrates, Journal of Geophysical Research, **76**, 2090–2094.

Stoll, R. D., 1974, Effects of gas hydrates in sediments, in Natural gases in marine sediments, ed. I. R. Kaplan, 235–248.

Stoll R. D., and G. M. Bryan, 1979, Physical properties of sediments containing gas hydrates, Journal of Geophysical Research, **84**, No. B4 1629–1634.

Sychev, V. V., A. A. Vasserman, V. A. Zagoruchenko, A. D. Kozlov, G. A. Spiridonov, and V. A. Tsymarny, 1987, Thermodynamic properties of methane, Hemisphere Publishing Corporation, Washington.

Touloukian, Y. S., R. K. Kirby, R. E. Taylor and J. Y. R. Lee, 1977, Thermophysical properties of matter, Vol 13, Plenum Press, New York, 1786 pp.

Tse, J. S., 1987, Thermal expansion of the clathrate hydrates of ethylene oxide and tetrahydrofuran, Journal De Physique, Colloque C1, Supplement #3, **48**, C1-543–549.

Tse, J. S. and M. A. White, 1988, Origin of glassy crystalline behavior in the thermal properties of clathrate hydrates: a thermal conductivity study of tetrahydrofuran hydrate, Journal of Physical Chemistry, **92**, 5006–5011.

Tse, J. S., V. P. Shpakov, V. V. Murashov and V. R. Belosludov, 1997, The low frequency vibrations in clathrate hydrates, Journal of Chemical Physics, **107**, 9271–9274.

Tulk, C. A., D. D. Klug and J. A. Ripmeester, 1998, Raman spectroscopic studies of THF clathrate hydrate, Journal of Physical Chemistry A, **102**, 8734–8739.

van der Waals, J. H. and J. C. Platteeuw, 1959, Clathrate Solutions, Advances in Chemical Physics, **2**, 1–57.

von Stackelberg, M and W. Jahns, 1954, Feste gashydrate VI: Die Gitteraufweitungsarbeit, Zeitschrift fur Electrochemie, **58**, 162–164.

Wallace, D. C., 1998, Thermodynamics of crystals, Dover Publications, Inc., Mineola, N.Y, 484pp.

Whalley, E., 1980, Speed of longitudinal sound in clathrate hydrates, Journal of Geophysical Research, **85**, 2539–2542.

Whiffen, B. L., H. Kiefte, and M. J. Clouter, 1982, Determination of acoustic velocities in xenon and methane hydrates by Brillouin spectroscopy, Geophysical Research Letters, **9**, 645–648.

White, M. A. and M. T. MacLean, 1985, Rotational freedom of guest molecules in tetrahydrofuran clathrate hydrate as determined by hear capacity measurements, Journal of Physical Chemistry, **89** 1380–1383.

Wittebolle, R. J., and D. C. Sego, 1985, A laboratory facility for testing sediments containing gas hydrates, in Proceedings, Fourth International Offshore Mechanics and Arctic Engineering Symposium, ed. J. S. Chung et al., American Society of Chemical Engineering, New York, 52–58.

Yamamuro O., M. Oguni, T. Matsuo and H. Suga, 1988, Heat capacity measurements under high pressure, Thermochimica Acta, **123**, 73–83.

Yamamuro O., Y. P. Handa, M. Oguni, and H. Suga, 1990, Heat capacity and glass transition of ethylene oxide clathrate hydrate, Journal of Inclusion Phenomena and Molecular Recognition in Chemistry, **8**, 45–58.

Chapter 3

Propane Gas Hydrate Experiments

3.1 Introduction

As described in Chapter 2, there are only a few published measurements of the elastic properties of gas hydrate. To address this lack of data, I proposed to form sI and sII gas hydrates in the laboratory in clear walled pressure vessels by bubbling hydrate forming gas through water and water saturated sediments in order to visually observe and record the hydrate formation process. In addition to providing the physical property measurements themselves, I hoped this observation capability would provide some insight into the gas hydrate formation process and perhaps help explain the lack of previous publications. In this chapter I report on the limited success obtained with this approach to forming sII propane gas hydrate. These experiments provided several hours of video footage and a significant amount of qualitative information, but quantitative physical property measurements were almost impossible to make. In this chapter, I classify the various visual forms of propane hydrate observed during the course of these experiments and report on one successful run in which an increase in compressional wave speed was recorded in a water saturated glass bead pack containing propane hydrate. These experiments showed that successful measurement of gas hydrate elastic properties would require a completely different approach to forming gas hydrate in the laboratory. This new approach and the successful measurements of compressional and shear wave speed in sI methane hydrate that resulted from it are described in Chapters 4 and 5.

3.2 Apparatus and Procedure

The propane gas hydrate experiments were conducted in a cylindrical glass pressure vessel 17.5 cm long with an inside diameter of 7.2 cm and a wall thickness of 1.0 cm. This central chamber was sealed at both ends with custom-designed and built aluminum endcaps held in place by nuts and lock washers located on three threaded steel rods passing through holes in the endcaps. The three steel rods also served as a stand for the pressure vessel and provided clearance for the ports in the bottom endcap. Two o-rings in each cap provided pressure seals along the inside diameter and against the ends of the glass cylinder. The pressure vessel is shown in Figure 3.1.

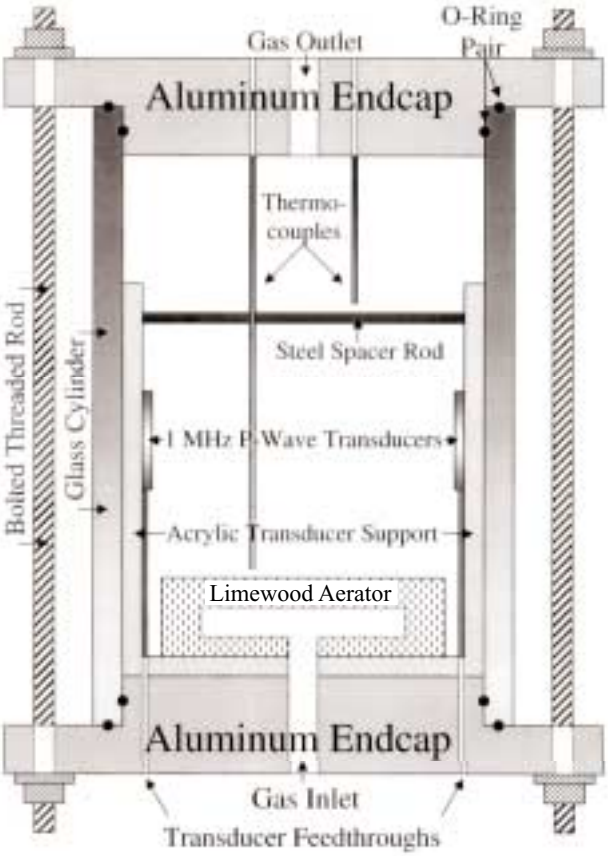

Figure 3.1: Glass-walled pressure vessel. Thermocouple readings are made at different depths within the pressure vessel. Gas pressure measurements are made in the inlet and outlet gas lines. Compressional wave transducers are mounted on an acrylic support structure within the pressure vessel. Aerator is used to disperse injected gas into a collection of fine bubbles. Figure courtesy W. F. Waite.

The pressure vessel was placed within an acrylic temperature bath filled with clear ethylene glycol and water. The temperature of the bath was controlled by a heater/circulator which opposed the cooling applied by an immersion chiller. Thermocouples (from one to three depending on the needs of the experiment) measured the temperature within the pressure vessel. Pressure was measured in the inlet and outlet gas lines. All pressure and temperature data (including bath temperature) were digitally recorded for later review and analysis. Also within the pressure vessel were two compressional wave transducers (1 MHz center frequency) located a fixed distance apart and a Coralife limewood aerator for breaking the propane gas into streams of very fine bubbles. In the early stages of the research, a back-pressure regulator and two digital flow meters were also used in the system. The flow meters were intended for monitoring the volume of gas which entered and exited the pressure vessel, to provide an estimate of the amount of propane hydrate that had formed in the apparatus. Unfortunately, the accuracy and repeatability of the data produced by the flow meters were insufficient for this task (for example, when connected in series they did not report equal values). Therefore, they were removed from the system. During the course of the experiments, the back pressure regulator began to leak and eventually failed. After it had been removed, the pressure was controlled by manually operating a simple valve. A schematic representation of the equipment layout is given in Figure 3.2.

Before each experiment, the pressure vessel was filled approximately 2/3 to 3/4 full with laboratory tap water. For runs with bulk, coarse sand, pre-wetted sand was slowly sprinkled in and allowed to settle to the bottom of the pressure vessel until it covered the compressional wave transducers. The entire system was then either evacuated or (occasionally in pure water cases only) purged of air by pumping propane gas through the system at temperatures well above the propane hydrate stability limit (see Figure 2.4). The pressure vessel was then placed in the bath and allowed to reach an equilibrium temperature generally between 0.5 and 1.5°C. At this point, the pressure vessel was pressurized with propane from a source bottle and the task of forming propane gas hydrate began.

The process of propane hydrate formation and dissociation has been observed under several different conditions in the glass pressure vessel. In all cases, the state of the propane/water interface had a strong influence on the visual characteristics (i.e., habit) of the propane hydrate that formed. The state of the propane/water interface depended on

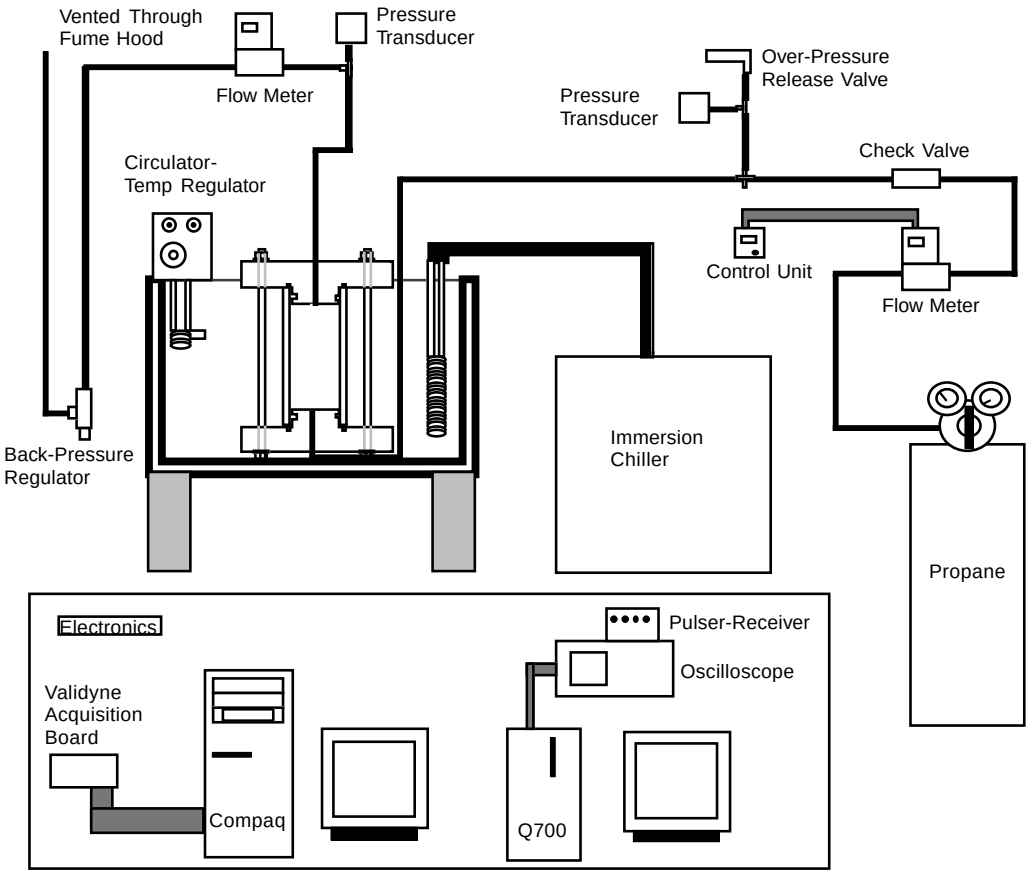

Figure 3.2: Schematic representation of laboratory system for forming propane hydrate. System is pressurized from the propane bottle. Pressure within the apparatus is controlled by setting the back pressure regulator. Temperature in the bath is controlled by the circulator and the immersion chiller. Gas pressure transducers monitor the inlet and outlet line pressures. Pressure and temperature data are digitized via a Validyne brand acquisition board and stored on computer. Waveforms are digitized using a Tektronix oscilloscope and stored on computer for later analysis.

the method used to mix the propane and water. Therefore, I will describe the observations made during the experiments in terms of the six different methods used to mix propane with water: 1) An active interface produced by bubbling propane through water, 2) an active interface produced by vigorously mixing propane and water, 3) a passive interface between propane and water in the absence of propane hydrate, 4) a passive interface between propane and water in the presence of propane hydrate, 5) an active interface produced by bubbling propane through water saturated coarse sand and 6) an active interface produced by alternately pumping propane gas and water through water saturated glass beads.

3.3 Observations on Propane Hydrate Formation in Water

Both liquid propane and propane gas are less dense than water. Therefore, any propane injected into the pressure vessel eventually finds its way to the top of the pressure vessel and forms an essentially horizontal propane/water interface. Although there were occasional exceptions, the vast majority of visually discernible propane hydrate nucleation sites were found at this interface. The water interface may be of particular importance to gas hydrate formation because of the ordering that surficial water molecules undergo in response to electrostatic forces at the interface (Isrealachvili and Wennerstrom, 1996). This forced ordering of water in the presence of a large reservoir of clathrate-forming molecules is generally presumed to be the reason for enhanced gas hydrate nucleation and growth at the gas/water interface (Brewer et al., 1997; Sloan, 1998).

3.3.1 Bubbling Propane Through Water

Directly bubbling propane gas into a pressurized chamber of water at low temperature produces a large amount of unconnected interfacial area between the water and the propane. The result is that solid rinds of gas hydrate often form around the gas bubble, isolating the gas from further contact with the water. These bubbles float up through the water column and form a hydrate foam at the propane/water interface. As the gas-hydrate-coated bubbles accumulate some collapse and some coalesce, but many appear to retain their original shape. Over the course of several days, the foam self-compacts and appears to become more dense and coherent, but it essentially remains a collection of gas hydrate rinds. There is probably some diffusion-limited secondary propane hydrate formation occurring, in particular cementing the rinds together, but no significant propane hydrate formation is observed to occur in the absence of active gas bubbling.

The thermodynamic conditions for these experiments were in the two-phase (hydrate/water or hydrate/gas) regions of the pressure-temperature phase diagram for propane hydrate (see Figure 2.4). The persistent co-existence of the three phases (hydrate, gas and water) indicates the significant degree of metastability in the system. Without agitation, ample supplies of water and propane can co-exist for days in the presence of propane hydrate without any apparent additional propane hydrate formation. However, on two occasions,

prodigious amounts of propane hydrate formed long after active agitation had stopped (see below). The stochastic nature (Sloan, 1998) of the gas hydrate nucleation process is clearly evident from these experiments.

These observations of propane hydrate growth at the surface of propane gas bubbles in water are consistent with a theoretical model of bubble surface hydrate formation proposed by Selim and Sloan and described in Sloan (1990). Recently, observations of methane hydrate formation from gas bubbled through water were also reported by Brewer et al. (1997) during an experiment carried out in Monterrey Bay using an unmanned submersible at 910 m depth. In the experiment reported by Brewer et al., the gas hydrate bubble mass also self-compacted but retained its distinct, frothy nature for the several-hours duration of the experiment. Trapped gas bubbles from subsea natural gas seeps have also been observed to readily form gas hydrate (Torres et al., 1998). The frothy concoction of gas hydrate, trapped gas and trapped water that results from bubbling gas through water is poorly suited for gas hydrate physical property measurements. The intermingling of phases prevents measuring the pure gas hydrate phase and the metastability of the system leads to long reaction times.

3.3.2 Vigorously Mixing Propane and Water

Propane liquifies at relatively low pressures (see Figure 2.4), so it is possible to form liquid propane in a clear walled pressure vessel. Once liquid propane is present, there are two ways to stimulate propane hydrate production: 1) reduce the propane pressure so that the liquid propane phase begins to boil off and 2) vigorously shake the pressure vessel. In the first case, solid forms at the liquid propane/water interface as the propane boils away. Thermocouples in the pressure vessel show that the Joule-Thompson cooling caused by the boiling lowers the temperature at the interface significantly, raising the possibility that water ice is forming. However, after this process, the bath temperature was always raised well above 0°C (usually to 2.5°C) and the solid would last until the end of the run several days later, strongly suggesting the solid was propane hydrate.

In the second method, the pressure vessel is lifted out of the bath and vigorously shaken for approximately 30 seconds. Shaking the water/liquid propane mixture does not always lead immediately to propane hydrate production. However, if the system of liquid propane and water is left to sit overnight or if a small amount of propane hydrate is already present,

then physical agitation produces dispersed flakes of propane hydrate or a propane hydrate slurry. The temperature in the pressure vessel also raises by several degrees, presumably from the heat of formation released by the propane hydrate. This enhanced propane hydrate production from vigorously mixing liquid propane and water has been observed by previous experimenters as well (Stoll and Bryan, 1979; Pandit and King, 1982). The solid formed during the shaking slowly floats up through the remaining fluid (whose visually estimated viscosity is well above that of the original water) and collects at the water/propane interface. Over time, the dispersed flakes bond together and subsequent shaking episodes must be particularly vigorous to break up the propane hydrate plug that forms. If left for a sufficiently long time (variable from experiment to experiment), the plug becomes undislodgeable.

After one run in which propane hydrate was formed by repeatedly shaking the pressure vessel, the remaining water was drained from the system. The solid propane hydrate plug remained suspended in the pressure vessel. This ability of gas hydrate to attach itself to smooth surfaces is one of the reasons it is such a nuisance to the oil industry when it forms in pipelines. The strength of this bond can be quite strong, persisting under pressure differences of 10s of psi in some of the experiments.

In this particular experiment, after the water was removed, the propane was bled off and the pressure vessel opened. The solid appeared dry and felt dry to the touch. A small piece was chipped off and placed in a sealed syringe. As the solid decomposed, the gas released pushed the syringe stopper entirely out of the syringe. This was equivalent to a volume increase of greater than 6 times.

The samples made by vigorously shaking mixtures of water and liquid propane produced by far the most gas per unit volume of solid upon disassociation. This method of producing propane hydrate also made the densest looking samples. However, even this procedure did not lead to a complete consumption of the reactants in the pressure vessel and the macroscopic samples were still highly porous. The presence of gas and/or liquid pockets within the solid could not be discounted. For this reason the samples were unsuitable for measuring bulk elastic properties.

3.3.3 Passive Interface in the Absence of Gas Hydrate

The stochastic nature of gas hydrate formation means that propane (liquid and/or gas) and water can coexist within the propane hydrate stability field for very long periods of time without any reaction taking place (Sloan, 1998). Many of the propane hydrate experiments that had a passive interface went well over 24 hours within the propane hydrate stability field without forming any propane hydrate. However, on one occasion, when green food coloring was added to the water phase to help distinguish between the water and liquid propane layer (the green dye does not enter the liquid propane phase), time lapse video showed propane hydrate forming at the passive water/liquid propane interface. Over the course of approximately 12-16 hours, propane hydrate grew from the interface, through the liquid propane layer and into the gas phase. It may be possible that the presence of dye in the water phase affected the arrangement of water molecules and lowered the barrier to gas hydrate formation. This is similar to the observation that methane hydrate forms more readily from "dirty" sea water (Brewer et al., 1997) containing suspended particulates or lab water that has been seeded with chemicals and particulates commonly found in oil and natural gas pipelines (Bylov and Rasmussen, 1997). From these cases, it appears that "dirty" water is better than purified water for forming gas hydrate.

3.3.4 Passive Interface in the Presence of Gas Hydrate

Once propane hydrate has formed in the pressure vessel, subsequent formation can occur without physical agitation, but the induction times are highly unpredictable. In some instances there were "bursts" of propane hydrate formation in the passive interface systems between periods with little or no apparent nucleation or growth. Another interesting observation was that in at least one case bubbles of propane introduced into a passive interface system became trapped within the water phase a significant distance from the water/hydrate interface. Though the water was clear, shaking the pressure vessel revealed the water had developed a viscous "jelly-like" quality. Subsequent bubbling into the pressure vessel revealed an inverted conical root that extended approximately 3 cm from the water/hydrate interface into the liquid phase. A similar observation was made in a methane hydrate experiment reported by Y. F. Makogon (1997). Unfortunately, a sample of the viscous fluid was

never recovered from the propane hydrate experiments because the liquid always reverted to regular water upon depressurizing the apparatus.

The creation of an abnormal fluid phase in passive interface systems was also reported by Stoll and Bryan (1979) who described a "clear liquid with a slightly jellylike appearance" that showed up in their experiments after a dormant period of 12-24 hours. This "gel-water" may be the result of water organizing around propane molecules that find their way into the water phase. The solubility of propane in water is very low, only a few molecules per thousand of water molecules (Sloan, 1998), but there may be enough to form a sparse array of filled hydrate cages which induce a loose ordering of the remaining water. Koh et al. (1997) reported observing methane molecules arranging themselves into a regular grid and water cages subsequently forming around them when they used neutron diffraction to study the gas hydrate formation process. The jelly-like liquid observed in the propane hydrate experiments may be caused by this same behavior. Stoll and Bryan (1979) noted that stirring the viscous water phase led to "a significant quantity of hydrate 'flakes' almost immediately." Vigorous shaking of this fluid in our experiments similarly produced copious amounts of propane hydrate flakes. Interestingly, after the agitation, the water appeared to return to a non-viscous state, just as it did after the system was depressurized. Both observations suggest that propane in the water phase (subsequently removed by propane hydrate formation or depressurization) was the cause of the abnormal water viscosity.

3.3.5 Summary

From the experiments described above, it became clear that some form of mechanical compaction would be necessary in order to make meaningful elastic property measurements on the pure propane hydrate phase that was produced. It was also recognized that even then it might not be possible to eliminate the presence of gas or liquid inclusions because it was never possible to drive the formation reaction to completion (i.e., some of the reactants were always left over). This problem was eventually viewed as insurmountable and was the main reason for switching to an entirely different way of making gas hydrate. That new way is described in Chapters 4 and 5.

3.4 Observations on Propane Hydrate Formation in Water Saturated Sediments

While the pure propane hydrate experiments discussed above were being performed, experiments on forming propane hydrate in water saturated coarse sediments were also being conducted. These experiments provided several hours of interesting video footage, but meaningful quantitative measurements were very difficult to obtain. In the next two sections I describe some of the visual observations made during these experiments. This is followed by a description of one successful experiment that showed an increase in compressional wave speed through a water saturated glass bead pack in which propane hydrate had formed.

3.4.1 Propane Hydrate Formation in Coarse-Grained Sands

The first attempts at forming propane hydrate in sediment were done by filling the pressure vessel with water and sprinkling in coarse, poorly sorted sand. The pressure vessel was then evacuated, cooled and pressurized from the propane bottle. Gas was periodically forced through the saturated sand pack initially by setting a fixed release pressure for the back pressure regulator and then increasing the gas supply from the bottle. After the regulator failed, the release of gas was manually controlled. It was found that the formation of propane hydrate in the sand was made easier by first forming propane hydrate in the water above the sand by boiling off a layer of liquid propane. This was how most of the experiments were started. Formation of propane hydrate in the sediment appeared to be stimulated by the active pumping of gas through the sediment. The presence of propane hydrate was indicated by an anomalous appearance (brightening and increased reflectivity) of the pore space and by the appearance, where visible, of solid, clear/translucent crystals. It is interesting to note that in these experiments little grains of sand were often suspended in what appeared to be clear water, suggesting something was present in the water that could not be seen, presumably because of a lack of contrast between its optical properties and those of water.

A number of interesting observations were made during these preliminary experiments. The first was that the system was very dynamic on time scales from minutes to hours.

The path of gas through the sediment was continually changing. Because there was no additional overburden pressure (as is the case near the sea floor), the gas was occasionally able to physically push apart sand grains or clumps of sand grains and create paths or void spaces which would partially fill with propane hydrate. Often the walls of the newly created pathways became "armored" with propane hydrate. During one experiment, video footage of a gas pathway becoming armored and eventually clogged with propane hydrate was recorded. These observations showed that gas hydrate deposits can be actively changing on human time scales, especially in sedimentary systems such as active accretionary margins where fluxes of gas and water through the sediment can be quite large.

These initial experiments performed in sands clearly showed that gas hydrate formation in sediments is a very complex process. It also became apparent that relatively small amounts of propane hydrate were being formed and that the hydrate was distributed throughout the entire pressure vessel. As a result, very little propane hydrate was forming in the region between the compressional wave transducers. Therefore, a way was needed to simplify the system that would also form more propane hydrate. These needs were addressed by decreasing the volume of "sediment" in the system, by focusing the propane hydrate formation efforts into that specific sub-volume of the pressure vessel and by switching from poorly sorted sand to more uniform glass beads (0.6 mm diameter).

3.4.2 Propane Hydrate Formation in Glass Beads

Previous investigators (Evrenos et al., 1971; de Boer et al., 1985) have indicated that enhanced gas hydrate formation was stimulated by alternately pumping hydrate forming gas and water through sediments. In the initial experiments this effect was experienced as a nuisance. The fine pores of the aerator used to disperse the gas into bubbles were constantly clogging with propane hydrate that formed as gas and water alternately passed through them. On one occasion an aerator was recovered following an experiment and its central chamber was found to be completely filled with solid propane hydrate. In response to this observation, a balsawood sample chamber was designed which fit inside the glass pressure vessel and between the compressional wave transducers. The balsawood chamber had two acrylic view ports. Gas bubbled in through the bottom and out through the top. To improve propane hydrate formation, the gas line plumbing was rearranged so that gas

pressure could be applied from above or below, thereby allowing both gas and water to be alternately pumped through the glass bead pack.

While water saturated, the glass bead pack appeared dark gray. The presence of gas and/or propane hydrate significantly whitened the overall appearance of the glass bead pack. Using these visual clues, it was possible to watch gas and water alternately pass through the glass bead pack. Unfortunately, it was difficult to determine when gas hydrate instead of gas was present in the pore space. Additional evidence from the compressional wave speed was needed to confirm the presence of propane hydrate. The compressional wave speed results from one of these experiments are discussed in detail in the next section.

3.5 Compressional Wave Speed in Water Saturated Glass Beads Containing Propane Gas Hydrate

3.5.1 Description of Experiment

The general design of the experiment is described above. Here, I focus on the details applicable to this specific experiment. During this experiment, one thermocouple was located within the pressure vessel and another was located in the temperature bath. These thermocouples and the inlet and outlet line gas pressure transducers were connected to a Validyne UPC 601-U data acquisition board located in a Compaq Presario CDS 954 computer. This board has the capability to sample data at intervals from .1 to 99999.9 seconds. For this experiment, the P-T data sampling interval was 120 seconds. The compressional wave transducers were one inch in diameter, 1/4” thick and had a center frequency of 1 MHz. They were mounted on a U-shaped acrylic holder which was braced at the top by a metal rod (see Figure 3.3). This holder fit around the gas inlet and rested upon the bottom cap of the pressure vessel. The transducer wires exited the pressure vessel through fittings in the bottom endcap.

Between the transducers was a rectangular block of balsawood. The block had been hollowed out by drilling holes completely through the two pairs of vertical faces. The hole perpendicular to the axis of the transducers was covered at both ends with acrylic windows. The two remaining holes fit over the compressional wave transducers, giving them direct

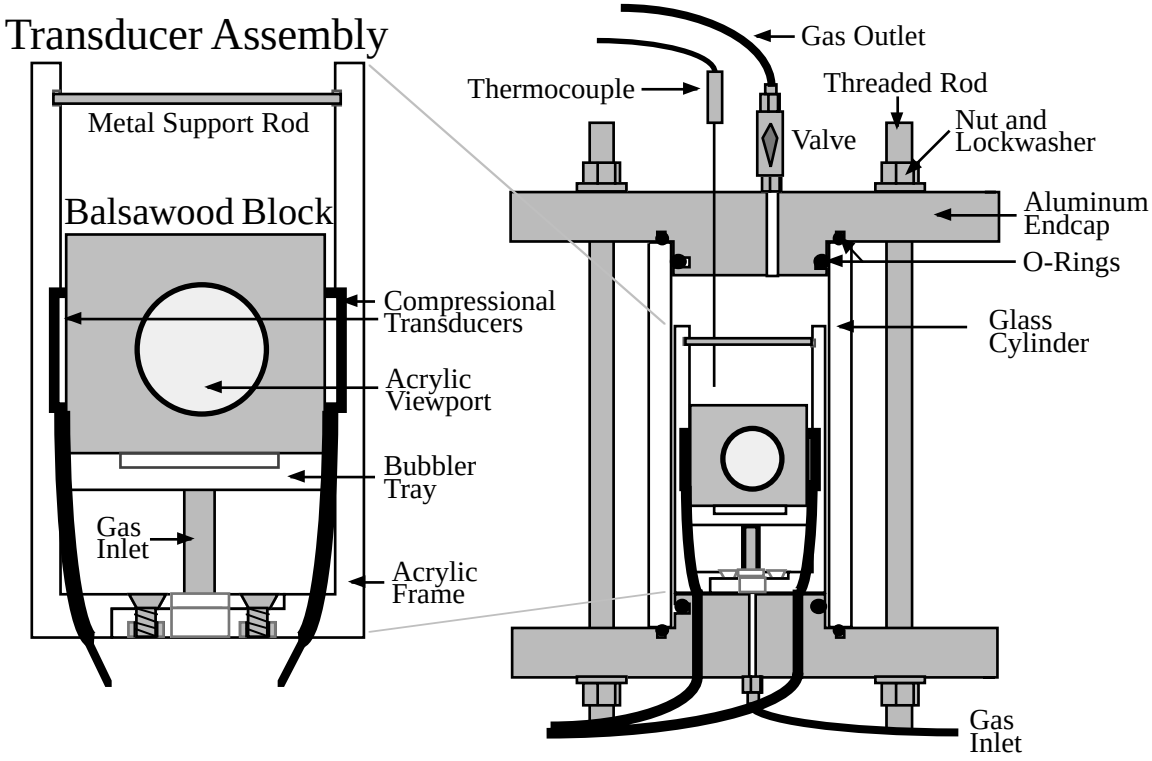

Figure 3.3: Pressure vessel with detail of compressional transducer assembly. Balsawood block is hollow between transducers and filled with glass beads (0.6 mm diameter). Both transducers are in direct contact with the glass beads. The glass bead pack is visible through the acrylic viewport.

contact with the water saturated glass beads. The block was mounted on an acrylic holder that was screwed onto a metal tube connected to the gas inlet (see Figure 3.3). Gas entered the apparatus through the metal tube, pooled in the acrylic holder beneath the balsawood block, and bubbled through the balsawood into the glass bead pack. The balsawood block served two purposes, it held the beads in place and it broke the propane gas stream into a collection of fine bubbles.

As mentioned above, alternately pumping gas and water through the granular system promoted the formation of propane hydrate. Most likely, this was due to improved mixing of gas and water in the pore space as one replaced the other in high permeability pathways. The pumping action was achieved by either alternately pressurizing from the inlet line and then the outlet line or by pressurizing and then depressurizing from the outlet line. Pressurizing from the inlet side or depressurizing the outlet side forced gas through the bead pack, displacing water. Pressurizing from the outlet side forced water back into the

bead pack. The second pumping technique had to be utilized after the inlet line became plugged with propane hydrate. A few cycles of pumping produced a visually discernible change in the character of the bead pack and significantly changed the waveform and arrival time of the compressional wave traveling through the bead pack.

3.5.2 Procedure Summary

The experiment ran for nine days at temperature and pressure conditions within the propane hydrate stability field. Gas hydrate production was stimulated in the glass bead pack on days two and three by alternately pumping gas and water through the pore space of the bead pack. Temperature and pressure data were recorded continuously throughout the experiment and waveforms were acquired on days one, three, four, five, six, seven and nine. During and following the two periods of pumping, significant changes in both signal amplitude and arrival time were observed. These changes were caused by propane gas hydrate formation within the pore space of the glass bead pack.

The first waveform was taken on day one, at a temperature of 0.4°C and a pressure of 0.45 MPa. The system was left at this pressure and temperature overnight. On the morning of day two, propane hydrate formation in the glass beads was stimulated by alternately pumping gas through the inlet and outlet lines of the system. After pumping was completed, the chamber pressure was raised to 0.48 MPa in order to form a layer of liquid propane on top of the water. The temperature was held constant at 0.4°C. The system was left undisturbed in this state overnight. On the morning of day three a waveform was recorded. The temperature was 0.5°C and the pressure 0.49 MPa. The liquid propane layer was then boiled off, minimizing as much as possible the Joule-Thomson cooling effect of the phase transition. Next, gas and water were pumped through the system again, this time using the second technique which utilized only the outlet line. This was done because the inlet line was plugged, presumably with propane hydrate. The propane hydrate seal was able to hold a pressure differential of 0.37 MPa. After a number of cycles pumping from the outlet line another waveform was recorded. The temperature was 1.9°C and the pressure 0.45 MPa. The temperature was elevated because the bath temperature controller setting had been inadvertently changed during the pumping process. The bath temperature was reduced to 0.7°C and the system was left to evolve overnight. The pressure logs showed the

pressure decreased sharply overnight and eventually bottomed out the following morning at the hydrate stability pressure for a temperature of 0.9°C. This exponential-like pressure decrease versus time coincided with heightened activity in the pressure vessel recorded on time lapse video. This evidence suggests a substantial amount of propane hydrate formed in the apparatus. Waveforms were recorded on the morning of day four following the overnight pressure decrease. The temperature and pressure conditions were 0.9°C and 0.21 MPa, respectively.

For the remainder of the experiment, pressure was added to the inlet and outlet line as necessary to maintain a pressure within the propane hydrate stability field. There appeared to be little or no pressure communication between the inlet and outlet lines. On day five, the bath temperature was raised to 1.5°C to ensure that no ice could be present in the system. The outlet pressure increased slightly as expected from thermal expansion, but the inlet pressure decreased to 0.01 MPa lower than it had been before the temperature increase. This suggests the temperature increase either stimulated propane hydrate production in the inlet gas line, consuming molecules of gas and reducing the pressure, or the temperature increase weakened the propane hydrate plug, allowing some gas to escape from the inlet line to the sample chamber. Any breach that may have occurred must have sealed itself quickly because the inlet and outlet lines maintained a pressure differential of 0.03 MPa after the new equilibrium temperature had been reached.

The day five waveform was acquired shortly after the temperature increase to 1.5°C. The P-T conditions were 1.6°C and 0.45 MPa. On day six, the system was left undisturbed. The day six waveform was recorded at 1.6°C and 0.41 MPa. The day seven waveform was recorded under similar conditions, 1.6°C and 0.43 MPa. On day nine the bath temperature was briefly increased to 3°C and then reduced to 1.7°C. The inlet and outlet pressures responded as before to the temperature increase. The outlet pressure increased and the inlet pressure decreased rapidly, this time dropping 0.03 MPa. After the pressure drop, a differential of 0.07 MPa remained between the inlet and outlet gas lines. After the system had reequilibrated, another waveform was recorded. At the time of waveform acquisition the pressure was 0.38 MPa and the temperature was 1.7°C.

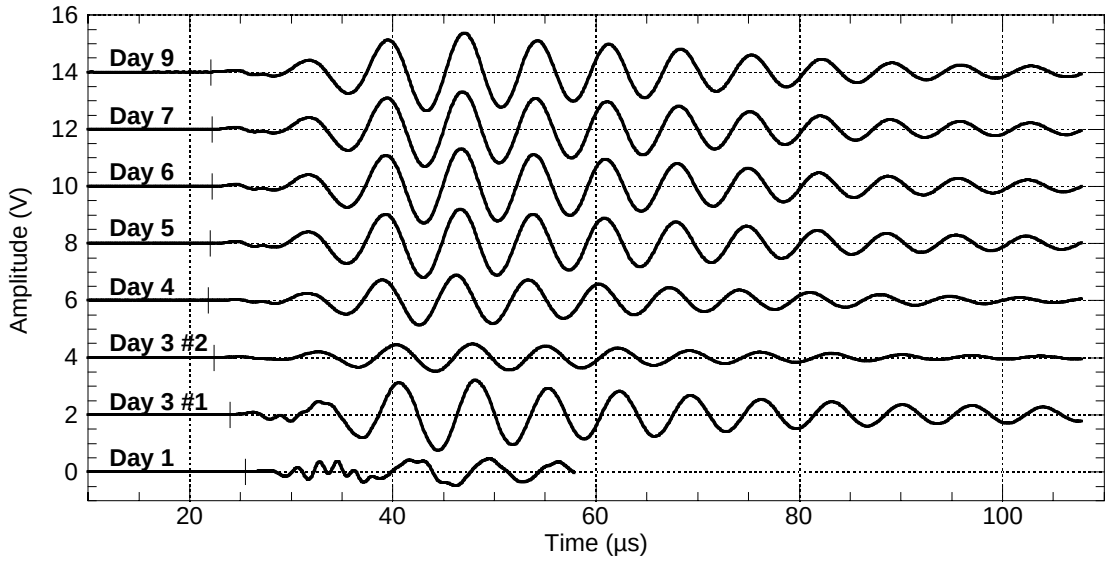

Figure 3.4: Waveforms acquired during the nine day experiment. Baseline voltage for each waveform is shifted in order to show all waveforms in the same plot. Dramatic amplitude, shape and arrival time changes occurred during and shortly after actively pumping water and propane gas through the glass bead (0.6 mm diameter) pack on days two and three. Notice the amplitude decrease between the Day 3 #1 and #2 waveforms. This is likely due to the presence of gas bubbles in the water saturated glass bead pack. No significant changes in the waveform were observed after day five. Short vertical lines show the first motion picks for each waveform. Uncertainties in the arrival time picks range from 0.1 to 0.4 μs.

3.5.3 Waveform Analysis

Figure 3.4 shows the waveforms acquired during the nine day experiment. For ease of viewing, they have been vertically shifted. All trace amplitudes should be considered relative to the initial trace value. The compressional wave speeds in the glass bead pack represented by the eight traces are collected in Table 3.1 and shown in Figure 3.5 as a function of experiment time. Figure 3.4 shows the amplitude variations between waveforms. Both the amplitude and arrival time variations can be analyzed in more detail if the eight traces are broken into three overlapping groups and plotted at the same scale (Figures 3.6-3.11). Group 1 consists of the first four waveforms, those taken on days one, three and four. This group reflects the properties of the glass bead pack before, during and just after the active pumping of gas and water. Group 2 is the second waveform taken on day three and the waveforms from days four and five. These are the waveforms taken in the days just after pumping gas and water through the glass bead pack. Group 3 is comprised of the final four

Table 3.1: Compressional Wave Speed in a Water Saturated Glass Bead (0.6 mm diameter) Pack Containing Propane Hydrate

Waveform	**Wave Speed**[a]	**Waveform**	**Wave Speed**[a]
Day 1	1820±20	Day 5	2120±50
Day 3 #1	1940±30	Day 6	2100±40
Day 3 #2	2080±40	Day 7	2100±40
Day 4	2140±40	Day 9	2110±20

[a]Transducer separation was 44.6 ± 0.2 mm. Travel times were determined from the first breaks of the waveforms (see Figure 3.4) and had uncertainties ranging from 0.1 to 0.4 μs. System delay time was 1.0 ± 0.1 μs.

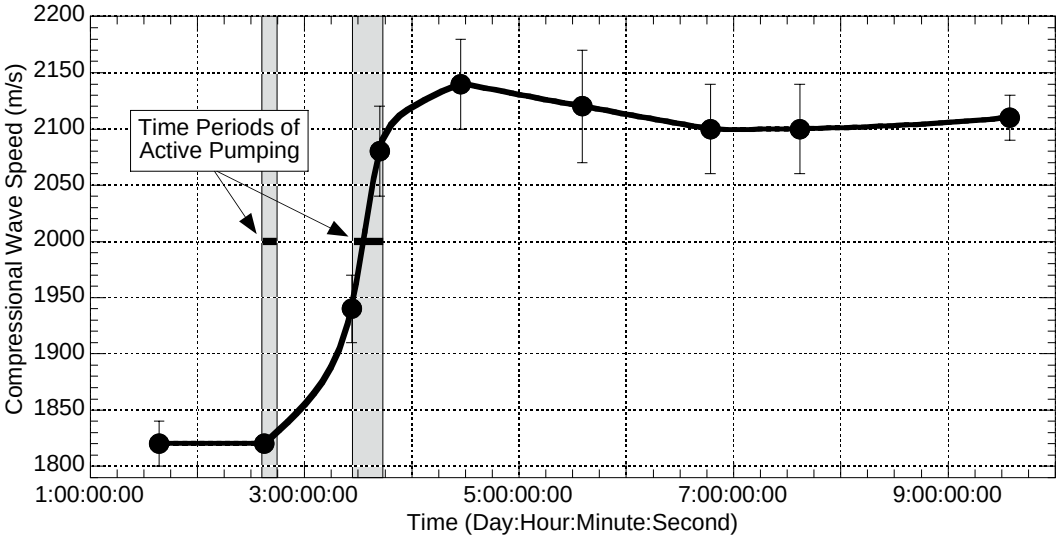

Figure 3.5: Compressional wave speed in water saturated glass bead (0.6 mm diameter) pack versus experiment time. Consecutive data points connected as a guide for the reader. Travel times determined from the first breaks of the waveforms. Increase in wave speed from day two to day four corresponds to propane hydrate formation in the glass bead pack. Periods when propane gas and water were actively pumped through the glass bead pack are noted on the graph.

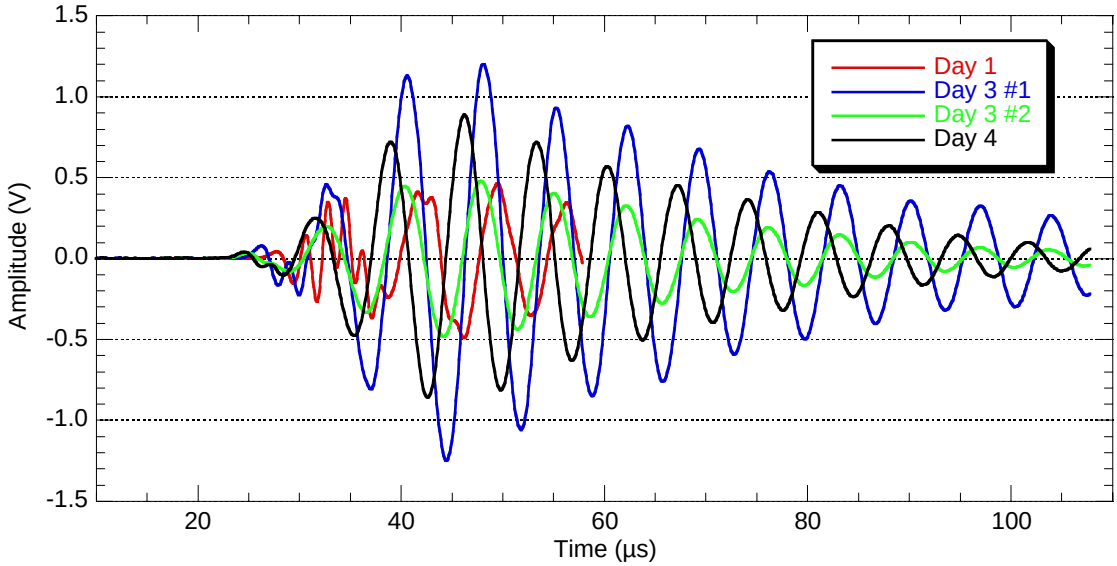

Figure 3.6: Group 1 full waveforms – taken during the active pumping stage of the experiment. Full waveforms show both amplitude and shape changes resulting from propane hydrate formation.

waveforms, those taken on days five, six, seven and nine. These waveforms were taken long after the active pumping of water and gas through the glass bead pack had stopped.

Group 1 highlights the changes produced in the bead pack by pumping gas and water through the system. Figures 3.6 and 3.7 show the waveforms that comprise Group 1. Figure 3.6 shows the four full waveforms on the same time and amplitude scales. Figure 3.7 concentrates on the first breaks of the four traces. These plots show the dramatic changes in amplitude and arrival time that occurred during the active pumping stage of the experiment. Although no waveform was recorded on day two, lab notes show that thirty minutes prior to the first period of pumping, the waveform arrival time had not changed from day one. Therefore, I attribute the waveform changes from day one to day three (#1) to propane hydrate formation during and following the first incidence of pumping on the morning of day two. Changes in the waveform between the two traces taken on day three represent changes caused by pumping in the middle of day three. The decrease in amplitude suggests the pumping process disturbed the grain packing and perhaps trapped some gas in the pore space of the bead pack. The decrease in arrival time suggests more propane hydrate had formed, replacing water in the pore space and increasing compressional wave speed through the glass bead pack. Between days three and four, the arrival time decreased

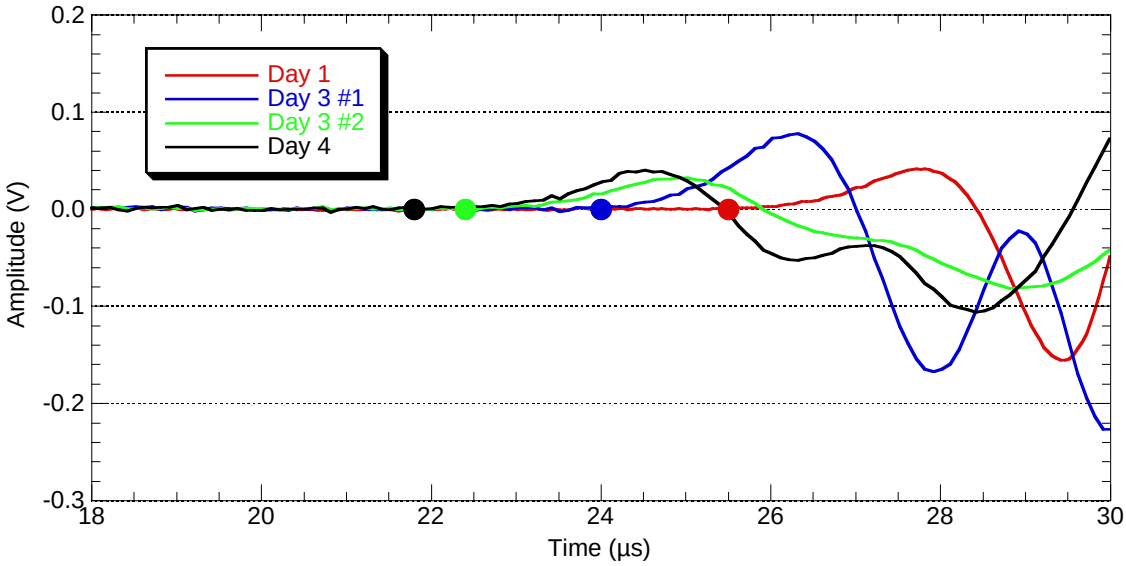

Figure 3.7: Group 1 first motions – taken during the active pumping stage of the experiment. The filled circles are located at the first-motion picks for each waveform. Propane hydrate formation decreased the observed compressional wave first break arrival time.

slightly, but the amplitude increased significantly. There was no pumping during this period, but visual and pressure evidence suggests that propane hydrate was forming in the chamber. The increase in transmitted energy is interpreted as evidence for improved cohesion between propane hydrate grains and at propane hydrate-glass bead contacts. It is probably also the case that the amount of residual gas in the pore space had decreased from propane hydrate formation and/or density driven drainage.

Group 2 shows the waveform changes following pumping. Group 2 is comprised of the waveforms from days three (#2), four and five. Figure 3.8 shows the three full waveforms on the same time and amplitude scale. This figure shows that the dominant change in the waveform over this time period was in the amplitude and not the shape or arrival time. Figure 3.9 focuses on the first motions. No significant change is apparent. This group shares significant overlap with Group 1, so I will only comment on the changes from day four to day five. During this time period, the only significant change to the physical condition of the system was a bath temperature increase and maintenance of the inlet and outlet gas pressures. The increase in amplitude without significant change in arrival time suggests the propane hydrate saturation had not changed appreciably between days four and five.

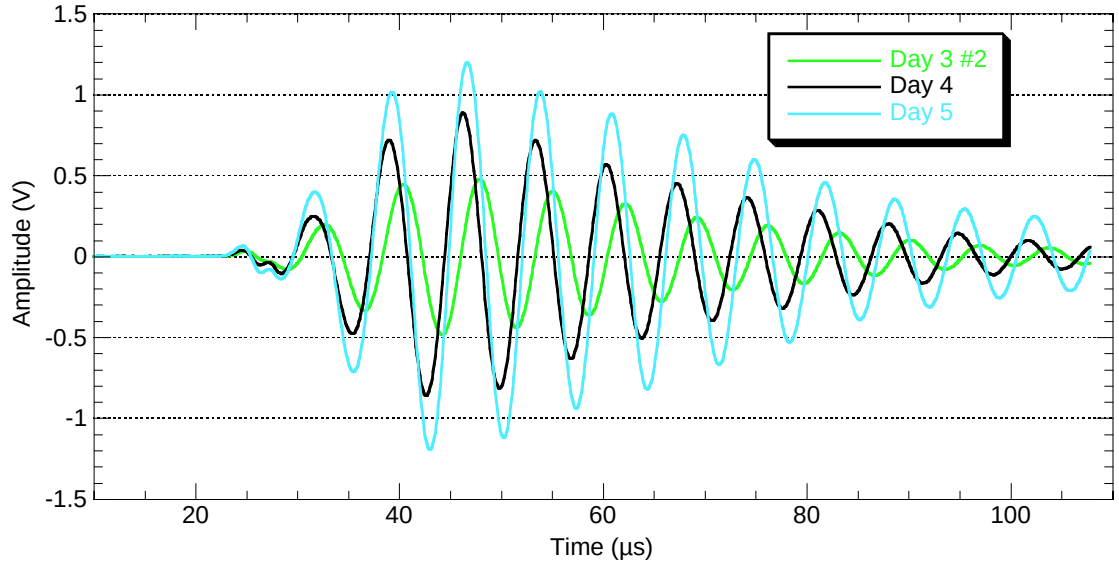

Figure 3.8: Group 2 full waveforms – taken during the 48 hours following active pumping. Observed signal strength increases without the waveform shape changes typical of the Group 1 waveforms.

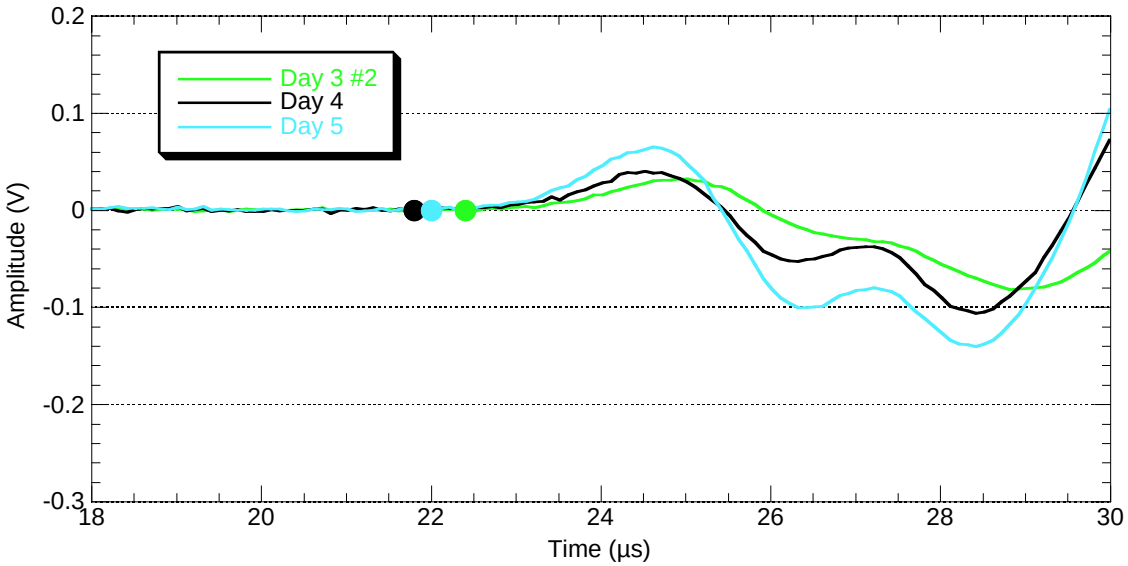

Figure 3.9: Group 2 first motions – taken during the 48 hours following active pumping. The filled circles are located at the first-motion picks for each waveform. No significant change in first break arrival time is observed.

Group 3 shows how the system behaved at long times after pumping had stopped. Group 3 contains the waveforms from days five, six, seven and nine. Figure 3.10 shows the four full waveforms on the same time and amplitude scale. Figure 3.11 concentrates on the first motions. From these figures it is clear the elastic properties of the glass bead pack did not change significantly over the course of five days. This was expected because no pumping had occurred and therefore, no significant mixing of gas and water had taken place in the pore space of the bead pack. The slight increase in amplitude over this period without an accompanying change in arrival time suggests a physical process that improves energy transmission without affecting the elastic properties of the bead pack. This requires either improved coupling between source, receiver and sample or improved coupling within the sample itself. However, it is difficult to envision a process which could improve the internal coupling of the glass bead pack without affecting its elastic properties. Another possibility is that forming gas hydrate in the pore space changed the characteristic length of heterogeneities in the system, thereby changing the amount of energy scattered within the bead pack (T. Mukerji, pers. comm.). A more likely explanation is some local effect due to gas bubbles on or near the transducers.

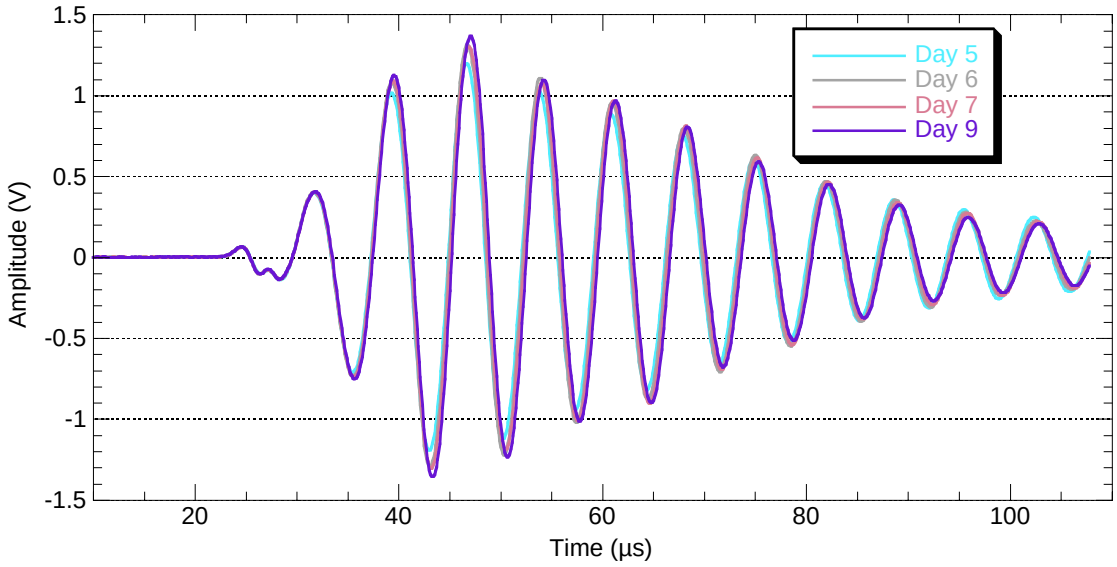

Figure 3.10: Group 3 full waveforms – taken between two to six days after active pumping. Amplitude increases slightly but shape changes are minimal.

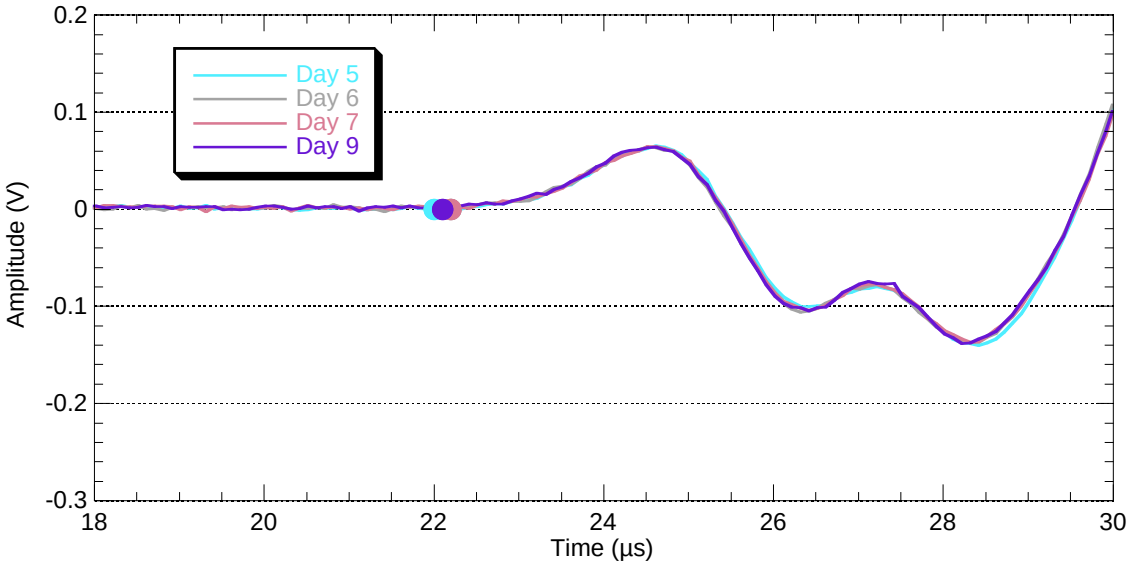

Figure 3.11: Group 3 first motions – taken between two to six days after active pumping. The filled circles are located at the first-motion picks for each waveform. No significant change in first break arrival time is observed.

3.5.4 Eliminating Non-Hydrate Causes to Observed Changes

Three potential non-hydrate causes of the observed wave speed increase were examined: compaction from gas pressure, compaction from glass bead reorganization and ice formation. Compaction from applied gas pressure would require a correlation between gas pressure and the recorded wave speed, but wave speeds of 1800 and 2100 m/s were recorded at essentially the same gas pressure. Furthermore, the fastest wave speed was recorded at the lowest gas pressure, the exact opposite of what would be expected if high gas pressure was compacting the glass bead pack. Wave speed increase due to bead reorganization can also be rejected as a cause for the compressional wave speed increase. A control experiment was performed at room pressure and 0.7°C. The system was left undisturbed for over 48 hours and no change in either waveform shape, amplitude or arrival time was observed. Finally, the presence of ice can be ruled out on the basis of recorded internal temperature. The cylinder temperature was below 0°C for only a few minutes on day three between the time the two waveforms were recorded. Any small amount of ice that may have formed during that time could not have lasted from day five to day nine at temperatures at or above 1.5°C. Therefore, I conclude the presence of propane gas hydrate in the glass bead pack led

to the observed increase in compressional wave speed.

3.5.5 Summary

The experiment ran for nine days. The system was within the propane gas hydrate pressure and temperature stability field for the duration of the experiment. For the first day, the system was left undisturbed and no significant change was observed in either physical appearance or transmitted compressional waveform. On the second and third days gas and water were pumped through the glass bead pack in order to stimulate propane hydrate production. Pumping changed the visual appearance of the glass bead pack and significantly changed the amplitude and arrival time of the transmitted compressional waveform. For the final six days, the system was allowed to evolve with only minor occasional changes to gas pressure and temperature.

Compressional waveforms were recorded on days one, three, four, five, six, seven and nine. No waveform was recorded on day two, but lab notes show that the waveform was inspected thirty minutes prior to pumping on day two and no change in arrival time was observed. While the sample was undisturbed from day two to day three, the amplitude of the recorded signal rose from 0.5 to 1.3V and the wave speed increased from 1820 to 1940 m/s (Figure 3.12). The permeability on the inlet side of the glass bead pack was reduced essentially to zero. This evidence leads to the conclusion that pumping gas and water through the glass bead pack formed propane gas hydrate in the pore space away from grain to grain contacts. If the propane hydrate had formed at grain contacts, a much more dramatic wave speed increase would have occurred (see Chapter 6).

The second period of pumping occurred between the two waveforms recorded on day three. Those two waveforms record a large drop in amplitude from 1.3 to 0.5V and an increase in compressional wave speed from 1940 to 2080 m/s. The wave speed increase suggests the second episode of pumping was again successful at forming propane hydrate in the glass bead pack. The dramatic decrease in signal amplitude is more difficult to explain. It would usually be attributed to the presence of gas in the pore space, but this gas should cause a significant wave speed decrease. Instead, a significant wave speed increase was observed. The amplitude loss may be attributable to decreased coupling efficiency either within the glass bead pack or between the bead pack and the transducers. This could

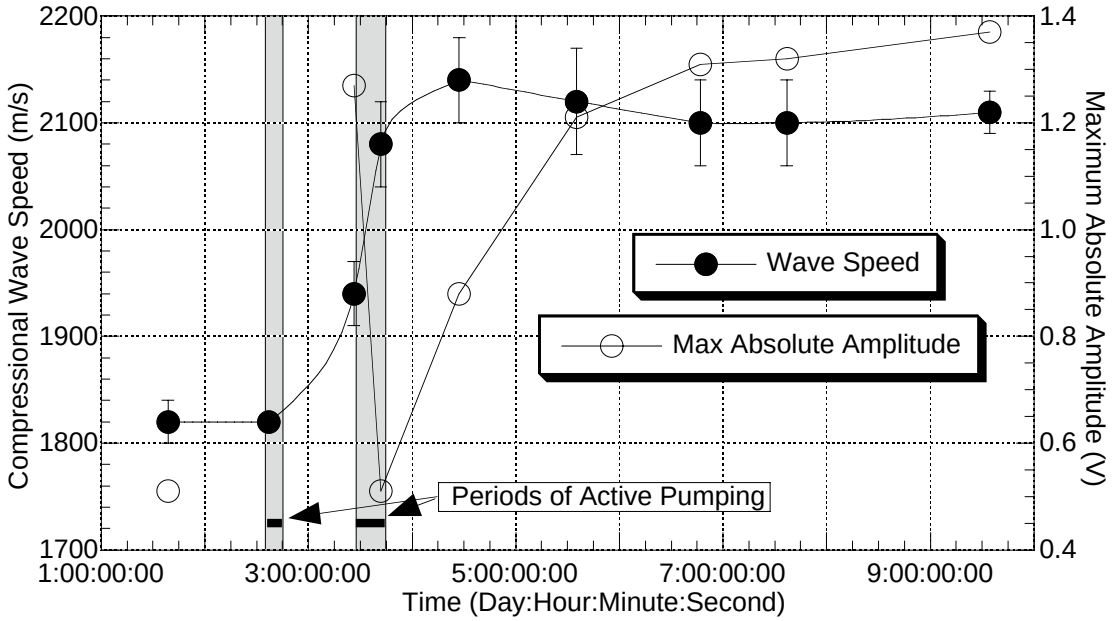

Figure 3.12: Compressional wave speed and amplitude variations versus experiment time. Consecutive data points connected as a guide for the reader. Wave speed increase from day two to day four corresponds to propane hydrate formation in the glass bead pack. Amplitude decrease immediately following the of pumping gas and water through the glass bead pack is probably caused by trapped propane gas. Observed amplitude recovery without a corresponding increase in compressional wave speed at long times following pumping is difficult to explain (see text).

conceivably by achieved by subtle grain movement during pumping or by gas bubbles forming on the transducers faces.

The period following the second episode of pumping is characterized by amplitude recovery from 0.5 to 1.4V but only minor changes in wave speed. This suggests a physical mechanism which promotes coupling either within the sample or between the transducer and sample without significantly affecting elastic properties. This amplitude behavior is difficult to explain. Clearly, the efficiency with which the glass bead pack transmits compressional wave energy is increasing. If the sample were consolidating or being cemented by propane hydrate formation, a significant wave speed increase would occur. For example, a frozen water saturated glass bead pack had a maximum compressional wave speed of 4500 m/s. The most likely explanation is improved coupling at the transducer/glass bead interface from gravity-assisted drainage of propane gas bubbles located at or near the surface of the transducers.

3.6 Conclusions

Propane gas hydrate formation was repeatedly observed in a pressurized glass cylinder located within a temperature bath. Gas hydrate was formed by bubbling propane gas through water or water saturated sediment or by vigorously mixing liquid propane and water. Propane hydrate growth and dissociation were monitored by recording real-time and time-lapse video. Pressure and temperature inside the pressure vessel were logged throughout the experiments. It was found that active mixing of the water and propane phases was necessary for significant amounts of propane hydrate to be produced but that this active mixing produced porous propane hydrate samples with inclusions of water and propane, making the samples unsuitable for gas hydrate physical property testing.

The original design of this project was to perform a number of preliminary experiments, learn about the gas hydrate formation process and then design a procedure that produced samples suitable for elastic property measurements. Unfortunately, that final stage was never reached. The complexity of the gas hydrate formation process from propane and water was underappreciated prior to the beginning of this project. I was never able to produce a sample of either pure propane hydrate or propane hydrate in sediment that I felt could be adequately characterized. The system of gas hydrate, propane and water was always too complex. In this sense, the goal of mimicking the natural system was too closely achieved. The results of these experiments clearly showed that a different way of making gas hydrate samples had to be used. Instead of trying to form gas hydrate as I assumed it formed in nature, namely from the water and gas phases, I instead needed to focus on simply making gas hydrate samples that were suitable for physical property testing. The new method of making gas hydrate that was adopted and the successful compressional and shear wave speed measurements on methane hydrate that resulted from it are described in Chapters 4 and 5.

3.7 References

Brewer, P.G., F.M. Orr, Jr., G. Friederich, K.A. Kvenvolden, D.L. Orange, J. McFarlane, W. Kirkwood, 1997, Deep-ocean field test of methane hydrate formation from a remotely operated vehicle, Geology, **25**, 407–410.

Bylov, M and P. Rasmussen, The effect of impurities on ethane hydrate induction times, Proceedings of the 213th ACS National Meeting, San Francisco, CA, April 13-17, **42(2)**, 507–511.

de Boer, R. B., J. H. C. Houbolt, and J. Legrand, 1985, Formation of gas hydrates in a permeable medium, Geologie in Minjbouw, **64**, 245–249.

Evrenos, A. I., J. Heathman, and J. Ralstin, 1971, Impermeation of porous media by forming hydrates in situ, Journal of Petroleum Technology, **23**, 1059–1066.

Isrealachvili, J. and H. Wennerstrom, 1996, Role of hydration and water structure in biological and colloidal interactions, Nature, **379**, 219–225.

Koh, C. A., A. K. Soper, R. E. Westacott, R. P. Wisbey, X. Wu, W. Zhang, J. L. Savidge, 1997, Neutron diffraction measurements of the nucleation and growth mechanisms of methane hydrate, Proceedings of the 213th ACS National Meeting, San Francisco, CA, April 13-17, **42(2)**, 563–567.

Makogon, Y. F., 1997, Hydrates of Hydrocarbons, PennWell Publishing Company, Tulsa, 482pp.

Sloan, E. D., Jr., 1990, Clathrate Hydrates of Natural Gases, Marcel Dekker, New York, 641pp.

Sloan, E. D., Jr., 1998, Clathrate Hydrates of Natural Gases, 2nd Ed., Marcel Dekker, New York, 705pp.

Stoll R. D., and G. M. Bryan, 1979, Physical properties of sediments containing gas hydrates, Journal of Geophysical Research, **84**, 1629–1634.

Torres, M. E., K. Brown, S. Colbert, R. W. Collier, M. A. deAngelis, D. E. Hammond, K. Heeschen, D. Hubbard, J. McManus, C. Moyer, G. Rehder, A. Trehu, M. Tryon, P. Whaling, 1998, Active gas discharge resulting from decomposition of gas hydrates on Hydrate Ridge, Cascadia margin, Eos Transactions Suppl., **79**, p. F461.

Chapter 4

Methane Gas Hydrate Experiments – Stage One

4.1 Introduction

It became clear from the propane hydrate experiments described in Chapter 3 that a different method for forming gas hydrate samples in the laboratory had to be found. A new method had recently been described by Stern et al. (1996; 1998), in which methane hydrate was formed from granulated ice. In this chapter, I briefly describe the methodology detailed by Stern et al. for making gas hydrate in the laboratory. Next, I describe the apparatus that was designed in collaboration with Stern and co-workers to make wave speed measurements on samples of methane hydrate. Finally, I describe results from the first stage of experiments performed on compacted methane hydrate and compacted ice samples. The first stage of experiments showed that the apparatus worked and the methodology chosen was successful. The results from these initial experiments showed that simultaneous measurements of compressional and shear wave speed could be made and that the observed wave speed values were consistent from sample to sample.

4.2 Experiment Description

In this section I describe the methane hydrate synthesis procedure, the apparatus and data acquisition systems and the processing steps applied to the data. The methane hydrate synthesis procedure is described in detail by Stern et al. (1996; 1998). Here, I summarize the general process.

4.2.1 Methane Gas Hydrate Synthesis Procedure

The technique described by Stern et al. (1996; 1998) for making methane hydrate is different from other published methods in that it forms gas hydrate from granulated ice instead of liquid water. Large, single crystal blocks of ice are formed from triply distilled water and ground into small grains at freezer temperature ($\sim -20^{\circ}$C). These grains are sifted to select the 180-250 μm diameter fraction and then packed into a cold, cylindrical steel pressure vessel. The pressure vessel is submerged in a temperature bath at approximately -20°C and attached to a high pressure gas line. The pressure vessel is evacuated and then flooded with methane gas at approximately 3800 pounds per square inch absolute (psia). The temperature bath containing the pressure vessel is slowly warmed to 17°C. As the temperature in the pressure vessel passes through the melting point of ice, methane gas is consumed as the ice changes phase to sI methane hydrate (see Stern et al., 1996, 1998, for pressure-temperature plots). Since a considerable amount of methane is needed to convert the ice to methane hydrate, a fixed volume methane gas reservoir is also attached to the high pressure gas line and submerged in the same temperature bath as the pressure vessel. When the reaction is complete, the temperature bath is cooled. A qualitative estimate of the true completeness of the reaction can be obtained from the pressure-temperature path of the system as it cools. If a small amount of residual water is left in the system, it will manifest itself as a spike in the pressure-temperature curve as the system passes through the freezing point of water (see Figure 6 in Stern et al., 1998). If this freezing anomaly is observed during the cooling stage (a relatively rare occurrence), the sample can be put through another temperature cycle, generally eliminating the freezing anomaly. Using x-ray diffraction (XRD), Stern et al. (1996) were able to show that this technique could convert nearly all of the ice to methane hydrate (the accuracy of the XRD derived estimate was $\pm 3\%$). Recent

thermometry and gas volume experiments have shown that the technique can repeatably convert more than 99% of the ice to methane hydrate (Stern et al., 2000).

4.2.2 Description of Apparatus and Data Acquisition Systems

The general process described above for making methane hydrate is highly repeatable and produces structurally uniform but porous samples. To obtain solid methane hydrate, the samples must be compacted.

Instead of the simple pressure vessels used by Stern et al. (1996; 1998), a larger pressure vessel with a hydraulic ram and the capability to make wave speed measurements was needed. This new pressure vessel was designed in partnership with the gas hydrate research group under the leadership of Dr. Steve Kirby at the U. S. Geological Survey in Menlo Park, CA. The ability to compact and study samples in the synthesis vessel (without handling them) was an important feature of this apparatus. Once the gas hydrate was formed, it stayed within the gas hydrate stability field for the remainder of the experiment, eliminating any possible complications that might arise from handling the sample at one atmosphere.

A schematic drawing of the pressure vessel is shown in Figure 4.1. It consists of three main parts, a hollow cylinder and two endcaps that screw onto the cylinder. The smaller, bottom endcap contains a fixed piston which is 25.2 mm in diameter. The larger, top endcap contains a translating piston which is also 25.2 mm in diameter. The translating piston is part of a hydraulic ram, compacting the sample against the fixed piston. A teflon liner fits around the pistons within the main body of the pressure vessel. The liner holds the sample between the pistons, prevents the piston from gouging the side walls and allows the sample to be extracted from the apparatus at the end of each run. The hydraulic oil system which drives the translating piston is rated to 5,000 psi. The area acted upon by the hydraulic oil is three times the area of the piston face applied to the sample. Therefore, the oil pressure is multiplied by a factor of three, giving a maximum uniaxial pressure of 15,000 psi applied to the sample.

The piston in each endcap has a removable tip (Figure 4.1) that contains a custom-designed transducer (either P- or S-wave) used for pulse-transmission wave speed measurements. Each transducer is built around a ValpeyFisher PZT 4 or 5A piezoelectric crystal cut

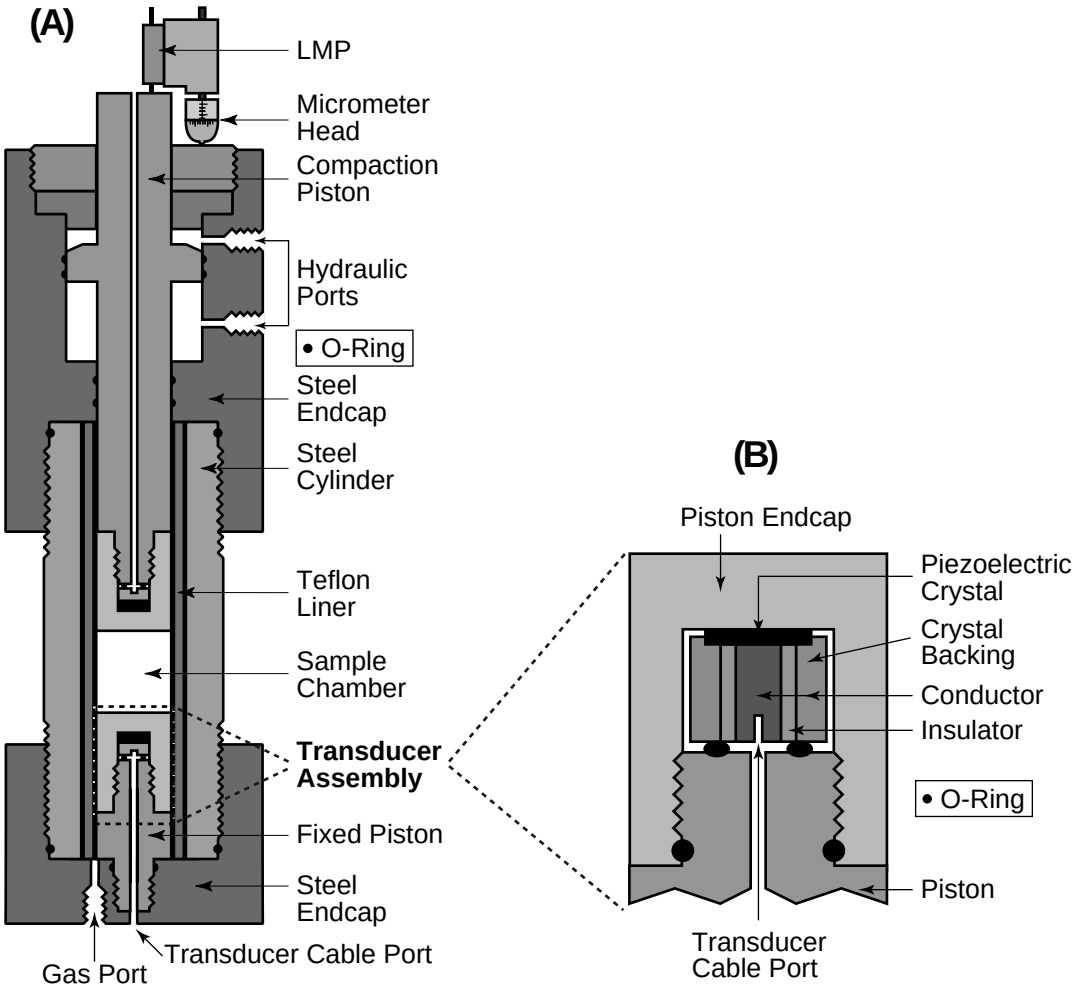

Figure 4.1: Methane hydrate synthesis and compaction vessel. (A) Schematic representation of the pressure vessel showing the hydraulic system, the sample chamber, the transducer locations and the linear motion potentiometer (LMP). For scale, the diameter of the sample chamber is one inch and the central cylinder is seven inches long. (B) Detailed schematic of the transducer contained in each piston endcap. For scale, the diameter of the piston cap is 1 inch.

to vibrate in either compressional or shear mode with a 1 MHz center frequency. The crystal located in each transducer is attached to the piston cap with a thin layer of Panametrics brand shear couplant and is backed by a holder made of concentric cylinders of conductor and insulator. The holder is designed to insulate the two electrical poles of the crystal and also provide a pathway for supplying voltage to or receiving voltage from the transducer. Contact between the crystal and the piston cap is maintained by screwing the piston cap on the piston and compressing a rubber O-ring located on the end of the piston shaft (see Figure 4.1). The piston cap seals over another O-ring and mates with the piston. As a result, the crystal remains at atmospheric pressure and supports none of the compressional loading generated by the hydraulic system.

Voltage is applied to or read from the transducers by modified BNC cables which are inserted down the central axes of the pistons and plugged into the crystal backings using mini-banana plugs. The central core of the backing connects the crystal's positive electrode to the mini-banana plug. The crystal's ground electrode contacts the grounded sample vessel, completing the circuit.

For the experiments described in this chapter, a Hewlett-Packard 214A pulse generator was used to drive the transducer located in the translating piston with a broad square wave. The signal generated by the leading edge of the square wave and received at the fixed piston was amplified by a Hewlett-Packard 465A amplifier and displayed on a Tektronix TDS 340 oscilloscope. The oscilloscope was set to continuously average over 256 cycles in order to reduce the random noise present in the signal. The oscilloscope settings and display could be changed and/or queried at regular time intervals by a Labview Virtual Instrument program which I wrote to time-stamp and copy the displayed waveform to a computer hard disk for later analysis.

The starting length of each sample was determined from the dimensions of the components of the pressure vessel (piston lengths, pressure vessel cap separation, etc.) and the length of piston protruding from the top of the pressure vessel. Changes in sample length during an experiment were monitored with a 12.7 mm total travel length linear motion potentiometer (LMP) attached to the translating piston (see Figure 4.1). The LMP was made by ETI Systems from a linear conductive plastic. The LMP was attached to a modified

micrometer head, allowing the LMP to be calibrated during each experiment. The micrometer head also made it possible to precisely adjust the reference height of the LMP when the limit of its travel length had been reached.

During an experiment, the pressure vessel was connected to the high pressure gas line (rated to 5,000 psi) through a port in the bottom endcap. The pressure vessel was suspended from the high pressure gas line and was partially submerged in an ethyl alcohol bath located in a freezer (see Figure 4.2). The temperature of the bath was controlled by balancing the cooling power of the freezer against a heater placed beneath the temperature bath. The temperature in the bath was monitored with an RTD and the output of the heater was controlled manually with a rheostat.

Throughout an experiment, bath temperature, oil pressure, gas pressure and LMP voltage readings were collected from a Hewlett-Packard 34970A multiplexer by a Labview data acquisition and display program. The data sampling rate was user selectable and could vary during an experiment. The collected data were timestamped and recorded to a computer hard disk for later analysis.

4.2.3 Data Processing

The timestamps applied to the waveform and pressure-temperature-length (PTL) data made it possible to process the waveform and PTL data independently. The two data sets were then recombined according to their timestamps and used to calculate wave speeds. These wave speeds could then be displayed as functions of time, length, piston pressure, temperature or any other time referenced property.

The temperature reported by the previously calibrated RTD in the bath was assumed to be accurate and no correction was applied to its recorded reading. The voltage reported by the pressure transducer in the hydraulic oil line was converted to uniaxial piston pressure by applying a calibration obtained from a low resolution (200 psi/div) dial gauge also attached to the oil line and then multiplying by three. The factor of three accounted for the ratio between the area acted upon by the oil and the area of the piston face applied to the sample. The voltage reported by the pressure transducer in the gas line was converted to pressure using a calibration obtained from a high resolution (1 psi/div) Heise dial gauge attached to the gas line.

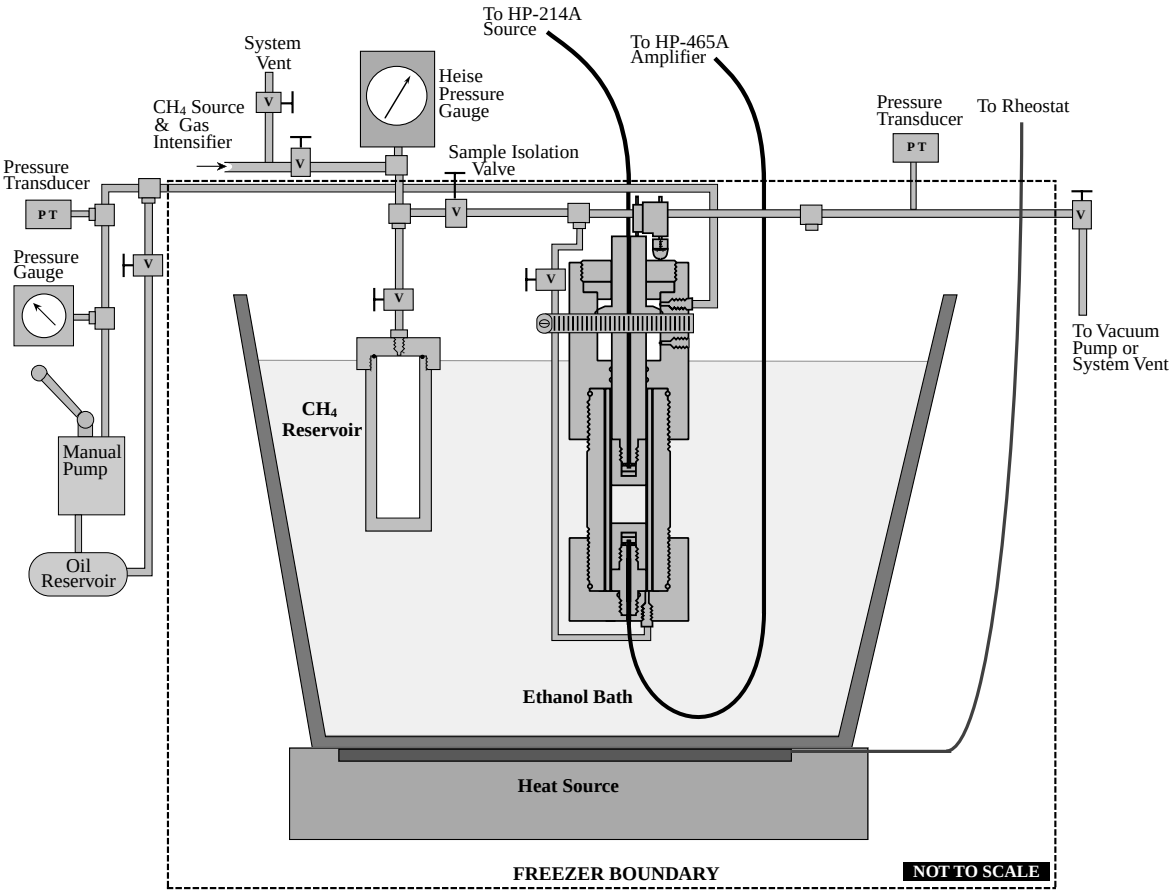

Figure 4.2: System for synthesizing, compacting and observing wave speeds in methane hydrate. Samples are formed in a pressure vessel located in an ethyl alcohol bath contained in a freezer. Sample temperature is controlled by a heater located beneath the bath. Samples are formed from granulated ice warmed from -20 to 17°C in a pressurized methane atmosphere. The resultant porous methane hydrate samples are compacted with the hydraulic ram contained in the pressure vessel. Compressional or shear transducers located in the pressure vessel make it possible to determine compressional and shear wave speeds in the sample as it is compacted. Sample lengths are determined from the dimensions of the pressure vessel and the position of the translating piston relative to the top of the pressure vessel.

As described above, the sample length was determined from the dimensions of the pressure vessel and by monitoring the height of the translating piston protruding from the top of the pressure vessel. During compaction, the samples (both methane hydrate and ice) always shortened by more than 15 mm, but the LMP had a travel of only 12.7 mm. As a result, the reference height of the LMP had to be adjusted in the middle of each experiment. The micrometer head attached to the LMP was used for this purpose. Resetting the LMP reference height added a static shift to the LMP voltage data that had to be removed manually. However, the LMP reset was only performed when the sample length was changing very slowly, so the offset could be unambiguously identified and removed without introducing any significant error. Resetting the LMP using a micrometer also allowed the LMP to be calibrated during each run by recording the LMP voltage change as a function of known height adjustment (as measured by the micrometer). The length versus voltage calibrations obtained from these adjustments were used to convert the LMP voltage changes to sample length changes. These length changes were combined with the original sample length to give the sample length as a function of time during the experiment.

In these early experiments only minimal processing was applied to the acquired waveforms. The recorded waveforms often had a small baseline DC offset. Whenever possible, this offset was removed by subtracting the mean of the first 100 data points in the recorded waveform. This correction was only applied when the first 100 data points preceeded the arrival of the transmitted waveform. The HP-465A amplifier also applied some "processing" to the waveform, namely a fairly flat 40 dB (i.e., 100x) boost in the frequency range 0.3 to 1.5 MHz. This was equivalent to applying a band-pass filter to the raw data. No additional digital filtering was applied.

An example compressional waveform transmitted through a compacted methane hydrate sample is given in Figure 4.3. An example shear waveform transmitted through a different compacted methane hydrate sample is given in Figure 4.4. Figure 4.5 shows the arrival of the precursor "noise" wavetrain which preceeded the arrival of the shear signal shown in Figure 4.4. One of the discoveries from these early experiments was that the arrival of this precursor "noise" was easily distinguishable from the background noise and that it traveled at the compressional wave speed in the medium. This meant the shear wave transducers could be used to measure both compressional and shear wave travel times in the

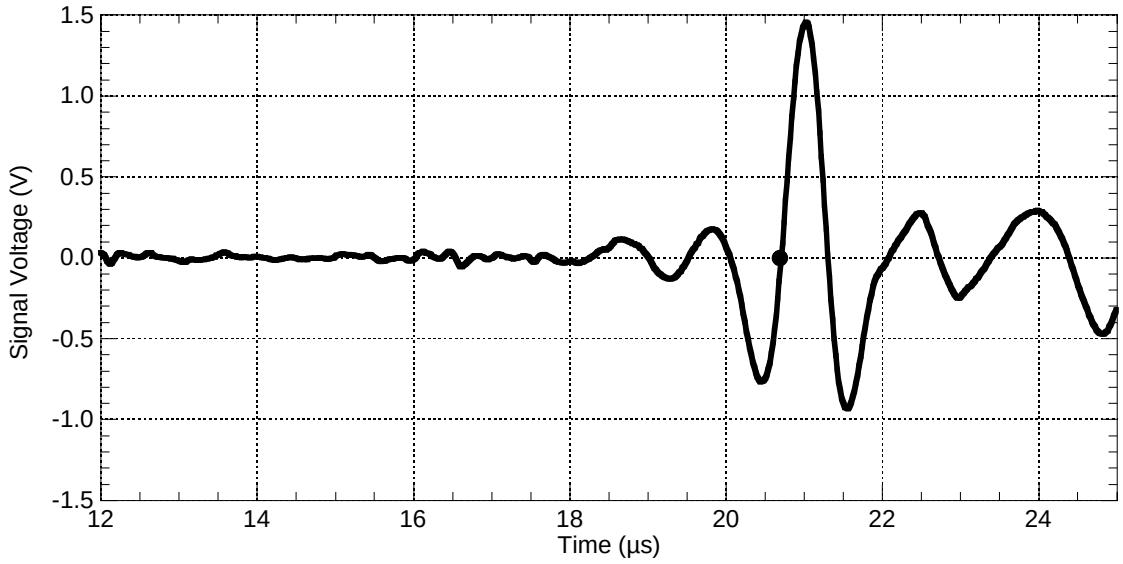

Figure 4.3: Example of compressional wave generated and received by compressional transducers. Signal has traveled through a partially compacted methane hydrate sample. Filled circle shows the waveform feature used to determine the arrival time of the signal.

same sample. Below I show that compressional wave speeds determined from the signals generated by the the compressional and shear transducers were the same.

Wave speeds were calculated from the waveform and sample length data using the pulse transmission technique. This technique measures wave speed by determining the time it takes a waveform to travel through a sample of known length. The sample length was determined as described above. The amount of time it took a waveform to travel through the sample was measured by comparing the waveform that traveled through the sample to a waveform acquired when the pistons were directly in contact. The zero crossing that preceeded the largest positive peak in each waveform was used to determine the time delay for each waveform. This feature was chosen because it was the most robust feature and thus the most easily picked during all stages of compaction. A Matlab program was written to automate picking this zero crossing for the several hundred waveforms acquired during an experiment.

Wave speed values were calculated from

$$V = \frac{l}{t - t_0} \tag{4.1}$$

where V is wave speed, l is sample length, t is the arrival time of the desired zero crossing

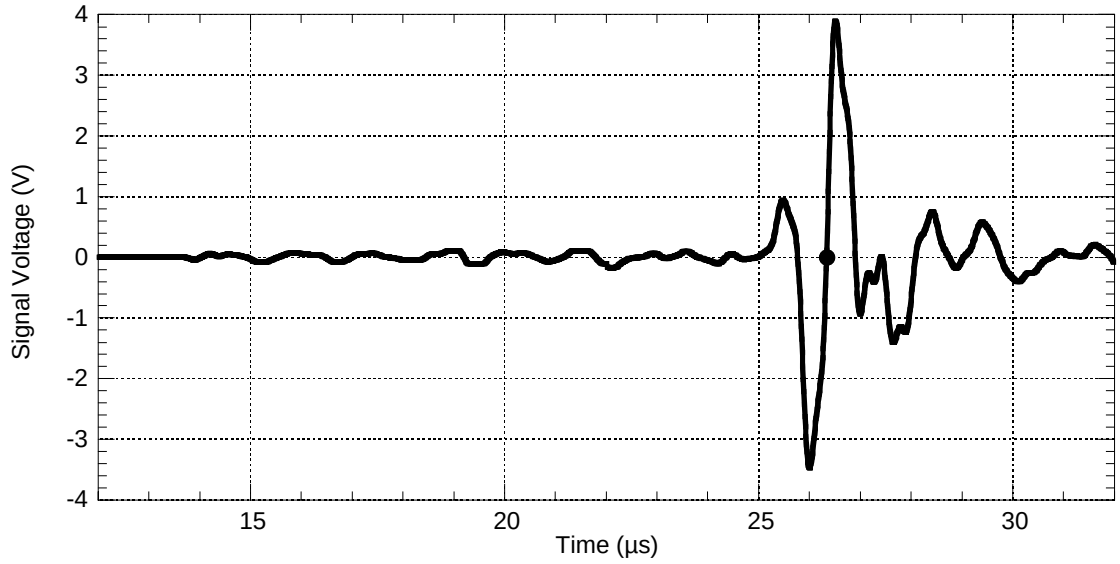

Figure 4.4: Example shear wave generated and received by shear transducers. Signal has traveled through a partially compacted methane hydrate sample. Filled circle shows the waveform feature used to determine the arrival time of the shear signal.

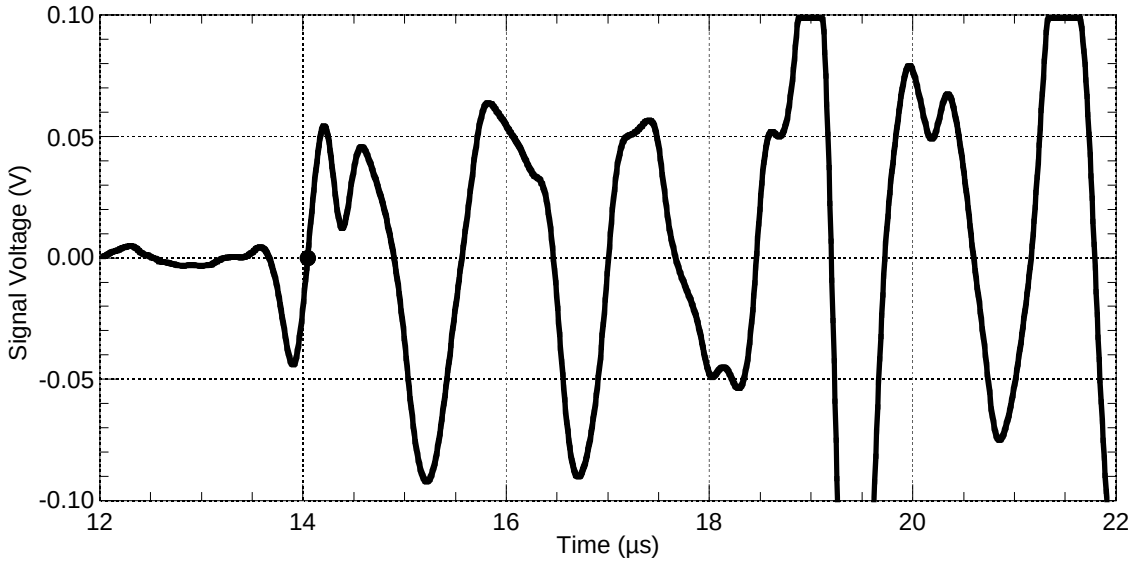

Figure 4.5: Example of compressional precursor “noise” generated and received by the shear transducers. This signal is the precursor associated with the shear wave signal shown in Figure 4.4. Filled circle shows the waveform feature used to determine the arrival time of the precursor compressional signal.

in a waveform that has traveled through a sample and t_0 is the arrival time of the same zero crossing in a reference waveform acquired when the pistons were head to head. t_0 was considered a constant but t and l varied throughout the experiment. The sample length associated with each waveform was determined by interpolating the time referenced length data at the time the waveform was acquired.

4.3 Stage One Experiments

The first set of measurements performed with the system described above were used to test the methane hydrate formation process in the new apparatus and to learn the general characteristics of the compaction and data acquisition systems. This first stage took approximately six months. The initial experiments suffered from electrical grounding problems that distorted the observation of the transmitted waveforms. These problems were eventually resolved and subsequent successful experiments showed the system worked extremely well for studying methane hydrate, that shear wave transducers could be used to reliably measure both compressional and shear wave speeds on the same sample and that we could reproduce literature values for compacted polycrystalline ice samples. I describe four of these successful experiments below.

4.3.1 Procedure

The same initial procedure is followed in all of the experiments reported in this Chapter. First, the transducer packages were assembled and screwed onto the pistons. If shear transducers were being used, the two pistons were placed in contact and the alignment of the shear transducers was checked. Marks were placed on the pressure vessel caps so that this alignment could be achieved when the pressure vessel was completely assembled. Next, the pressure vessel was partially assembled by screwing the cylindrical body of the pressure vessel into the larger endcap and inserting a thick teflon liner (I.D. 25.4 mm, wall thickness 3.175 mm) down the shaft of the pressure vessel and over the piston. This liner held the sample between the pistons and kept the translating piston from sticking to or gouging the side walls. All the components of the pressure vessel were then placed in a freezer and allowed to cool for several hours.

When the pressure vessel had achieved thermal equilibrium in the freezer, ice was ground and sieved to extract the $180 - 250$ μm fraction. 16 grams of sieved ice were measured out in a beaker and transferred to the teflon liner in the pressure vessel. Assembly of the pressure vessel was completed and it was quickly transported to another freezer in which the temperature bath was located and where the experiment would take place. Before lowering the pressure vessel into the temperature bath, a modified BNC cable was inserted into the transducer in the bottom endcap. After placing the sealed pressure vessel in the temperature bath, it was connected to the high pressure gas line and the bath was lowered so the pressure vessel hung freely from the gas line. Next, the hydraulic oil line was connected to the pressure vessel and the LMP was screwed into the end of the translating piston. At this point, the LabView PTL log file was started and a pulse of methane gas was often let into the pressure vessel to check for leaks. If no leaks were observed, the pressure vessel and all gas lines were evacuated and then repressurized with methane gas to $\sim$ 3800 psia. The heater was activated and its output controlled by a rheostat set to slowly increase the bath temperature to 17°C. The heating process took approximately 24 hours, by which point the reaction was complete (signified by no further uptake of methane gas into the sample). Once the pressure-temperature data showed the reaction was complete, the rheostat setting was reduced to achieve whatever new temperature was desired. When the new temperature was achieved, the gas pressure was often reduced, usually to 1450 psia (10 MPa), and the sample was compacted.

During an experiment, the hydraulic oil pressure was controlled by manually operating a Haskell hand pump and a pressure release valve. The oil pressure was monitored with a dial pressure gauge located in the oil line. The sample was compacted by pressurizing the oil in the reservoir behind the translating piston until the LMP registered piston motion. At that point, pumping stopped until the length change decayed to zero. Then the piston pressure was increased by 600 psi and held constant until the length change again decayed to zero. This cycle was repeated until the LMP reached the approximate end of its travel. At that point, the system was allowed to relax until the sample length had stopped changing significantly. Next, the LMP was reset to the beginning of its travel by turning the micrometer head attached to the LMP holder. This procedure allowed the LMP to be calibrated in the middle of each run without introducing a significant error due to piston movement.

Once the LMP was reset, the pressurization steps resumed.

The piston pressure steps would repeat until the pressure limit of the system (5,000 psi oil pressure, 15,000 psi piston pressure) was reached. When the pressure limit was reached, the pressure would be held at 15,000 psi for a period of time that varied between experiments. Then the piston pressure would be allowed to decay as the sample shortened. In some experiments, during the compaction process, the piston pressure was reduced by several thousand psi and the piston would be pushed off the sample by the gas pressure. The oil pressure would then quickly be reinstated to its previous higher value. This was done to achieve additional compaction and worked to varying degrees of success in different experiments.

At the end of an experiment, the temperature would be reduced to freezer temperature, the oil pressure would be reduced to zero, the gas line would be sealed off, the oil line would be removed and the LMP would be unscrewed from the piston. The pressure vessel would then be disconnected from the gas line and placed in a freezer where the residual alcohol evaporated away. When the pressure vessel was dry, it was removed from the freezer, liquid nitrogen was poured over the central cylinder and the endcaps were removed from the pressure vessel on the benchtop. Liquid nitrogen was used because methane hydrate is stable at one atmosphere below 195 K. The teflon liner/sample holder would then be pushed out of the pressure vessel and placed in a liquid nitrogen bath. Unfortunately, it was generally difficult to extract the sample from the teflon liner because the internal diameter of the teflon was deformed by the compacted hydrate. This design flaw was corrected in later revisions of the apparatus (see Chapter 5).

In a few of the runs, the sample was allowed to disassociate in the pressure vessel in an attempt to recover the gas and estimate the cage occupation number for the hydrate. However, due to the design of the gas line, these attempts were largely unsuccessful because water and ice tended to get trapped in the gas line.

For all experiments, pressure, temperature and length data were acquired throughout the entire experiment. Once waveforms were detected, they too were recorded for the remainder of the experiment.

As discussed in the results section below, experiments involving only granulated ice were also conducted. The ice experiments were performed in order to test results from

our system against previously published measurements on polycrystalline ice (Tables 4.1 and 5.5). In our ice experiments, the only modifications to the procedure described above were that there was no gas hydrate synthesis cycle (i.e., no methane gas was added to the system), the temperature never exceeded -5°C and the pressure vessel was disassembled at freezer temperature after a run was completed. In all other respects the procedure was the same as for the gas hydrate runs. As discussed in detail below, the pressure required to compact the ice samples was far less than that required to compact the methane hydrate samples. Consequently, piston pressure in the ice experiments did not exceed 6,000 psi.

4.3.2 Results

In this section I describe the results from three successful experiments on methane hydrate, one using compressional wave transducers and two using shear wave transducers. I will then compare those methane hydrate results to an experiment conducted on granulated ice using shear wave transducers. The comparison illustrates the similarities and important differences between the two materials. The results described in this section showed the system could be used to successfully study polycrystalline methane hydrate and polycrystalline ice samples, that shear transducers could be used to simultaneously measure compressional and shear wave speed in the same sample and that the results were reproducible from run to run.

Compressional Wave Transducers – Methane Hydrate

Figure 4.6 plots compressional wave speed in a compacting polycrystalline methane hydrate sample as a function of sample length. The maximum compressional wave speed observed in this sample was 3310 m/s at -22.7°C and 9860 psi piston pressure. The final sample length was 35.69 mm. The large change in wave speed at the initial sample length ($\sim$ 49.3 mm) occurred as the sample transformed from porous, granular ice Ih to porous, granular methane hydrate. The compressional wave speed during this time was very poorly sampled because the signal transmitted through the sample was very weak to non-existent. This was because no positive piston pressure was maintained during methane hydrate synthesis. Consequently, there was very little (if any) contact between the pistons

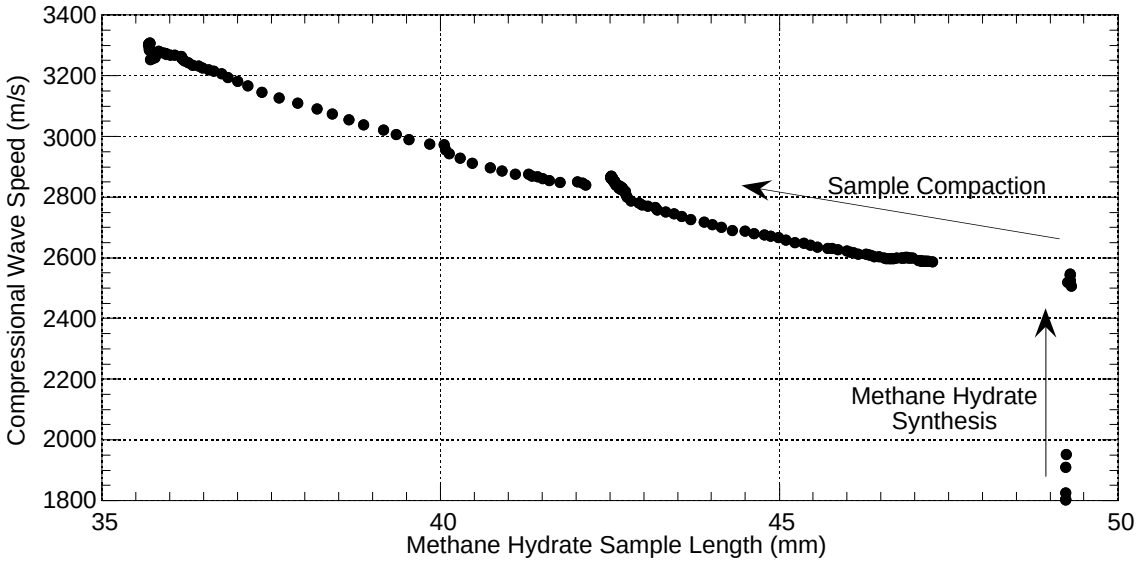

Figure 4.6: Compressional wave speed vs sample length in a compacting methane hydrate sample using compressional wave transducers. The large change in wave speed at $\sim$ 49.3 mm occurred during the hydrate synthesis process. The peak feature at $\sim$ 42.5 mm occurred while no active compaction of the sample was taking place. See text for an explanation of the origin of these features.

and the sample. This was done to insure a free path for gas to enter the sample. Additionally, over the course of several experiments, we observed that the signal decayed to zero as the temperature neared the melting point of ice regardless of the strength of the signal up to that point. The signal then occasionally reappeared hours later (as it did during this experiment), as the reaction neared completion.

This reappearance is likely due to the $\sim$ 15% volume increase that occurs during the ice Ih to sI gas hydrate transition. The sample cannot expand laterally because of the rigid side walls, so the volume change causes either a length change, a decrease in porosity or both. The net result is to improve (or initiate) contact between sample and transducer.

Two other interesting features of the plot are the near linearity of the wave speed versus length profile and the peak in the curve at 42.5 mm. The peak at 42.5 mm (see Figure 4.7) represents a time period when the length did not change significantly but the wave speed continued to increase. The length was essentially constant because active compaction was stopped in order to reset the LMP as described above. The fact the wave speed kept changing suggests that some physical or chemical process was continuing in the sample. Whatever that process was, restarting compaction essentially reversed its effects because the data

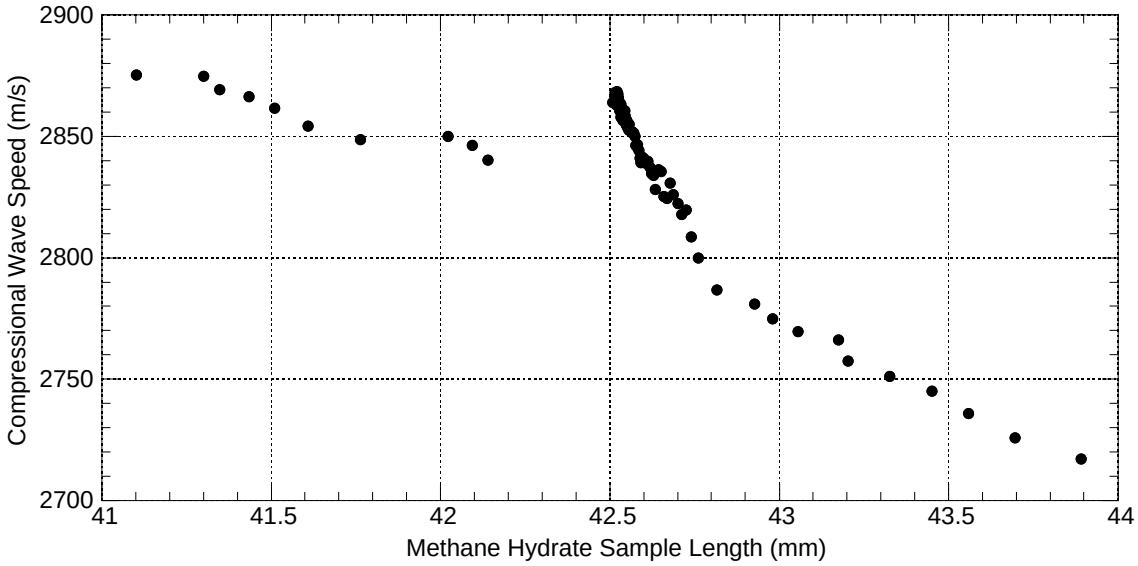

Figure 4.7: Detailed view of the increase in compressional wave speed observed during a pause in compacting a methane hydrate sample (same sample as in Figure 4.6). When compaction resumed, wave speed decreased before returning to the wave speed vs length trend defined prior to the pause in compaction. This behavior can be explained in terms of the formation and destruction of bonds between neighboring methane hydrate grains in the sample (see text).

returned to the trend defined prior to the pause in compaction.

The most likely candidate process for this effect is cementation at grain to grain contacts. It is a well known property of ice that two ice grains which come into contact form a bond at the contact point and this bond grows over time (Hobbs, 1974). This process is called sintering. In a material like methane hydrate which is similar to ice, we expect a similar process to occur. Bonds should constantly be forming between methane hydrate grains that are in contact. However, during active compaction, any grain to grain bonds that form are broken as the piston advances through the sample. As a result, on average, the character of the uncompacted material remains a collection of individual grains. However, when the piston is no longer being driven into the sample, bonds are able to grow, leading to the observed increase in wave speed at fixed sample length. When compaction resumes, the bonds are broken and the system returns to its original state, a collection of grains. If the bonds did not grow significantly while the piston was stopped, relative grain sizes and intergranular relationships should be essentially the same after compaction resumes as they were before compaction stopped. This is reflected in the wave speed versus length curve

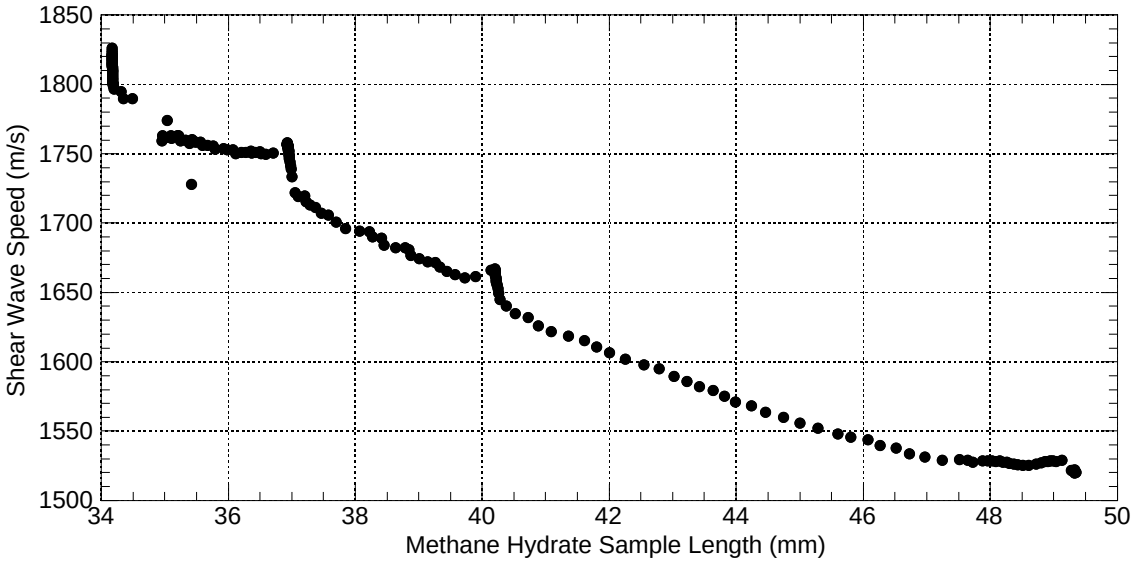

Figure 4.8: Shear wave speed vs sample length determined from the shear transducers for a compacting methane hydrate sample. Peaks in the curve correspond to pauses in compaction. The increase in wave speed at $\sim$ 34 mm occurred as the sample cooled to -25°C.

returning to its original trend. Note that the plot shows a brief reduction in wave speed as compaction resumes. This hypothesized cementing process requires that water molecules be mobile within the system and also suggests a comparable property with ice. Table 2.7 in Sloan (1998) shows that the mobility of water in ice Ih is much higher than in sI gas hydrate. Therefore, if this process is occurring, its effect should be even more dramatic in ice. As shown below, this is in fact the case.

Shear Wave Transducers – Methane Hydrate

Figure 4.8 shows a plot of shear wave speed versus sample length for a sample compacted between shear wave transducers. As with the compressional wave transducer experiment described above, the cusps in the curve correspond to times when the hydraulic pressure was not being actively maintained. There are multiple cusps in this plot because in addition to the LMP being reset the system was also left unattended overnight. The increase in wave speed at $\sim$ 34 mm occurred while the system cooled to -25°C. The fastest shear wave speed observed in this sample was 1825 m/s at -25.6°C and 9440 psi piston pressure. At 4.4°C, the fastest observed shear wave speed was 1795 m/s at 13,200 psi piston pressure.

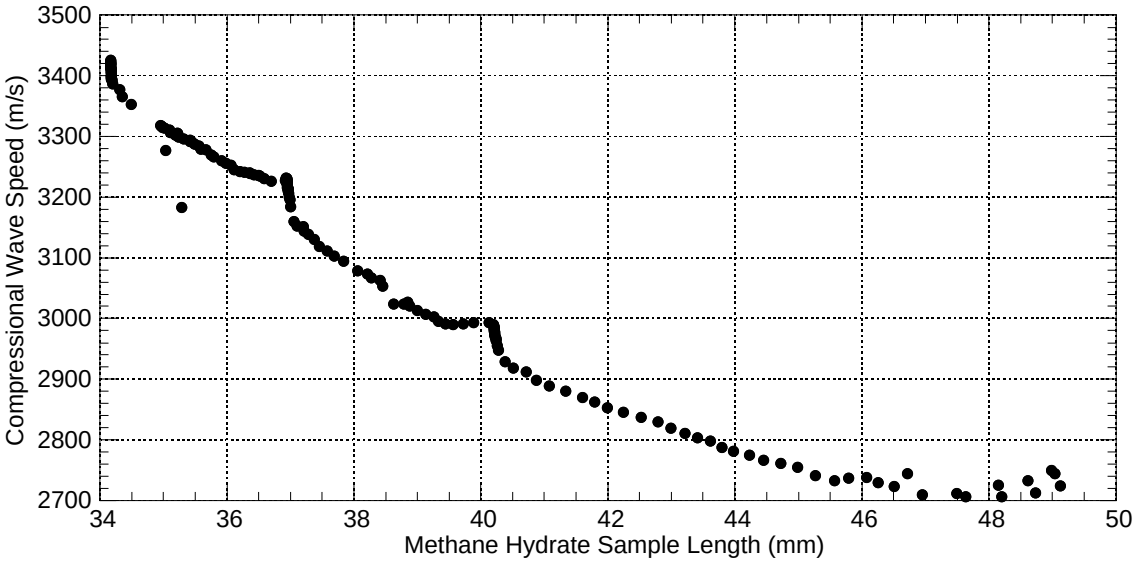

Figure 4.9: Compressional wave speed versus sample length determined from the shear transducers for a compacting methane hydrate sample. Peaks in the curve correspond to pauses in compaction. The increase in wave speed at $\sim$ 34 mm occurred as the sample cooled to -25°C.

During these experiments, in addition to recording the shear wave, the "noise" preceeding the shear wave was also recorded. The "noise" is non-shear wave energy produced and received by the shear transducers. By comparing the travel time of this waveform feature to the travel time in the compressional wave experiments, it became clear that the earliest arrival in this pre-shear "noise" was traveling at the compressional wave speed. Therefore the travel time of this shear-transducer generated wave feature could be used to measure compressional wave speed through the sample. The compressional wave speed so determined is plotted versus sample length in Figure 4.9. Note that the cusps present in the shear wave speed data are present in the compressional wave speed data as well.

In order to confirm the accuracy and repeatability of the determined compressional and shear wave speeds, the shear wave transducer experiment was repeated. The compressional wave speeds determined in the three methane hydrate experiments (two with shear transducers and one with compressional transducers) are plotted as a function of length in Figure 4.10. The agreement between the compressional wave speed results obtained from the compressional transducers and the shear transducers is excellent. As is the agreement

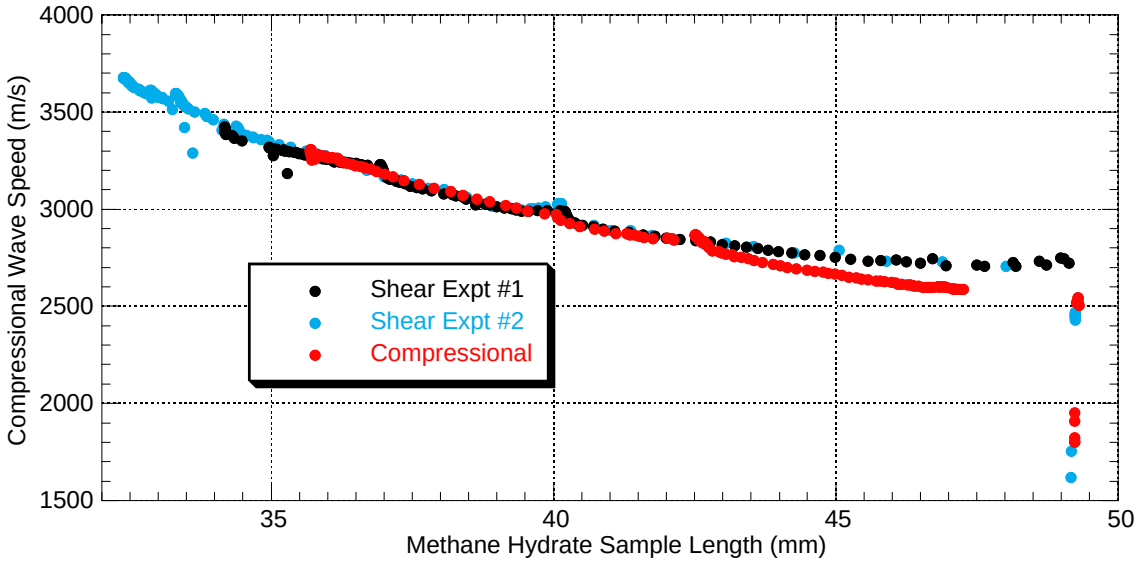

Figure 4.10: Comparison of compressional wave speed versus methane hydrate sample length for two shear transducer experiments and one compressional transducer experiment. Agreement at sample lengths less than 40 mm is excellent. Disagreement for sample lengths greater than 40 mm is probably due to the difficulty in picking shear transducer generated compressional wave arrivals because of low signal to noise ratio.

between the two shear-wave-transducer-based experiments. The fastest observed compressional wave speed was 3680 m/s at 3.9°C and 7500 psi piston pressure. The fastest observed shear wave speed was 1908 m/s at the same temperature and pressure. The disagreement in measured compressional wave speed at large sample lengths is probably due to the decreased signal to noise ratio and the resultant difficulty in picking the compressional wave arrival in the shear transducer experiments. Figure 4.11 shows the shear wave speeds determined in the two shear-transducer experiments as a function of sample length. Again, the agreement is excellent. These results showed that the shear wave transducers could be used to measure compressional and shear wave speeds on a sample simultaneously and that the results were repeatable from experiment to experiment.

With compressional and shear wave speed information available for the same sample and assuming homogenous, isotropic linearly elastic material, Poisson's ratio can be calculated from (Mavko et al., 1998)

$$\nu = \frac{1}{2}\frac{V_P^2 - 2V_S^2}{V_P^2 - V_S^2} \tag{4.2}$$

where V_P is compressional wave speed, V_S is shear wave speed and ν is Poisson's ratio,

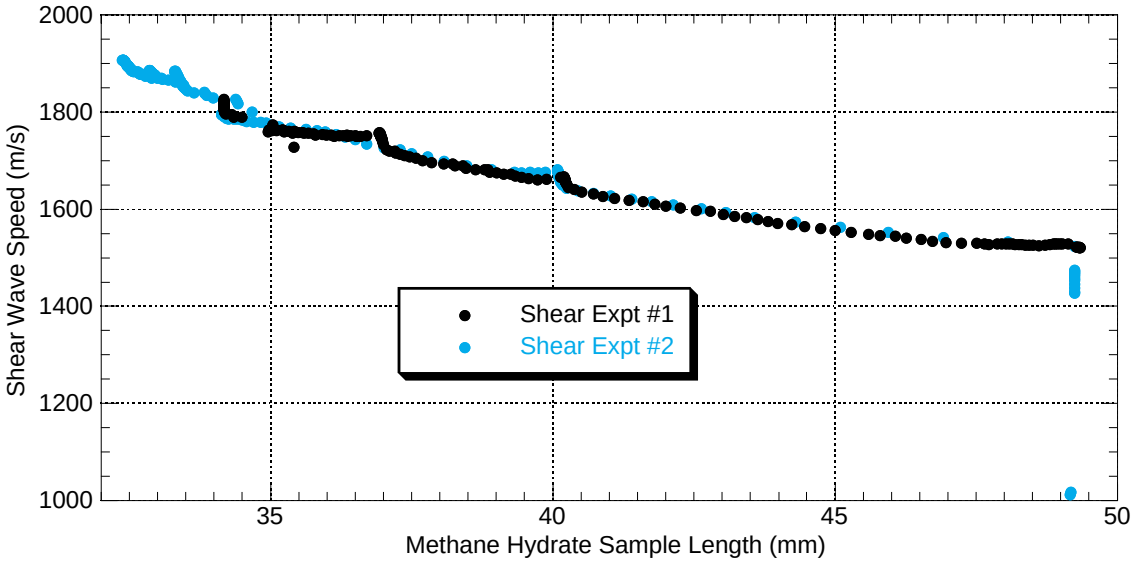

Figure 4.11: Comparison of shear wave speed versus methane hydrate sample length for two shear transducer experiments. Agreement at all sample lengths is excellent.

respectively. The plot of Poisson's ratio versus sample length computed from the compressional and shear wave speeds measured in the two shear transducer experiments is shown in Figure 4.12. The Poisson's ratio at maximum compaction (4°C and 7600 psi piston pressure) was 0.316.

Shear Wave Transducers – Ice

To help gain confidence in the results obtained from our apparatus we had also conducted experiments on pure ice. The sample I describe here was compacted at -21°C and then warmed to -10°C. Figure 4.13 shows the plot of compressional and shear wave speeds versus sample length for this polycrystalline ice sample. Figure 4.14 shows Poisson's ratio versus sample length as determined from Equation 4.2. Note that Figure 4.13 shows even stronger cusp features than the methane hydrate runs did (Figures 4.10 and 4.11). Note also that the ice wave speed versus length trends are not the same before and after the cusp feature, suggesting the process had a larger, irreversible effect in the ice sample than in the methane hydrate samples. This difference could have been caused by the greater water mobility in ice leading to a more efficient and widespread redistribution of water molecules during the pause in compaction. This more efficient redistribution would change the ice

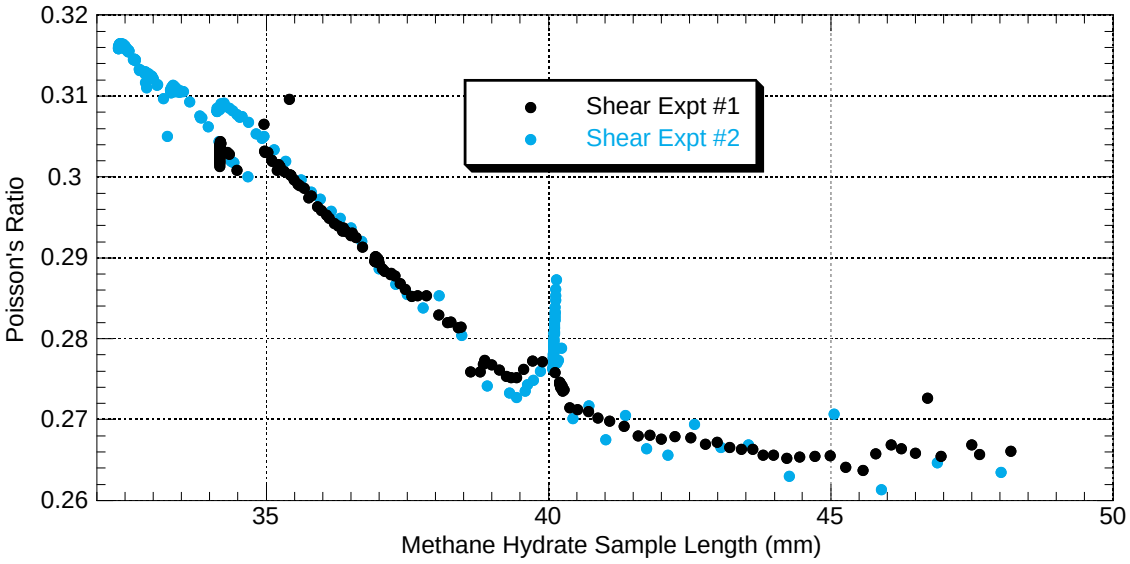

Figure 4.12: Poisson's ratio versus methane hydrate sample length for two shear transducer experiments. The peaks at $\sim$ 40 mm correspond to the times when active compaction of the samples was not occurring.

grain sizes and shapes during the pause in compaction. Renewing compaction would then effectively create a "new" granular material when the grain to grain bonds were broken. This new material would have slightly different composite physical properties and hence not fall along the previously defined wave speed versus length trends.

Analysis

The fact that both compressional and shear wave speeds could be measured simultaneously on the same sample meant that elastic moduli could also be calculated, provided sample bulk density could be estimated. Also of interest was the porosity of each sample at a given sample length. Knowing density and porosity would make it possible to perform effective medium modeling of the data. Density could be calculated from the mass of the initial seed ice, the sample volume and (for hydrate) the amount of methane taken up during synthesis. The theory for estimating porosity is also simple because of the geometry of the system, provided we can assume conservation of water molecules. The porosity derivation follows below.

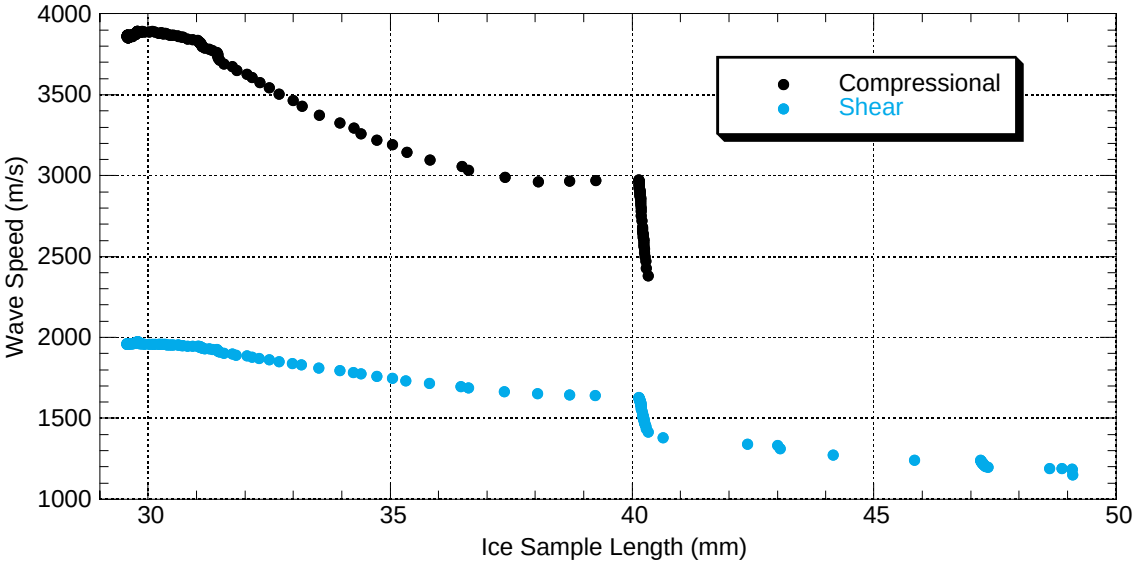

Figure 4.13: Compressional and shear wave speeds versus ice sample length. No compressional wave speed data are available prior to $\sim$ 40 mm because the compressional wave signal could not be reliably distinguished from the background noise. Peaks in the data at $\sim$ 40 mm occurred during a pause in compaction. Note that the magnitude of the wave speed increases at $\sim$ 40 mm are larger in this ice sample than in the three methane hydrate samples discussed previously and that the shear wave speed data did not return to the trend defined prior to the pause in compaction when compaction resumed.

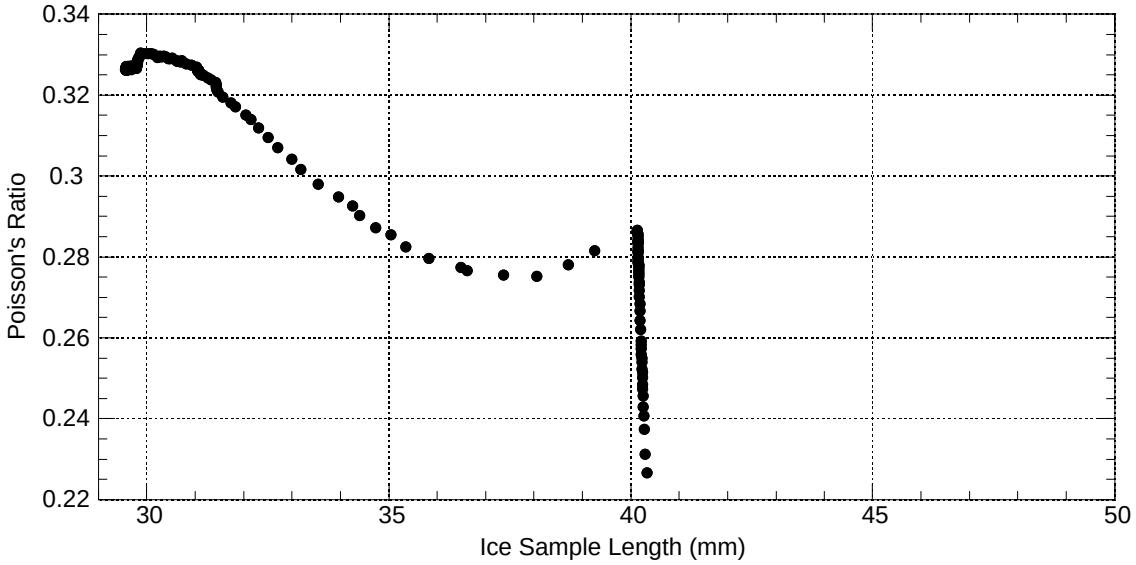

Figure 4.14: Poisson's ratio versus ice sample length. The peak at $\sim$ 40 mm occurred during a pause in compaction and signifies that the V_p/V_s ratio increased significantly during that pause.

The porosity of a sample is defined as

$$\phi = 1 - \frac{V_{solid}}{V_{total}} \tag{4.3}$$

where V_{solid} is the volume of solid material in the sample and V_{total} is the total volume of the sample. Because the sample chamber is a right circular cylinder, the total volume of the sample can be expressed as

$$V_{total} = \pi r^2 h, \tag{4.4}$$

where r is the radius and h is the height of the sample chamber, respectively. V_{solid} can also be expressed as a cylindrical volume,

$$V_{solid} = \pi r^2 h_0, \tag{4.5}$$

where h_0 is the height of the cylinder of radius r that could be formed from the volume of solid material in the sample. Substituting Equations 4.4 and 4.5 into Equation 4.3 and canceling the common factor πr^2, we see that

$$\phi = 1 - \frac{h_0}{h}. \tag{4.6}$$

Porosity can, therefore, be determined directly from the sample height, provided the predicted zero porosity sample height (h_0) can be found.

From Equation 4.5, we see that h_0 is given by

$$h_0 = \frac{V_{solid}}{\pi r^2}. \tag{4.7}$$

For the ice experiment, V_{solid} is simply the volume of ice (V_{ice}) present in the sample. The volume of ice is calculated from the mass of seed ice (n) used to make the sample,

$$V_{ice} = \frac{n}{\rho_{ice}}, \tag{4.8}$$

where ρ_{ice} is the density of ice. Substituting this expression for V_{ice} into Equation 4.7 in the place of V_{solid} we find that the height of a zero porosity, right circular cylindrical sample of ice with radius r made from n grams of granulated ice is given by

$$h_0 = \frac{n}{\rho_{ice}\pi r^2}. \tag{4.9}$$

The h_0 given by Equation 4.9 is not the appropriate h_0 for methane hydrate. In order to determine the predicted zero porosity height for a right circular cylindrical methane hydrate sample of radius r, we must first convert the initial mass of seed ice to an equivalent volume of methane hydrate. This can be done easily if it is assumed that all the water molecules in the initial seed ice are used to form the methane hydrate crystal lattice. In this case, the volume of methane hydrate (V_{hyd}) that can be formed from n grams of ice is given by

$$V_{hyd} = \frac{n}{\rho_I} \tag{4.10}$$

where ρ_I is the density of empty sI gas hydrate (i.e., Equation 2.42 with $x_s = x_l = 0$).

For the methane hydrate experiment utilizing compressional wave transducers described above, the initial mass of ice in the sample was 15.9 g. The internal diameter of the teflon sleeve used to hold the sample was 2.54 cm. In Chapter 2, I showed that the empty cage density of sI gas hydrate was approximately 0.80 g/cm^3. Therefore, the predicted zero porosity sample length is

$$h_0 = \frac{15.9\text{g}}{0.80\text{g/cm}^3 \pi \left(\frac{2.54\text{cm}}{2}\right)^2} = 3.9 \text{ cm}. \tag{4.11}$$

The final sample length for this experiment was 3.571 cm, significantly shorter than the predicted value. The discrepancy is worse for the two shear wave transducer experiments which had slightly larger starting ice masses (15.95 g and 16.0 g, respectively), but whose final lengths were less than 3.571 cm.

The disagreement between theory and measurement can be explained by the violation of two fundamental assumptions, 1) right cylindrical sample volume and 2) conservation of water molecules. Taking apart the pressure vessel after each run showed that the teflon sample holder deformed under the force of compaction and the samples bowed out in the middle. Upon disassembly it was also evident that a small but significant amount of the solid material had escaped from between the pistons. The combination of these two occurrences made accurate determination of density and porosity in the samples essentially impossible. Modifications to the apparatus (see Chapter 5) corrected both these problems. For this reason, wave speeds measured in these preliminary experiments are not used to calculate elastic moduli for methane hydrate. Instead, elastic moduli are calculated from the results described in Chapter 5.

Table 4.1: Ice Ih Wave Speeds – Literature Values

Source	Technique	V_p (m/s)	V_s (m/s)	ν
Gagnon et al. (1987)	Brillouin Spectroscopy	3914	1995	0.325
Smith and Kishoni (1986)	Pulse-Echo	3940	1990	0.329
Shaw (1986)	Pulse Transmission	3890	1900	0.343

If zero porosity (or some fixed but small porosity) had been achieved in these experiments, the compressional and shear wave speeds would have leveled off as the sample shortened. This would signify that even though the sample length was changing, presumably by extrusion of material, the elastic properties of the material between the pistons was remaining the same. Since this did not occur, some residual porosity must have remained and the values provided by these experiments can serve only as a lower limit on estimating the pure hydrate values for compressional and shear wave speeds and Poisson's ratio.

Unlike in the methane hydrate experiments, Figures 4.13 and 4.14 show that in the ice sample wave speed and Poisson's ratio values did begin to level off towards the end of the experiment, suggesting a very low porosity had been achieved. This is consistent with the observation that measured compressional and shear wave speeds (3850–3890 m/s and 1955–1975 m/s, respectively) and Poisson's ratios (0.326–0.330) closely matched literature values for polycrystalline ice samples (see Table 4.1). These results show that the methodology is sound and that the use of shear wave transducers to measure compressional and shear wave speeds simultaneously is justified.

Another interesting comparison between ice Ih and methane hydrate that can be made from these experiments is the relative strength of the two materials. It is much harder to compact methane hydrate than it is to compact ice Ih. Since the compaction was performed by manually operating a hand pump, this difference was a very tangible experience for the experimenter. It can also be seen in the data by plotting sample length versus piston pressure (Figure 4.15). The pressure needed to compact the methane hydrate sample was as much as 10 times the pressure required to compact the ice Ih sample to the same length. Only a small portion of this difference can be accounted for by the extra gas pressure in the methane hydrate experiments and the differences in porosity at the same sample length for the two materials. This disparity in strength between methane hydrate and ice has

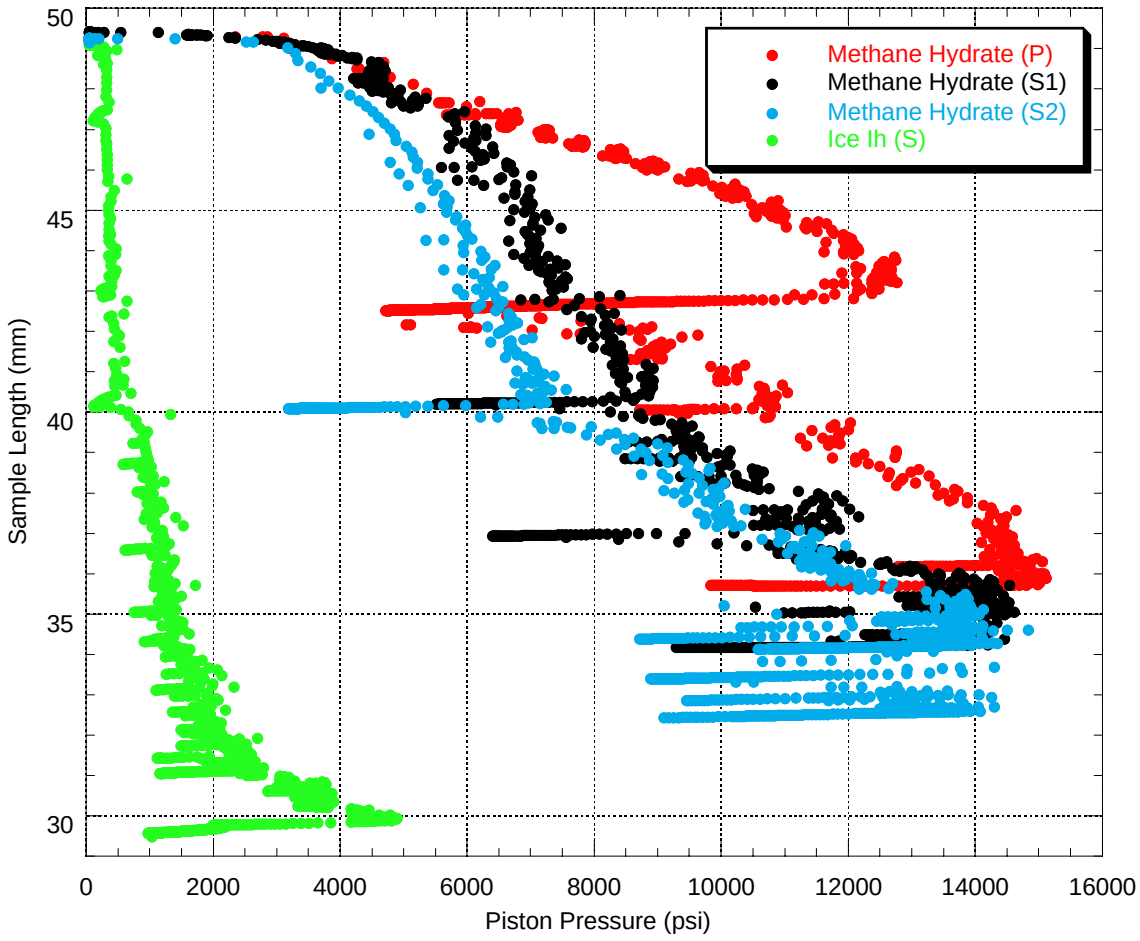

Figure 4.15: Sample length versus piston pressure for three methane hydrate samples and one ice sample. These compaction curves show that porous methane hydrate samples are much more resistant to compaction than porous ice samples.

been observed by other experimenters (Zhang et al., 1999; Durham et al., 2001) and may be important in studies of sea floor stability and the crustal mechanics of hydrate-bearing planets and moons in the outer solar system.

4.4 Conclusions

- The results described in this chapter show that the apparatus and procedure for making methane hydrate and for measuring compressional and shear wave speeds in methane hydrate and ice produce repeatable and reliable results.

- The shear transducers produce detectable precursor compressional wave signals and thus can be used to measure both compressional and shear wave speeds in the same sample, making it possible to measure Poisson's ratio as well.
- Experiments on similarly prepared samples give consistent results.
- Changes in wave speed when the samples were not being actively compacted suggest that grain to grain bonds form in the ice and methane hydrate samples. The magnitude of the wave speed increase suggests this process is more efficient in ice, perhaps because of the higher mobility of water molecules in ice compared to methane hydrate.
- Porous methane hydrate is much more resistant to compaction than porous ice. This result may have important implications for underwater slope stability; seafloor stability during the emplacement of offshore structures; drilling through methane hydrate layers; and hydrofracture design in gas hydrate bearing oceanic sediments. This strength difference between ice and methane hydrate may also be important in analyzing crustal deformation on celestial bodies thought to have a significant amount of gas hydrate in their crust (e.g., moons of the outer solar system, comets, etc.).
- In this chapter I reported wave speeds in methane hydrate and ice from the pressure-temperature points where the samples became essentially fully dense (i.e., approximately zero porosity). However, with relatively minor changes to the setup, it would become possible to make measurements of wave speeds as a function of temperature and pressure. That work is the subject of Chapter 5.

4.5 References

Durham, W. B, W. Zhang, L. A. Stern and S. H. Kirby, 2001, The strength of methane clathrate hydrate, in preparation.

Gagnon, R., H. Kiefte, M. Clouter and E. Whalley, 1987, Elastic Constants of Ice Ih, up to 2.8 kbar, by Brillouin spectroscopy, Journal de Physique, **48**, 23–28.

Shaw, G., 1986, Elastic properties and equation of state of high pressure ice, Journal of Chemical Physics, **84**, 5862–5868.

Sloan, E. D., Jr., 1998, Clathrate hydrates of natural gases, 2nd Ed., Marcel Dekker, New York, 705pp.

Smith A., and D. Kishoni, Measurement of the speed of sound in ice, AIAA Journal, **24**, 1713–1715.

Stern, L. A., S. Kirby and W. B. Durham, 1996, Peculiarities of methane clathrate hydrate formation and solid-state deformation, including possible superheating of water ice, Science, **273**, 1843–1848.

Stern, L. A., S. H. Kirby and W. B. Durham, 1998, Polycrystalline methane hydrate: synthesis from superheated ice, and low-temperature mechanical properties, Energy and Fuels, **12**, 201–211.

Stern, L. A., S. H. Kirby, W. B. Durham, S. Circone and W. F. Waite, 2000, Laboratory synthesis of pure methane hydrate suitable for measurement of physical properties and decomposition behavior, in Natural gas hydrate in oceanic and permafrost environments, M. D. Max ed., 323–348.

Waite, William F., Michael B. Helgerud, Amos Nur, John C. Pinkston, Laura A. Stern, Stephen H. Kirby, and William B. Durham, 2000, Laboratory measurements of compressional and shear wave speeds through methane hydrate, in Gas hydrates: Challenges for the future, G. D. Holder and P. R. Bishnoi eds., 1003–1010.

Zhang, W., Durham, W.B., Stern, L.A., and Kirby, S. H., 1999, Experimental Deformation of Methane Hydrate: New Results, EOS Trans AGU, **80**, S337.

Appendix A:

Stage One Experiments – Summary Table

This Appendix provides a table with summary information for the experiments discussed in Chapter 4. Included in the table are the start and end dates for each respective experiment, the temperature at which each sample was compacted, the gas pressure in the system while each sample was compacted, the maximum wave speeds observed in each sample, the figure numbers for figures displaying data from the respective experiments and the names of ASCII data files containing data from each respective experiment. The ASCII data files are included only with the version of this thesis distributed on the Stanford Rock and Borehole Geophysics (SRB) web site.

Table A.1: Stage One Methane Hydrate and Ice Ih Experiments – Summary Information

Sample Material	Methane Hydrate	Methane Hydrate	Methane Hydrate	Ice Ih
Reference #	081398	102098	110298	100198
Transducer	P	S	S	S
Start Date	8/13/98	10/20/98	11/2/98	10/1/98
End Date	8/18/98	10/23/98	11/6/98	10/5/98
Compaction Temperature	-20 °C	3 °C	5 °C	-23 °C
Compaction Gas Pressure	3,200 psia	1,500 psia	1,600 psia	NA
Maximum V_P	3,310 m/s	3,425 m/s	3,680 m/s	3,890 m/s
Maximum V_S	NA	1,825 m/s	1,908 m/s	1,970 m/s
Associated Figures	4.3, 4.6, 4.7, 4.10, 4.15	4.8, 4.9, 4.10, 4.11, 4.12, 4.15	4.4, 4.5, 4.10 4.11, 4.12, 4.15	4.13, 4.14, 4.15
Associated Data Files[a]	081398PTL 081398PResult	102098PTL 102098PResult 102098SResult	110298PTL 110298PResult 110298SResult	100198PTL 100198PResult 100198SResult

[a] Thesis distributed on Stanford Rock and Borehole Geophysics (SRB) web site includes data files associated with each experiment, as well as individual waveform files

Chapter 5

Methane Gas Hydrate Experiments – Stage Two

5.1 Introduction

The experiments described in Chapter 4 demonstrated that the apparatus and methodology for making wave speed measurements on methane hydrate worked well. However, they also showed that improvements to the experiment were possible and that those improvements could lead to measurements of compressional and shear wave speed as a function of temperature and axial pressure. In pursuit of this goal, twenty-two experiments were performed and a number of changes were implemented in the apparatus, procedures and data processing steps. A number of systematic error sources were identified and eliminated. The changes culminated in precise measurements of compressional and shear wave speed in the compacted ice and compacted methane hydrate samples described in this chapter. The methane hydrate elastic moduli values determined from these wave speed measurements are assumed to be representative of natural methane hydrates and are used in Chapter 6 to model the effect that methane hydrate has on sediment elastic properties.

5.2 Modifications to Apparatus and Data Acquisition Systems

The first issues to address in modifying the apparatus described in Chapter 4 were the sample loss and deformation problems. To address sample loss, an O-ring was placed between two porous metal washers on the fixed piston in the pressure vessel. The O-ring prevented solid material from being pushed down the sides of the piston during compaction. The porous metal washers allowed gas to reach the sample. The washers were supported by a cylindrical steel spacer (Figure 5.1).

To prevent sample deformation, the teflon sample holder was replaced with a split steel cylinder, a thin internal teflon liner and a thin external teflon liner. The end of the internal teflon liner which covered the translating piston was slotted in order to allow gas into the sample. Once compaction began, the translating piston advanced and closed off the slots, preventing any solid material from being lost. After a number of experiments, the split steel cylinder was replaced with an intact steel cylinder when it became clear that a small amount of sample deformation was still occurring. The internal teflon liner made it possible to extract the compacted sample from the steel cylinder.

The transducer package was redesigned to make it simpler. In the previous design, the piezoelectric crystals were not permanently bonded to their backings and the backings were loose in the piston caps. This meant the transducer packages had to be reconstructed for every run. It also meant the shear transducers did not have the same alignment from experiment to experiment. Additionally, the crystals had a coaxial electrode arrangement that made the design of the backings unnecessarily complicated (i.e., alternating conductor and insulator). To address some of these issues, the crystals used in the original experiments were replaced with new ones made from the same material (PZT 5A) and with the same characteristics (1 MHz center frequency) but with simple plate electrodes. This made it possible to redesign and thereby simplify the crystal backing and holder.

The new design for the transducer package is shown in Figure 5.1. The backing is a solid, conductive tungsten-epoxy cylinder supplied by ValpeyFisher. It is bonded to the crystal with conductive epoxy. The crystal and backing are epoxied into a holder made of an insulating plastic. The holder is threaded so that it can be screwed into a piston end cap guaranteeing good contact with the internal face of the piston cap.

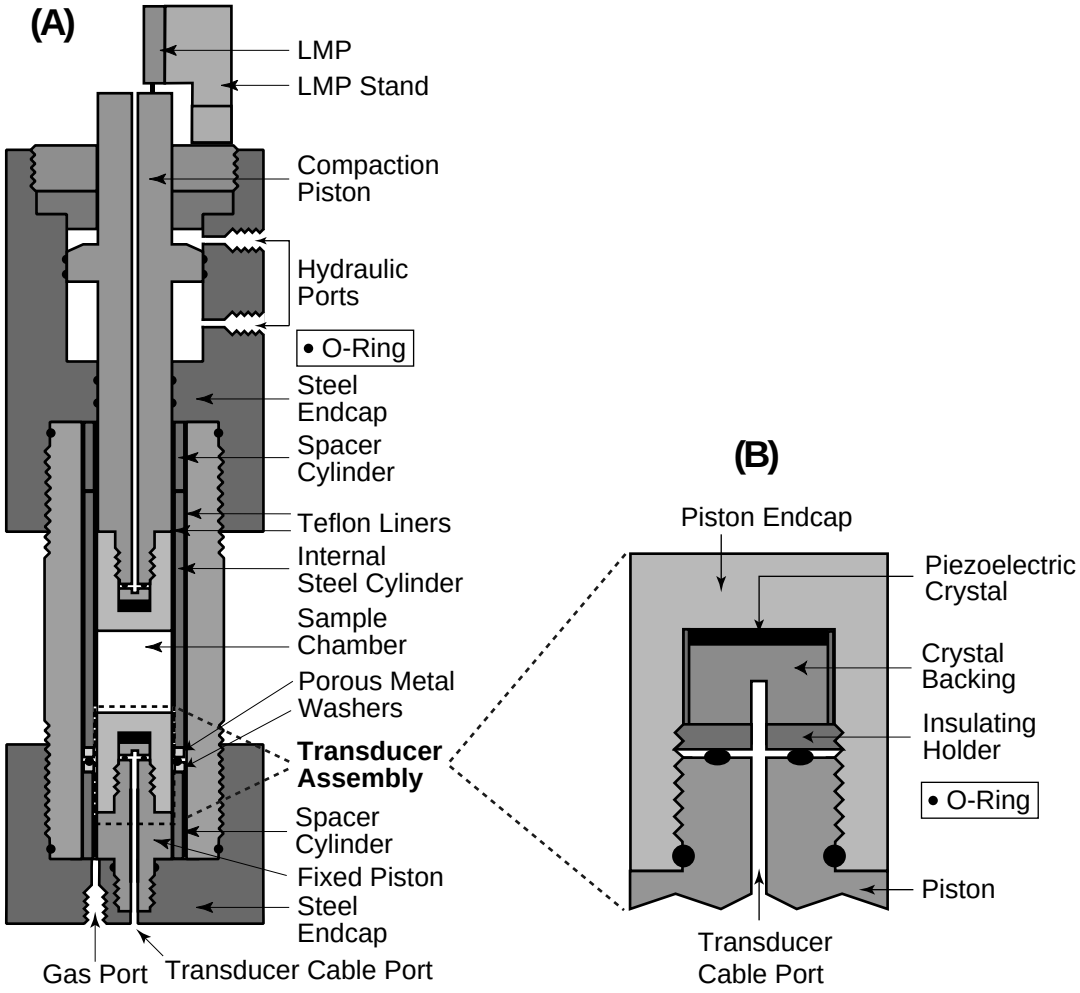

Figure 5.1: Methane hydrate synthesis and compaction vessel. (A) Schematic representation of the pressure vessel showing the hydraulic system, the sample chamber, the transducer locations and the linear motion potentiometer (LMP). For scale, the diameter of the sample chamber is one inch and the central cylinder is seven inches long. (B) Detailed schematic of the transducer contained in each piston endcap. For scale, the diameter of the piston cap is 1 inch.

Once the new crystal stack has been screwed into the piston endcap, it does not need to be removed between experiments. This reduces variability. It also improves the quality and repeatability of length measurements by making it possible to assemble the apparatus with the same alignment and relative spacing of parts every time (see below).

Improvements to the sample length measurement were made by replacing the linear motion potentiometer (LMP) and its stand. The LMP used in the original experiments (Chapter 4) had a travel of only 12.7 mm. It was replaced with a similar model with a 25.4 mm travel. Now it was no longer necessary to stop compacting in the middle of an experiment to rezero the LMP. The LMP stand was also completely redesigned. Instead of balancing on the micrometer head attached to the original stand, the new stand had a broad, solid base (see Figure 5.1). This improved its stability.

Since the micrometer head was removed from the stand, manual piston height measurements were made with a depth micrometer during the course of the experiments. These manual measurements were taken throughout the experiment and made it possible to determine an LMP voltage to piston height calibration valid for an entire experiment (see data processing section below). These manual measurements also gave a much better estimate of the uncertainty in the sample length measurements.

Improvements were also made to the temperature and pressure control systems and the electronics driving the transducers. A temperature controller designed around an Omega Model CN76000 Proportional with Integral and Derivative (PID) process controller was built by John Pinkston of the U. S. Geological Survey in Menlo Park, California. The temperature controller works by adjusting the voltage sent to the heater located beneath the temperature bath based on the temperature reading sent to the controller by an RTD located in the temperature bath. The temperature controller is able to maintain a constant, user selectable temperature to within $\pm 0.2^{\circ}$C from -20 to 20°C.

A precision rotary pressure generator was added to the hydraulic oil line. This pressure generator was used to manually maintain a constant piston pressure to within ± 15 psi. The pressure generator also gave very fine control over the compaction rate of the samples.

After the failure of three HP-214A square wave sources, the HP-214A was replaced with a Panametrics Model 5800 Spike Pulser-Receiver. The characteristics of the Panametrics source are significantly different from those of the HP-214A, but the waveforms

generated by the Panametrics source are still of excellent quality (see below).

Towards the end of the work described in this thesis, thermal conductivity experiments were conducted simultaneously with the wave speed experiments (DeMartin et al., 1999). The thermal conductivity experiments were performed in a separate pressure vessel containing a thermal probe which continually measured temperature in the sample using a thermistor. Both the wave speed and thermal conductivity pressure vessels were located in the same temperature bath and attached to the same gas line. As a result, the temperature measured within the thermal conductivity experiment was considered a proxy internal temperature measurement for the wave speed sample. This extra temperature information helped in monitoring the methane hydrate synthesis process and helped determine when the system had achieved thermal equilibrium at a given temperature.

5.3 Modifications to Data Processing

In addition to the changes in the apparatus and data acquisition systems described above, a number of improvements to the data processing steps were also made: the accuracy of the pressure transducer calibrations was improved; a very precise thermometer was used to calibrate the bath RTD; the accuracy of the sample length measurements was improved; and the capabilities of the program used to analyze the waveforms were significantly expanded.

5.3.1 Changes to Pressure, Temperature and Length Data Processing

During the course of the experiments it was noted that the reference voltage supplied by the constant voltage (5 V) power source to the pressure transducers and the LMP varied by $\pm 0.1\%$. These fluctuations could be seen directly in the voltages read from the pressure transducers and the LMP. To remove these artificial variations, the recorded pressure transducer and LMP voltages were multiplied by the ratio $\frac{5}{V_{out}}$ in post processing, where V_{out} was the actual voltage being output by the power source at the time the data were acquired. This successfully removed the signature of the power source variation from the data.

The calibrations of the oil and gas pressure transducers were also improved. A Heise dial pressure gauge with a resolution of 1 psi/div was used to calibrate the oil pressure transducer from 0 to 5,000 psi (0 to 15,000 psi piston pressure). The standard deviation

of the fit was 6 psi (18 psi piston pressure). A Heise digital pressure gauge with 0.1 psi resolution was used to calibrate the gas pressure transducer in the range relevant for the methane hydrate experiments, 300 to 4,200 pounds per square inch absolute (psia). The standard deviation of the fit was 3 psi. For ice experiments, the first recorded voltage was assumed to represent 14.695 psi and the lowest voltage obtained during evacuation of the apparatus was assumed to be 0 psi. A linear fit between those two points for each ice run was used to convert voltage to gas pressure. A more exact calibration was not needed because gas pressure during ice experiments was used only to monitor the integrity of the gas line seal.

While conducting experiments to test the temperature controller, it was discovered that the bath RTD and the temperature controller RTD were not reporting the same bath temperature. A calibrated Hart digital thermometer (resolution 0.001°C) was used in all subsequent experiments to calibrate the bath RTD and temperature controller outputs. The calibrations were determined by taking digital readings directly from the Hart thermometer (which has no analog or digital data output capabilities) after thermal equilibrium had been achieved at each temperature. Readings taken throughout an experiment were used to calculate the calibration. The standard deviations of the calibrations were generally less than 0.1°C. As mentioned above, the presence of the calibrated thermistor in the thermal conductivity experiments also helped monitor the temperature behavior of the system.

For the experiments described in Chapter 4, initial sample length was determined from the dimensions of the pressure vessel and sample length changes from how much the piston moved during an experiment. The accuracy of this method was limited by the precision with which the dimensions of several pieces of the pressure vessel could be measured and by the accuracy of the LMP output used to monitor the change in piston height. The method gave satisfactory results, but a more accurate method was desired.

As described above, an improvement in accuracy was obtained by redesigning the LMP stand to have a broader base. This improved stability made the LMP output less sensitive to miscellaneous physical disturbances (i.e., loud noises, vibrations, etc.) that occurred in the laboratory. This redesign necessitated the removal of the micrometer from the LMP stand. To compensate for this loss, manual measurements of the piston height were made throughout an experiment in order to calibrate the LMP output. This made it possible to

determine an LMP voltage to piston height calibration valid for an entire experiment. It also made it possible to estimate better the accuracy of the piston height measurements.

An additional improvement in accuracy was obtained by changing how the sample length was determined. Instead of measuring the dimensions of several pressure vessel components and then compounding the uncertainty in those measurements by adding them together, only two measurements were made. Those measurements were the depth from the top of the pressure vessel to the top of the translating piston when the pistons were head-to-head and the height of the piston above the top of the pressure vessel when a sample was between the pistons. The total sample length was then the sum of those two measurements. With this technique, there were only two measurements to make and they were both referenced to the same surface. Additionally, after the redesign of the transducer packages described above, the pressure vessel was always assembled with the same relative part spacing. Therefore, one set of head-to-head piston depth measurements was appropriate for all experiments. The uncertainty in the manual head-to-head depth and piston height measurements was approximately 0.04 mm. This method of measuring sample length should then have a cumulative uncertainty of ≤ 0.10 mm. This predicted level of accuracy was achieved in a test using an aluminum sample of known length.

Performing the head-to-head depth measurements required for this sample length measurement method revealed a systematic error present in previous determinations of sample length. The maximum force applied to the translating piston is sufficient to increase the head to head depth measurement by 0.3 mm, or nearly 1% of the total length of a fully compacted methane hydrate or ice sample. This change in head to head depth is due to a combination of elastic shortening in the piston and miscellaneous deformations of the apparatus due to the applied pressure. To account for this change with piston pressure and a much smaller change with temperature, a two dimensional planar regression of head-to-head depth versus piston pressure and temperature was performed for 187 measurements. The residuals of the resultant regression had a standard deviation of 0.01 mm, much less than the estimated uncertainty of the depth measurements themselves (~ 0.04 mm). This regression was applied during post processing of the data to determine the lengths to be added to the piston height measurements in order to determine sample lengths during an experiment.

5.3.2 Changes in Waveform Processing

Significant changes in waveform processing were also made. The waveform analysis program's capabilities were significantly increased. Instead of a simple routine that picked a single zero crossing, a new program was written which picked a user-chosen number of zero crossings and extrema (peaks and troughs) within the waveforms. The user chooses a starting point in a reference waveform and the program automatically picks the requested number of zero crossings and extrema. The user then chooses a data set, is given the option of removing any vertical offset in the data by removing the mean of the first N points, and then picks a starting point in the first waveform. The program automatically picks the requested number of zero crossings and extrema in all the waveforms within the data set. If a feature shifts by more than 0.1μs from one waveform to the next, the user is asked to confirm the picks, or choose a new starting point. The time delay of each waveform feature is calculated as the difference between arrival times for the same feature in the through-sample and head-to-head waveforms.

The program also estimates through-sample signal delay time using the full waveform techniques of cross correlation and phase spectral analysis (e.g., Sachse and Pao, 1978). Cross correlation can be used to estimate signal delay time by cross-correlating the head-to-head and through-sample waveforms. The time shift of the maximum in the correlation is taken to be the signal's time delay through the sample. Windowing the signals based on the times of the first and last picked zero crossings is done prior to performing the cross-correlation to improve the reliability of the result.

Phase spectral analysis (PSA) is a frequency-domain-based estimate of signal delay time. It estimates the delay of each frequency component in the signal by looking at the phase advance of each frequency component,

$$\Delta t(\omega) = \frac{\omega}{\phi(\omega) - \phi_0(\omega)}, \tag{5.1}$$

where $\Delta t(\omega)$ is the time delay at angular frequency ω, $\phi(\omega)$ is the phase spectrum of the through-sample waveform and $\phi_0(\omega)$ is the phase spectrum of the reference waveform. $\phi(\omega)$ is obtained by unwrapping the phase of the windowed, Fourier transformed, through-sample waveform. $\phi_0(\omega)$ is similarly obtained by unwrapping the phase of the windowed, Fourier transformed, reference waveform.

Equation 5.1 is valid for plane waves, but typical laboratory transducers do not produce plane waves. To account for this fact, a number of authors (e.g., Williams, 1951; Seki et al., 1956; Bass, 1958; Tang et al., 1990; Green and Wang, 1991) have derived phase correction factors (ϕ_c) that depend on properties such as sample length, wave speed and frequency. For simplicity and speed of calculation, the program uses Williams' (1951) acoustic correction as formulated for efficient computation by Khimunin (1972), which Tang et al. (1990) showed was an adequate approximation for the phase correction required by both compressional and shear waves. Calculation of the correction factor is computer intensive, requiring the calculation of many integrals during an optimization process. For this reason, only the phase delay associated with the frequency of maximum power in the through-sample waveform is calculated.

The program calculates wave speed from

$$V = \frac{l}{t - t_0} \tag{5.2}$$

where V is wave speed, $t - t_0$ is estimated signal delay time and l is sample length. The program determines the sample length associated with a waveform by interpolating the sample length obtained from the PTL data at the time the waveform was acquired.

The acquisition time of the waveform; the (interpolated) sample length; the signal maximum, minimum and frequency of maximum power; and the waveform feature arrival times, signal delays and wave speed estimates are saved by the program in an ASCII output file. This file can be imported into any data analysis or plotting software package. The above data, along with the original waveforms and the user's choices for parameters are also saved in a Matlab workspace file, in case the user should want to reconstruct the processing flow at a later date. This program makes it possible to quickly analyze the several thousand waveforms acquired during each experiment.

The program was used to analyze the arrival times of the zero crossings (zeros), peaks and troughs in the head-to-head reference waveforms acquired during the head-to-head piston depth measurements mentioned above. From this analysis, it became clear that the shape and arrival times of the reference waveforms changed measurably with temperature and piston pressure. Fourier analysis showed that the shape changes were due to the relative power in the harmonics generated by the transducers. The arrival time changes were

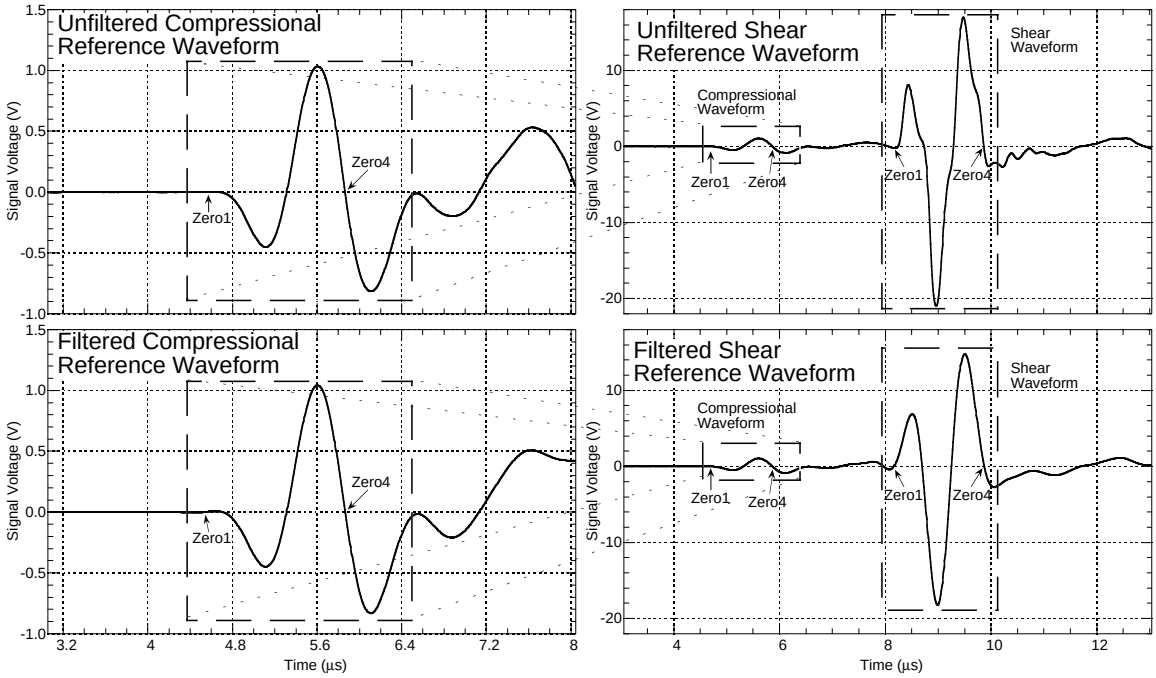

Figure 5.2: Effect of filtering on reference compressional and shear waveforms. The first column is the unfiltered (top) and filtered (bottom) compressional wave precursor to the shear waveform produced and received by the shear transducers when the compaction pistons are in contact. The time scale for both plots in column one is the same. The second column is the unfiltered (top) and filtered (bottom) shear waveform produced and received by the shear transducers when the compaction pistons are in contact. Both the top and the bottom plots have the same time scale. The precursor compressional wave signal is also shown in the shear wave data. In each plot, the location of the first and last zero crossing used to define the waveform arrival are distinguished with arrows. The compressional waveform shown in the first column was recorded 13 seconds after the shear waveform shown in column two was recorded.

presumed to be caused by changes in the elastic properties of the steel piston caps which housed the transducers. (One inch of steel separates the two piezoelectric crystals when the pistons are in contact.) Analysis of waveforms acquired during methane hydrate and ice experiments showed that significant waveform shape changes also occurred during compaction. Fourier analysis showed that this was due to changes in the attenuation of higher frequencies in the signals transmitted through the sample.

To reduce the variability in shape between head-to-head and through-sample waveforms, a low pass, zero phase, IIR Butterworth digital filter (shoulder frequency 1.5 MHz) was applied to the waveform data to remove the harmonics. The filter was applied to both the head-to-head and through-sample waveforms. Examples of head-to-head reference and through-sample waveforms before and after filtering are given in Figures 5.2 and 5.3.

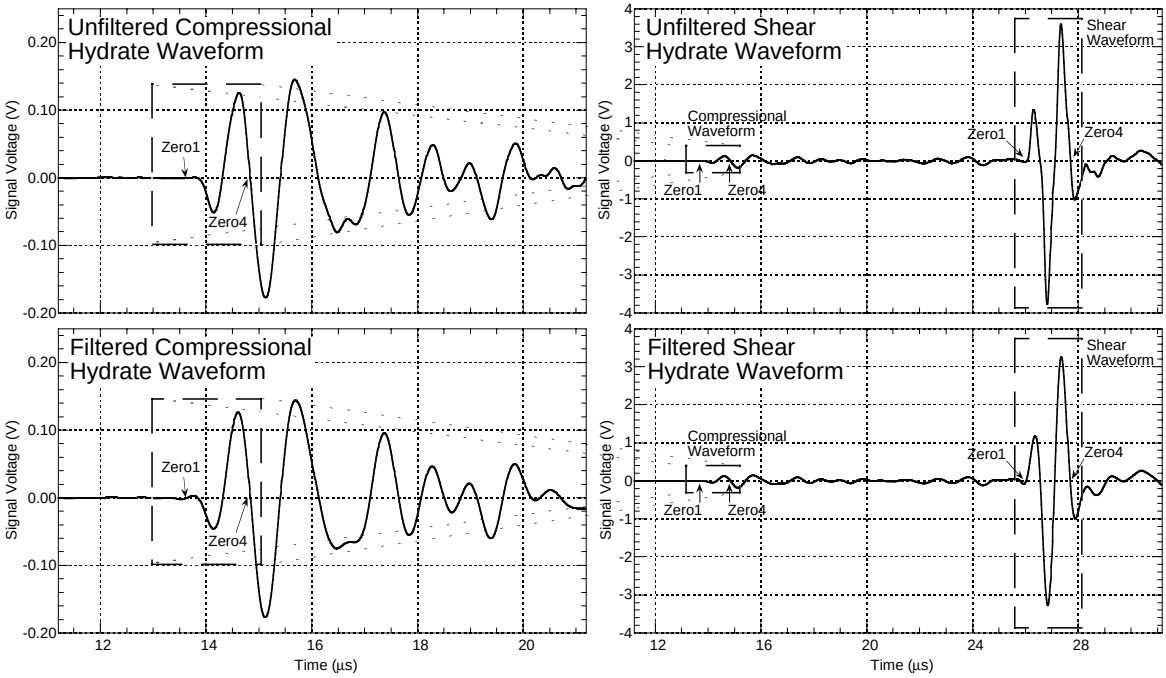

Figure 5.3: Effect of filtering on through-sample compressional and shear waveforms. The first column is the unfiltered (top) and filtered (bottom) compressional wave precursor produced by the shear transducers and transmitted through a compacted methane hydrate sample. The time scale for both plots in column one is the same. The second column is the unfiltered (top) and filtered (bottom) shear waveform produced by the shear transducers and transmitted through a compacted methane hydrate sample. Both the top and bottom plots have the same time scale. The precursor compressional wave signal is also shown in the shear wave data. In each plot, the location of the first and last zero crossing used to define the waveform arrival are distinguished with arrows. The compressional waveform shown in the first column was recorded 13 seconds after the shear waveform shown in the second column was recorded.

Figures 5.2 and 5.3 illustrate the significant effect the harmonics had on the shape of the shear waveforms. Removing them makes comparisons between the head-to-head and through-sample waveforms simpler and more reliable. Figures 5.2 and 5.3 also show that the effect of filtering was much less dramatic on compressional waveforms. This was because the relative contribution of the harmonics to the compressional waveforms was not as significant. Filters were applied to the compressional wave data mainly for consistency in processing and to reduce the high frequency noise in the raw data. Later, it was realized that the filters did in fact have a significant impact on the characteristics of the compressional waveforms, namely in their first motions. Because of the scale, this is hard to recognize in

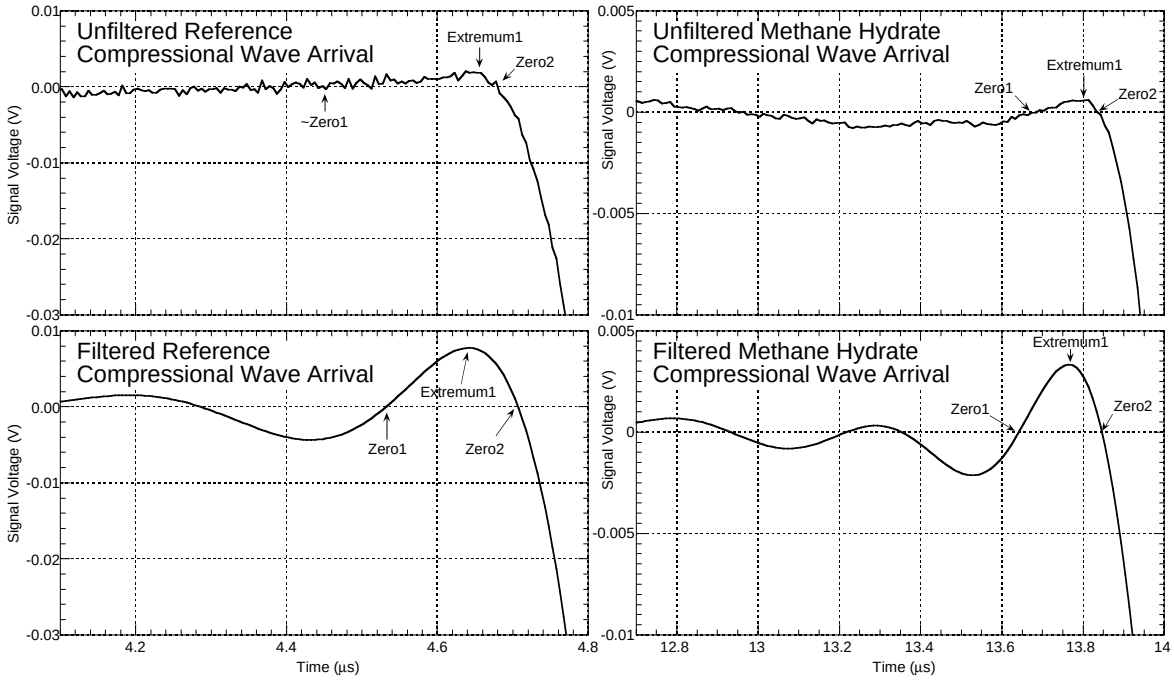

Figure 5.4: Effect of filtering on first motions of the reference and through-sample compressional waveforms. First column is the unfiltered (top) and filtered (bottom) first motions of the compressional waveforms shown in the first column of Figure 5.2. The time scale on both plots is the same. Second column is the unfiltered (top) and filtered (bottom) first motions of the compressional waveforms shown in the first column of Figure 5.3. The time scale on both plots is the same. In each plot, the location of the first two zero crossings and the first extremum (a peak) are distinguished by arrows. This figure reveals the enhancement of oscillations occurring in the first motions of the compressional waveforms when the high frequencies are removed by the filter. The advantage in the filtered waveforms is that automatic picking of the arrival times is more robust. For this and other reasons discussed in the text, the filtered waveforms are used to determine compressional wave arrival times.

Figures 5.2 and 5.3. Figure 5.4 reproduces the unfiltered and filtered compressional waveforms from Figures 5.2 and 5.3 but focuses on the region around the first break associated with each waveform. From Figure 5.4 it is clear that the filter produces a ripple artifact in the first motion of the filtered compressional waveforms. This is caused by the removal of high frequencies from the waveform by the Butterworth filter.

The artificially enhanced nature of the early waveform features in the filtered compressional waveforms called into question the validity of using those features to determine wave speeds. To address this question, a detailed comparison was made between initial peak/first motion features in unfiltered and filtered reference and through-sample compressional waveforms (see Appendix A following this chapter). The initial peak/first

motion feature in the unfiltered waveforms had to be picked manually because variations in the background noise and waveform shape prevented automatic picking from being reliable. Uncertainty in the manually determined feature arrival times ranged from ± 0.01 to ± 0.10 μs, depending on the character and amplitude of the background noise and the shape of the initial waveform motion in each individual waveform. By contrast, the time location of the corresponding initial peak feature in the filtered waveforms could be reliably, automatically picked to within one half the time sampling of the waveform (generally less than 0.02 μs). Comparisons between the unfiltered and filtered compressional waveform results showed that the initial peak in the filtered data arrived on average 0.02 μs earlier than the corresponding peak/first motion feature in the unfiltered data. This difference was the same for both the reference and through-sample waveforms and was often less than the uncertainty associated with the arrival time of the same feature in the unfiltered data. Advantages to using the program to automatically pick the filtered waveforms' peak arrival times are that it is much faster and it removes subjectivity from the picking process. For these reasons, results from the early features in the filtered waveforms were considered a valid proxy for the early features in the unfiltered waveforms and both compressional and shear waves were filtered before being analyzed for the experiments described in this chapter.

To account for the variability of the head-to-head waveform feature arrival times with temperature and pressure, the waveform analysis program was used to analyze the full database of filtered head-to-head waveforms. Two-dimensional planar regressions of filtered waveform feature arrival times versus temperature and piston pressure were fit to the first four zero crossings and the first three extrema in the over 900 reference waveforms in the database. The regressions and the standard deviations of the residuals are collected in Tables 5.1 and 5.2. The temperature and pressure dependent reference waveform feature arrival times determined from the regressions were combined with the time referenced PTL data and the acquisition times of the waveforms to calculate the pressure and temperature based corrections to the signal delay times output by the waveform analysis program. These corrected delay times were used to calculate pressure- and temperature-corrected wave speeds. All the results described below have had these pressure and temperature based corrections applied to them.

Table 5.1: Regressions of Reference Compressional Waveform Feature Arrival Times with Temperature and Piston Pressure

Waveform Feature	$F(T,P) = a \cdot T + b \cdot P + c$ Compressional Waveform a (μs/°C)	b (μs/psi)	c (μs)	std (μs)†
Zero 1	$(0.97 \pm 0.06) \times 10^{-3}$	$-(1.92 \pm 0.16) \times 10^{-6}$	4.566 ± 0.002	0.022
Extremum 1	$(1.13 \pm 0.04) \times 10^{-3}$	$-(2.94 \pm 0.11) \times 10^{-6}$	4.692 ± 0.001	0.016
Zero 2	$(1.15 \pm 0.04) \times 10^{-3}$	$-(3.24 \pm 0.12) \times 10^{-6}$	4.762 ± 0.001	0.017
Extremum 2	$(1.56 \pm 0.05) \times 10^{-3}$	$-(3.35 \pm 0.14) \times 10^{-6}$	5.174 ± 0.001	0.019
Zero 3	$(1.56 \pm 0.05) \times 10^{-3}$	$-(3.52 \pm 0.13) \times 10^{-6}$	5.377 ± 0.001	0.019
Extremum 3	$(1.74 \pm 0.05) \times 10^{-3}$	$-(3.02 \pm 0.15) \times 10^{-6}$	5.662 ± 0.002	0.021
Zero 4	$(1.63 \pm 0.06) \times 10^{-3}$	$-(2.54 \pm 0.18) \times 10^{-6}$	5.915 ± 0.002	0.025

† Standard deviation of the residuals to the fit equation $F(T,P) = a \cdot T + b \cdot P + c$.

Table 5.2: Regressions of Reference Shear Waveform Feature Arrival Times with Temperature and Piston Pressure

Waveform Feature	$F(T,P) = a \cdot T + b \cdot P + c$ Shear Waveform a (μs/°C)	b (μs/psi)	c (μs)	std (μs)†
Zero 1	$(2.39 \pm 0.07) \times 10^{-3}$	$(-1.32 \pm 0.24) \times 10^{-6}$	8.204 ± 0.003	0.025
Extremum 1	$(3.06 \pm 0.06) \times 10^{-3}$	$(-5.12 \pm 0.16) \times 10^{-6}$	8.608 ± 0.002	0.022
Zero 2	$(3.11 \pm 0.06) \times 10^{-3}$	$(-5.88 \pm 0.18) \times 10^{-6}$	8.809 ± 0.002	0.026
Extremum 2	$(3.62 \pm 0.08) \times 10^{-3}$	$(-7.31 \pm 0.22) \times 10^{-6}$	9.122 ± 0.002	0.030
Zero 3	$(3.80 \pm 0.09) \times 10^{-3}$	$(-8.77 \pm 0.26) \times 10^{-6}$	9.408 ± 0.001	0.037
Extremum 3	$(4.26 \pm 0.10) \times 10^{-3}$	$(-9.63 \pm 0.28) \times 10^{-6}$	9.674 ± 0.003	0.040
Zero 4	$(3.60 \pm 0.06) \times 10^{-3}$	$(-9.34 \pm 0.43) \times 10^{-6}$	10.035 ± 0.005	0.060

† Standard deviation of the residuals to the fit equation $F(T,P) = a \cdot T + b \cdot P + c$.

The discovery that the signals varied significantly with temperature and pressure meant that full waveform-based signal delay estimates could not be used to determine wave speeds in the experiments described in this chapter. The full waveform methods require a single reference waveform. In the temperature and pressure ranges used in the experiments described below, no single reference waveform was appropriate. Unlike the simple 2-D regressions used for the head-to-head waveform feature arrival times, no simple correction is appropriate for techniques which depend on an entire waveform to estimate wave speed.

Uncertainty in the wave speeds determined from the waveform features described above can be calculated from the generalized propagation of uncertainty formula given in Chapter 2 (Equation 2.66). The relative wave speed uncertainty ($\Delta V/V$) incurred by using Equation 5.2 due to uncertainties in the measured values of sample length (l), through-sample waveform feature arrival time (t) and head-to-head waveform feature arrival time (t_0) is:

$$\frac{\Delta V}{V} = \sqrt{\left(\frac{\Delta l}{l}\right)^2 + \frac{\Delta t^2 + \Delta t_0^2}{(t - t_0)^2}}, \tag{5.3}$$

where Δl, Δt and Δt_0 are the uncertainties in sample length, waveform feature arrival time and reference waveform feature arrival time, respectively. Except where noted specifically below, uncertainties in the sample length and waveform feature arrival times are 0.10 mm and one half the time sampling period of the waveform, respectively. Uncertainties in the reference waveform feature arrival times are taken to be the standard deviations of the residuals from the waveform feature arrival time regressions to temperature and piston pressure (Tables 5.1 and 5.2).

Equation 5.3 represents an estimate of the precision with which wave speeds are determined. Absolute accuracy of the measurements is much harder to quantify. It is typically assumed that laboratory measurements on non-dispersive samples can attain accuracies better than 1% (Bourbié et al., 1987). Tests on an aluminum sample suggest absolute errors due to any unidentified systematic errors should be less than 1.5% for compressional and shear wave speeds determined from through-sample and head-to-head waveforms having the same frequency content.

5.4 Ice Experiment

Ice and methane hydrate experiments were being conducted while changes to the apparatus and data processing capabilities were being implemented. Once the impact of those changes was understood, an ice experiment was conducted to test the system and try out a new procedure before conducting a methane hydrate experiment. In this section, I describe the procedure used and the results obtained from that experiment performed on a polycrystalline ice sample in the temperature range -20 to -5°C.

5.4.1 Procedure

The initial steps of the procedure were similar to those of the shear transducer ice experiment described in Chapter 4. The pressure vessel was partially assembled in a freezer with the shear transducers loaded into the pistons. After the pressure vessel had cooled to freezer temperature, the sample chamber was loaded with 14 grams of granulated, sieved ice. The fixed piston endcap was then screwed on such that the transducer polarity markers were aligned and separated by the correct distance. The assembled pressure vessel was transported to the freezer where the experiment would take place and suspended in the temperature bath by attaching the high pressure gas and hydraulic oil lines. Once the LMP had been attached to the translating piston, pressure-temperature-length (PTL) data logging began. Next, the initial height of the piston above the top of the pressure vessel was measured with a depth micrometer. Once the initial height of the piston was measured, the temperature controller was programmed to increase the bath temperature to -5°C. While the bath temperature was increasing from -25 to -5°C, two waveforms were acquired, one at -24°C and one at -15°C.

Once the system temperature had stabilized at -5°C, two more waveforms were acquired and then the system was evacuated. Ten minutes after the system evacuation was completed, two waveforms were acquired ten minutes apart. Approximately 20 minutes after the second waveform was acquired, a third waveform was acquired and the compaction of the sample began by using the pressure generator to increase the hydraulic oil pressure. When the LMP registered piston motion, the oil pressure was allowed to relax, a manual micrometer measurement of the piston height was made and the automatic waveform

acquisition interval was set to one minute.

The waveform acquisition cycle takes approximately 20 seconds to execute. After the waveforms were acquired, the hydraulic oil pressure was slowly increased for 30 seconds using the manual pressure generator. The oil pressure was then allowed to relax as the sample compacted and the hydraulic oil cooled for the 10 seconds prior to the next waveform acquisition cycle and during the acquisition cycle itself. This pattern was repeated every 60 seconds until the sample length reached 38.5 mm. At that point, active compaction was stopped for 30 minutes, but waveform acquisition continued. Active compaction was stopped in order to make a manual piston height measurement and to again record the "cementation" effect on wave speed mentioned in Chapter 4 and presented again below. After the 30 minute pause, compaction resumed on the 60 second cycle described above.

Compaction continued until the piston pressure reached 6,250 psi. At that point, piston pressure was allowed to relax freely and decreased from 6,250 to 5,200 psi in 30 minutes. 6,000 psi was chosen because results from previous experiments suggested ice was extruded from between the pistons at higher pressures. The piston pressure was left to vary freely overnight and it decreased to 4,000 psi over 16 hours as the sample shortened from 29.50 to 29.32 mm.

The next morning, piston pressure was increased to 6,000 psi and held at that value for 10 minutes, then decreased to 4,750 psi. At that point, temperature cycling began. The bath temperature was reduced from -5°C to -10°C and then to -20°C. It was then increased in 5°C steps from -20° to -5°C. This cycle from -5°C to -20° and back to -5°C was repeated to check the repeatability of the wave speed results at each temperature. The temperature history of the experiment is shown in Figure 5.5.

At each temperature, once thermal equilibrium had been achieved, the piston pressure was adjusted to 4,750 psi and held there for a period of time that varied from temperature to temperature (see Figure 5.6). At each temperature, the piston pressure was cycled from 4,750 to 3,250 and back to 4,750 psi over the course of approximately 30 minutes. Piston height was measured manually at least once and as many as three times at each temperature. The length of the sample as a function of time is shown in Figure 5.7.

After the second temperature cycle had been completed, waveform acquisition was

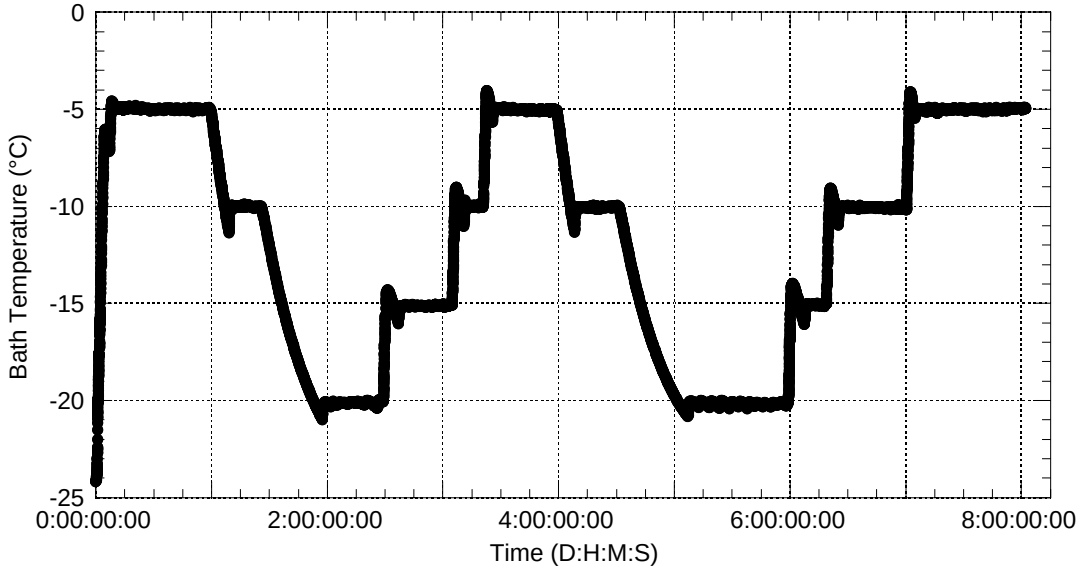

Figure 5.5: Bath temperature versus experiment time for the polycrystalline ice Ih experiment. Horizontal axis is time in days:hours:minutes:seconds. The plot shows the warming of the sample to -5°C prior to compaction and the two temperature cycles from -5 to -20 and back to -5°C. At each temperature there is some overshoot and/or undershoot before settling into the target temperature. Once the temperature has been achieved, the temperature is stable to within ± 0.2°C.

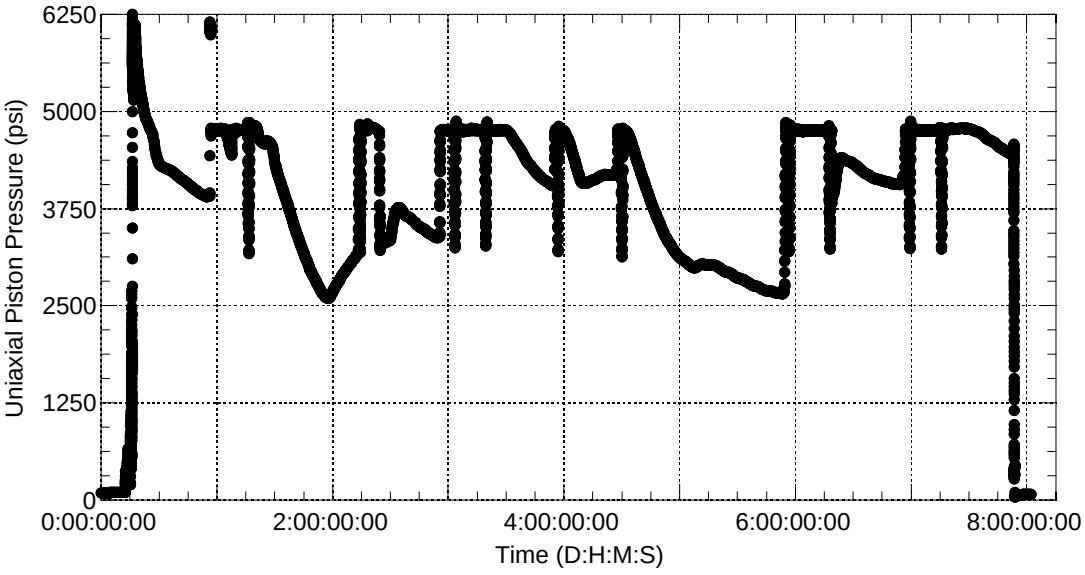

Figure 5.6: Piston pressure versus experiment time for the polycrystalline ice Ih experiment. Horizontal axis is time in days:hours:minutes:seconds. The plot shows the compaction of the sample, the cycling of pressure at each temperature and the depressurization of the sample at the end of the experiment. During temperature changes (see Figure 5.5), the oil pressure varied freely. Once the temperature was stable, the piston pressure was adjusted to 4750 psi, held constant for a period of time that varied from temperature to temperature and then cycled from 4750 to 3250 and back to 4750 psi (see text).

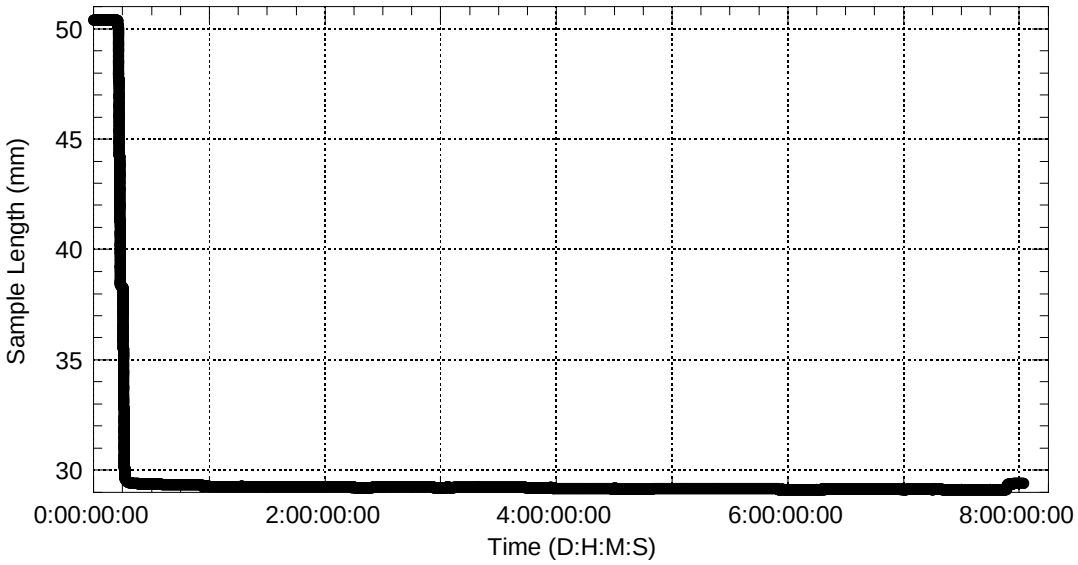

Figure 5.7: Sample length versus experiment time for the polycrystalline ice Ih experiment. Horizontal axis is time in days:hours:minutes:seconds. Because of the amount of shortening that occurred during compaction, small changes in sample length during the temperature and pressure cycling portions of the experiment are not apparent. These much smaller length changes can be seen in Figure 5.17.

stopped and the piston pressure was reduced to zero in anticipation of removing the pressure vessel from the system for sample extraction. However, upon reducing the piston pressure to zero, it was observed that a very strong signal was still being transmitted through the sample. At that point, waveform acquisition was reinitiated and the system was left undisturbed for three hours. At the end of three hours, waveform acquisition was terminated and the piston was fully retracted to its pre-compaction position. PTL data acquisition was terminated and the pressure vessel was removed from the temperature bath and placed in the sample preparation freezer.

The pressure vessel was disassembled in the sample preparation freezer and the teflon jacketed sample was extracted intact from the steel cylinder. A photograph of the jacketed, transparent, compacted polycrystalline ice sample is shown in Figure 5.8. After completion of the experiment, the sample was placed in a plastic bag (to reduce sublimation) and stored in a freezer, to be available for any future analysis.

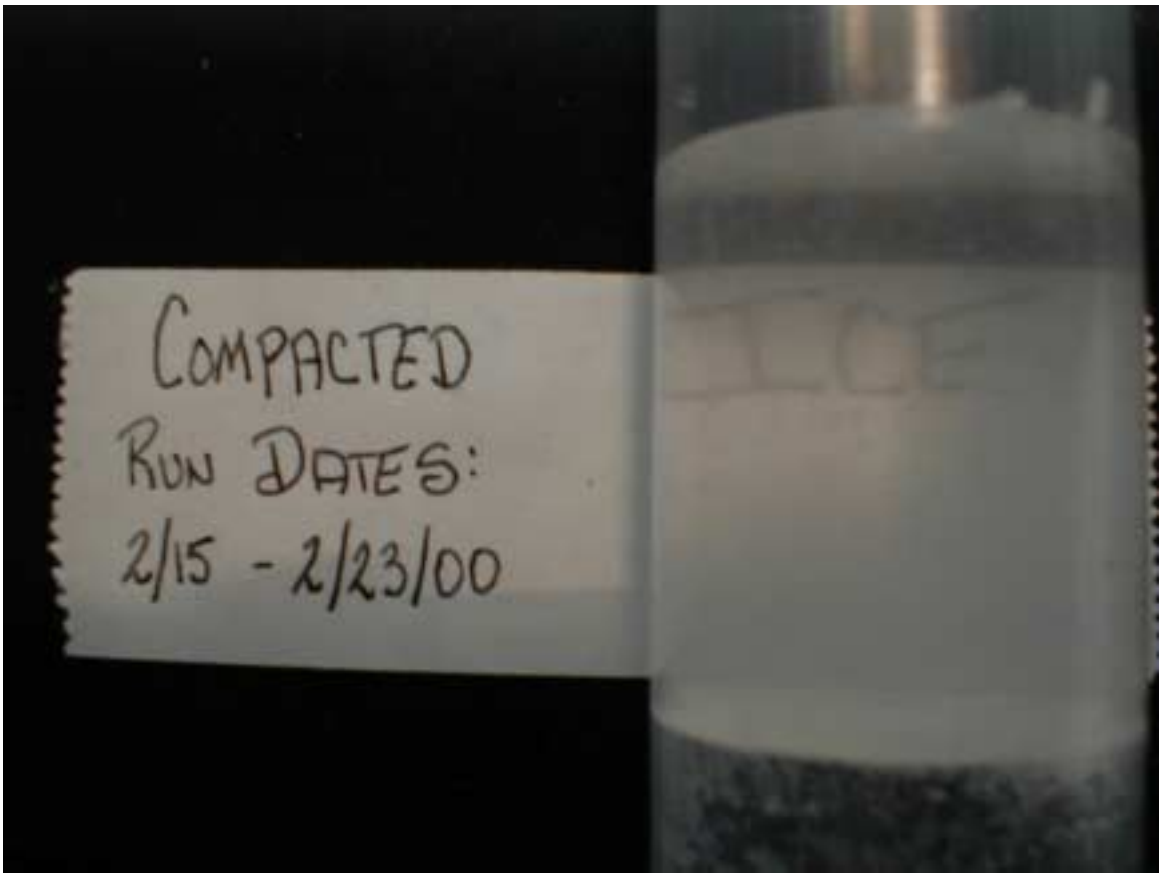

Figure 5.8: Picture of the compacted polycrystalline ice Ih sample. This picture was taken in a freezer shortly after the sample was removed intact from the pressure vessel. The sample is shown in the teflon jacket in which it was compacted. The high degree of optical transparency suggests that very little air was trapped in the sample during compaction. No cracks were visible in the sample upon its removal from the pressure vessel.

5.4.2 Data Processing

The pressure-temperature-length (PTL) data were processed as described above. The signature of the power source voltage variations was removed from the raw voltages output by the pressure transducers and the LMP. The oil and gas pressure transducer voltages were then converted to piston pressure and gas pressure, respectively, using the appropriate calibrations. The manual piston height measurements were plotted as a function of corrected LMP output and a linear fit was applied to the data. The standard deviation of the fit was 0.03 mm. This calibration was used to convert corrected LMP voltages to piston heights and the piston heights were used to calculate sample lengths as described above.

The processing flow for the compressional and shear waveform data was as described above. Waveforms were filtered to remove contributions from the harmonics generated by the transducers (frequencies greater than 1.5 MHz). The mean of the first 100 points in each waveform was subtracted, removing any DC offset. The picking routine was run and the resultant ASCII data files containing waveform data were imported into a data analysis software package. The system's gas pressure, piston pressure and bath temperature at each waveform time were determined by linearly interpolating each property as a function of time from the PTL data set. The piston pressure and bath temperature data appropriate for each waveform were used to calculate the pressure and temperature dependent reference waveform feature arrival times for each feature identified by the picking routine. The resultant pressure- and temperature-corrected delay times for waveform features were used to calculate compressional and shear wave speeds for all the picked waveform features for all the acquired waveforms.

Wave speeds determined from the automatically picked first zero crossings in the compressional and shear waveforms were contaminated by precursor noise and did not give reliable results. Later waveform features showed a systematic bias in calculated wave speed. The bias was a systematic increase or decrease in calculated wave speed as one progressed from earlier to later features of the waveform. This bias was caused by the relative frequency content of the through-sample and head-to-head waveforms. If the frequency distribution of the through-sample waveforms was centered higher than in the head-to-head waveforms, the through-sample waveforms were more compressed in time (i.e., had a shorter fundamental period) and later waveform features arrived relatively earlier than in the reference waveforms, biasing the estimated wave speed toward higher values and vice versa. Therefore, even though later waveform features had the greatest signal to noise ratio and could be located extremely accurately in time, they also carried a systematic error, and for that reason were unsuitable for determining wave speeds.

From this analysis, it was clear the earliest distinct waveform feature was the most appropriate for determining wave speed. For the majority of the experiment for both compressional and shear waveforms, that feature was the first extremum (a peak). There was one exception to this conclusion. The amplitude of the first peak in the compressional

waveforms was small and at the beginning of compaction, the compressional wave amplitude was not large enough for the first extremum to be reliably distinguished from the noise. As a result, until the sample was nearly completely compacted, compressional wave speed was determined from the arrival time of the second extremum, a trough. This feature was chosen over the second zero crossing because the second zero crossing was also subject to a high degree of uncertainty. Using the second extremum increased the error in the determined compressional wave speed, biasing it towards lower values because of the relatively low frequency content in the transmitted compressional waveform, but the wave speeds determined from the second extremum agreed well with estimates determined from the first extremum in the cases where the compressional wave speeds determined from the first extremum were not obviously contaminated by noise. I estimate the resultant error in the stated compressional wave speed during compaction was not more than 5%, and probably less than 3%. See below for a more detailed discussion of this source of systematic error.

5.4.3 Results and Discussion

The ice experiment produced a large volume of data. The properties of interest (i.e., piston pressure, temperature, wave speed, etc.) varied significantly throughout the course of the experiment. The large range of values in the data masks the fine details present. Therefore, in discussing the results, I break the experiment into four stages: setup, compaction, temperature cycling and sample depressurization. This allows for presentation of the fine detail in the data.

Setup

The first stage, setup, does not contain a large number of waveform measurements; it does, however, illustrate the impact of temperature and grain-to-grain bonding on the shear wave speed of the porous, granular ice sample. Figure 5.9 shows the bath temperature, gas pressure, sample length and shear wave speed as a function of experiment time, from 0 to 5 hours into the experiment. The lines connecting the wave speed data are explained below.

During the setup portion of the experiment, the only changes applied to the system

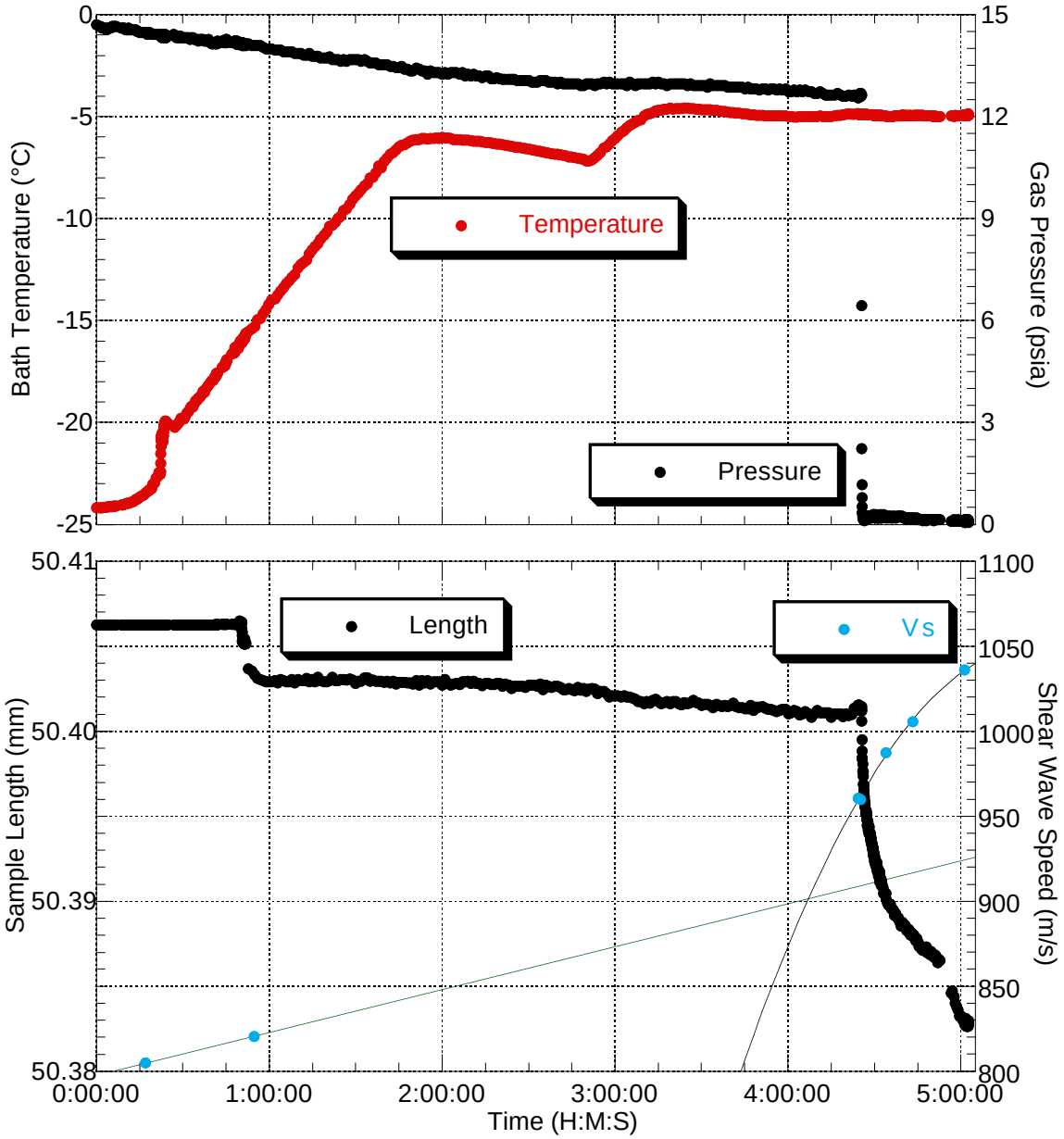

Figure 5.9: Bath temperature, gas pressure, sample length and shear wave speed data from the setup portion of the polycrystalline ice Ih experiment. Both plots have the same horizontal axis, time in hours:minutes:seconds. **Top:** Bath temperature and gas pressure versus experiment time. This plot shows the bath temperature warming to -5°C and the pressure vessel being evacuated once -5°C had been reached. **Bottom:** Sample length and shear wave speed versus time. The sample length changed slightly ($< 0.1\%$) during this portion of the experiment, but the shear wave speed increased significantly ($\sim 30\%$). This reflects a change in the elastic properties of the sample. The lines in the plot show the different trends in the shear wave speed with time while the sample was warming from -25 to -5°C and after the temperature had stabilized at -5°C. Note that the third shear wave speed point was obtained prior to the evacuation of the sample and the subsequent small decrease in sample length. The variation of shear wave speed with time can be explained by the competing effects of sample softening due to warming and grain to grain cementation (see text).

were a temperature increase from -25 to -5°C and the evacuation of the system once the temperature had stabilized at -5°C (at 4:25:30). The oil pressure (not shown) remained at ambient and the recorded sample length varied by less than 0.03 mm. During this portion of the experiment, only a weak signal was transmitted through the sample. It was strong enough to identify the shear wave arrival, but not strong enough to unambiguously detect the compressional wave arrival over the noise. Because the signal was weak, only seven waveforms were recorded during the setup period: two as the bath warmed from -25 to -5°C (at -24 and -15°C, respectively); two after the temperature had stabilized at -5°C and immediately before the apparatus was evacuated; two at 10 minute intervals after the evacuation was completed; and the seventh waveform at 5:01:25, just before compaction began.

The wave speed results are plotted in Figure 5.9. They show that the observed shear wave speed increased relatively slowly while the temperature increased from -25 to -5°C (signified by the straight line connecting the first two shear wave speed data points in Figure 5.9) and increased much more quickly after the temperature had stabilized at -5°C (signified by the second degree polynomial connecting the final five shear wave speed data points). As shown in Figure 5.9, the distance between the transducers changed by less than 0.03 mm ($< 0.01\%$) during this portion of the experiment, but the shear wave speed increased by approximately 30%. Therefore, the observed change in shear wave speed was almost exclusively a function of changes in waveform arrival time, reflecting a change in the elastic properties of the sample with time.

The uncertainty in the determined velocities as calculated from Equation 5.3 (using $\Delta t = 0.1\mu s$) is only ± 3 m/s. The uncertainty is particularly small because the estimates for Δl, Δt and Δt_0 are small compared to the sample lengths and signal delay times which are at their maximum values for the experiment. The uncertainty of ± 3 m/s does not reflect any potential systematic error due to the significantly different frequency contents of the head-to-head and through-sample waveforms.

The relative variation of shear wave speed with time can be explained by the competing effects of heating the sample and forming grain to grain bonds. Heating the sample softens the individual ice grains, reducing the wave speed. Forming grain to grain bonds stiffens the granular composite, increasing shear wave speed. When the temperature stabilized at

$-5°$C, the competing effect of heating the grains was gone and the unopposed stiffening effect of forming and growing grain to grain bonds caused the wave speed to increase more rapidly per unit time. The effects of grain to grain bond formation on elastic properties is discussed further below and in detail in Chapter 6.

Compaction

Bath temperature, piston pressure, sample length, compressional wave speed and shear wave speed are plotted versus time for the compaction stage of the experiment in Figure 5.10. These data show that once compaction began (still at $-5°$C), wave speeds increased slowly at first, but then more rapidly as compaction progressed. In the middle of this stage, during the pause in compaction, while sample length was essentially constant, wave speed continued to increase slowly. When compaction resumed, there was a slight delay before wave speeds again began to increase significantly. Finally, as the sample reached a length of 30 mm, wave speeds stopped changing with sample length. As I show below, these observations can be qualitatively explained by the formation and breaking of grain to grain bonds, the effects of porosity reduction through compaction and the deformation and/or extrusion of low porosity material.

The relative uncertainties (Equation 5.3) in the wave speeds given in Figure 5.10 are 0.4 to 0.7% for the compressional waves and 0.3 to 0.5% for shear waves. These uncertainties do not include any systematic errors that may arise from determining the waveform arrival times due to the significant difference in frequency content between the head-to-head and through-sample waveforms at large sample lengths (see Figure 5.11). As discussed above, this systematic error arises from the difference in fundamental periods ($T = \frac{1}{f}$) between the head-to-head and through-sample waveforms. The approximate magnitude of the error can be estimated by looking at the difference in arrival times for the first extremum (or second extremum for compressional waves at long sample lengths) for pure sinusoids possessing the same fundamental periods as the head-to-head and through-sample waveforms. This difference is the approximate error incurred by comparing waveform features between signals with different central frequencies (i.e., fundamental periods). Performing this exercise for the data given in Figures 5.10 and 5.11 suggests that this error should be less than 5% for compressional wave speeds and less than 1% for shear wave speeds. The larger effect

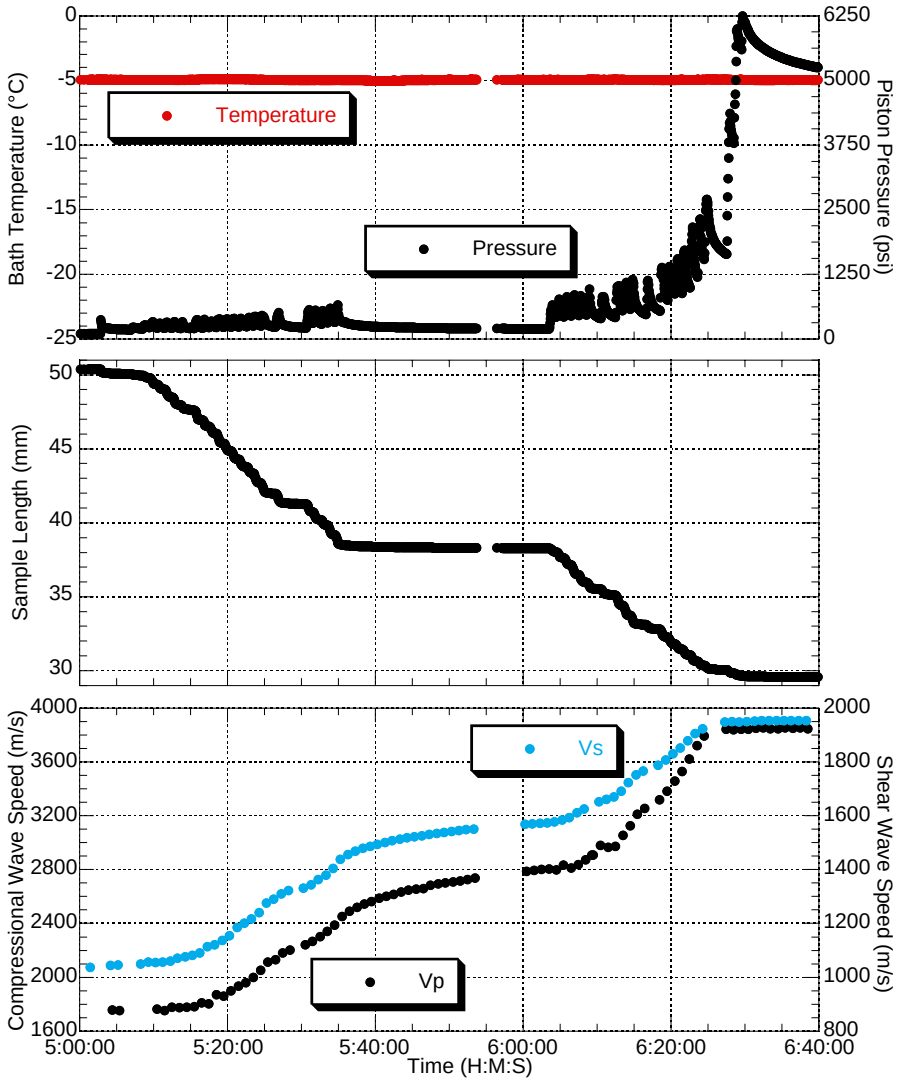

Figure 5.10: Bath temperature, piston pressure, sample length, compressional and shear wave speed data from the compaction portion of the polycrystalline ice Ih experiment. All three plots have the same horizontal axis, time in hours:minutes:seconds. **Top:** Bath temperature and piston pressure versus time. The bath temperature was constant at $-5°$C. The piston pressure was increased in the manner described in the text for 30 minutes, allowed to vary freely for 30 minutes and then increased to 6,250 psi over the course of 30 minutes. After reaching 6,250 psi, the piston pressure was allowed to vary freely. **Middle:** Sample length vs time. As the piston pressure was increased for the first 30 minutes, the sample length shortened from ~ 50 to ~ 38 mm. When active increase of the piston pressure stopped, the sample length remained essentially constant. When piston pressure increases resumed, the sample resumed shortening, eventually reaching a length of ~ 29.5 mm. Note that the piston pressure did not increase significantly until the sample was ~ 32 to 30 mm long. Up until that point, applied piston pressure was easily converted into porosity reduction. **Bottom:** Compressional and shear wave speeds versus time. Relative uncertainties in the compressional and shear wave speeds vary from 0.4 to 0.7% and 0.3 to 0.5%, respectively. Compressional and shear wave speeds do not increase immediately at the start of compaction, they do increase during the pause in active compaction when the sample length does not change and the maximum wave speeds are achieved as the sample reaches its minimum length. This behavior is explained by the interaction of porosity reduction through compaction with the forming (and breaking) of grain to grain bonds (see text).

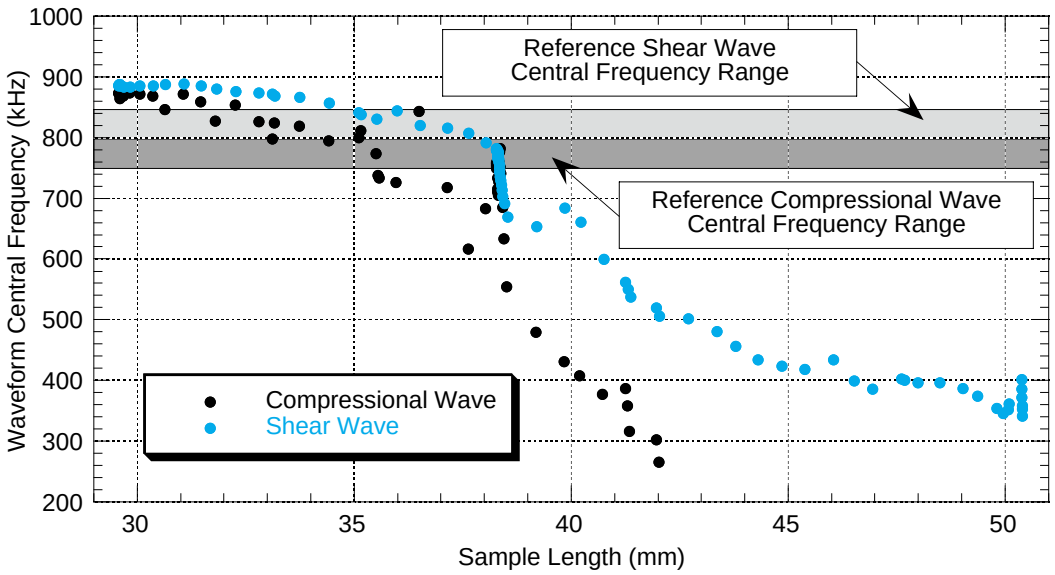

Figure 5.11: Compressional and shear waveform central frequency versus sample length for the compaction portion of the polycrystalline ice Ih experiment. The data points in the plot were obtained from compressional (black) and shear (blue) waveforms that traveled through the ice sample as it was compacted. The gray bands identify the range of central frequencies obtained from the head-to-head reference waveforms. As the sample shortened, higher frequencies were passed by the sample. The difference in central frequencies between through-sample and head-to-head waveforms can be used to estimate the systematic error incurred by comparing later waveform features to determine signal delay time through the sample (see text).

on compressional wave speeds is due to using the later waveform feature (the second extremum was used to determine compressional wave delay time for large sample lengths) and the smaller signal delay time for compressional waves traveling through the sample.

As discussed in Chapter 4, in order to model and interpret the data, sample length must be converted to porosity and the density of the sample must be known. The theory for determining porosity as a function of sample length for a right circular cylindrical sample of radius r was given in Chapter 4. The result was

$$\phi = 1 - \frac{h_0}{h}, \tag{5.4}$$

where ϕ is porosity, h_0 is the height of a zero porosity sample of radius r and h is the actual height of the sample. In Chapter 4, I showed that for ice, h_0 is given by,

$$h_0 = \frac{n}{\rho_{ice}\pi r^2} \tag{5.5}$$

where n is the mass ice in the sample and ρ_{ice} is the density of ice. In this experiment, the

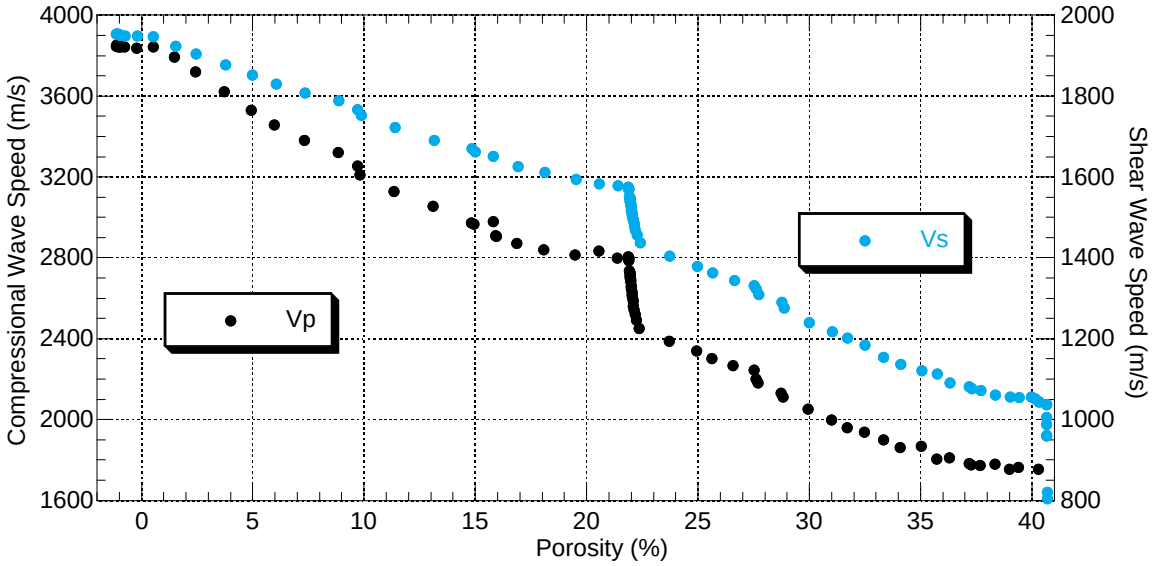

Figure 5.12: Compressional and shear wave speeds versus sample porosity for the compaction portion of the polycrystalline ice Ih experiment. Relative uncertainties in the compressional and shear wave speeds vary from 0.4 to 0.7% and 0.3 to 0.5%, respectively. The two vertical axes are scaled such that $V_P = 2V_S$. Therefore, when the data overlap, $V_P = 2V_S$ and Poisson's ratio is 0.33. At 41% and 22% porosity, the wave speeds increase significantly while the porosity (i.e., sample length) remains essentially constant. Once porosity reduction resumes, the porosity decreases a few percent before wave speeds begin increasing significantly again. These two observations can be explained through the formation of grain to grain bonds in the absence of active porosity reduction and the breaking of grain to grain bonds when active porosity reduction resumes (see text).

initial mass of ice was 14.0 grams. Equation 2.53 from Chapter 2 gives the density of ice at -5°C (and 1 atm) as 0.917 g/cm^3. The radius of the sample chamber is 1.27 cm.

When taking apart the apparatus after any experiment, a small amount of ice (or methane hydrate) is always found on the sides of the pistons. The amount is generally very small. It is difficult to determine how much of the original ice mass is lost during setup and compaction, but it is estimated to be 0.1 ± 0.1g. Therefore, $n = 13.9 \pm 0.1$g is used to calculate h_0 for ice according to Equation 5.5. The result is $h_0 = 29.9$ mm. Compressional and shear wave speeds versus porosity calculated using $h_0 = 29.9$ mm are given in Figure 5.12. Figure 5.12 includes the shear wave speeds observed in the setup portion of the experiment.

The uncertainty in the porosity estimate is given by

$$\Delta\phi = \sqrt{\left(\frac{h_0 \Delta h}{h^2}\right)^2 + \left(\frac{\Delta h_0}{h}\right)^2}, \tag{5.6}$$

where Δh and Δh_0 are the uncertainties in sample height and zero porosity sample height,

respectively. As stated above, the uncertainty in the sample height is 0.10 mm. The relative uncertainty in h_0 is given by

$$\frac{\Delta h_0}{h_0} = \sqrt{\left(\frac{\Delta n}{n}\right)^2 + \left(\frac{\Delta \rho_{ice}}{\rho_{ice}}\right)^2 + 4\left(\frac{\Delta r}{r}\right)^2}, \tag{5.7}$$

where $\Delta n, \Delta\rho_{ice}$ and Δr are the uncertainties in the ice mass, ice density and sample radius, respectively. Reasonable error bounds on the sample radius are ± 0.01 cm. Due to a lack of isothermal compressibility measurements in ice (see Figure 2.9 and associated text), it is uncertain how much the applied pressure might increase the density of ice. Previous studies have reported that the density of non-porous ice Ih can exceed 0.93 g/cm^3 at pressures over a kilobar (Gagnon et al., 1990; Shaw, 1986). At the relatively modest pressures used in this experiment (≤ 0.4 kbar), ice Ih density probably does not exceed 0.93 g/cm^3. Therefore, the uncertainty in density can be estimated as ± 0.013 g/cm^3. Using the above values for n, ρ_{ice}, r and their associated uncertainties gives a relative error estimate of 2% for h_0. Therefore, the uncertainty in porosity given by Equation 5.6 varies from ± 0.01 at $h = 50.0$ mm to ± 0.02 at $h = 29.9$ mm.

Density is defined as the amount of mass per unit volume. Therefore, sample density is given by

$$\rho = \frac{n}{\pi r^2 h} \tag{5.8}$$

where r and h are the radius and height of the right, circular cylindrical sample, respectively, and n is the mass of ice in the sample. When $h = h_0$, the density given by Equation 5.8 is the same as the density assumed for fully dense ice. This occurs at $\phi = 0$ in Figure 5.12. Figure 5.12 shows that wave speeds no longer change significantly with porosity for porosities below 0.5%. This implies that for sample heights h less than h_0, the elastic properties of the material between the pistons were no longer changing. This would be true if the sample were shortening by extruding material from between the pistons or by deforming from a right circular cylinder of radius r (perhaps by deforming the internal teflon liner). In either case, the implication is that the density of the material between the pistons would no longer be changing. Therefore, for $h < h_0$, the density of the sample is assumed to be

0.917 ± 0.013 g/cm^3. The full relationship for density versus sample height is thus

$$\rho = \begin{cases} \frac{n}{\pi r^2 h} & , \quad h \geq h_0 \\ 0.917 & , \quad h < h_0 \end{cases} . \tag{5.9}$$

The relative uncertainty in ρ for $h \geq h_0$ is given by,

$$\frac{\Delta\rho}{\rho} = \sqrt{\left(\frac{\Delta n}{n}\right)^2 + \left(\frac{\Delta h}{h}\right)^2 + 4\left(\frac{\Delta r}{r}\right)^2}. \tag{5.10}$$

Using Equation 5.9 for density, the compressional and shear wave speeds in Figure 5.12 can be converted to dynamic elastic moduli using the relations (Mavko et al., 1998),

$$M = \rho V_P^2, \tag{5.11}$$

$$G = \rho V_S^2, \text{ and} \tag{5.12}$$

$$K = \rho\left(V_P^2 - \frac{4}{3}V_S^2\right), \tag{5.13}$$

where M, G and K are the compressional wave, shear and bulk moduli, respectively. Another elastic modulus of interest, Poisson's ratio, can be calculated from V_P and V_S using (Mavko et al., 1998)

$$\nu = \frac{1}{2}\,\frac{V_P^2 - 2V_S^2}{V_P^2 - V_S^2}. \tag{5.14}$$

Figure 5.13 shows the resultant dynamic moduli versus porosity.

The relative uncertainties in the calculated moduli are given by

$$\frac{\Delta M}{M} = \sqrt{\left(\frac{\Delta\rho}{\rho}\right)^2 + 4\left(\frac{\Delta V_P}{V_P}\right)^2}, \tag{5.15}$$

$$\frac{\Delta G}{G} = \sqrt{\left(\frac{\Delta\rho}{\rho}\right)^2 + 4\left(\frac{\Delta V_S}{V_S}\right)^2}, \tag{5.16}$$

$$\frac{\Delta K}{K} = \frac{1}{K}\sqrt{\left(\left(V_P^2 - \frac{4}{3}V_S^2\right)\Delta\rho\right)^2 + (2\rho V_P \Delta V_P)^2 + \left(\frac{8}{3}\rho V_S \Delta V_s\right)^2}, \text{ and} \tag{5.17}$$

$$\frac{\Delta\nu}{\nu} = \frac{1}{\nu}\,\frac{V_P V_S}{(V_P^2 - V_S^2)^2}\,\sqrt{(V_S\Delta V_P)^2 + (V_P \Delta V_S)^2}. \tag{5.18}$$

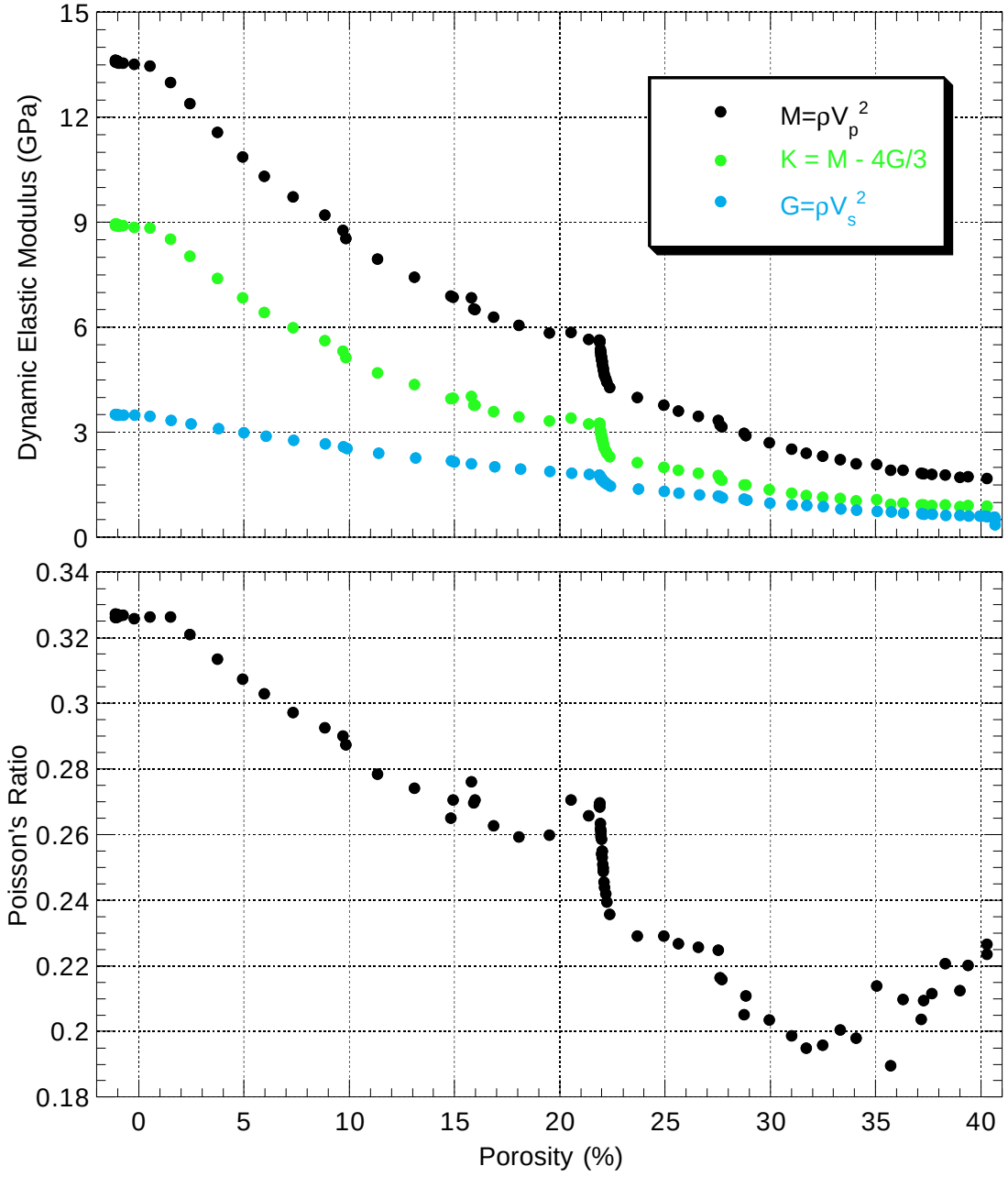

Figure 5.13: Compressional wave, bulk and shear moduli and Poisson's ratio versus porosity for the compaction portion of the ice Ih experiment. Both plots have the same horizontal axis, porosity in percent. **Top:** Dynamic compressional wave, bulk and shear moduli determined from the wave speeds in Figure 5.12 versus porosity. Relative uncertainties in the dynamic compressional wave, bulk and shear moduli are 2%, 2 to 3% and 2%, respectively. **Bottom:** Poisson's ratio determined from the wave speeds in Figure 5.12 versus porosity. Relative uncertainty is 1 to 3%.

Using the values given above, $\frac{\Delta M}{M}$ and $\frac{\Delta G}{G}$ are approximately 2%, $\frac{\Delta K}{K}$ varies from 2-3% and $\frac{\Delta \nu}{\nu}$ decreases from 3% to 1% as the porosity decreases.

To find an appropriate effective medium model for the effective elastic moduli of a porous material one must specify three properties of the material: 1) the volume fractions of the various components; 2) the elastic moduli of the components; and 3) the geometric arrangement of those components. If the geometric arrangement of the components is unknown, the best that can be done is to determine upper and lower bounds for the composite's elastic properties. That is the situation faced with the compacting ice sample. The elastic properties of ice and air (assumed to have zero bulk modulus) and the porosity of the sample are known at all times during the experiment, but the geometrical arrangements of solid and void are unknown. Therefore, unless *a priori* assumptions are made about the internal geometry of the sample, the best that can be done is to predict the range within which the moduli must be found. In general, for mixtures between solid and void, the bounds are exceptionally wide (the lower bound is always zero). However, as I show below, by applying the concept of critical porosity, we find the compressional wave and shear moduli data closely match the trend predicted by the modified upper Hashin-Shtrikman bound (e.g., Gal et al., 1998).

Hashin and Shtrikman (1963) showed that the tightest bounds on bulk ($K^{HS\pm}$) and shear ($G^{HS\pm}$) moduli for an isotropic, two component system are given by

$$K^{HS\pm} = K_1 + \frac{f2}{(K_2 - K_1)^{-1} + f_1(K_1 + \frac{4}{3}G_1)^{-1}} \tag{5.19}$$

$$G^{HS\pm} = G_1 + \frac{f2}{(G_2 - G_1)^{-1} + \frac{2f_1(K_1+2G_1)}{5G_1(K_1+\frac{4}{3}G_1)}}, \tag{5.20}$$

where K_i, G_i and f_i are the bulk and shear moduli and fractional amount of the ith component, respectively. The upper and lower bounds (signified by the superscripted $\pm$) are obtained by interchanging which material is termed 1 and which material is termed 2. The upper bound is obtained when the stiffest component is termed 1 and vice versa. One physical interpretation of the bounds is space filled by an assemblage of different sized spheres of material 2, each surrounded by a shell of material 1 (see Figure 5.14). In each individual composite sphere the inner sphere has fractional volume f_2, and the outer shell has fractional volume f_1.

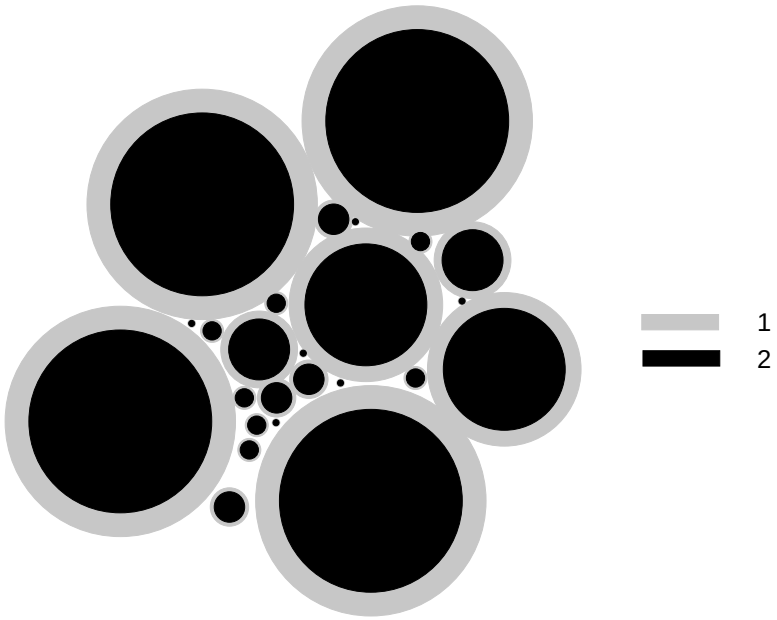

Figure 5.14: Physical interpretation of the Hashin-Shtrikman bounds for a two-phase material. Space is filled by an assembly of spheres comprised of a spherical core of material 2 (black), which is surrounded by a shell of material 1 (gray). In each sphere, the relative volume of the core is f2 and the relative volume of the shell is f1. The upper bound is realized when the stiffer material forms the shell and the lower bound when it is the core (after Mavko et al., 1998).

For a composite comprised of one solid phase and void space, the traditional Hashin-Shtrikman (H-S) bounds are very broad because the lower bound for both bulk and shear moduli is zero. This is because the model is mixing solid and void as its end members. When the void space is the "shell" component the resulting composite has no stiffness. However, a number of laboratory experiments have shown that a more representative model of porous materials is obtained if the two end members are taken to be the solid material and the properties of a porous material made from the solid but with a porosity equal to the porosity at which the mineral grains become load bearing (i.e., the critical porosity, see Mavko et al., 1998). This model says, conceptually, that the granular composite (e.g., sedimentary rock) is a mixture of solid material and critical porosity granular material instead of solid material and void space.

In order to use Equations 5.19 and 5.20 to calculate the modified H-S bounds, the elastic properties of the critical porosity material must be known. They can be estimated from the Hertz-Mindlin (Mindlin, 1949) model of a random packing of identical elastic spherical

grains:

$$K_{HM} = \left[\frac{n^2(1-\phi_c)^2G^2}{18\pi^2(1-\nu)^2}P_{eff}\right]^{\frac{1}{3}}, \tag{5.21}$$

$$G_{HM} = \frac{5-4\nu}{5(2-\nu)}\left[\frac{3n^2(1-\phi_c)^2G^2}{2\pi^2(1-\nu)^2}P_{eff}\right]^{\frac{1}{3}}; \tag{5.22}$$

where P_{eff} is the effective pressure (generally confining pressure minus pore pressure); G and ν are the shear modulus and Poisson's ratio of the solid phase; n is the average number of contacts per grain in the sphere pack, about 8-9 (Mavko et al., 1998); and ϕ_c is the critical porosity of the granular material.

For the ice sample, critical porosity is 41% (i.e., the porosity at the start of the experiment), the shear modulus and Poisson's ratio of ice are taken to be 3.5 GPa and 0.33, respectively (i.e., the moduli values determined at zero porosity) and n is taken as 8.1 (Mavko et al., 1998). The piston pressures applied to the ice sample during compaction ranged from 0 to 6,000 psi, so the Hertz-Mindlin (H-M) model was evaluated at $P_{eff} = 0$ and $P_{eff} = 6,000$ psi. The piston pressure is not a hydrostatic pressure, so the Hertz-Mindlin model evaluated at 6,000 psi should be an upper limit for describing the material, assuming the uncompacted portion of the porous ice sample remained a collection of independent grains at 41% porosity during compaction.

The H-M modeling results are used in Equations 5.19 and 5.20 to calculate the upper bound for combinations of granular ice (41% porosity) and solid ice. The fractional values f_1 (solid ice) and f_2 (granular ice) vary according to $1 \geq f_2 \geq 0$ and $f_1 = 1 - f_2$. The porosity of the resulting material ranges from 0 to 41%. One idealized interpretation of this arrangement is a sample volume filled by spheres of critical porosity granular material surrounded by shells of solid ice (e.g., Figure 5.14 with the solid black material replaced with porous ice).

The results of this modeling for compressional wave and shear moduli are compared to the wave-speed-based measurements in Figure 5.15. The compressional wave modulus estimate (M^{HS+}) was obtained from the modified upper H-S estimates of K and G using $M^{HS+} = K^{HS+} + \frac{4}{3}G^{HS+}$. Also shown in Figure 5.15 are the H-S bounds for ice and void space and the results of cementation modeling at high porosities (described below).

As shown in Figure 5.15, the modified upper H-S bounds closely mimic the trends in

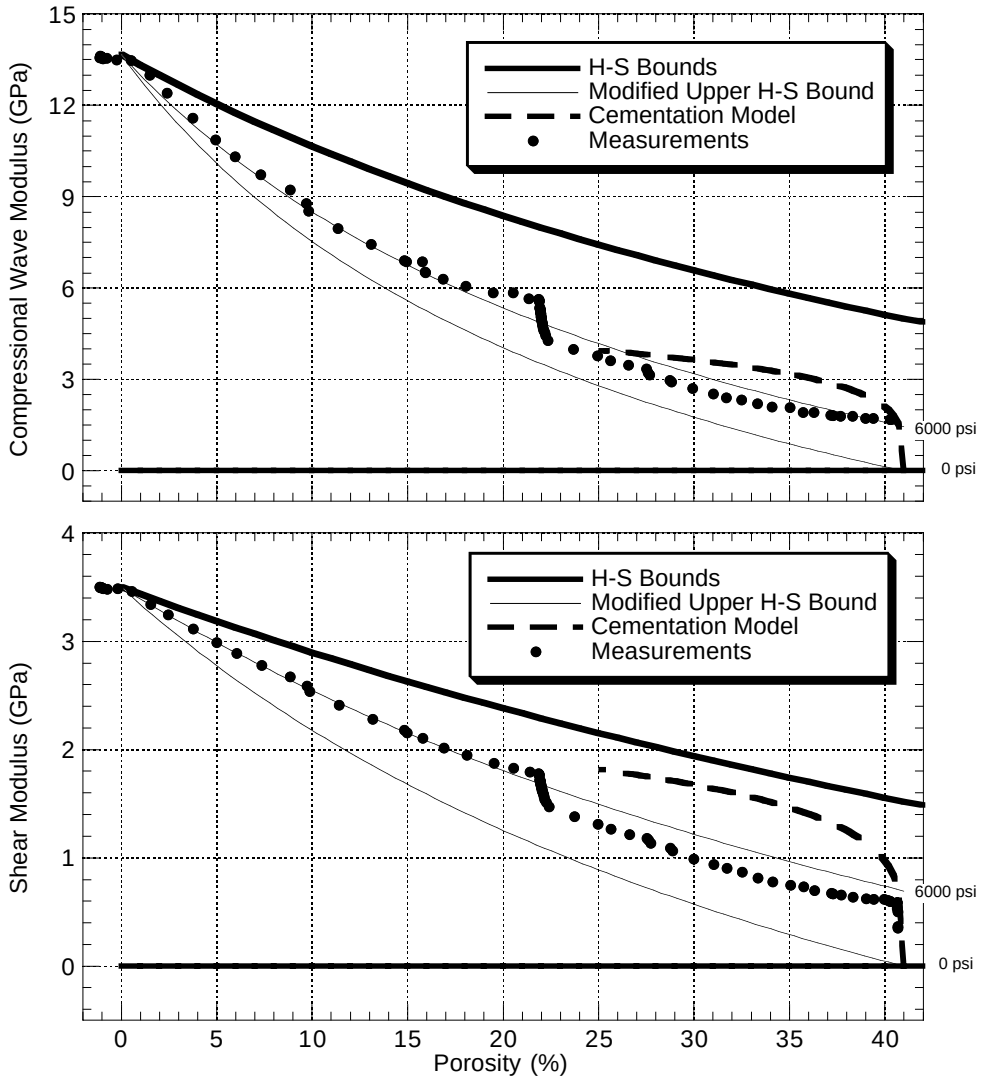

Figure 5.15: Modeling dynamic compressional wave and shear moduli changes with porosity during the compaction portion of the polycrystalline ice Ih experiment. Both plots have the same horizontal axis, porosity in percent. **Top:** The thick solid lines are the Hashin-Shtrikman (H-S) bounds for compressional wave moduli using ice and void space as the two endpoints; the thin solid lines are the (modified) upper H-S bound for compressional modulus evaluated using the Hertz-Mindlin (H-M) model for a sphere pack at 41% porosity and effective pressure 0 or 6,000 psi and solid ice as the end points; the thick dashed line is the compressional wave modulus result obtained from the cementation model (see text); and the data points are the compressional wave moduli derived from the compressional wave speeds measured in the experiment. Relative uncertainty in the data is $\sim 2\%$. **Bottom:** The thick solid lines are the Hashin-Shtrikman (H-S) bounds for shear wave moduli using ice and void space as the two endpoints; the thin solid lines are the (modified) upper H-S bound for shear modulus evaluated using the Hertz-Mindlin (H-M) model for a sphere pack at 41% porosity and effective pressure 0 or 6,000 psi and solid ice as the end points; the thick dashed line is the shear modulus result obtained from the cementation model (see text); and the data points are the shear moduli derived from the shear wave speeds measured in the experiment. Relative uncertainty in the data is $\sim 2\%$.

the data. The matches are not exact, however, because the piston pressure applied to the sample is actually less than 2,000 psi until the sample has reached nearly zero porosity. The data, on the other hand, approach the 6,000 psi bound by 20% porosity. This discrepancy could reflect a violation of the assumption that the porosity of the uncompacted material remains at 41% or it could represent some bond formation between the grains. Regardless, the qualitative agreement between model and data is excellent. This suggests that as the ice compacts, pockets of uncompacted material remain and that they are slowly compacted to zero porosity.

There are two segments of the data where the modified upper H-S bound does not adequately represent the data. Those segments are at 41% and 22% porosity. Those are the points when active compaction of the sample was not occurring. Above, I asserted that this behavior could be explained by the formation of grain to grain bonds which were then broken once active compaction occurred. In addition to the H-S bounds and the wave-speed-based measurements of moduli, Figure 5.15 also shows the result of the cementation model (Dvorkin et al., 1994; Dvorkin and Nur, 1996), described in detail in Chapter 6, for a granular ice sample with critical porosity 41% where ice cement forms at the grain to grain contacts. This model predicts significant moduli increases with only a small amount of cement. In the actual experiment, no new ice enters the sample to form the cement. Rather, water molecules redistribute within the sample and accumulate at grain to grain contacts, a process called sintering, which has long been studied in ice (Hobbs, 1974).

The cementation model was derived for high porosity sandstones, and, as formulated by Dvorkin et al. (1994), is not appropriate for directly modeling the feature in the moduli data at 22% porosity. However, the similarity in the features at 41% and 22% porosity (and in the experiments described in Chapter 4) strongly suggests that a similar process occurred on both occasions. Comparing the cementation model predictions to the data at 41% porosity shows that the cementation of ice grains at their contacts is one possible explanation for the observed wave speed increases at constant sample length.

To close the discussion of the data from this stage of the experiment, Figure 5.16 shows the variation of sample length with piston pressure for the ice sample. As with the ice experiment presented in Chapter 4 (Figure 4.15), the amount of pressure required to compact the sample is modest. Nearly all the compaction occurs below 2000 psi. By comparison,

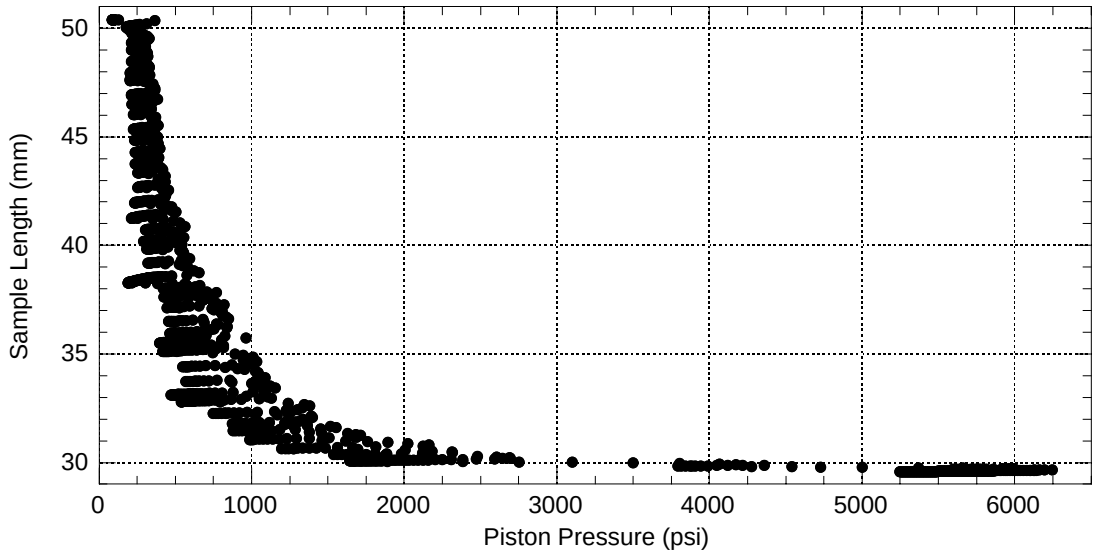

Figure 5.16: Sample length versus piston pressure for the compaction stage of the polycrystalline ice Ih experiment. Note that the piston pressure is less than 2000 psi until the sample length reaches approximately 30 mm.

the majority of the compaction in the three hydrate samples presented in Chapter 4 had not been achieved until 12,000 psi had been reached. Clearly, porous methane hydrate is much more resistant to compaction than porous ice Ih.

Temperature Cycling

Figure 5.17 shows a summary of the bath temperature, piston pressure and sample length measurements during the temperature cycling stage of the experiment that followed the principal compaction. The temperature was cycled in steps between -5°C and -20°C, twice. At each temperature, once thermal equilibrium had been reached, the piston pressure was adjusted to 4750 psi and then cycled between 4750 and 3250 psi over approximately 30 minutes. The slow pressure cycling was done in order to measure an approximation to the static compressional wave modulus (see below).

Figure 5.17 also shows the changes in sample length for this portion of the experiment. The total change in sample length is less than 2%. Approximately half the change occurs in the 24 hours before active temperature cycling begins. The remainder occurs over the next $6\frac{1}{2}$ days. As shown in the depressurization section below, much of the shortening is

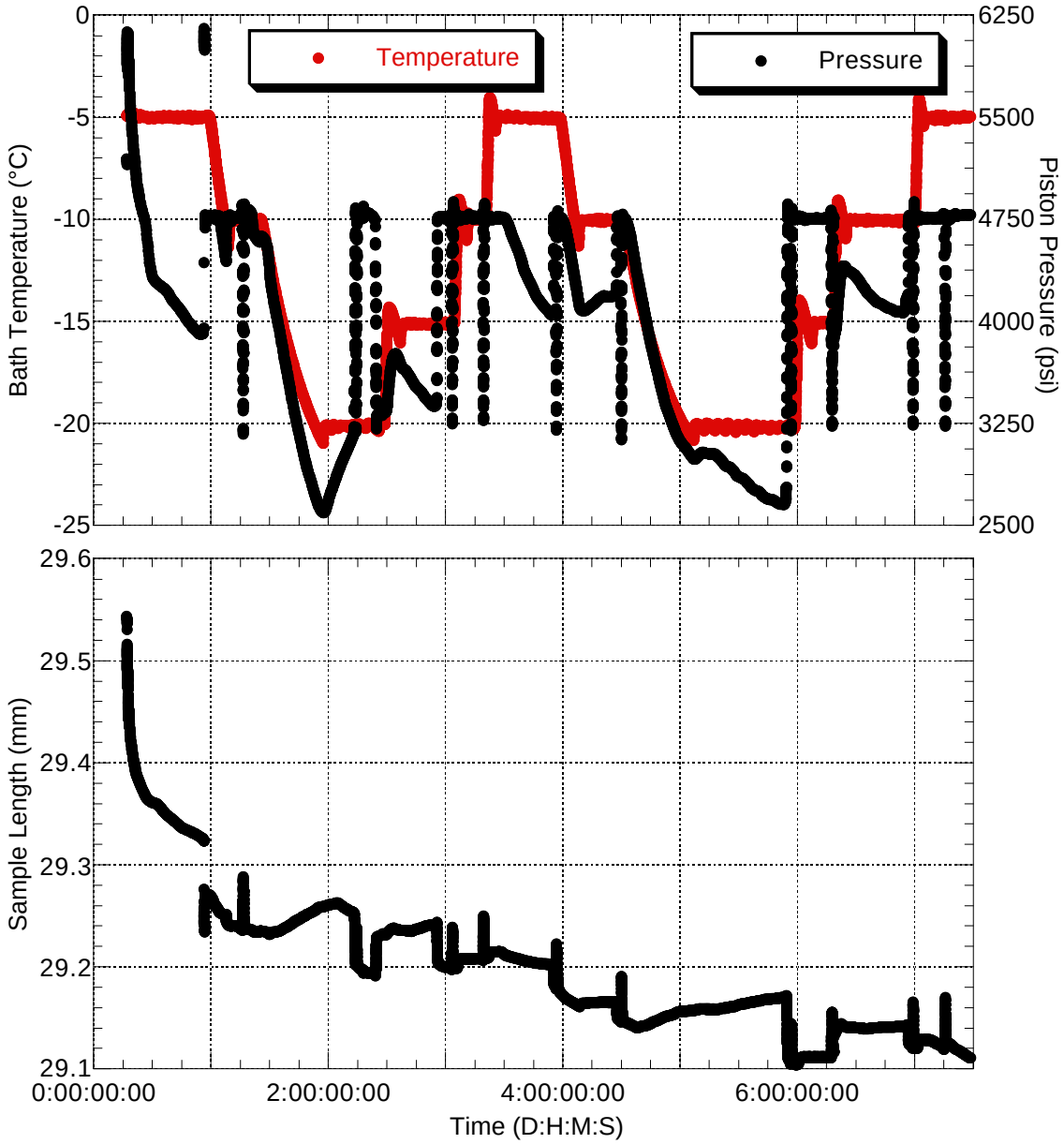

Figure 5.17: Bath temperature, piston pressure and sample length versus time for the temperature cycling portion of the polycrystalline ice Ih experiment. Both plots have the same horizontal axis, time in days:hours:minutes:seconds. **Top:** Bath temperature and piston pressure versus time. This plot shows the two temperature cycles from -5 to -20 and back to -5°C. Also evident are the piston pressure excursions which occurred at each temperature. **Bottom:** Sample length versus time. The total length change during this portion of the experiment is less than 2%. There is a net decrease in sample length with time. The length changes associated with each pressure cycle can be seen in the data.

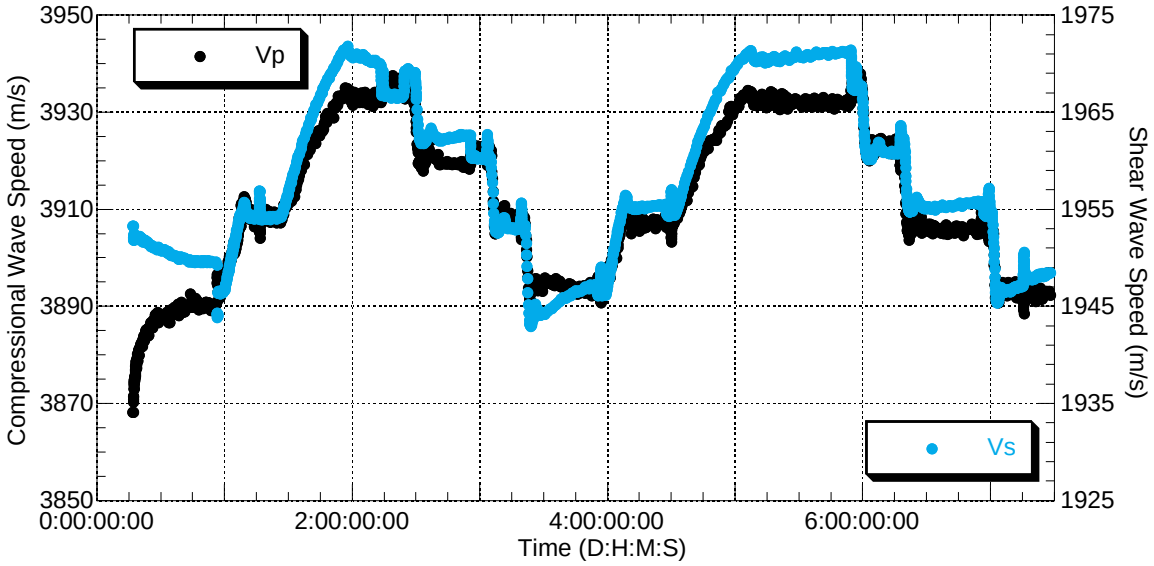

Figure 5.18: Compressional and shear wave speeds versus time for the temperature cycling portion of the polycrystalline ice Ih experiment. The relative uncertainty in the wave speeds is 0.4%. The vertical axes' scales are chosen such that $V_P = 2V_S$. Therefore, if the data overlap, $V_P/V_S = 2$ and Poisson's ratio is 0.33. The effect of temperature, and to a lesser degree pressure can be seen in this plot (see also Figure 5.17). Note that both compressional and shear wave speeds increase with decreasing temperature, but that shear wave speed increases and compressional wave speed decreases with decreasing pressure. This can be seen more clearly in Figures 5.22 and 5.24 below.

recovered when the piston pressure being applied to the sample is decreased to zero. Note that there are small changes in sample length associated with each piston pressure cycle.

Figure 5.18 provides a summary of the compressional and shear wave speed results for this portion of the experiment. The relative uncertainty in the wave speeds (Equation 5.3) is 0.4%. Note that the vertical axes are scaled $V_P = 2V_S$. Therefore, when the V_P and V_S data overlap, $V_P/V_S = 2$ and Poisson's ratio is 0.33. These results show the effect of temperature on wave speed, but they also include the effects of piston pressure variations. Separating out the wave speed measurements made during the controlled piston pressure variations at constant temperature makes it possible to separate the contributions of temperature and piston pressure to observed compressional and shear wave speeds. This is done below.

The initial purpose for cycling piston pressure at each temperature was to measure the associated length changes and from that calculate the static compressional wave modulus ($M = K + \frac{4}{3}G$), which is defined as the ratio of axial stress to axial strain in a uniaxial strain state (Mavko et al., 1998). The sample is contained in a holder with rigid side walls, so

the uniaxial strain state is obtained. Therefore, the M modulus can be measured directly by observing the small change in sample length with piston pressure and applying the relationship

$$M = \frac{\Delta P}{\Delta l} l_0, \tag{5.23}$$

where ΔP is the change in piston pressure, Δl is the change in sample length and l_0 is the initial sample length. Since the pressure changes occur over a 30 minute period while the system is in a fixed temperature bath, the resultant value for M is an approximation to the static, isothermal compressional wave modulus.

Figure 5.19 shows the variations in piston pressure and sample length during one of the pressure cycles (at -10°C). The variation in sample length is small (0.04 mm), but the signal of the change is easily detected. Note also that the sample length begins and ends at approximately the same value, suggesting the deformation was predominantly elastic. However, the longest sample length occurs after the minimum in piston pressure. This offset may be due to some non-elastic behavior in the sample, the effects of friction when the piston motion was reversed or a small measurement error in the sample length. In any case, the discrepancy is too small to change the fundamental conclusion that the observed deformation was predominantly elastic.

Plotting the data as piston pressure versus sample length (Figure 5.20) shows the hysteresis in the pressure-sample length path caused by the offset in the oil pressure and sample length peaks. It is common in piston cylinder experiments (S. Kirby, pers. comm.) to assume that this hysteresis is due entirely to friction opposing piston motion within the apparatus. The effect is often removed empirically by adjusting the pressures to the midpoint values between the two branches of the hysteresis loop. Instead of making this empirical correction to the measurements, I split the data into two branches, depressurization (where the piston is moving outward) and repressurization (where the piston is moving inward) and analyze them independently to obtain two estimates of $\frac{\Delta P}{\Delta l}$. Fitting straight lines to the two branches shows the two slopes are essentially equal in this example. Multiplying by the sample length and converting the pressure units to GPa gives static M-modulus estimates of 6.3 GPa for both the depressurization and repressurization branches of the data.

This analysis was carried out for all the pressure cycles performed during the experiment. The results are summarized in Figure 5.21. The estimates from the repressurization

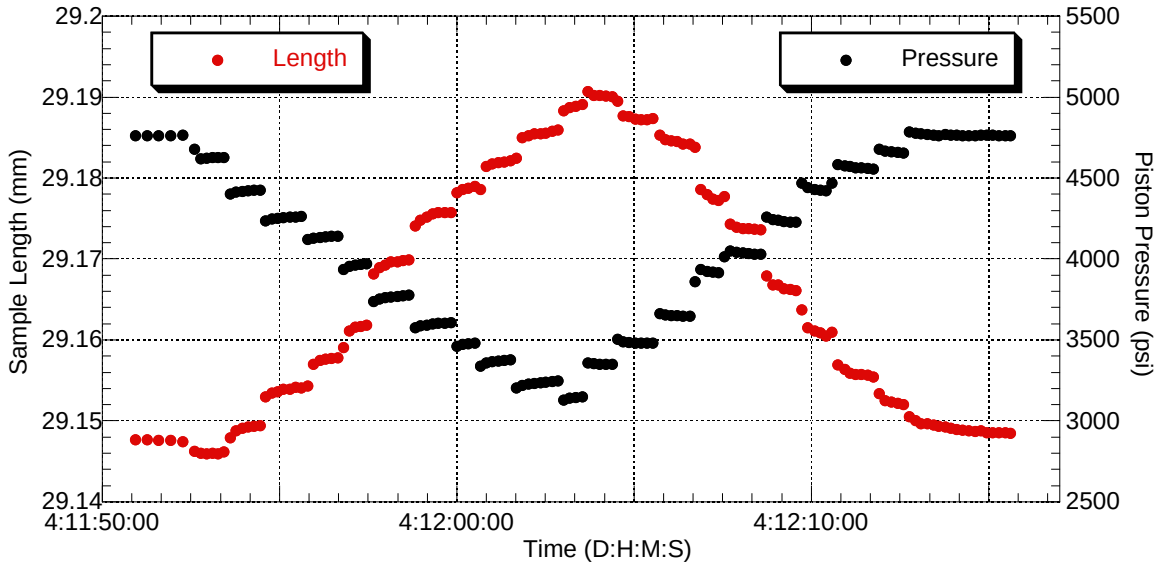

Figure 5.19: Variations in piston pressure and sample length at constant temperature (-10°C) when manually cycling the piston pressure between 4,750 and 3,250 psi in the polycrystalline ice Ih experiment. Note that the maximum in sample length and the minimum in piston pressure do not exactly coincide in time, but that the sample length is essentially the same at the end of cycle as it was at the beginning, suggesting the deformation was predominantly elastic.

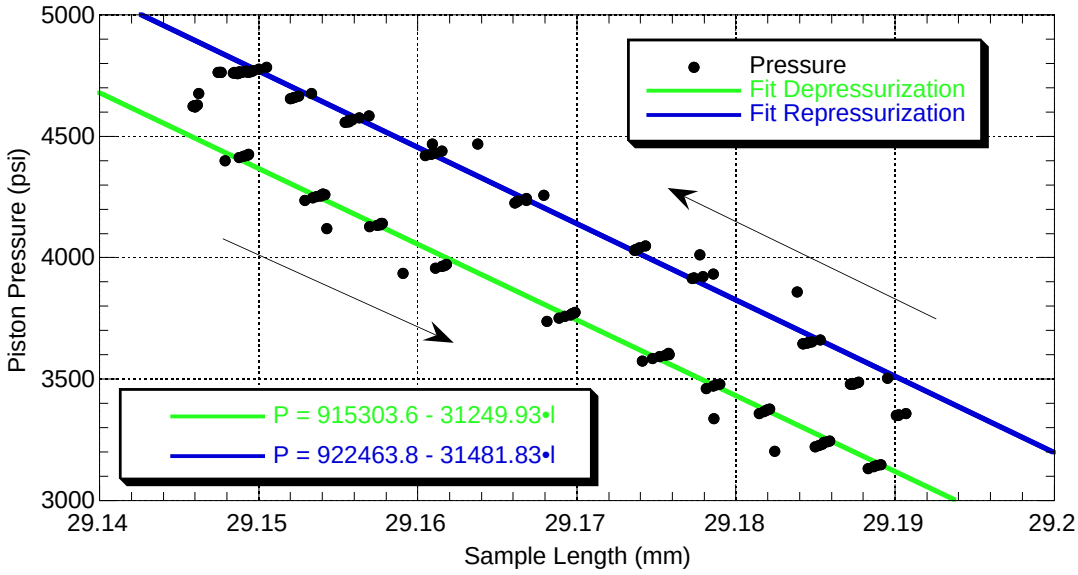

Figure 5.20: Piston pressure versus sample length for a pressure cycle between 4,750 and 3,250 psi at -10°C for the polycrystalline ice Ih experiment. Due to the hysteresis apparent in the plot, straight lines were fit to the different branches of the data (depressurization and repressurization) independently. The slopes of the linear fits are used to estimate the static compressional wave modulus (see text).

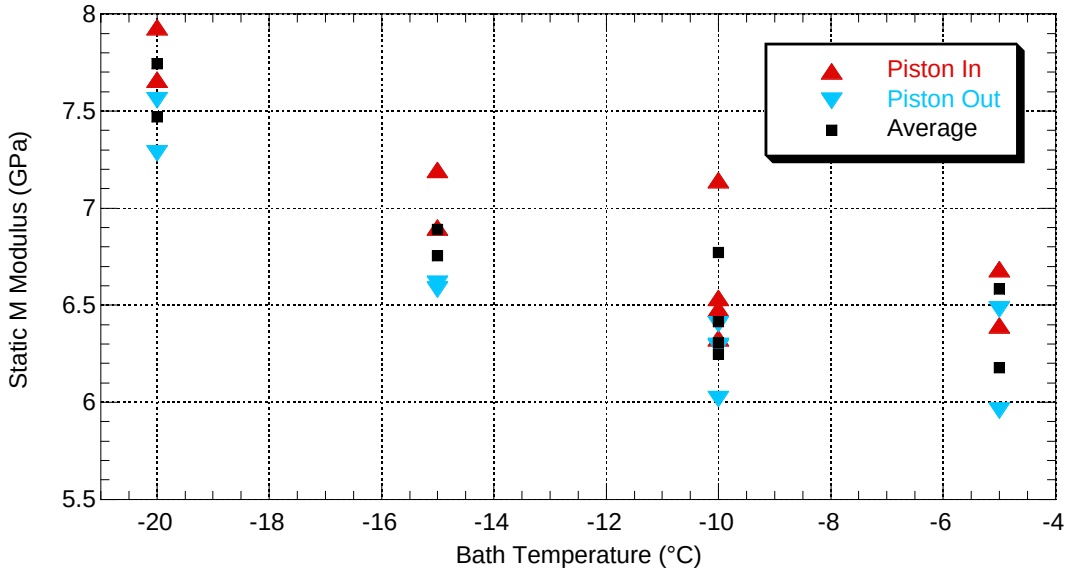

Figure 5.21: Measurements of the static compressional wave modulus from the temperature cycling portion of the polycrystalline ice Ih experiment. The values obtained from the repressurization (piston in) branch of the data are systematically higher than those obtained from the depressurization (piston out) branch. The average of the piston in and piston out M-modulus measurements is also plotted. There is a net trend of decreasing modulus value with increasing temperature. The static moduli values shown here are approximately half the value of the dynamic moduli obtained from the compressional wave speeds (Figure 5.25).

(piston in) portion of the pressure cycle are consistently higher, but the difference is generally less than 10%. The data also reveal a trend of increasing modulus with decreasing temperature, as would be expected. However, the value of the modulus is lower than expected over the entire temperature range, given the values observed for the dynamic compressional wave modulus obtained from the wave speed measurements (approximately 14 GPa, see below).

It is well known that reliable static moduli are difficult to obtain for polycrystalline ice samples (Hobbs, 1974; Gold, 1958; Dorsey, 1940). For example, Hobbs (1974) gives a range of 0.3 to 11.0 GPa for reported values of the static Young's modulus (the ratio of axial normal stress to axial linear strain in a uniaxial stress state). The rate, duration and amount of load applied to the samples appears to significantly affect the observed "static" modulus value. Relative movement between individual ice grains and the movement of lattice imperfections (e.g., dislocations) are generally cited as the causes for the rate dependant observations (Hobbs, 1974). Gold (1958) observed that stresses less than 10 bar

(145 psi) applied for less than 10 seconds resulted in deformations which were completely reversible (i.e., elastic). The "static" M-modulus measurements reported in this thesis involved a total pressure change an order of magnitude larger than 10 bar, and the pressure was applied and removed in steps over a 30 minute period. Therefore, it is likely that some form of grain movement (internal, external or both) occurred during the pressure cycling. This could bias the measured moduli to lower values (i.e., more total strain would occur per applied pressure than would occur if the deformation was completely elastic). A second possible source of systematic bias toward lower observed static moduli values is a violation of the rigid side walls assumption. The internal teflon liner may have deformed during the pressure cycling, changing the diameter of the sample slightly. This could lead to greater sample length changes per unit of applied pressure, again biasing the M-modulus estimate toward lower values. Consistent with previously reported observations (Hobbs, 1974; Gold, 1958; Dorsey, 1940), I consider the dynamic moduli values obtained from the wave speed measurements to be more robust measurements of the elastic properties of ice.

The compressional and shear wave speed measurements made during the pressure cycle shown in Figure 5.19 are plotted versus experiment time in Figure 5.22. The two vertical scales are given such that $V_P = 2\ V_S$. Therefore, when the two wave speeds overlap, $V_P/V_S = 2$ and Poisson's ratio is 0.33. Note that the wave speeds observed at the beginning and end of the pressure cycle are equal to within measurement error. Note also that unlike the pressure versus sample length plot (Figure 5.20), the hysteresis in the wave speed versus pressure curves is negligible (Figure 5.23).

As seen in Figures 5.22 and 5.23, the wave speed changes during the pressure cycle are small, but clearly detectable. The shear wave speed increases and the compressional wave speed decreases as the piston pressure decreases. The decrease of compressional wave speed with decrease in pressure is typical behavior for stable solids. The increase in shear wave speed is not. The decrease of shear wave speed with increasing confining pressure is a known property of ice Ih and is believed to represent a shear instability in the crystal lattice (Gagnon et al., 1988; Shaw, 1986).

Combining the compressional and shear wave speed measurements from all the pressure cycles makes it possible to quantify the variations of wave speed with temperature and

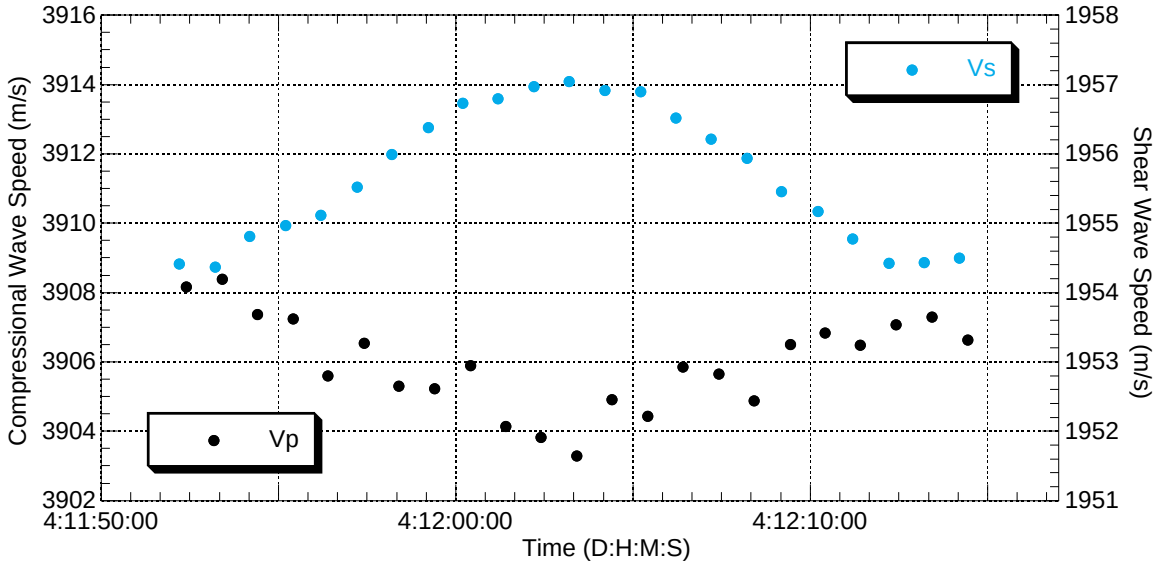

Figure 5.22: Compressional and shear wave speeds observed during a piston pressure cycle (Figure 5.19) between 4,750 and 3,250 psi for the polycrystalline ice Ih experiment. The relative uncertainty in the wave speeds is 0.4%. Note that compressional wave speed decreases but shear wave speed increases with decreasing piston pressure (and vice versa) and that wave speeds at the beginning and end of the pressure cycle are equal.

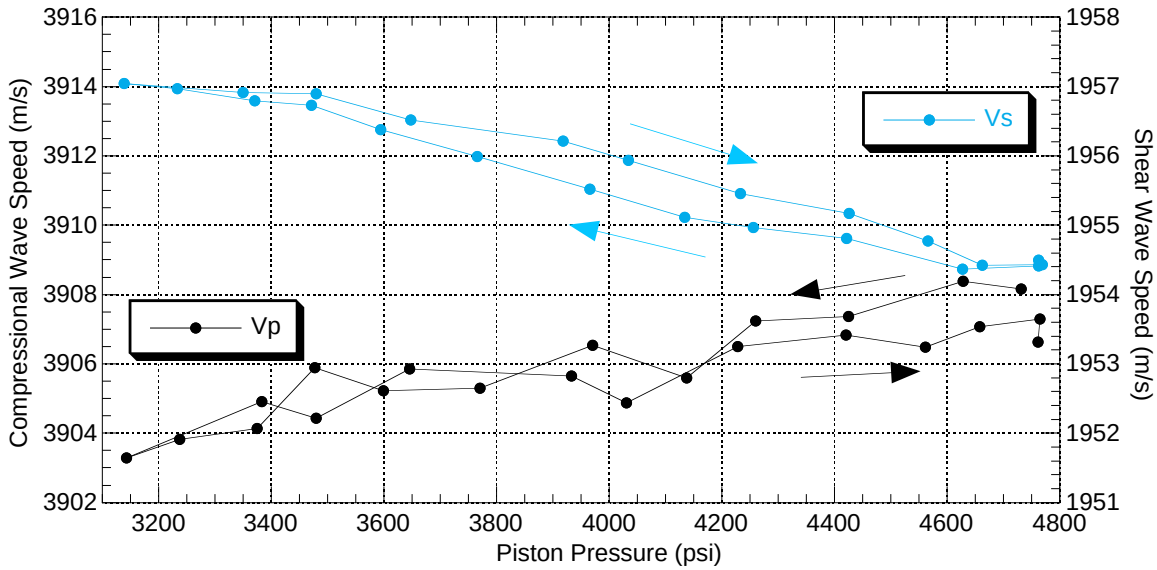

Figure 5.23: Compressional and shear wave speeds versus pressure during a piston pressure cycle (Figure 5.19) between 4,750 and 3,250 psi for the polycrystalline ice Ih experiment. The arrows show the direction in which the curves were traversed. The small hysteresis in the curves is probably due to friction opposing piston motion within the apparatus (see text).

piston pressure. Figure 5.24 plots compressional and shear wave speeds, respectively, versus piston pressure. The measurements fall into four bands representing the measurements made at $-5, -10, -15$ and -20°C. From these measurements of wave speed, Poisson's ratio can be calculated via Equation 5.14. The result is also shown in Figure 5.24 as a function of piston pressure. For Poisson's ratio there is no clear dependence on temperature.

Assuming a density of 0.917 ± 0.013 g/cm^3, the wave speed measurements presented in Figure 5.24 can be converted to compressional wave, shear and bulk moduli using Equations 5.11 through 5.13, respectively. The results are shown in Figure 5.25 versus piston pressure.

Fitting 2-D planar regressions of the wave speed and moduli results to temperature and piston pressure produce the relations given in Table 5.3. As shown in Table 5.3, the standard deviations of the residuals to the regressions are quite small, much smaller than the estimated relative uncertainties in the individual measurements themselves (Table 5.4). This is due to the high degree of internal consistency within the data and demonstrates that linear variations of the properties with temperature and piston pressure are appropriate models for representing the data. The results shown in Figures 5.24 and 5.25 and summarized in Table 5.3 are in excellent agreement with previously published wave speed measurements on ice Ih (Table 5.5), giving us a high degree of confidence in the apparatus and methodology used to obtain the results.

Depressurization

The final stage of the ice experiment was depressurization. At -5°C, the piston pressure applied to the sample was reduced from 4,600 to 0 psi in the span of 15 minutes. The piston pressure remained at ~ 0 psi until the pressure vessel was removed from the temperature bath three hours later. Figure 5.26 shows the variation of temperature, piston pressure and sample length with time for this portion of the experiment. Note that the sample length increased by approximately 1% during unloading and continued to rebound slowly during the three hours the piston pressure was at 0 psi.

Compressional and shear wave speed and Poisson's ratio are plotted versus time for this portion of the experiment in Figure 5.27. The uncertainties in the values are the same as those given in Table 5.4 for the measurements in the temperature cycling portion of

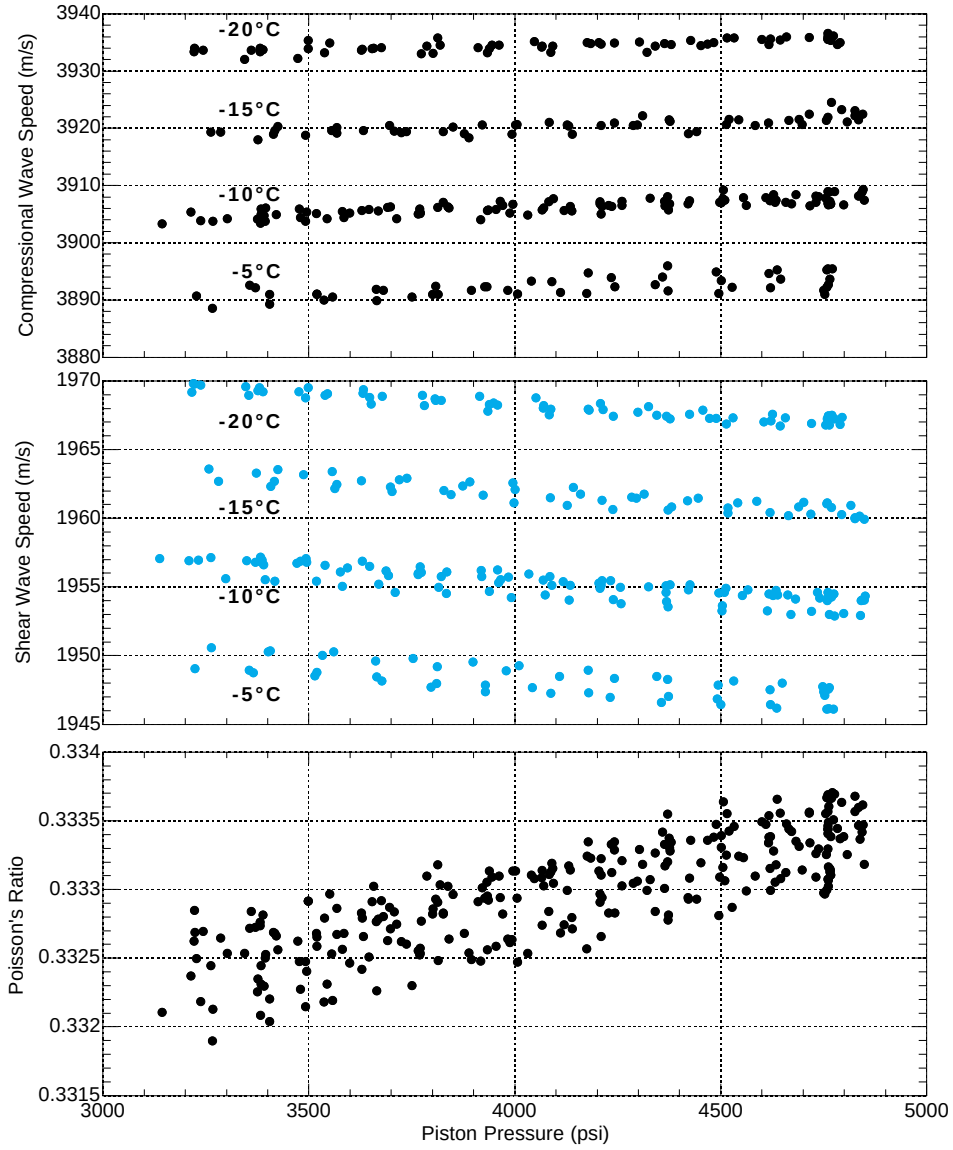

Figure 5.24: Compressional wave speed, shear wave speed and Poisson's ratio versus piston pressure for both temperature cycles (Figure 5.17) of the polycrystalline ice Ih experiment. Separation of the data points at a given temperature and pressure represent wave speed measurements collected on different temperature cycles. All three plots have the same horizontal axis, piston pressure in psi. **Top:** Compressional wave speed versus piston pressure. Relative uncertainty in the data is 0.4%. The four linear clusters of data were acquired at $-20, -15, -10$ and -5°C. At all four temperatures, compressional wave speed increases with increasing piston pressure. **Middle:** Shear wave speed versus piston pressure. The relative uncertainty in the data is 0.4%. The four linear clusters of data were acquired at $-20, -15, -10$ and -5°C. At all four temperatures, shear wave speed decreases with increasing piston pressure. **Bottom:** Poisson's ratio versus piston pressure. Relative uncertainty in the data is 0.9%. No trend with temperature is apparent. Poisson's ratio increases with increasing piston pressure.

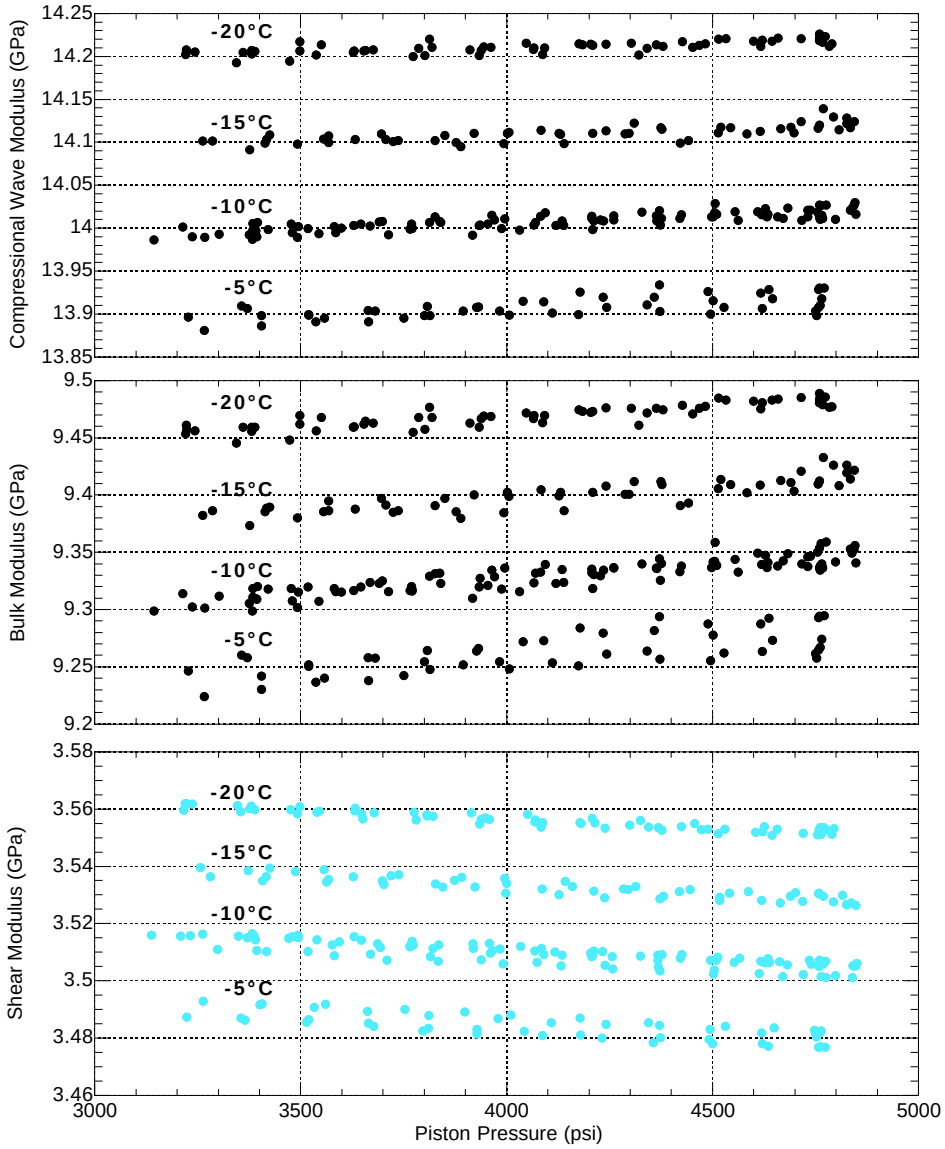

Figure 5.25: Dynamic compressional wave, bulk and shear moduli versus piston pressure for both temperature cycles (Figure 5.17) of the polycrystalline ice Ih experiment. Moduli calculated assuming $\rho_{ice} = 0.917 \text{g/cm}^3$. Separation of the data points at a given temperature and pressure represent measurements collected on different temperature cycles. All three plots have the same horizontal axis, piston pressure in psi. The relative uncertainty in all three moduli is 2%. **Top:** Compressional wave modulus versus piston pressure. The four linear clusters of data were acquired at $-20, -15, -10$ and -5°C. At all four temperatures, compressional wave modulus increases with increasing piston pressure. **Middle:** Bulk modulus versus piston pressure. The four linear clusters of data were acquired at $-20, -15, -10$ and -5°C. At all four temperatures, bulk modulus increases with increasing piston pressure. **Bottom:** Shear modulus versus piston pressure. The four linear clusters of data were acquired at $-20, -15, -10$ and -5°C. At all four temperatures, shear modulus decreases with increasing piston pressure.

Table 5.3: Regressions of Wave Speeds and Dynamic Elastic Moduli versus Temperature (-20 to -5°C) and Piston Pressure (3250 to 4750 psi) in the Compacted, Polycrystalline Ice Ih Sample

	$F(T,P) = a \cdot T + b \cdot P + c$			
$F(T,P)$	a†	b†	c†	std††
Vp (m/s)	-2.80 ± 0.01	$(1.98 \pm 0.11) \times 10^{-3}$	3870.1 ± 0.5	0.9
Vs (m/s)	-1.31 ± 0.01	$-(1.83 \pm 0.07) \times 10^{-3}$	1949.3 ± 0.3	0.6
ν	$-(2.0 \pm 0.2) \times 10^{-5}$	$(6.4 \pm 0.2) \times 10^{-7}$	0.3301 ± 0.0001	0.0002
M (GPa)	$-(2.01 \pm 0.01) \times 10^{-2}$	$(1.41 \pm 0.08) \times 10^{-5}$	13.748 ± 0.003	0.007
G (GPa)	$-(4.72 \pm 0.02) \times 10^{-3}$	$-(6.6 \pm 0.3) \times 10^{-6}$	3.488 ± 0.001	0.002
K (GPa)	$-(1.38 \pm 0.01) \times 10^{-2}$	$(2.30 \pm 0.09) \times 10^{-5}$	9.097 ± 0.004	0.008

† Units for a are the units of the property being fit divided by $^{\circ}$C. Units for b are those of the property being fit divided by psi. Units for c are those of the property being fit.

†† Standard deviation of the residuals to the fit equation $F(T,P) = a \cdot T + b \cdot P + c$. Units are those of the property being fit.

Table 5.4: Calculated Uncertainties in Wave Speeds and Dynamic Elastic Moduli for the Compacted, Polycrystalline Ice Ih Sample

Property	Uncertainty	Property	Uncertainty
Vp	$\pm$17 m/s	M	$\pm$0.2 GPa
Vs	$\pm$7 m/s	G	$\pm$0.06 GPa
ν	$\pm$0.003	K	$\pm$0.2 GPa

Table 5.5: Comparison with Published Wave Speed Measurements in Polycrystalline Ice Ih

Source	Method	P (psi)	T (°C)	$V(T,P)^{\dagger}$ (m/s)
This Work	Pulse Transmission	3250 to 4750	−20 to −5	$V_P = 3870.1 - 2.80\,T + 1.98\times10^{-3}\,P$ $V_S = 1949.3 - 1.31\,T - 1.83\times10^{-3}\,P$
Gagnon et al., 1988	Brillouin Spectroscopy	0 to 40,600	−35.5 to −4 −35.5	$V_P = 3809 - (3.90 + 2.7\times10^{-2}\,T)\,T + \cdots$ $(3.12\times10^{-3} - 1.5\times10^{-8}\,P)\,P$ $V_S = 1997 - (1.72\times10^{-3} + 5.2\times10^{-9}\,P)\,P$ $[V_S = 1996 - 1.83\times10^{-3}\,P]$
Shaw, 1986	Pulse Transmission	0 to 31,000	−25 −25	$V_P = 3888 + 3.40\times10^{-3}\,P$ $[V_P = 3940 + 1.98\times10^{-3}\,P]$ $V_S = 1895 - 9.12\times10^{-4}\,P$ $[V_S = 1982 - 1.83\times10^{-3}\,P]$
Smith and Kishoni, 1986	Pulse Echo	0	−26 −26	$V_P = 3940$ [3943] $V_S = 1990$ [1983]
Gammon, 1983	Brillouin Spectroscopy	0	−16 −16	$V_P = 3845$ [3915] $V_S = 1957$ [1970]
Gold, 1958	Pulse Transmission	0	−40 to −3 −20 to −2	$V_P = 3860 - 2.32\,T$ $[3870 - 2.80\,T]$ $V_S = 2030 - 1.08\,T$ $[1949 - 1.31\,T]$
Northwood, 1947	Pulse Transmission	0	−15 −15	$V_P = 3980$ [3912] $V_S = 2010$ [1969]

† Values and expressions within brackets [] are the results obtained by evaluating the wave speed regressions given in Table 5.3 at the pressure and temperature conditions reported by the other references cited in this table.

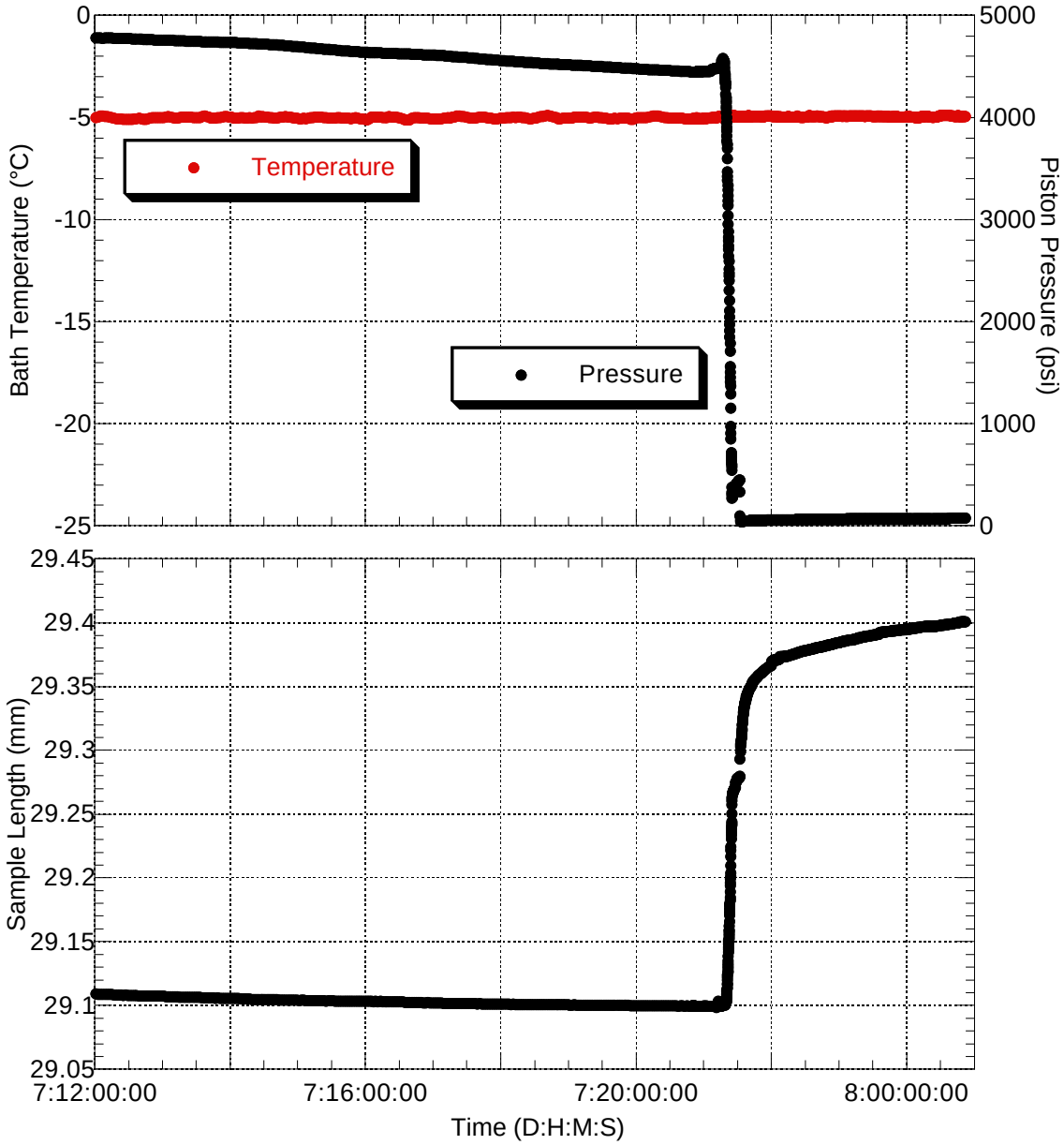

Figure 5.26: Bath temperature, piston pressure and sample length versus time for the depressurization portion of the polycrystalline ice Ih experiment. The horizontal axis for both plots is the same, time in days:hours:minutes:seconds. **Top:** Bath temperature was constant at -5°C for this portion of the experiment. Piston pressure was decreased from $\sim 4,600$ to 0 psi in 15 minutes. **Bottom:** Sample length versus time. The sample length increased by less than 1% as the piston pressure decreased to 0 psi. While the piston pressure remained at ~ 0 psi, the sample length continued to increase.

the experiment. During the initial pressure drop, compressional wave speed decreased and shear wave speed increased, as expected from data acquired earlier in the experiment. Both wave speeds increased slightly as the sample sat at 0 psi piston pressure for three hours. These small increases (less than 1%) may have been due to the "healing" of small cracks formed in the sample during pressure unloading. Any cracks that did form must have been small because no cracks were visible in the sample when it was recovered from the apparatus (Figure 5.8).

It is interesting to compare these wave speed and Poisson's ratio measurements at -5°C and 0 psi to the predictions made by the regressions in Table 5.3 for the same conditions. At -5°C and 0 psi, the regressions predict a compressional wave speed of 3884.1 ± 0.9 m/s, a shear wave speed of 1955.9 ± 0.6 m/s and a Poisson's ratio of 0.3302 ± 0.0002. The measured values for compressional wave speed, shear wave speed and Poisson's ratio are 3885 ± 17 m/s, 1966 ± 7 m/s and 0.328 ± 0.003, respectively. The agreement between predicted and measured compressional wave speed at -5°C and 0 psi piston pressure is excellent. The regression based estimate falls well within the error bounds of the measurement. For the shear wave speed, the measurement and regression differ by ~ 10 m/s, or $\frac{1}{2}$% of the total value. Thus the regression based estimate falls just outside the error bounds (± 7 m/s) of the measurement. This suggests the variation in shear wave speed with pressure is slightly non-linear within the range 0 to 3,250 psi piston pressure. Unfortunately, no shear waveforms were recorded in this pressure interval so no shear wave speed information is available to test the hypothesis. The higher measured shear wave speed is the reason the measured Poisson's ratio is larger than the regression based prediction. However, the regression based prediction still falls within the uncertainty of the measurement.

Assuming a density of 0.917 ± 0.013 g/cm^3, the measured wave speeds can be converted to elastic moduli. At -5°C and 0 psi, the results are 13.9 ± 0.2, 9.1 ± 0.2 and 3.55 ± 0.06 GPa for the compressional wave, bulk and shear moduli, respectively. The regression based estimates of 13.849 ± 0.007, 9.166 ± 0.008 and 3.512 ± 0.002 GPa for the compressional wave, bulk and shear moduli, respectively, all fall within the respective measured values' uncertainty.

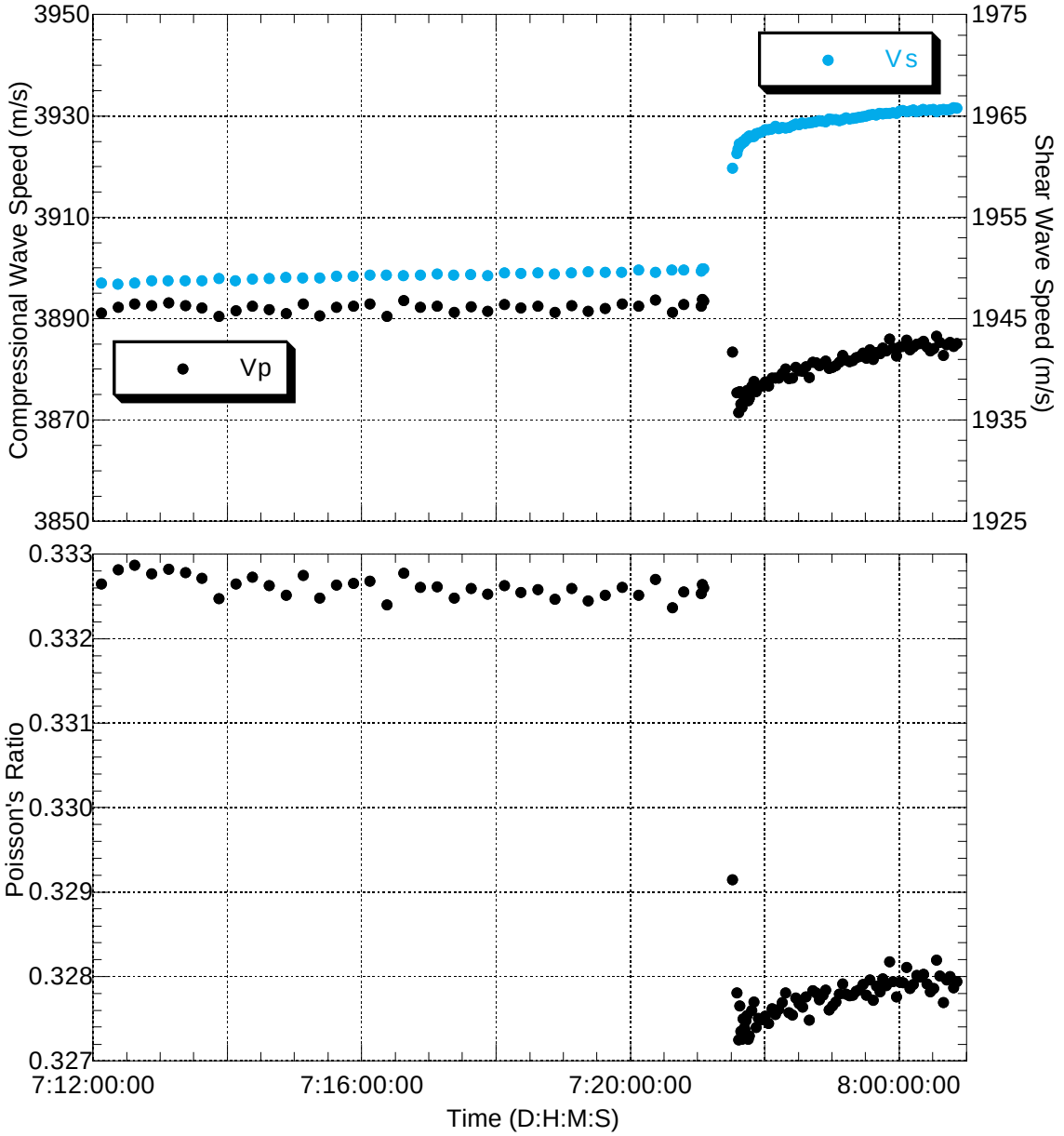

Figure 5.27: Compressional wave speed, shear wave speed and Poisson's ratio versus time for the depressurization portion of the polycrystalline ice Ih experiment. Both plots have the same horizontal axis, time in days:hours:minutes:seconds. **Top:** Compressional and shear wave speeds versus time. Relative uncertainty in the data is 0.4%. When the piston pressure is reduced to zero, the compressional wave speed decreases but the shear wave speed increases. Both compressional and shear wave speeds increase slightly as the sample sits at zero piston pressure for three hours. **Bottom:** Poisson's ratio versus time. Relative uncertainty in the data is 1%.

5.5 Methane Hydrate Experiment

The procedure used in the polycrystalline methane hydrate experiment combined elements from the procedure used in the preliminary methane hydrate experiments described in Chapter 4 and the procedure used in the ice experiment described in section 5.4. The procedure and results are described below.

5.5.1 Procedure

The pressure vessel was partially assembled in the sample preparation freezer and allowed to cool. The sample chamber was loaded with granulated, sieved ice (13.98 ± 0.02 g) and the assembly of the pressure vessel was completed. The pressure vessel was transferred to the freezer where the experiment would take place and suspended in the temperature bath by attaching the gas and hydraulic oil lines. The linear motion potentiometer (LMP) was attached to the translating piston and the pressure-temperature-length (PTL) data logging was begun. The logging continued for the remainder of the experiment.

Once the PTL data logging had begun, the Panametrics source was turned on but no waveform was detected. This signified that the sample was not long enough to make significant contact with both transducers simultaneously. The apparatus was evacuated and subsequently pressurized with methane gas to 3800 psia. The synthesis cycle began by setting the temperature controller to warm the temperature bath to 17°C. There were still no observable waveforms, but the waveform acquisition system was set to record waveforms every 20 minutes in case any should become detectable during methane hydrate synthesis. No waveforms were observed in the data recorded during the methane hydrate synthesis portion of the experiment.

The temperature bath warmed from -20 to 17°C in eight hours. The temperature was held at 17°C until methane gas pressure no longer decreased with time (22 hours), signifying that methane was no longer being incorporated into the sample. At that point, the temperature controller was set to -20°C, and the bath cooled to that temperature over the course of 48 hours. No residual water freezing signature was present in either the temperature or pressure data (see below), indicating that the amount of unreacted water was negligible.

At -20°C, the gas pressure was reduced to 300 psia and the sample was compacted. Gas pressure increased only slightly during compaction, suggesting no significant loss of gas from the hydrate crystal structure occurred. The sample was compacted at -20°C instead of the higher temperatures used in the preliminary experiments because the preliminary experiments showed that free gas was trapped in samples compacted at higher gas pressures. Therefore, compacting at the lowest possible gas pressure is advantageous, and the stability pressure required for methane hydrate decreases with temperature (see Figure 2.2). The lowest stable temperature achievable with the system is -20°C and 300 psia is well within the stability field of methane hydrate at that temperature.

The initial compaction of the methane hydrate sample was done in the same manner as the ice sample described in section 5.4. A preliminary manual depth micrometer measurement of the piston height above the top of the pressure vessel was made. The oil pressure was then increased slowly until the LMP registered piston motion. At that point, another manual piston height measurement was made. Once that measurement was completed, the waveform acquisition system was set to record waveforms at 60 second intervals, and active sample compaction began. As in the ice experiment, waveform acquisition took 20 seconds. Oil pressure was slowly increased for the next 30 seconds, and was then allowed to relax freely for the 10 seconds prior to the next waveform acquisition cycle and during the cycle itself. This 60 second cycle was repeated until the piston pressure reached 15,000 psi. At that point, the pressure was held between 14,500 and 15,000 psi for $6\frac{1}{2}$ hours. Toward the end of the $6\frac{1}{2}$ hour period, more manual piston height measurements were made.

The piston pressure was allowed to relax freely overnight and dropped from 15,000 to 11,000 psi as the sample shortened. The next morning, another manual piston height measurement was made before increasing the gas pressure to 2400 psia in anticipation of increasing the bath temperature to 5°C. By this point in the experiment, it had become apparent that the LMP was malfunctioning. The voltage output produced by the LMP was too high given the manual piston height measurements. The LMP's output was also becoming uncharacteristically noisy. In an attempt to discern if ice formation within the LMP or beneath the LMP stand was the cause of the problem, the LMP was left undisturbed while the bath warmed to 5°C.

When the system temperature had equilibrated at 5°C, the gas pressure was increased

to 3,600 psia and a manual piston height measurement was made. The piston pressure was increased to 14,500 psi and held at that value for 15 minutes. Unfortunately, the LMP data taken during this pressure increase proved conclusively that the LMP was malfunctioning and that it would have to be replaced. The LMP was replaced with a new one of the same model.

While the LMP was being replaced, the temperature controller RTD was accidentally lifted out of the temperature bath. The temperature controller interpreted the resultant decrease in sensor temperature as a signal the bath was getting too cold and increased the output of the heater accordingly. This problem was caught after only a few minutes, but it took several minutes for the temperature to return to equilibrium. The signature of this event is visible in the temperature data (Figure 5.28, see below) on day 4. The temperature was left at 5°C overnight and the piston pressure was allowed to relax freely.

The next morning, a manual piston height measurement was made and the temperature controller was set to increase the bath temperature from 5°C to 20°C. Once stable at 20°C, the gas pressure was increased from 3,900 to 4,000 psia to insure the thermodynamic stability of the methane hydrate. Once the temperature and gas pressure had equilibrated, the piston pressure was increased to 14,700 psi and held at that value for one hour to squeeze out any remaining porosity in the sample. At the end of the hour, a manual piston height measurement was made and the piston pressure was allowed to vary freely for six hours. During this time, the temperature was held constant at 20°C. At the end of the six hours, the temperature controller was set to 5°C and the system was allowed to cool overnight.

The next morning, at 5°C, a manual piston height measurement was made, the gas pressure was reduced to 3,600 psia and the piston pressure was reduced to 9,000 psi. The piston pressure was maintained at 9,000 psi for 2 hours. 10 compressional and 10 shear waveforms were then recorded at 30 second intervals and stored in a separate folder from the rest of the acquired waveforms. These waveforms and subsequent ones taken at other temperatures were used to analyze the variations of compressional and shear wave speed with temperature (see analysis section below). After the 10 shear and 10 compressional waveforms were acquired, the oil pressure was maintained at 9,000 psi for another hour to provide three hours of background data for the special subset of waveforms. Another manual piston height measurement was made and the temperature controller was set to

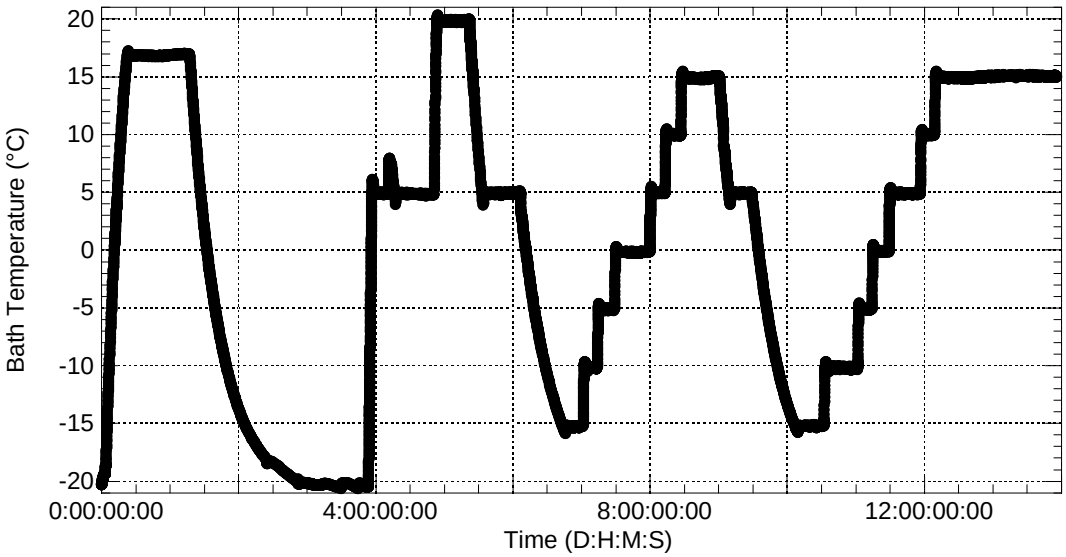

Figure 5.28: Bath temperature versus time for the polycrystalline methane hydrate experiment.

-15°C.

When the system reached equilibrium at -15°C, the entire process was repeated: the piston height was manually measured; the gas and piston pressures were adjusted to 3,600 psia and 9,000 psi, respectively; the piston pressure was held constant for two hours; a special subset of 10 compressional and 10 shear waveforms was acquired; the piston pressure was held constant for another hour; and another manual piston height measurement was made. These steps were repeated at -10, -5, 0, 5, 10, 15, 5, -15, -10, -5, 0, 5, 10 and 15°C. The temperature cycle was repeated twice in order to test the repeatability of the results. A summary of the temperature data is given in Figure 5.28. During temperature changes and overnight, the gas and piston pressures were allowed to vary freely. Once the system had stabilized at a given temperature, the gas pressure was always adjusted to 3,600 psia and the piston pressure was always adjusted to 9,000 psi. A summary of the pressure data is given in Figure 5.29. As many as four (and always at least two) manual depth micrometer measurements were made at each temperature. The manual depth micrometer measurements made it possible to tightly constrain the small changes in sample length that occurred during the temperature cycling.

When the second temperature cycle concluded at 15°C, the final phase of the experiment began. The temperature and gas pressure were held constant at 15°C and 3,600 psia,

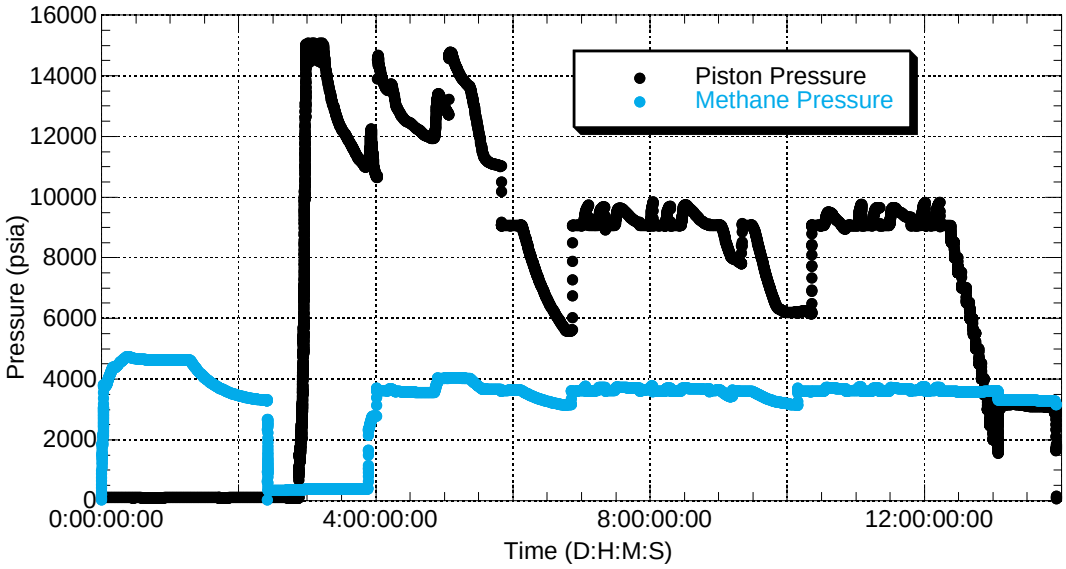

Figure 5.29: Piston pressure and methane pressure versus time for the polycrystalline methane hydrate experiment.

respectively. The piston pressure was systematically decreased in 500 psi steps from 9,000 to 1,500 psi. After each pressure step, the piston pressure was held constant for approximately one hour. Manual piston height measurements were generally made at the beginning and end of each constant pressure segment. During the pressure step from 2,000 to 1,500 psi, the translating piston was pushed off the sample, effectively ending the experiment.

Once the piston had been fully retracted, the pressure vessel's gas line valve was closed and the pressure vessel was disconnected from the gas and hydraulic oil lines. The pressure vessel was removed from the temperature bath and transported to the sample preparation freezer, where it was left overnight for the excess ethyl alcohol to evaporate. The next morning, the pressure vessel was placed on the benchtop, cooled with liquid nitrogen (to insure the methane hydrate sample's stability) and disassembled. The intact, teflon jacketed sample was extracted and stored in a liquid nitrogen dewar in case future analysis was desired.

Figure 5.30 is a digital photograph of the recovered sample. The cracks visible in the sample likely formed either when the sample was depressurized in the apparatus or from the thermal shock of cooling the pressure vessel with liquid nitrogen prior to its disassembly.

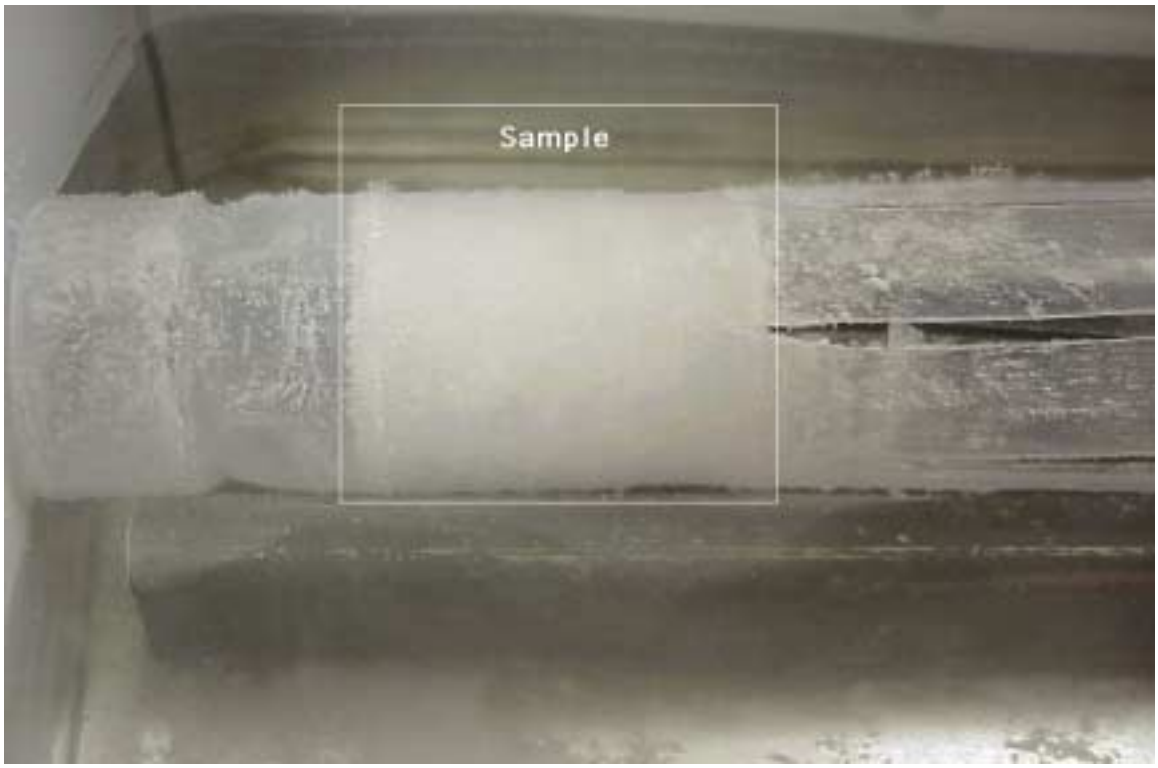

Figure 5.30: Photograph of the methane hydrate sample extracted from the pressure vessel at the end of the experiment. The sample is shown in the teflon liner in which it was compacted. The sample and liner are suspended above a liquid nitrogen bath to maintain the sample's thermodynamic stability. The crystals seen on the outside of the teflon liner are frost formed from water which has condensed out of the air. It is difficult to see in this image, but the sample contained several apparently planer cracks perpendicular to the axis of the sample, and a smaller number of cracks parallel to the axis of the sample. These cracks may have formed during the pressure unloading, from the thermal shock of being cooled by liquid nitrogen, or both. See text for further discussion.

As shown below, the wave speed results obtained during the depressurization portion of the experiment strongly suggest the cracks formed during unloading. The results obtained from the data acquired during the experiment are analyzed and discussed below.

5.5.2 Data Processing

The general processing of the pressure-temperature-length (PTL) data was the same as in the ice experiment described earlier in this chapter. The signature of the power source variations was removed from the raw voltages output by the pressure transducers and the LMP. The oil and gas pressure transducer voltages were converted to piston pressure and gas pressure, respectively, using the appropriate calibrations.

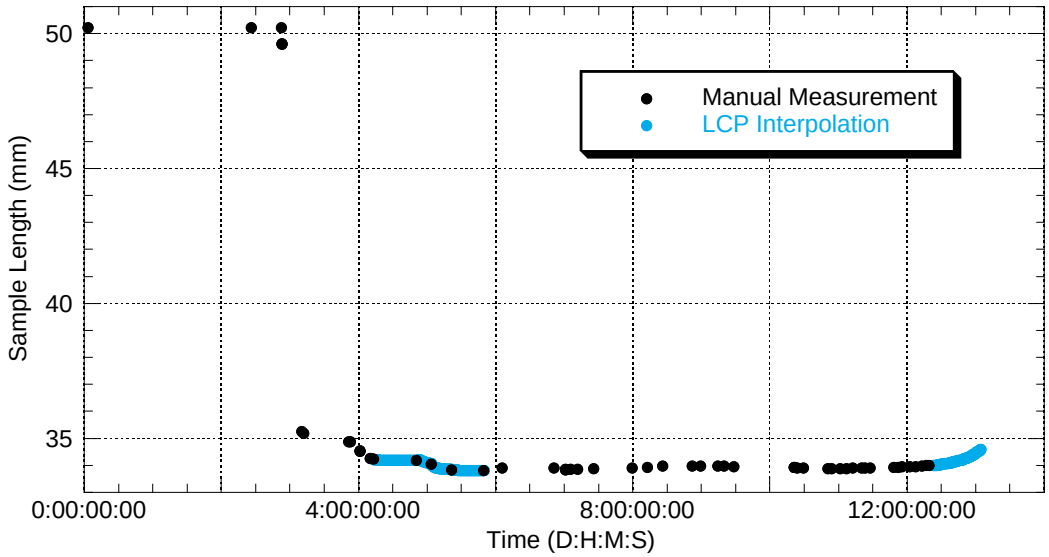

Figure 5.31: Sample length versus time for the polycrystalline methane hydrate experiment. Sample lengths determined from the LMP were unreliable for the compaction and temperature cycling portions of the experiment. Manual measurements were too sparse to recover length information during compaction, but manual measurements were made often enough to recover length information during temperature cycling (see text).

Because of the failure of the original LMP, the sample length data were processed significantly differently from the ice experiment. The voltages obtained from the original LMP were deemed unusable. The only data on sample length available prior to the replacement of the original LMP were eight manual measurements. As can be seen in Figure 5.31, these manual measurements were not made often enough to accurately determine sample length during the compaction at -20°C. Therefore, no wave speeds are reported prior to the replacement of the defective LMP.

When the voltages from the new LMP were plotted against the manual piston height measurements for the remainder of the experiment, it was discovered that the manual measurements and the LMP voltages had significant discrepancies during the temperature cycling portion of the experiment (e.g., the manual measurements would change but the LMP voltage would remain constant). Therefore, the remaining length measurements were broken into three groups. A conversion from LMP voltage to piston height was obtained for the LMP voltages from the time the LMP was replaced until temperature cycling began at 5°C (just before the beginning of day 6). From that point until depressurization began on day 12, the manual piston height measurements were used to determine sample length.

Sample length varied by only ± 0.10 mm during this portion of the experiment; therefore, the error incurred by linearly interpolating sample lengths between manual measurements should be much less than ± 0.10 mm.

For the final stage of the experiment, depressurization, another LMP voltage to piston height calibration was obtained. The resultant combination of manual and LMP based sample length measurements is given in Figure 5.31. The manual measurements are not shown during the depressurization portion of the experiment because the manual length sampling was so dense that to plot them would obscure the LMP based estimates.

The bad LMP data acquired during the temperature cycling portion of the experiment were attributed to rocking of the LMP stand as the piston direction reversed several times. This problem has been corrected for future experiments by redesigning the LMP stand to be bolted onto the top of the pressure vessel.

The processing flow for the compressional and shear waveform data was the same as in the ice experiment. The waveforms were filtered, the mean of the first 100 points were removed from each waveform and the picking routine was run. The system's gas pressure, piston pressure and temperature at each waveform time were determined from linearly interpolating each property as a function of time from the PTL data set. The piston pressure and temperature data were used to correct the signal delay times. The corrected delay times were used to calculate compressional and shear wave speeds for all waveforms with valid associated sample lengths (i.e., those waveforms acquired after the original LMP was replaced).

5.5.3 Results and Discussion

The methane hydrate experiment lasted approximately twice as long as the ice experiment described earlier in this chapter and produced approximately twice the amount of data. The properties of interest varied significantly throughout the two week experiment. Therefore, as with the ice experiment, I break the methane hydrate experiment into four stages: setup and synthesis, compaction, temperature cycling and depressurization, and analyze the results from each stage independently below.

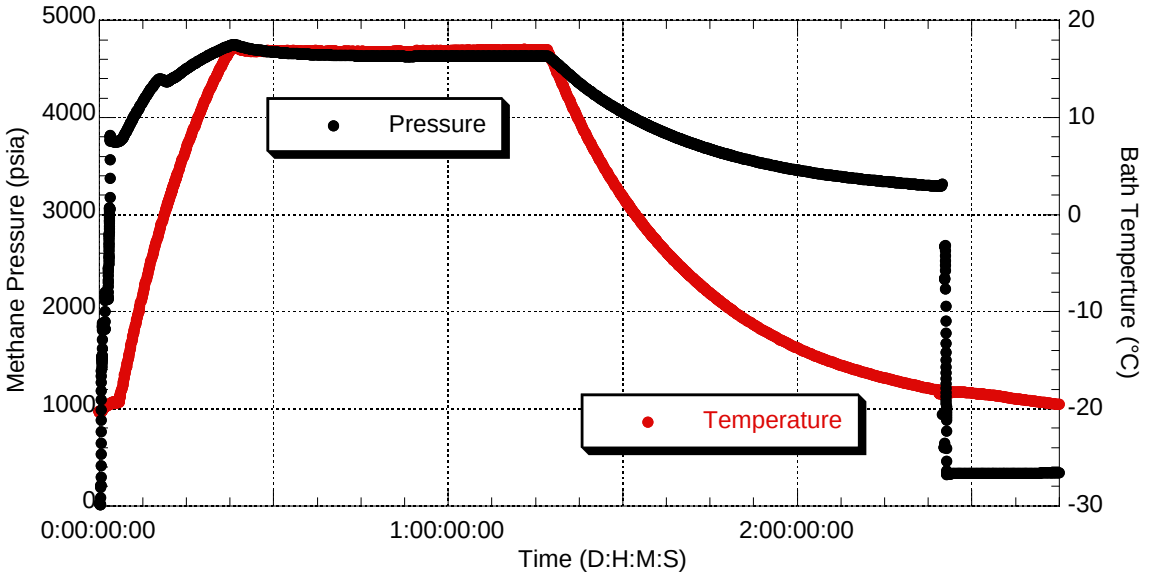

Figure 5.32: Methane pressure and bath temperature versus time for the hydrate synthesis portion of the polycrystalline methane hydrate experiment.

Setup and Synthesis

No waveforms were detected during the setup and synthesis portion of the methane hydrate experiment. The sample length and piston pressure did not vary significantly. Therefore, the analysis in this section will focus on the bath temperature and methane gas pressure which are shown in Figure 5.32.

Figure 5.32 shows the variation of bath temperature and methane gas pressure during the setup and synthesis portions of the experiment. It shows the initial pressurization of the system with methane gas and the depressurization of the system prior to compaction. It also shows the heating of the sample during methane hydrate synthesis and the cooling of the sample in preparation for compaction.

Plotting methane gas pressure versus bath temperature for the time period between initial gas pressurization and pre-compaction gas depressurization emphasizes the 5 stages of the methane hydrate synthesis process (Figure 5.33). In stage 1, methane gas pressure increases linearly with temperature. The slope of the curve is a function of the system volume available to and the thermodynamic properties of methane gas. In stage 2, which began at $\sim -2°C$, the gas pressure deviated from the previous linear trend and actually decreased

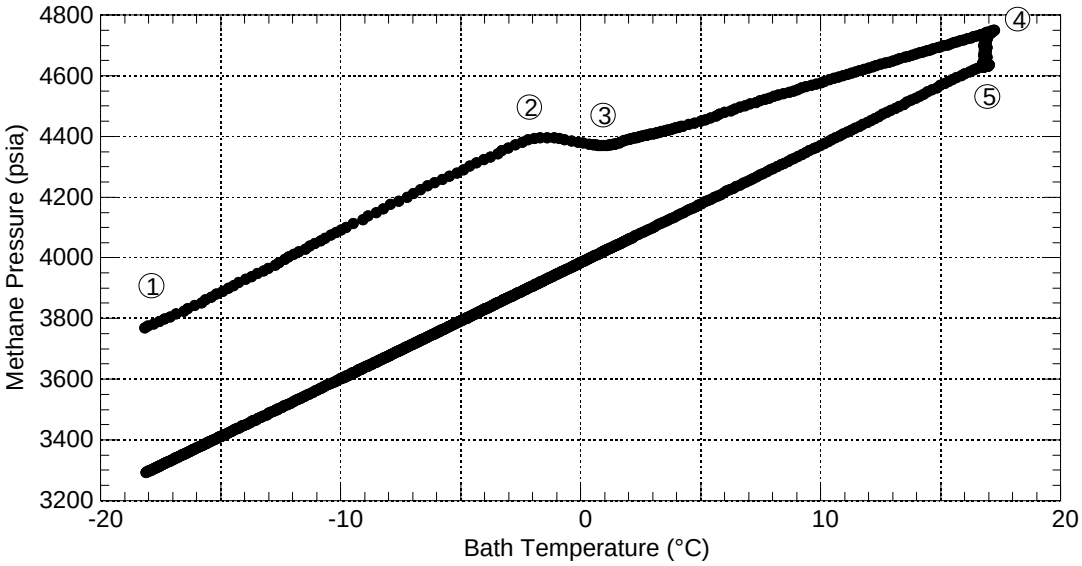

Figure 5.33: Methane pressure versus bath temperature for the hydrate synthesis portion of the polycrystalline methane hydrate experiment. The methane hydrate synthesis pressure-temperature curve is broken into five stages: (1) Initial heating, (2) onset of ice melting and significant methane hydrate formation, (3) continuation of methane hydrate formation with increasing temperature, (4) continuation of methane hydrate formation at constant temperature and (5) sample cooling once the reaction has completed.

as temperature increased. The deviation was caused by two factors, the consumption of methane gas in the methane hydrate formation reaction and the partial melting of some ice grains. If bulk melting had occurred, the deviation of the pressure-temperature curve would have been much more dramatic (e.g., Figure 6 in Stern et al. 1998). Thirty minutes later, stage 3 had begun, and the pressure was again varying linearly with temperature, although with a different slope than in stage 1. The slope of the curve in stage 3 was a function of the new system volume available for methane gas, the rate of methane gas consumption in the methane hydrate formation reaction, and the thermodynamic properties of methane gas. The volume available to gas was continuously decreasing during this stage because the water crystal lattice expands when it transforms from ice Ih to sI methane hydrate. In stage 4, the temperature stabilized at 17°C and gas pressure decreased as the methane hydrate formation reaction continued to consume methane gas molecules. The pressure decreased for approximately 16 hours and then stabilized. After the methane gas pressure had been stable for six hours, the methane hydrate formation reaction was declared complete and stage 5, sample cooling began. In stage 5, the sample cooled slowly from 17°C to −20°C over 27

hours. The pressure versus temperature curve is again linear and it is important to note that there is no hitch in the curve as the sample passes through 0°C or at any temperature below 0°C. This signifies that there was no detected free-water-to-ice phase transition occurring in the pressure vessel (see Figure 6 in Stern et al. 1998, for an example of a freezing event).

The vertical separation between the pressure-temperature curve during stages 1 and 5 is a function of the free gas volume in the system during stages 1 and 5, the thermodynamic properties of methane gas and the amount of gas taken up by the sample during the hydrate formation reaction. Unfortunately, it is extremely difficult to accurately measure the total gas volume of the system and this experiment was conducted in parallel with a thermal conductivity experiment. Therefore, only part of the gas consumed in the reaction was incorporated into the wave speed sample. This makes it impractical to use this data to infer the cage occupancy rate of the methane hydrate formed in this specific experiment. However, Stern and co-workers (Stern et al., 2000) have performed a number of experiments specifically designed to determine the conversion efficiency and resultant stoichiometry of methane hydrate formed using this method. They have shown, using precise thermometry and disassociation experiments, that this method is better than 99% efficient at converting ice to methane hydrate and that the resultant bulk, porous methane hydrate samples have a stoichiometry of 5.89 ± 0.01 H_2O to 1 CH_4 (Stern et al., 2000), slightly greater than the ideal, 100% cage occupancy rate stoichiometry of 5.75 H_2O to 1 CH_4. In the wave speed experiments, the stoichiometry of the compacted methane hydrate has not been measured directly. Therefore, I assume a "standard" ratio of 6 H_2O to 1 CH_4, corresponding to a cage occupancy rate of 95.8%. This occupancy rate is assumed in the methane hydrate density calculations performed below. 100% conversion of the initial 13.98 g of ice to methane hydrate with a 95.8% cage occupancy rate gives an estimate of approximately 0.1 moles (or over 2000 cm^3 at STP) of methane gas incorporated into the sample.

Compaction

Once the system had equilibrated at -20°C and $\sim$ 300 psia gas pressure, the sample was compacted. The bath temperature, piston and methane pressure and sample length data for this portion of the experiment are given in Figure 5.34. As discussed in the procedure section above, the sample was compacted initially to 15,000 psi piston pressure at -20°C,

then warmed to 5°C and compacted again and warmed to 20°C and compacted a third time. The sample length data prior to the completion of the compaction at 5°C were not accurate enough to calculate wave speeds. To summarize the waveform data results for this portion of the experiment, I plot the shear signal delay times (based on the arrival of the first peaks) and the frequency of maximum power (i.e., central frequencies) of the shear waveforms in Figure 5.35.

Figure 5.35 shows that the signal delay time varied smoothly, monotonically decreasing, until the sample was warmed from −20°C to 5°C. As the sample warmed, the signal delay increased as would be expected for a sample that was thermally expanding and/or "softening" as it got warmer. At the same time, oil pressure increased as expected for a thermally expanding fluid (i.e., hydraulic oil) in a constant volume system. However, as the temperature bath passed through 0°C, the signal delay time began to decrease, as did the oil pressure. At the same time, the central frequency of the shear waveform dropped discontinuously. Unfortunately, the LMP had not yet been replaced, and manual length measurements were not made during this time. Therefore, it is unknown exactly how the sample length changed during this time period. However, it can be inferred from the decrease in piston pressure that the sample shortened at this point, displacing the piston and increasing the oil reservoir volume. An increase in oil reservoir volume explains the quick decrease in piston (oil) pressure, but does not explain why the sample would have shortened at that point. The sample shortening can be explained by looking at the temperature at which this anomalous behavior occurred.

As stated above, all three of the features, the change in oil pressure, the change in signal delay time and the discontinuous jump in shear wave central frequency all occurred as the bath was warming from −20 to 5°C. In fact, they all occurred as the bath temperature passed through 0°C, the melting point of ice. Based on the available evidence in this portion of the experiment and the data discussed in the temperature cycling section below, the most reasonable conclusion is that some ice was present in the sample, apparently formed during the initial compaction of the sample at −20°C, and that this trace amount of ice melted as the sample warmed through 0°C.

The amount of ice present cannot have been large: no freezing signature was present in the gas pressure data during cooling following synthesis; the gas pressure increased less

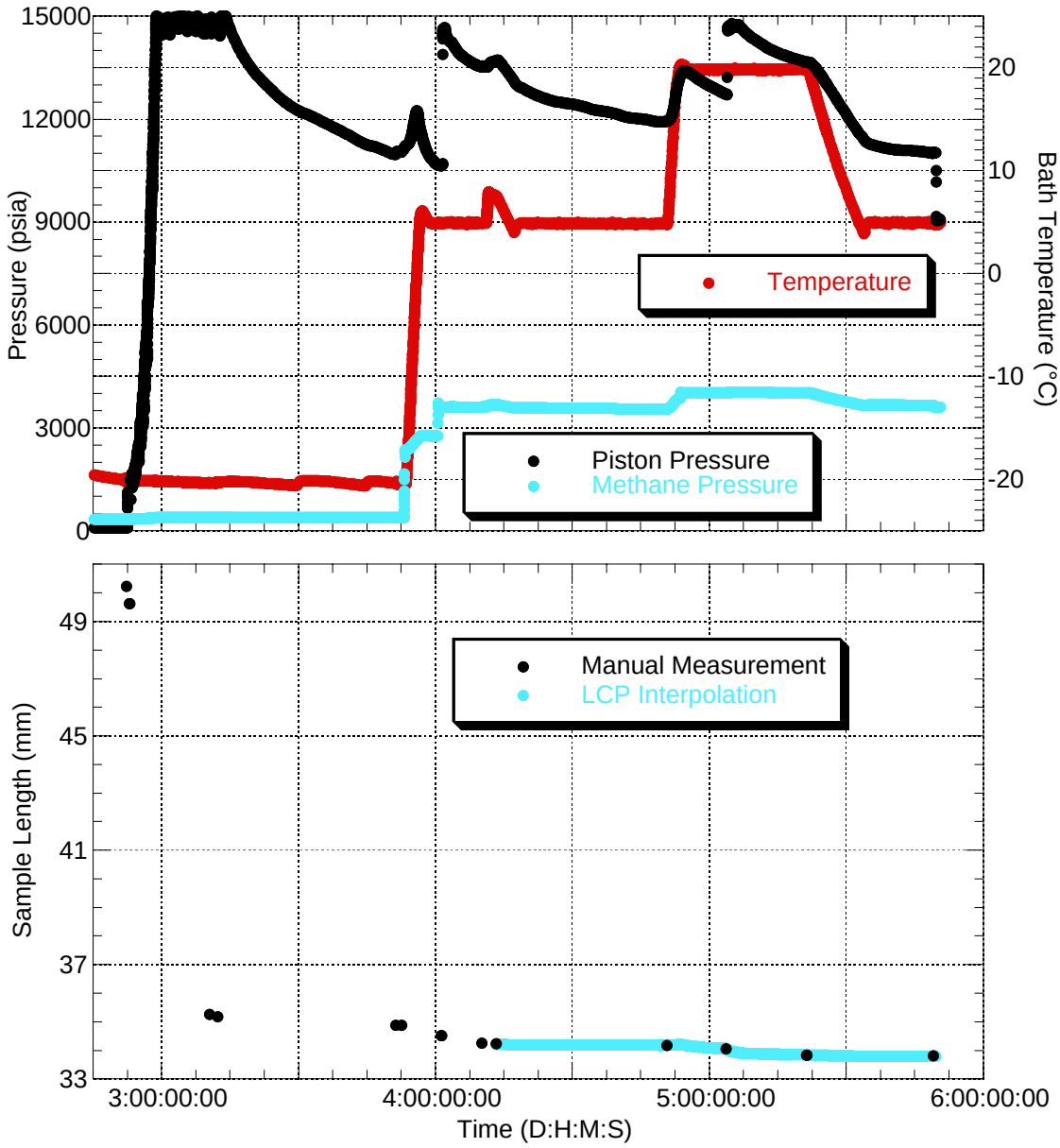

Figure 5.34: Piston pressure, methane pressure, bath temperature and sample length versus time during the compaction portion of the polycrystalline methane hydrate experiment. Both plots have the same horizontal axis, time in days:hours:minutes:seconds. **Top:** Piston pressure, methane pressure and bath temperature versus time. The data show the initial compaction at -20°C and the subsequent additional compaction at 5 and 20°C. The glitch in the bath temperature during day 4 is associated with replacing the faulty LMP (see text). On day 3, as the sample warmed from -20 to 5°C, the piston pressure increased and then quickly rolled over and began to decrease as the bath temperature passed through -2°C. **Bottom:** Manual (black) and LMP based (blue) sample length measurements versus time. The LMP was found to be faulty during this experiment and was replaced with a new one of the same model. The manual measurements are too sparse to reliably estimate sample length during compaction.

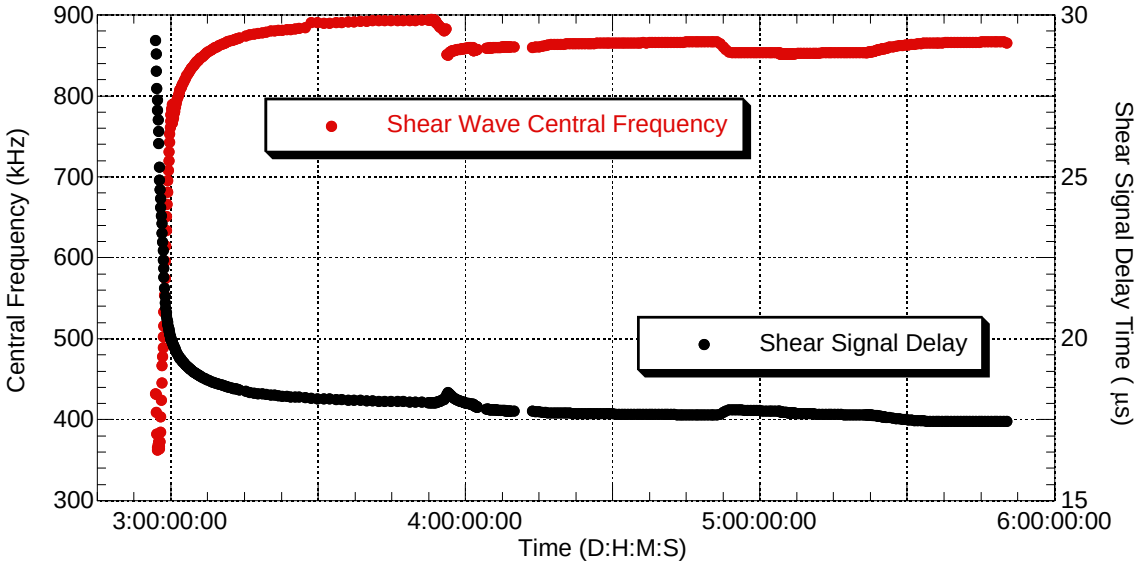

Figure 5.35: Central frequency and shear wave signal delay time versus time for the compaction portion of the polycrystalline methane hydrate experiment. On day three, as the bath temperature increased from -20 to 5°C, the shear wave signal delay time increased and then began to decrease as the temperature passed through -2°C. At the same time, the central frequency decreased discontinuously. When combined with evidence from the temperature cycling portion of the experiment, these observations strongly suggest that free water(ice) was present in the sample (see text).

than 45 psi during the initial compaction, much less than would be expected if a significant amount of gas had been liberated from the methane hydrate; no methane pressure anomaly was visible during the heating from -20°C to 5°C; and the effect on wave speeds (see temperature cycling section below) was very small. Nevertheless, had this "ice-melting" signature been recognized for what it was at the beginning of the experiment, the sample would have been put through another synthesis cycle or the run would have been stopped. This signature had not been seen in any of the previous twenty-three methane hydrate experiments and its significance went unrecognized. Fortunately, the effect of this trace amount of ice/water was too small to significantly change any of the fundamental conclusions drawn from the results (see below).

Compressional and shear wave speeds could be calculated from the waveforms acquired after the original LMP was replaced. Those wave speeds are plotted versus time in Figure 5.36. As was done for the wave speed plots in the ice experiment section, the two vertical axes are scaled such that $V_P = 2V_S$. Therefore, when the compressional and shear wave speed data overlap, $V_p/V_S = 2$ and Poisson's ratio is 0.33, the accepted value

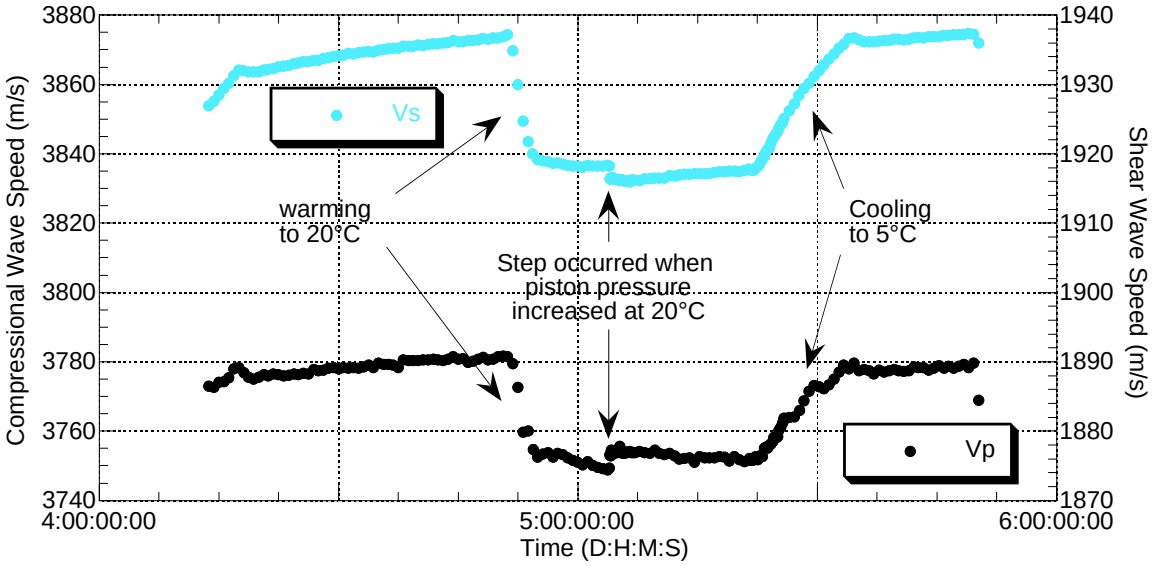

Figure 5.36: Compressional and shear wave speed versus time for a portion of the compaction stage of the polycrystalline methane hydrate experiment. Relative uncertainty in the compressional and shear wave speed data is 0.4 and 0.3%, respectively. This plot shows the variation of the compressional and shear wave speeds as the sample was heated from 5 to 20°C, compacted, and then cooled back down to 5°C. Since the wave speeds did not change significantly when the sample was compacted at 20°C and the wave speeds measured at 5°C before and after compaction at 20°C are the same, we can conclude the sample is fully compacted. This conclusion is supported by the expected zero porosity sample length calculated in the text.

for ice. As can be seen in Figure 5.36, there is significant separation between the two wave speeds, much more so than in the ice experiment (e.g., Figure 5.18). The pressure, temperature and length data associated with the wave speeds presented in Figure 5.36 are given in Figure 5.37.

The relative uncertainties in the wave speeds presented in Figure 5.36 are calculated from Equation 5.3 with Δl as 0.1 mm, Δt as one half the time sampling of the relevant waveform and Δt_0 as the standard deviation of the fit to the arrival time of the first extremum of the reference waveform as given in Tables 5.1 and 5.2. The result is a calculated relative uncertainty of $\pm 0.4\%$ (~ 14 m/s) for compressional wave speeds and $\pm 0.3\%$ (~ 6 m/s) for shear wave speeds. Because of the presence of free water/ice in the sample, this is likely an underestimate of the error in the measurements. However, the observed effect of the water freezing (ice melting) is very small (see below) and the total error in the measurements is probably less than 1-2%.

The data in Figures 5.36 and 5.37 show that the sample was essentially fully compacted.

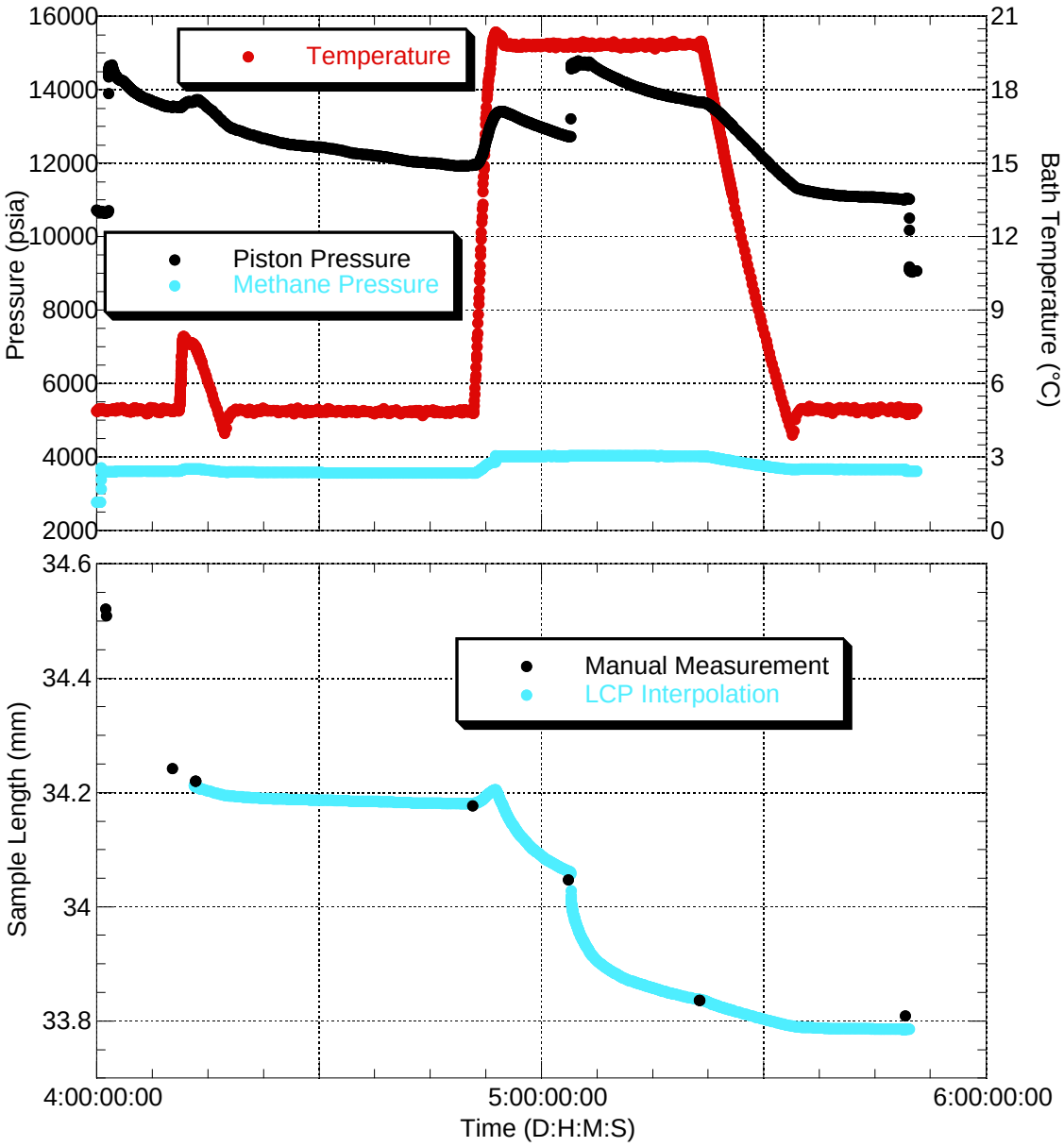

Figure 5.37: Piston pressure, methane pressure, bath temperature and sample length versus time for a portion of the compaction stage of the polycrystalline methane hydrate experiment. Both plots have the same horizontal axis, time in days:hours:minutes:seconds. **Top:** Piston pressure, methane pressure and bath temperature versus time for the portion of the compaction stage of the experiment where compressional and shear wave speeds could be determined. **Bottom:** Sample length versus time. Wave speeds were calculated in the time interval where LMP based sample length measurements were considered reliable.

The wave speeds at 5°C before and after the compaction at 20°C are equal and the changes in wave speed during compaction were minimal. That the sample was fully compacted is also supported by the zero porosity length estimate obtained for this sample.

In Chapter 4, I showed that the sample height expected for a right, cylindrical sample of radius r for fully dense methane hydrate formed from n grams of ice was

$$h_0 = \frac{n}{\rho_{hyd}\,\pi\,r^2}, \tag{5.24}$$

where ρ_{hyd} is the density of sI hydrate with all of its cages empty. As in the ice experiment, the sample radius was 1.27 ± 0.01 cm and the estimated loss of initial ice mass was 0.1 g. Therefore, the total mass of ice available for incorporation into the methane hydrate sample was 13.88 ± 0.10 g. The density of empty sI clathrate hydrate calculated from the unit cell dimension of sI hydrate given as a function of temperature in Equation 2.42 is approximately 0.80 g/cm^3 in the temperature range 5°C to 20°C. This density value is relatively unconstrained because there are very few published measurements of the sI unit cell dimension. I estimate the uncertainty in ρ_{hyd} as ± 0.01g/cm^3. Applying these values and their uncertainties to the calculation of h_0, I obtain, $h_0 = 34.2 \pm 0.7$ mm, where $\Delta h_0 = 0.7$ mm was calculated from Equation 5.7 by replacing ρ_{ice} and $\Delta\rho_{ice}$ with ρ_{hyd} and $\Delta\rho_{hyd}$. As shown in Figure 5.37, the measured sample lengths fall within this interval, suggesting the sample was fully compacted.

It is interesting to note in Figure 5.36 that shear wave speed decreased and compressional wave speed increased when piston pressure was increased at 20°C. This suggests that, like ice Ih, shear wave speed in methane hydrate decreases with increasing confining pressure. This is confirmed by data acquired during the depressurization stage of the experiment (see below).

Temperature Cycling

The pressure, temperature and length data from the temperature cycling portion of the experiment are shown in Figure 5.38. As discussed in the processing section above, the LMP voltages obtained during this portion of the experiment were unreliable. Therefore, only the manual measurements were used to determine sample length. The number of manual measurements was high and the total sample length varied by only ± 0.10 mm during this

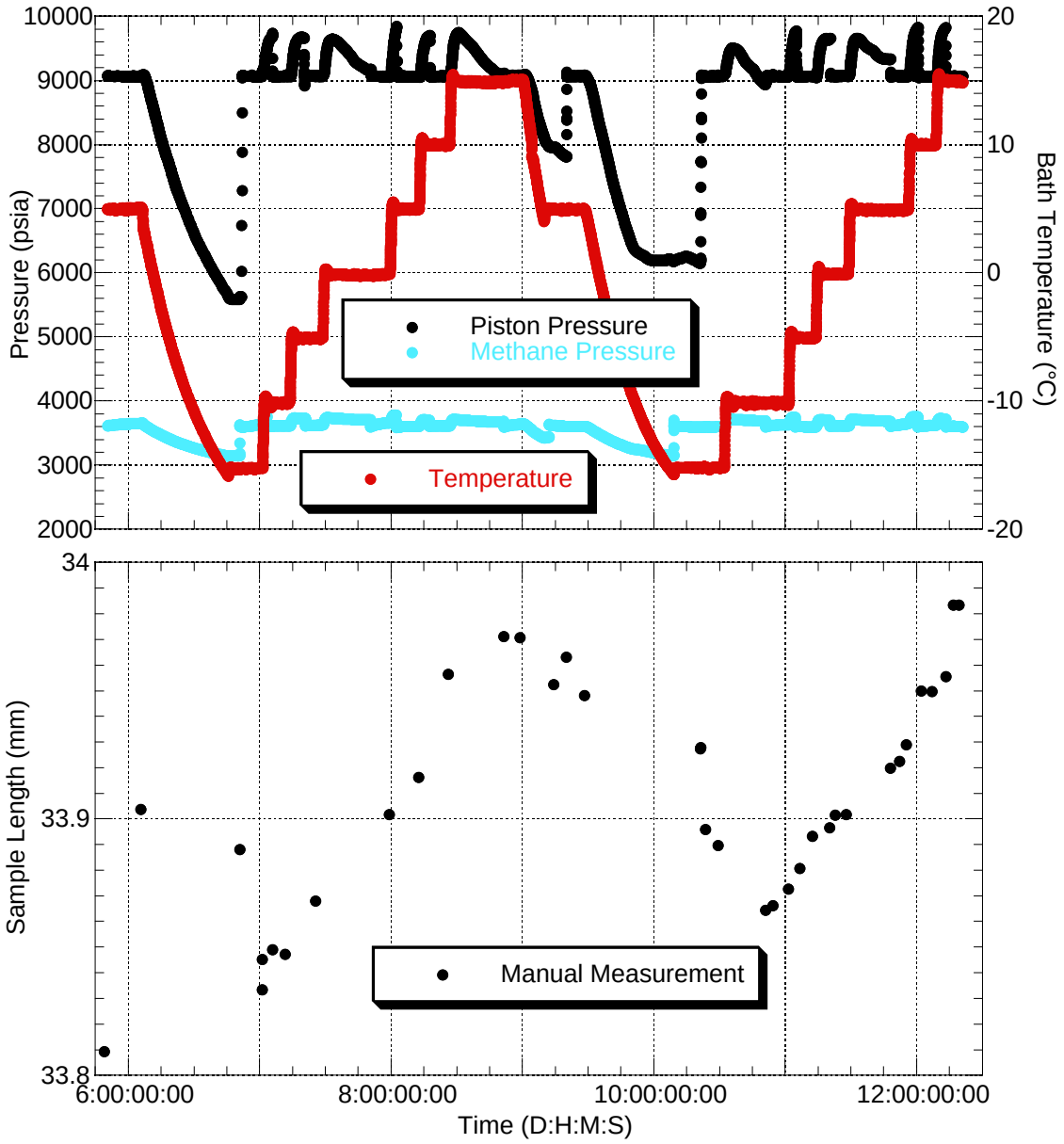

Figure 5.38: Piston pressure, methane pressure, bath temperature and sample length versus time for the temperature cycling portion of the polycrystalline methane hydrate experiment. Both plots have the same horizontal axis, time in days:hours:minutes:seconds. **Top:** Piston pressure, methane pressure and bath temperature versus time. **Bottom:** Sample length versus time. LMP output was unreliable during this portion of the experiment. Only manual measurements were used to determine sample length. The small total sample length variation ($\pm$0.1mm) meant that linearly interpolating between the manual measurements did not incur a significant error.

portion of the experiment. The total error in linearly interpolating sample lengths between manual measurements should be much less than 0.10 mm.

The compressional and shear wave speeds obtained for this portion of the experiment are shown in Figure 5.39 along with the central frequencies of the associated compressional and shear waveforms. The calculated relative uncertainties in the plotted wave speeds are the same as in the compaction section, $\pm 0.4\%$ and $\pm 0.3\%$ for compressional and shear wave speeds, respectively.

A close inspection of the wave speed results reveals there are four step-like discontinuities in the compressional and shear wave speeds, two positive and two negative. The two negative step discontinuities are associated with the two -5 to 0°C temperature steps and the two positive step discontinuities are associated with the two 5 to -15°C temperature steps. These four discontinuities are more distinct in the shear wave central frequency data (bottom plot Figure 5.39). The two negative step discontinuities in the frequency data are similar to the negative step discontinuity in the frequency data from the compaction stage of the experiment (Figure 5.35).

The fact that the wave speed and center frequency discontinuities were all associated with crossing the freezing temperature of water strongly suggests that free water was present in the sample. The sense of change in the wave speeds (i.e., up when going from positive to negative temperatures and vice versa) supports this hypothesis. The magnitude of the wave speed changes suggests the amount of water was very small. The shear wave speed changed by only 10 m/s at the discontinuities, the compressional wave speed by only 20 m/s. In both cases, a change of 0.5%, only slightly larger than the estimated uncertainty in the measurements themselves. Because the wave speed shifts induced by the freezing of free water (and the melting of ice) were small, no attempt was made to remove them.

As discussed above, a subset of compressional and shear waveforms were taken two hours after thermal equilibrium had been achieved at each temperature. The wave speeds determined from those waveforms are plotted versus temperature in Figure 5.40. The lines in the figure are the best fit curves through the data (Table 5.6). Poisson's ratios calculated from the wave speeds in Figure 5.40 (Equation 5.14) are plotted in Figure 5.41 versus temperature. There is no net trend with temperature, so Poisson's ratio is quoted as the mean of the measurements plus or minus the standard deviation, $\nu = 0.3205 \pm 0.0003$.

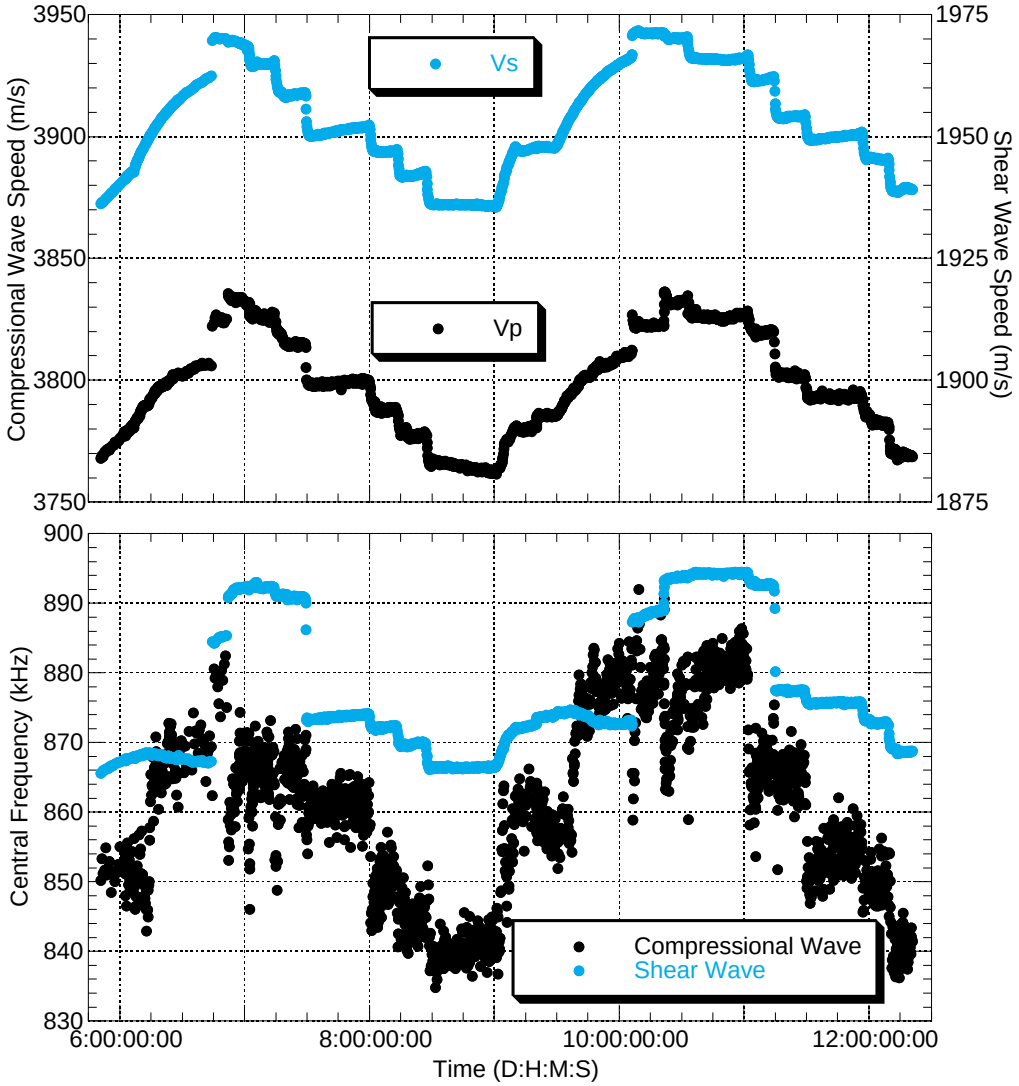

Figure 5.39: Compressional wave speed, shear wave speed, compressional waveform central frequency and shear waveform central frequency versus time for the temperature cycling portion of the polycrystalline methane hydrate experiment. Both plots have the same horizontal axis, time in days:hours:minutes:seconds. **Top:** Compressional and shear wave speed versus time. Relative uncertainties in the compressional and shear wave speeds are 0.4 and 0.3%, respectively. The vertical axes are scaled such that $V_P = 2V_S$, so if the data overlap, $V_P/V_S = 2$ and Poisson's ratio is 0.33. There are four step-like discontinuities in the wave speed data, two positive ones associated with temperature changes from 5 to -20°C and two negative ones associated with temperature changes from -5 to 0°C. For both the compressional and shear wave speeds, the magnitude of the step discontinuity is approximately 0.5% of the wave speed. These data strongly suggest a small amount of free water was present in the sample. **Bottom:** Compressional and shear waveform central frequency versus time. Four step discontinuities are clearly evident in the shear waveform central frequency data. They occur at the same time as the step discontinuities in the wave speed measurements. This observation suggests that the frequency discontinuity observed in the shear waveform central frequency data acquired during sample compaction also signified the presence of free water/ice in the sample.

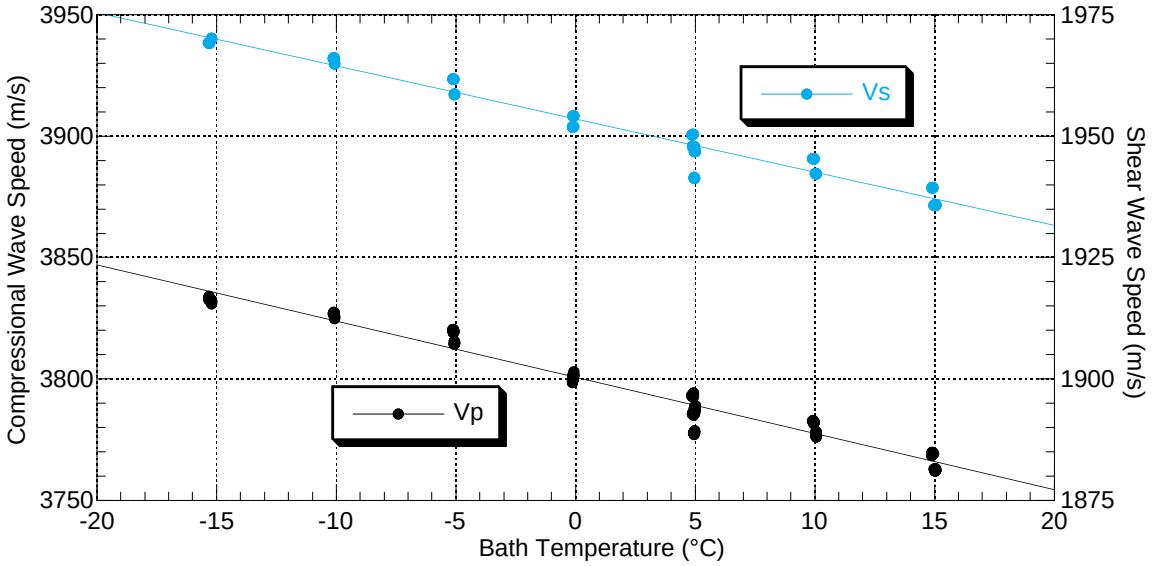

Figure 5.40: Compressional and shear wave speed versus temperature at 9,000 psi piston pressure for the temperature cycling portion of the polycrystalline methane hydrate experiment. Relative uncertainty in the compressional and shear wave speeds is 0.4 and 0.3%, respectively. These data are a subset of the measurements presented in Figure 5.39. They are sets of 10 waveforms acquired at each temperature after the sample had be stable at that temperature for two hours. Lines through the data are linear regressions of wave speed versus temperature (see Table 5.6).

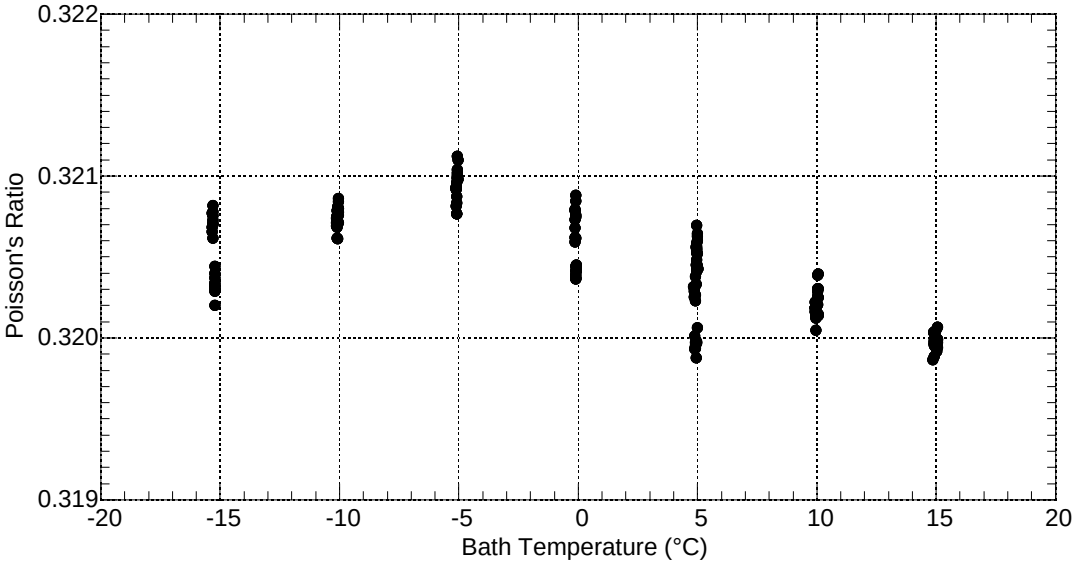

Figure 5.41: Poisson's ratio versus temperature at 9,000 psi piston pressure for the temperature cycling portion of the polycrystalline methane hydrate experiment. Relative uncertainty in the data is 0.6%. No net trend with temperature is observed, so Poisson's ratio is reported as the mean $\pm$ the standard deviation, 0.3205 ± 0.0003.

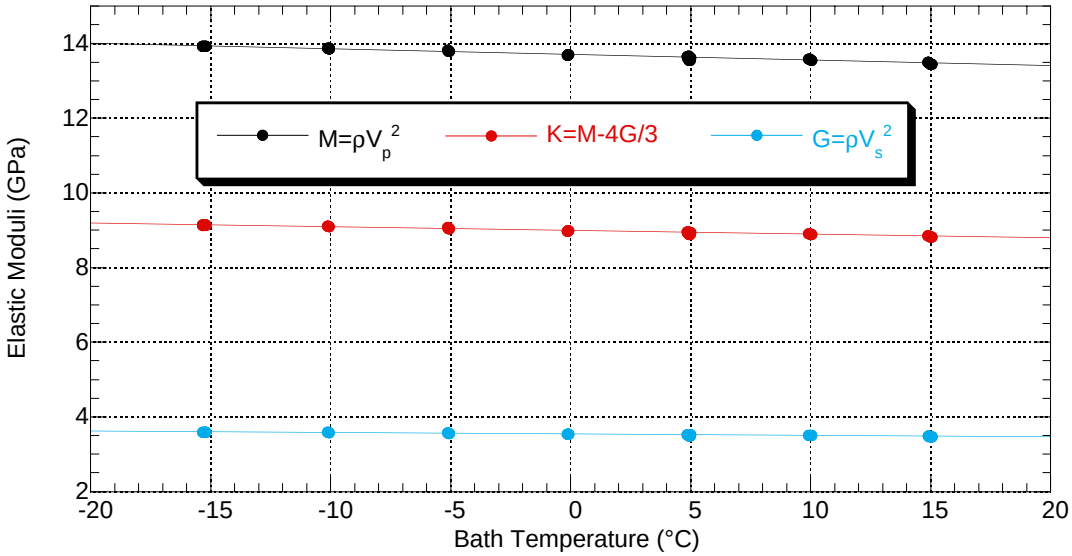

Figure 5.42: Dynamic compressional wave, bulk and shear moduli versus temperature at 9,000 psi piston pressure for the temperature cycling portion of the polycrystalline methane hydrate experiment. The relative uncertainty in all three dynamic moduli is 2%. Lines through the data are linear regressions of dynamic moduli versus temperature (see Table 5.6).

The density of methane hydrate with 95.8% of the available cages occupied can be calculated from Equation 2.54 in the temperature range -15 to 15°C. The result is 0.924 to 0.930 g/cm^3. These values are relatively uncertain, however, because of the limited number of published methane hydrate unit cell measurements, the unknown effect of confining pressure on unit cell volume, assumptions about cage occupancy and the small amount of water/ice present in the sample. The density could easily vary by ± 0.02 g/cm^3. Therefore, to convert the compressional and shear wave speeds in Figure 5.40 to compressional wave, bulk and shear moduli via Equations 5.11 through 5.13, I set the density of the sample equal to 0.927 ± 0.020 g/cm^3. The results for the moduli are plotted as functions of temperature in Figure 5.42. The relative uncertainty is approximately 2% for all three moduli (Equations 5.15 to 5.17).

The regressions of compressional wave speed, shear wave speed, Poisson's ratio, compressional wave modulus, shear modulus and bulk modulus versus temperature at 9,000 psi piston pressure are given in Table 5.6.

Table 5.6: Regressions of Wave Speeds and Elastic Moduli vs Temperature (−15 to 15°C) for the Compacted, Polycrystalline Methane Hydrate Sample at 9000 psi Uniaxial Pressure

	$F(T) = a \cdot T + c$		
$F(T)$	a†	c†	std††
Vp (m/s)	-2.32 ± 0.04	3800.5 ± 0.3	4
Vs (m/s)	-1.10 ± 0.02	1953.5 ± 0.2	2
ν	0	0.3205	0.0003
M (GPa)	$-(1.56 \pm 0.02) \times 10^{-2}$	13.703 ± 0.002	0.03
G (GPa)	$-(3.98 \pm 0.07) \times 10^{-3}$	3.538 ± 0.001	0.01
K (GPa)	$-(1.03 \pm 0.02) \times 10^{-2}$	8.986 ± 0.001	0.02

† Units for a are the units of the property being fit divided by °C. Units for c are those of the property being fit.

†† Standard deviation of the residuals to the fit equation $F(T) = a \cdot T + c$. Units are those of the property being fit.

Depressurization

The pressure, temperature and sample length data from the final stage of the experiment, depressurization, are shown in Figure 5.43. Note that the temperature bath was at 15°C for this portion of the experiment, so no ice was present in the sample. The sample length data stop when the piston pressure rises from 1,700 to 3,600 psi because that is the point at which the piston was pushed off the sample by gas pressure. Compressional wave speed, shear wave speed and Poisson's ratio for this portion of the experiment are given in Figure 5.44. The relative uncertainties in compressional wave speed, shear wave speed and Poisson's ratio are 0.4, 0.3 and 0.6%, respectively.

From Figures 5.43 and 5.44, one can see that compressional wave speed decreases as piston pressure decreases but shear wave speed increases. For piston pressures less than the gas pressure of 3,600 psi, both the compressional and shear wave speeds drop discontinuously when the piston pressure is reduced in a 500 psi step. Then, as the piston pressure is held constant at the new level, the wave speeds recover to a value slightly below their level at the previous pressure value. This is strong evidence that once the piston pressure falls below the gas pressure, gas can force its way into cracks formed within the sample as the confining pressure is reduced (e.g., Meglis et al., 1995). While the piston

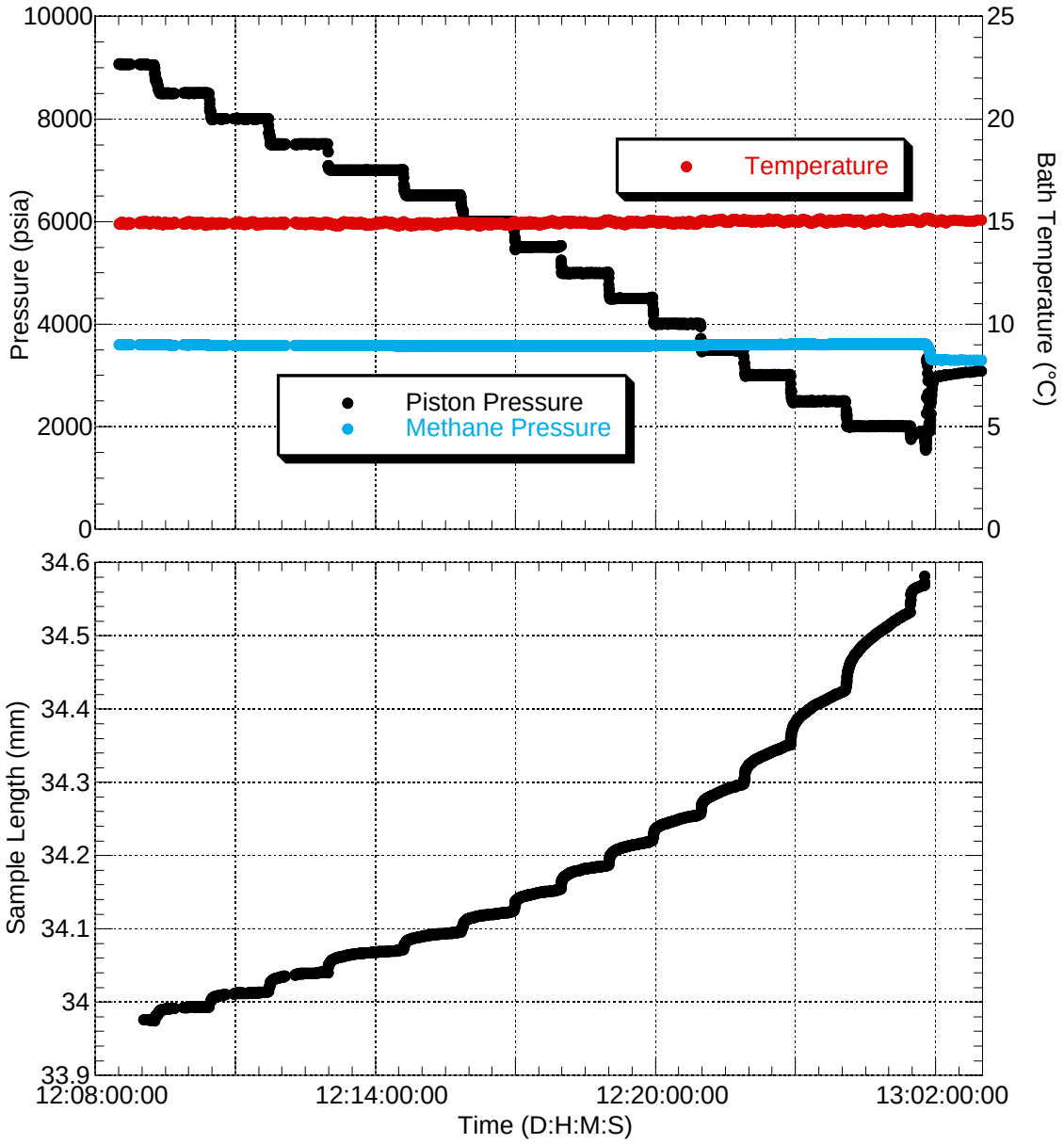

Figure 5.43: Piston pressure, methane pressure, bath temperature and sample length versus time for the depressurization portion of the polycrystalline methane hydrate experiment. Both plots have the same horizontal axis, time in days:hours:minutes:seconds. **Top:** Piston pressure, methane pressure and bath temperature versus time. Bath temperature was held constant at 15°C. The piston pressure was decreased in 500 psi steps approximately every hour until the piston was pushed off the sample going from 2,000 to 1,500 psi. It is interesting to note that the stability pressure for methane hydrate at 15° is $\sim 2,000$ psi. **Bottom:** Sample length versus time. The sample length increased with each pressure reduction step and then continued to increase slowly while the piston pressure was held constant. The sample length change per pressure step increased as the piston pressure decreased. The sample length data stop where the piston was pushed off the sample.

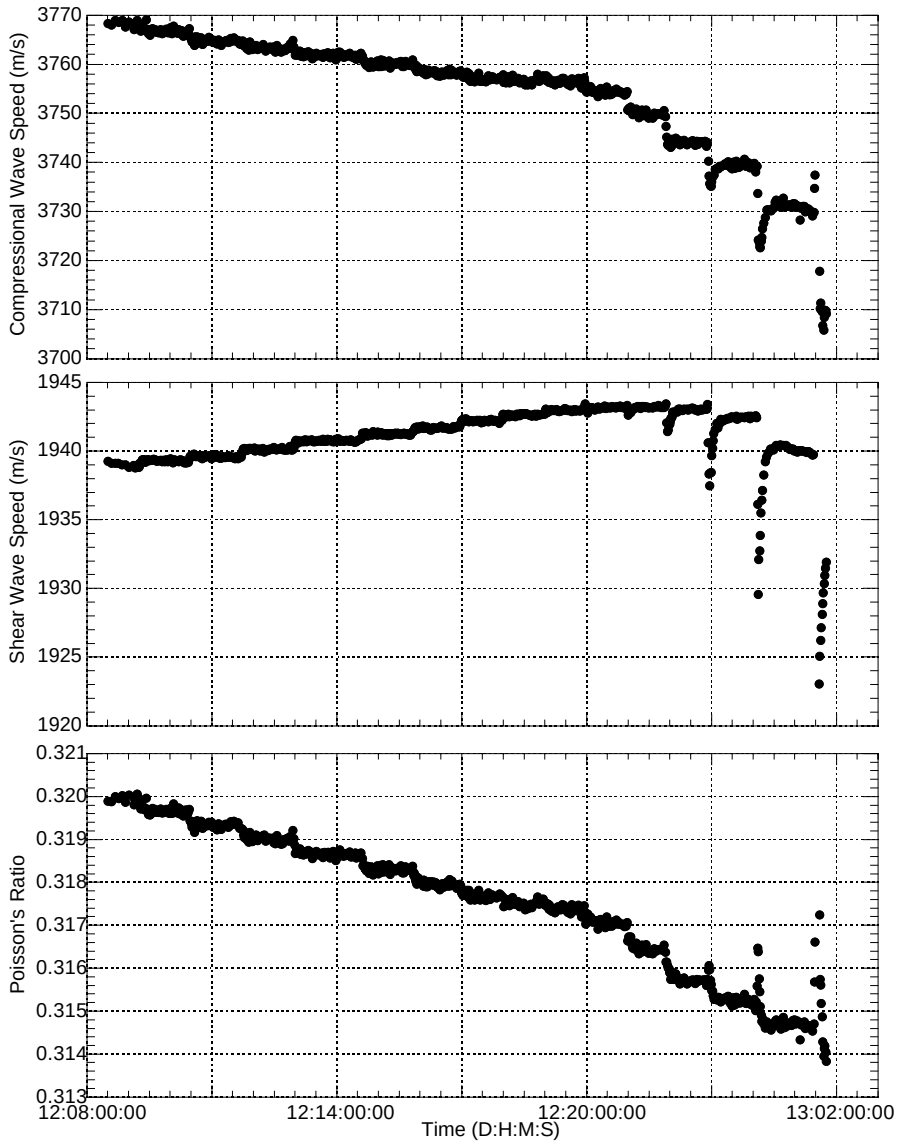

Figure 5.44: Compressional wave speed, shear wave speed and Poisson's ratio versus time during the depressurization portion of the polycrystalline methane hydrate experiment. Horizontal axis is the same as in Figure 5.43, time in days:hours:minutes:seconds. **Top:** Compressional wave speed versus time. Relative uncertainty is 0.4%. Compressional wave speed decreases linearly with time until about 12:20:00:00, when it begins to decrease in significant steps and then recover to a value slightly below the pre-step value. This transition occurs when the piston pressure falls below the methane gas pressure, suggesting this phenomenon is caused by gas forcing its way into cracks that formed in the sample during unloading. Compressional wave speed recovery with time at constant piston pressure suggests these cracks "heal" after they form. **Middle:** Shear wave speed versus time. Relative uncertainty is 0.3%. Shear wave speed increases linearly with time until about 12:20:00:00, when it begins to decrease in significant steps and then recover to a value slightly below the pre-step value. This transition occurs when the piston pressure falls below the methane gas pressure, suggesting that this phenomenon is caused by gas forcing its way into cracks that formed in the sample during unloading. Shear wave speed recovery with time at constant piston pressure suggests these cracks "heal" after they form. **Bottom:** Poisson's ratio versus time. Relative uncertainty is 0.6%.

pressure is held constant after each pressure decrease, some of the cracks "heal" and the wave speeds recover. This conclusion is supported by the cracks visible in the sample when it was recovered from the apparatus (Figure 5.30). This cracking and healing process continued at each pressure step below 3,500 psi until the piston was eventually pushed off the sample by the gas pressure. At that point, the condition of the sample could no longer be monitored acoustically.

Because shear wave speed increased and compressional wave speed decreased in the sample with decreasing piston pressure, Poisson's ratio decreased with decreasing piston pressure. Poisson's ratio dropped by about 1% from 0.320 to 0.317 as the pressure applied by the piston dropped from 9,000 to 4,000 psi.

Assuming a density of 0.927 ± 0.020 g/cm^3 for methane hydrate, these wave speeds can be converted to compressional wave, bulk and shear moduli via Equations 5.11 through 5.13. The relative uncertainty in the calculated compressional wave, shear and bulk moduli is 2%. The effects of sample cracking contaminate the data for piston pressures less than 4,000 psi. Therefore, in Figure 5.45, compressional and shear wave speeds, Poisson's ratio, compressional wave, bulk and shear moduli are plotted versus piston pressure from 4,000 to 9,000 psi. The lines in the plots are the linear regressions fit to the data. The regressions are provided in Table 5.7.

By combining data from the temperature cycling and depressurization stages of the experiment, 2-D planar regressions of compressional and shear wave speeds; Poisson's ratio; and compressional wave, bulk and shear moduli versus temperature and pressure can be calculated. The regressions are presented in Table 5.8.

5.6 Conclusions

Results from the experiments described in this chapter and in Chapter 4 illustrate several relationships between ice Ih and methane hydrate:

- Porous methane hydrate is much more resistant to compaction than porous ice Ih. A pressure of 6,000 psi fully compacted the ice sample at -5°C while a pressure of 15,000 psi was required to fully compact the methane hydrate sample at -20°C.

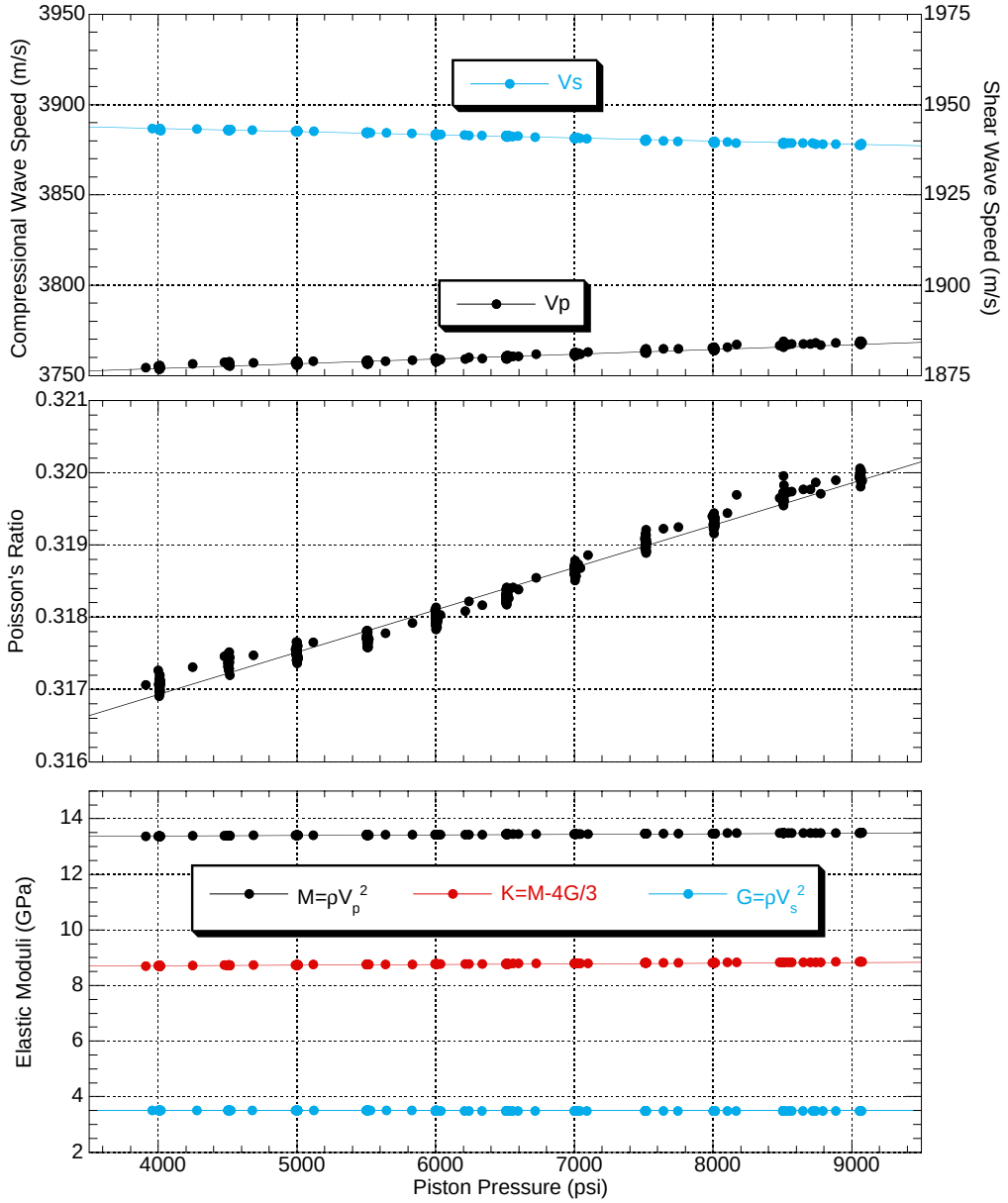

Figure 5.45: Compressional wave speed, shear wave speed, Poisson's ratio, and dynamic compressional wave, bulk and shear moduli versus piston pressure at 15°C for the depressurization portion of the polycrystalline methane hydrate experiment. The horizontal axis is the same for all three plots, piston pressure in psi. **Top:** Compressional and shear wave speed versus piston pressure from 4,000 to 9,000 psi at 15°C. Relative uncertainties are 0.4 and 0.3% for the compressional and shear wave speeds, respectively. Lines are regressions to the data versus pressure (see Table 5.7). Note that the vertical axes are scaled the same as in Figure 5.40. **Middle:** Poisson's ratio versus piston pressure from 4,000 to 9,000 psi at 15°C. Relative uncertainty is 0.6%. Line through the data is a regression versus pressure (see Table 5.7). **Bottom:** Dynamic compressional wave, bulk and shear moduli versus piston pressure from 4,000 to 9,000 psi at 15°C. Relative uncertainties are 2% for all three dynamic moduli. Lines are regressions to the data versus pressure (see Table 5.7).

Table 5.7: Regressions of Wave Speeds and Elastic Moduli vs Pressure (9000 to 4000 psi Uniaxial Pressure) for the Compacted, Polycrystalline Methane Hydrate Sample at 15°C

	$F(P) = b \cdot P + c$		
$F(P)$	b†	c†	std††
Vp (m/s)	$(2.69 \pm 0.03) \times 10^{-3}$	3743.2 ± 0.2	0.8
Vs (m/s)	$-(9.13 \pm 0.05) \times 10^{-4}$	1947.09 ± 0.03	0.2
ν	$(5.87 \pm 0.04) \times 10^{-7}$	0.31459 ± 0.00003	0.0001
M (GPa)	$(2.24 \pm 0.01) \times 10^{-5}$	13.293 ± 0.001	0.003
G (GPa)	$-(3.29 \pm 0.02) \times 10^{-6}$	3.5143 ± 0.0001	0.0005
K (GPa)	$(2.68 \pm 0.01) \times 10^{-5}$	8.607 ± 0.001	0.003

† Units for b are the units of the property being fit divided by °C. Units for c are those of the property being fit.

†† Standard deviation of the residuals to the fit equation $F(P) = b \cdot P + c$. Units are those of the property being fit.

Table 5.8: Regressions of Wave Speeds and Dynamic Elastic Moduli versus Temperature (−15 to 15°C) and Piston Pressure (4000 to 9000 psi) in the Compacted, Polycrystalline Methane Hydrate Sample

	$F(T,P) = a \cdot T + b \cdot P + c$			
$F(T,P)$	a†	b†	c†	std††
Vp (m/s)	-2.27 ± 0.01	$(2.52 \pm 0.07) \times 10^{-3}$	3778.0 ± 0.6	2
Vs (m/s)	-1.04 ± 0.01	$-(1.08 \pm 0.03) \times 10^{-3}$	1963.6 ± 0.3	1
ν	0	$(6.83 \pm 0.06) \times 10^{-7}$	0.31403 ± 0.00005	0.0003
M (GPa)	$-(1.47 \pm 0.01) \times 10^{-2}$	$(1.99 \pm 0.05) \times 10^{-5}$	13.527 ± 0.004	0.02
G (GPa)	$-(3.77 \pm 0.03) \times 10^{-3}$	$-(3.9 \pm 0.1) \times 10^{-6}$	3.574 ± 0.001	0.004
K (GPa)	$-(9.71 \pm 0.06) \times 10^{-3}$	$(2.51 \pm 0.03) \times 10^{-5}$	8.762 ± 0.003	0.01

† Units for a are the units of the property being fit divided by °C. Units for b are those of the property being fit divided by psi. Units for c are those of the property being fit.

†† Standard deviation of the residuals to the fit equation $F(T,P) = a \cdot T + b \cdot P + c$. Units are those of the property being fit.

- Compressional and shear wave speed in the ice and methane hydrate samples increased in the absence of active compaction (i.e., at constant sample length), strongly suggesting that grain to grain bonds formed between adjacent ice (methane hydrate) grains in the porous samples. The relative wave speed increases with time further suggested that ice was more efficient at this process, perhaps due to the higher mobility of water in ice's crystal lattice.

- 2-D linear regressions fit to the wave speed data (Tables 5.3 and 5.8) show that within the piston pressure and temperature ranges where measurements were made on both methane hydrate and ice (4,000 to 4,750 psi and -5 to -15°C, respectively), compressional wave speed was greater in fully dense ice Ih and shear wave speed was greater in fully dense methane hydrate. As a result, the wave-speed-based calculations of Poisson's ratio were smaller in methane hydrate than they were in ice Ih.

- In the temperature range where compressional and shear wave speed measurements were made on both methane hydrate and ice (-5 to -15°C), Whalley's method (using the methods and values of properties adopted in this thesis) predicts a compressional wave speed ratio between hydrate and ice of 0.976 to 0.973 (Equation 2.12) and a shear wave speed ratio of 0.997 to 0.994 (Equation 2.64). Both are in excellent agreement with the actual measured compressional and shear wave speed ratios of 0.976 to 0.975 and 1.005 to 1.003, respectively.

- Converting wave speeds to dynamic moduli showed that within the piston pressure and temperature ranges where both methane hydrate and ice were studied (4,000 to 4,750 psi and -5 to -15°C, respectively), compressional wave and bulk moduli were smaller and shear modulus was greater in fully dense methane hydrate than in fully dense ice Ih.

- The "static", high-strain, "isothermal" compressional wave modulus measured for ice was approximately one half the value of the dynamic, low-strain, "adiabatic" compressional wave modulus determined from the compressional wave speed measurements.

- Shear wave speed decreased with increasing confining pressure in both fully dense ice Ih and fully dense methane hydrate. This behavior has been observed by others for ice Ih. No previously reported measurements of shear wave speed in methane hydrate are available for comparison.

- Within the pressure and temperature ranges studied, shear wave speed varied less with temperature and pressure in fully dense methane hydrate than it did in fully dense ice Ih. Compressional wave speed in fully dense methane hydrate varied less with temperature but more with pressure than it did in fully dense ice Ih.

- Additional experiments are planned to confirm and extend these results. The methodology and apparatus described in this chapter should also be applicable for studying methane gas hydrate in sediments and other types of pure gas hydrate. Experiments on sII gas hydrates and methane hydrate in sediments are planned.

5.7 References

Bass, R., 1958, Diffraction effects in the ultrasonic field of a piston source, Journal of the Acoustical Society of America, **30**, 602–605.

Bourbié, T., O. Coussy and B. Zinszer, 1987, Acoustics of porous media, Editions Technip, Gulf Publishing Co., Houston, 334 p.

DeMartin, B., W. Waite, C. Ruppel, J. Pinkston, L. Stern and S. Kirby, 1999, Laboratory thermal conductivity measurements of methane hydrate and hydrate-sediment mixtures under simulated in situ conditions, EOS, Transactions of the American Geophysical Union, **80**, 337.

Dorsey, N. E., 1940, Properties of ordinary water–substance in all its phases: water–vapor, water and all the ices, American Chemical Society Monograph Series, Reinhold Publishing Corporation, New York, 673 pp.

Dvorkin, J., A. Nur and Yin, H., 1994, Effective properties of cemented granular material, Mechanics of Materials, **18**, 351–366.

Dvorkin, J., and A. Nur, 1996, Elasticity of High-Porosity Sandstones: Theory for Two North Sea Datasets, Geophysics, **61**, 1363–1370.

Gagnon, R. E., H. Kiefte, M. J. Clouter and E. Whalley, 1988, Pressure dependence of the elastic constants of ice Ih to 2.8 kbar by Brillouin spectroscopy, Journal of Chemical Physics, **89**, 4522–4528.

Gagnon, R. E., H. Kiefte, M. J. Clouter and E. Whalley, 1990, Acoustic velocities and densities of polycrystalline ice Ih, II, III, V, and VI by Brillouin spectroscopy, Journal of Chemical Physics, **92**, 1909–1914.

Gal, D., J. Dvorkin and A. Nur, 1998, A physical model for porosity reduction in sandstones, Geophysics, **63**, 454–459.

Gammon, P. H., H. Kiefte and M. J. Clouter, 1983, Elastic constants of ice samples by Brillouin spectroscopy, Journal of Physical Chemistry, **87**, 4025–4029.

Green, D. H. and H. F. Wang, 1991, Shear wave diffraction loss for circular, plane-polarized source and receiver, Journal of the Acoustical Society of America, **90**, 2697–2704.

Gold, L. W., 1958, Some observations on the dependence of strain on stress for ice, Canadian Journal of Physics, **36**, 1265–1275.

Hashin, Z. and S. Shtrikman, 1963, A variational approach to the elastic behavior of multiphase materials, Journal of the Mechanics and Physics of Solids, **11**, 127–140.

Hobbs, P. V., 1974, Ice physics, Clarendon Press, Oxford, 837pp.

Khimunin, A. S., 1972, Numerical calculation of the diffraction corrections for the precise measurement of ultrasound absorption, Acustica, **27**, 173–181.

Mavko, G, T. Mukerji and J. Dvorkin, 1998, The rock physics handbook, Cambridge University Press, Cambridge, 329pp.

Meglis, I. L., R. E. Gagnon and R. P. Young, 1995, Microcracking during stress-relief of polycrystalline ice formed at high pressure, Geophysical Research Letters, **22**, 2207–2210.

Mindlin, R. D., 1949, Compliance of elastic bodies in contact, Journal of Applied Mechanics, **16**, 259–268.

Northwood, T. D., 1947, Sonic determination of the elastic properties of ice, Canadian Journal of Research, **A25**, 88–95.

Sachse, W. and Y-H. Pao, 1978, On the determination of phase and group velocities of dispersive waves in solids, Journal of Applied Physics, **49**, 4320–4327.

Seki, H., A. Granato and R. Truell, 1956, Diffraction effects in the ultrasonic field of a piston source and their importance in the accurate measurement of attenuation, Journal of the Acoustical Society of America, **28**, 230–238.

Shaw, G., 1986, Elastic properties and equation of state of high pressure ice, Journal of Chemical Physics, **84**, 5862–5868.

Smith A., and D. Kishoni, Measurement of the speed of sound in ice, AIAA Journal, **24**, 1713–1715.

Stern, L. A., S. H. Kirby and W. B. Durham, 1998, Polycrystalline methane hydrate: synthesis from superheated ice, and low-temperature mechanical properties, Energy and Fuels, **12**, 201–211.

Stern, L. A., S. H. Kirby, W. B. Durham, S. Circone and W. F. Waite, 2000, Laboratory synthesis of pure methane hydrate suitable for measurement of physical properties and decomposition behavior, in Natural gas hydrate in oceanic and permafrost environments, ed. M. D. Max, 323–348.

Tang, X. M., M. N. Toksöz and C. H. Cheng, 1990, Elastic wave radiation and diffraction of a piston source, Journal of the Acoustical Society of America, **87**, 1894–1902.

Williams, A. O. Jr., 1951, The piston source at high frequencies, Journal of the Acoustical Society of America, **23**, 1–6.

Appendix A:

Effect of Filtering on Compressional Wave Arrivals

In Chapter 5, I showed that applying a low pass digital filter to the compressional waveforms created and received by the shear transducers introduced a ripple artifact in the first motion of the compressional waveforms (Figure 5.4). In this Appendix, I demonstrate that the ripple artifact does not introduce a bias in the signal delay times determined from the filtered waveforms and that applying the filter significantly reduces the scatter in the data.

As discussed in Chapter 5, the ripple artifact arises because the low pass, zero phase, IIR Butterworth digital filter applied to the compressional wave signal strongly damps frequencies greater than 1.5 MHz. Without these high frequencies, the "sharp" first break in the original signal cannot be reproduced and a "low" frequency ripple is introduced in its place. Since this is a fundamental change in the waveform, a study was undertaken to confirm that the first peak in the filtered compressional waveforms (as identified in Figure 5.4) was a valid proxy for the arrival of the corresponding feature in the unfiltered compressional waveforms.

To study the effect of the filter on compressional wave first motions, subsets of the reference and through-sample waveforms used in Chapter 5 were selected. The temperature and piston pressure ranges represented in the 196 selected reference waveforms were -20 to 20°C and 5,000 to 15,000 psi, respectively. The through-sample waveforms were selected from the first temperature cycle of the temperature cycling portion of the ice Ih experiment (Figure 5.17) and included 943 waveforms acquired within temperature and piston pressure ranges of -20 to -5°C and 2,500 to 6,000 psi, respectively. The automatic picking routine described in Chapter 5 was used to analyze these unfiltered waveforms. Unfortunately, the results were unreliable. The small amplitude initial features of the compressional wave signal were often overwhelmed or distorted by the background noise in the data. This caused

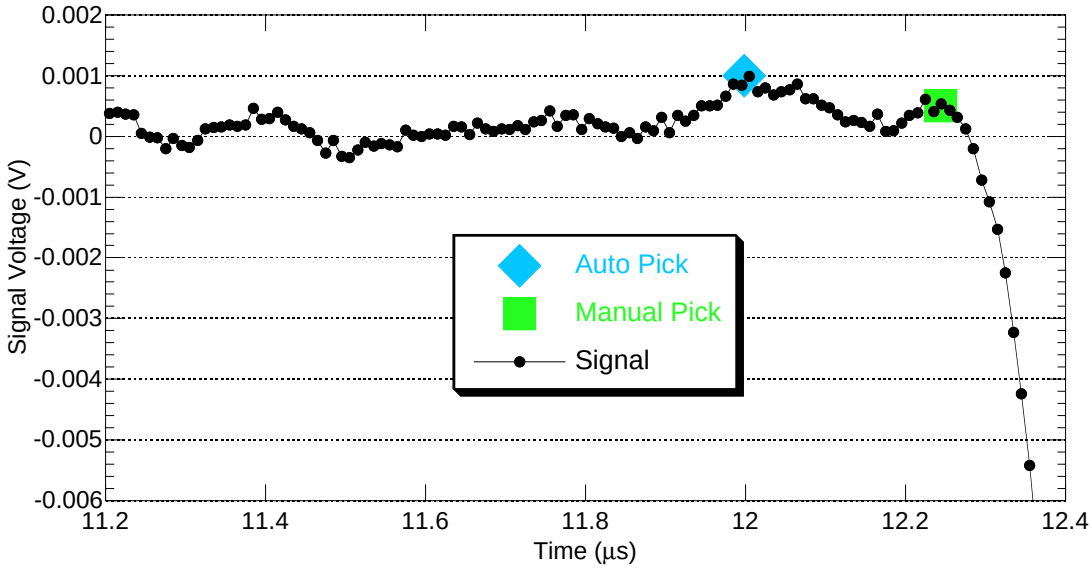

Figure A.1: This is an example of a common error that occurs when trying to automatically pick the arrival time of the first peak in the unfiltered compressional waveforms. The routine picks the extrema within the signal by first identifying the zero crossings in the signal and then locating the time at which the maximum absolute value is obtained on the interval between the zero crossings. In this particular signal, the "true" location of the first peak (green square) differs from the automatically picked peak location (blue diamond) because the background noise in the system prevents the signal from crossing zero before it enters into a noise peak. Because of this, the noise peak is misidentified by the program as the first peak in the signal.

the automatic picking routine to frequently mislocate the first peak in the signal (see Figure A.1 for a typical example of this picking error). Therefore, I was forced to manually pick the arrival times of the first peaks in the 196 reference and 943 through-sample waveforms. The estimated uncertainties in the manual picks ranged from ± 0.01 μs to ± 0.10 μs, depending on the shape of the signal, the character of the background noise and the overall signal to noise ratio (which was much higher in the reference waveforms).

Figure A.2 compares the manually picked first peak arrival times of the unfiltered reference waveforms to the automatically picked first peak arrival times of the filtered reference waveforms. As seen in the figure, the arrival times are approximately 0.02 μs earlier in the filtered waveforms. This can be seen more clearly in Figure A.3 which shows the difference between the first peak arrival times. These two figures demonstrate that arrival times determined from the filtered reference waveforms are systematically less than those determined from the unfiltered reference waveforms.

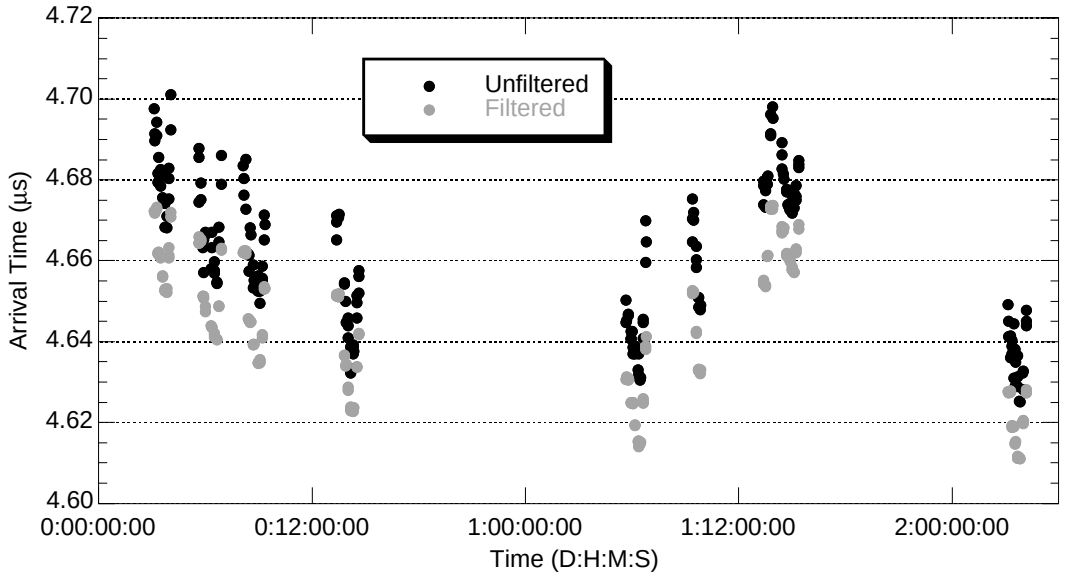

Figure A.2: A comparison between first peak arrival times in filtered and unfiltered reference compressional waveforms. Arrival times for the unfiltered waveforms (black) were determined manually. Arrival times for filtered waveforms (gray) were picked by a computer program (see text). Note that the arrival times determined from the filtered waveforms are systematically smaller than those determined from the unfiltered waveforms. Time on the x-axis is referenced to the start of the reference waveform acquisition experiment. Each data cluster represents a series of measurements at a fixed temperature. The variation in each cluster of points is due to the variation of piston pressure at each temperature.

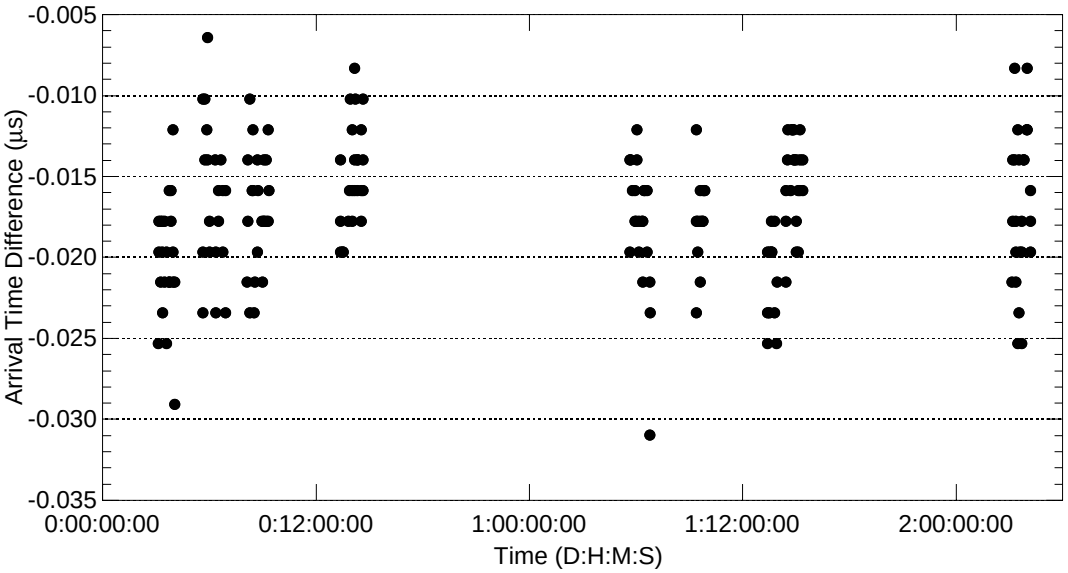

Figure A.3: Difference between first peak arrival times in filtered and unfiltered reference compressional waveforms (filtered−unfiltered). Time on the x-axis is referenced to the start of the reference waveform acquisition experiment. Each data cluster represents a series of measurements at a fixed temperature.

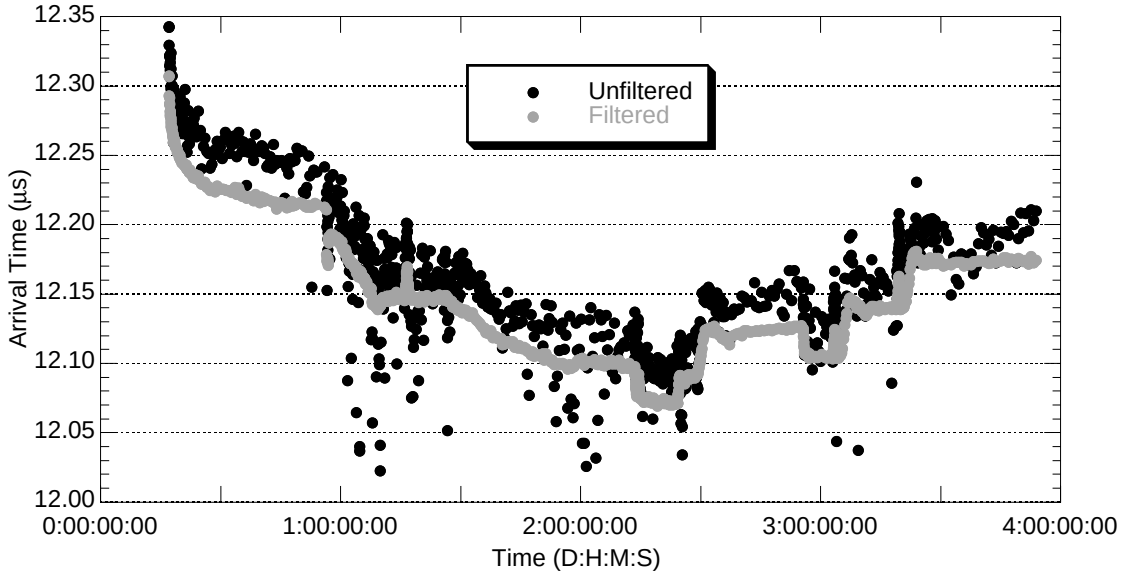

Figure A.4: A comparison between first peak arrival times in filtered and unfiltered through-sample compressional waveforms. Arrival times for the unfiltered waveforms (black) were determined manually. Arrival times for filtered waveforms (gray) were picked by a computer program (see text). Note that the arrival times determined from the filtered waveforms are systematically smaller than those determined from the unfiltered waveforms and that the scatter in the data obtained from the filtered waveforms is much less than in the data obtained from the unfiltered waveforms. Time on the x-axis is referenced to the start of the experiment.

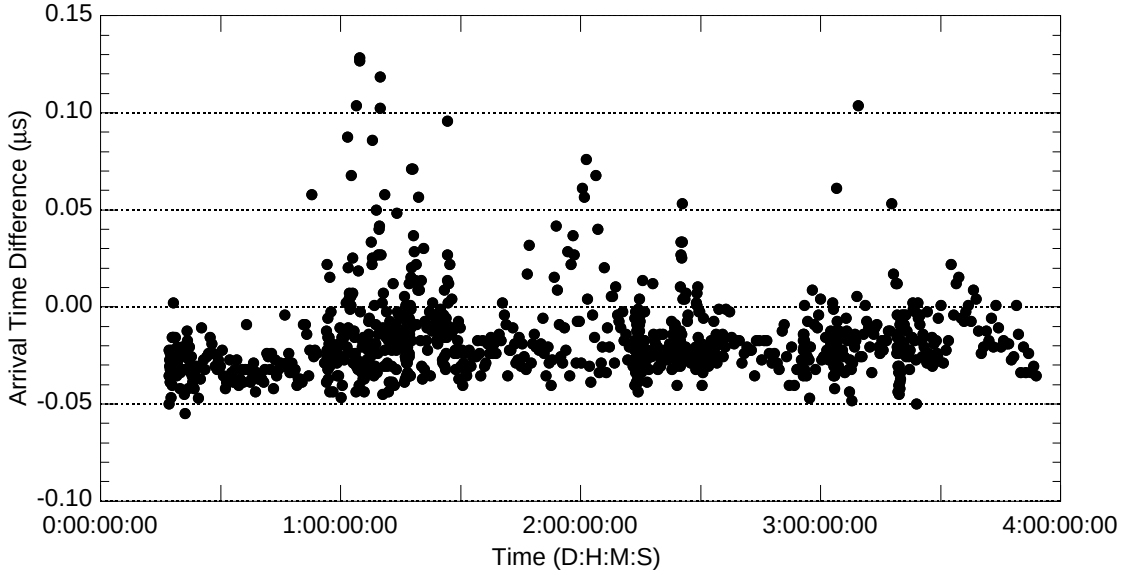

Figure A.5: Difference between first peak arrival times in filtered and unfiltered through-sample compressional waveforms (filtered−unfiltered). Time on the x-axis is referenced to the start of the experiment.

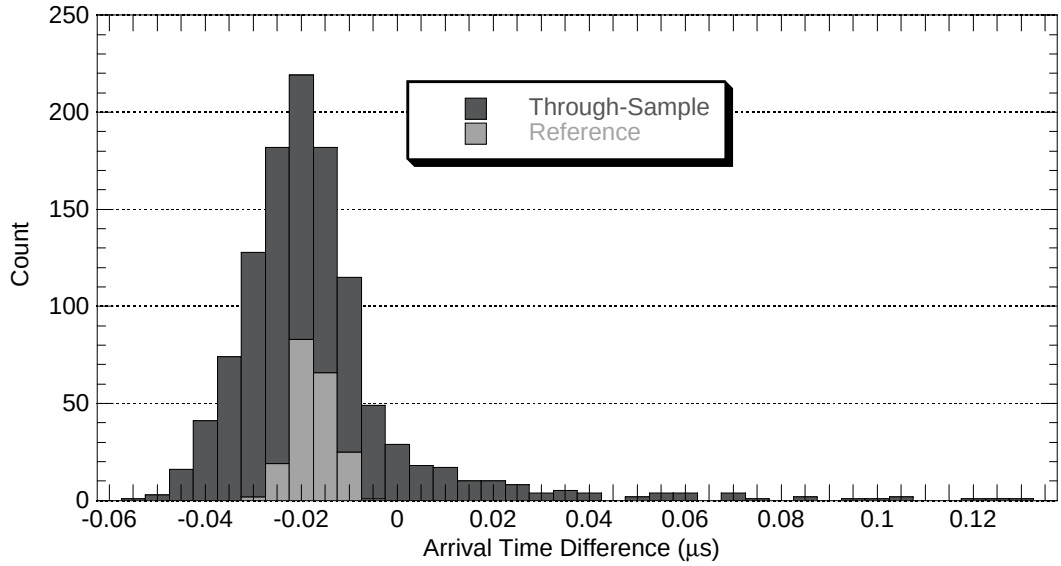

Figure A.6: Histograms of the first peak arrival time differences between filtered and unfiltered compressional waveforms for both reference and through-sample waveforms. On average, both the reference and through sample compressional waveforms have their first peak locations shifted 0.02 μs earlier in time. As a result, no net bias is introduced in the measured signal delay times by using the filtered compressional waveforms instead of the unfiltered compressional waveforms.

Figure A.4 compares the manually picked first peak arrival times of the unfiltered, through-sample waveforms to the automatically picked first peak arrival times of the filtered through-sample waveforms. This figure demonstrates the reduced scatter in and the earlier arrival times of the first peaks in the filtered, through-sample waveforms. The earlier arrival of the first peaks in the filtered waveforms can also be seen in Figure A.5 which shows the differences between the first peak arrival times. Comparing histograms of the first peak arrival time differences between the reference and through-sample waveforms (Figure A.6), we see that, on average, the filter shifts the first peaks of both waveforms 0.02 μs earlier in time. Therefore, applying the filter does not introduce any systematic bias in the signal delay time measurement.

From the analysis presented above, I concluded that no net bias was introduced by applying the low pass digital filter to both the reference and through-sample compressional waveforms, that applying the filter reduced scatter in the waveform arrival time determinations, and that the filter made it possible to use the automatic picking routine to reliably pick the arrival times of the waveforms. Using the automatic picking routine makes the picking

process much faster and less subjective. Therefore, the filtered compressional waveforms were used in place of the original compressional waveforms to determine compressional wave speeds in the ice and methane hydrate samples.

Appendix B:

Stage Two Experiments – Summary Tables

This Appendix provides summary information tables for the experiments discussed in Chapter 5. The data files referred to in the tables are included only with the thesis version distributed on the Stanford Rock and Borehole Geophysics (SRB) web site.

Table B.1: Stage Two Ice Ih Experiment – Summary Information

Experiment Dates	2/15/00 to 2/23/00			
Experiment Stage	Setup	Compaction	Temperature Cycling	Depressurization
Reference #	021500-1	021500-2	021500-3	021500-4
Start Time[a] (dd:hh:mm:ss)	00:00:00:00	00:05:02:04	00:06:47:10	07:11:31:02
End Time[a] (dd:hh:mm:ss)	00:05:02:00	00:06:39:53	07:11:29:03	08:00:52:08
Temperature Range (°C)	-25 to -5	-5	-5 to -20	-5
Piston Pressure Range (psi)	NA	0 – 6,200	6,200 – 2,500	4,750 – 0
V_P Range (m/s)	NA	1,750 – 3,850	3,870 – 3,940	3,890 – 3,870
V_S Range (m/s)	810 – 1,040	1,040 – 1,953	1,945 – 1,970	1,950 – 1,965
Associated Figures	5.5, 5.6, 5.7, 5.8, 5.9	5.5, 5.6, 5.7, 5.8, 5.10, 5.11, 5.12, 5.13, 5.15, 5.16	5.5, 5.6, 5.7, 5.8, 5.17, 5.18, 5.19, 5.20, 5.21, 5.22, 5.23, 5.24 5.25	5.5, 5.6, 5.7, 5.8, 5.26, 5.27
Associated Data Files[b]	021500PTL 021500PResult 021500SResult			

[a] Time referenced from start of experiment

[b] Thesis distributed on Stanford Rock and Borehole Geophysics (SRB) web site includes data files associated with each experiment, as well as individual waveform files

Table B.2: Stage Two Methane Hydrate Experiment – Summary Information

Experiment Dates	4/10/00 to 4/24/00			
Experiment Stage	Setup and Synthesis	Compaction	Temperature Cycling	Depressurization
Reference #	041000-1	041000-2	041000-3	041000-4
Start Time[a] (dd:hh:mm:ss)	00:00:00:00	02:18:04:39	05:20:15:18	12:08:30:43
End Time[a] (dd:hh:mm:ss)	02:17:59:59	05:20:15:08	12:08:29:43	13:22:20:55
Temperature Range (°C)	-20 to 17	-20 to 20	-15 to 15	15
Gas Pressure Range (psia)	0 – 4,750	350 – 4,000	3,100 – 3,800	3,600 – 3,150
Piston Pressure Range (psi)	NA	0 – 15,000	5,500 – 10,000	9,000 – 0
V_P Range (m/s)	NA	3,750 – 3,780[b]	3,760 – 3,835	3,770 – 3,705
V_S Range (m/s)	NA	1,916 – 1,938[b]	1,935 – 1,970	1,923 – 1,943
Associated Figures	5.28, 5.29, 5.30, 5.31, 5.32, 5.33	5.28, 5.29, 5.30, 5.31, 5.34, 5.35, 5.36, 5.37	5.2, 5.3, 5.4, 5.28, 5.29, 5.30, 5.31, 5.38, 5.39, 5.40, 5.41, 5.42	5.28, 5.29, 5.30, 5.31, 5.43, 5.44, 5.45
Associated Data Files[c]	041000PTL 041000PResult 041000SResult			

[a] Time referenced from start of experiment

[b] Due to failure of the linear motion potentiometer (LMP), wave speeds were not obtained until the end of the compaction stage

[c] Thesis distributed on Stanford Rock and Borehole Geophysics (SRB) web site includes data files associated with each experiment, as well as individual waveform files

Chapter 6

Modeling Wave Speeds in Sediment Containing Methane Hydrate

6.1 Introduction

Gas hydrate has been found in two general sedimentary environments: (1) clay rich, high porosity ocean and sea bottom sediments; and (2) arctic and subarctic onshore sands. In this chapter I present physics based effective medium models for the elastic properties of these two hydrate-sediment systems.

In both environments, I first model the elastic properties of the water saturated sediment as a function of porosity, mineral and fluid moduli, and effective pressure. Then I modify the model by placing gas hydrate in the pore fluid, in the sediment frame or, for sands, as a grain contact cement. In this chapter, I describe the models in detail and apply them to well log data from Northwest Eileen State Well #2 where gas hydrate was found in onshore sands in the Arctic (Figure 6.1) and to well logs and vertical seismic profile (VSP) data acquired offshore at site 995 on ODP Leg 164 off the southeastern coast of the United States (Figure 6.2) .

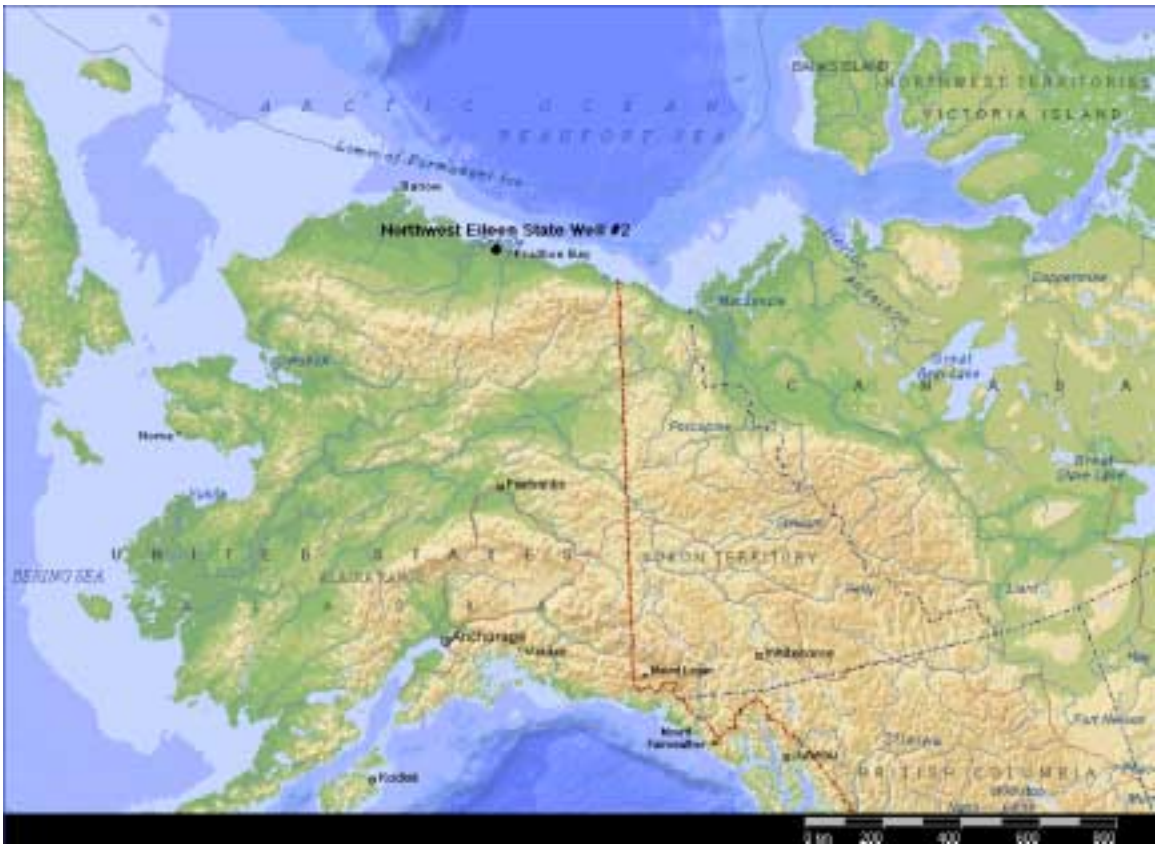

Figure 6.1: Map showing the location of Northwest Eileen State Well #2 on the North Slope of Alaska (70.36°N, 149.36°W). Map generated by Microsoft Encarta 97 World Atlas.

6.2 Background

Several recent attempts have been made to construct a relation between gas hydrate saturation of the pore space and compressional wave speed in sediments, particularly ocean bottom sediments (e.g., Pearson et al., 1983; Miller et al., 1991; Bangs et al., 1993; Scholl and Hart, 1993; Minshull et al., 1994; Wood et al., 1994; Holbrook et al., 1996; Lee et al., 1996; Collett, 1998). Many of the proposed relations are based on modifications of Wyllie's (1956) time average or weighted combinations of Wyllie's time average and Wood's (1955) relation. A limitation of this approach is that Wyllie's original time average equation is strictly empirical and was derived from a consolidated rock database (Dvorkin and Nur, 1998a). In contrast, all gas hydrate deposits found to date have been located in unconsolidated ocean bottom sediments or sands. Additionally, since Wyllie's time average

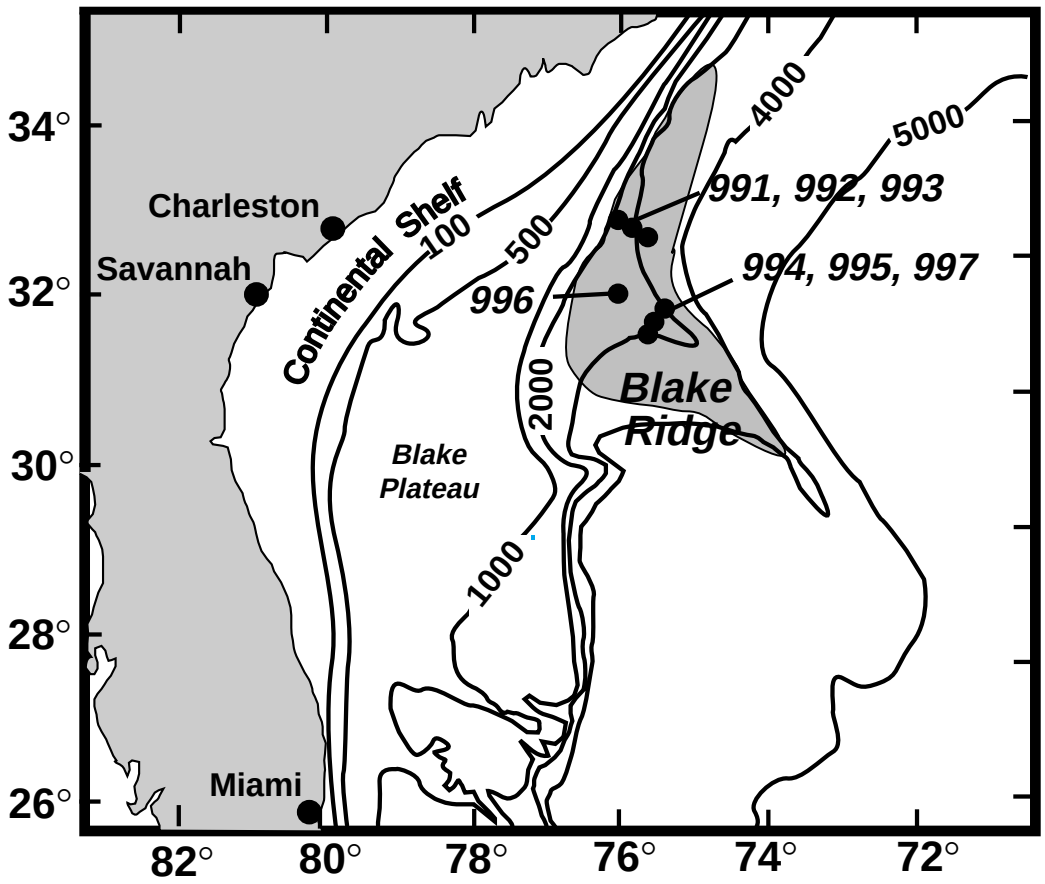

Figure 6.2: Map showing the location of holes drilled in the Blake Ridge on ODP leg 164 off the southeastern coast of the United States. Gray region is the inferred distribution of gas hydrate from seismic and other data. Map courtesy of T. Lorenson and the Shipboard Scientific Party of ODP Leg 164.

is a statistical fit to a specific data set, it cannot be generalized. This makes it difficult to establish a rational pattern for adapting "free" parameters to site-specific conditions.

A different, physically intuitive approach was taken by Hyndman and Spence (1992). They constructed an empirical relation between porosity and compressional wave speed for sediments without gas hydrate and approximated the effect of gas hydrate formation on wave speed as a simple reduction in porosity. By doing so they effectively assumed that gas hydrate became part of the sediment framework without altering the sediment's elastic properties.

In this thesis, instead of using Wyllie's time average or an empirical relationship to estimate wave speeds, I introduce physics-based models for gas hydrate-bearing sediments. The model for the elastic properties of water saturated granular and ocean-bottom sediments is based on the rock physics model of Dvorkin et al. (1999b), hereafter referred to as the "baseline model." This model relates the elastic properties of the sediment to porosity, mineralogy and effective pressure. The effect of water saturation is modeled by Gassmann's (1951) equations. In section 6.3, I describe the baseline model in detail. In sections 6.4–6.6, I extend the model to account for the effect of gas hydrate formation by theoretically placing gas hydrate within the sediment as (a) a pore fluid component; (b) a sediment frame component; or (c) a grain contact cement. In section 6.7, I further extend the model to account for the presence of free gas in the pore space. In section 6.8 I apply the models to generic sand and ocean bottom sediment examples, to explore the relative effects of gas hydrate's location in the pore space on compressional wave speed in the sediments. In section 6.9, I apply the models to two real world cases, gas hydrate in arctic onshore sands and gas hydrate in deep water, clay-rich sediments, and infer the location and amount of gas hydrate in the pore space from the data.

6.3 Baseline Model for Water Saturated Sediments

The porosity at which a granular composite ceases to be a suspension and becomes grain supported is called the critical porosity (ϕ_c). For a dense random packing of identical spheres, ϕ_c is approximately 36 to 40% (Nur et al., 1998). Many laboratory data on the elastic properties of porous materials can be explained if the material is modeled as a mixture of the critical-porosity material and the pure solid phase instead of pure solid material and void (the so-called "critical porosity concept" of Nur et al., 1998). The baseline model for water saturated sediments uses the effective moduli of a dense random packing of identical elastic spheres at critical porosity as its starting point.

The effective bulk (K_{HM}) and shear (G_{HM}) moduli of the dry rock frame at ϕ_c are calculated from the Hertz-Mindlin contact theory (Mindlin, 1949):

$$K_{HM} = \left[\frac{n^2(1-\phi_c)^2 G^2}{18\pi^2(1-\nu)^2} P_{eff}\right]^{\frac{1}{3}},$$

$$G_{HM} = \frac{5-4\nu}{5(2-\nu)}\left[\frac{3n^2(1-\phi_c)^2G^2}{2\pi^2(1-\nu)^2}P_{eff}\right]^{\frac{1}{3}}; \tag{6.1}$$

where P_{eff} is the effective pressure; G and ν are the shear modulus and Poisson's ratio of the solid phase; and n is the average number of contacts per grain in the sphere pack, about 8-9 (Dvorkin and Nur, 1996; Mavko et al., 1998). Effective pressure is calculated as the difference between the lithostatic and hydrostatic pressure:

$$P_{eff} = (\rho_b - \rho_w)gD, \tag{6.2}$$

where ρ_b is sediment bulk density; ρ_w is water density; g is the acceleration due to gravity; and D is depth below sea floor or land surface. ν can be calculated from K (the solid phase bulk modulus) and G using (Mavko et al., 1998):

$$\nu = \frac{1}{2}\,\frac{3K-2G}{3K+G}. \tag{6.3}$$

For porosity (ϕ) less than ϕ_c, the bulk (K_{Dry}) and shear (G_{Dry}) moduli of the dry frame are calculated via the modified lower Hashin-Shtrikman bound (Dvorkin and Nur, 1996):

$$\begin{aligned} K_{Dry} &= \left[\frac{\frac{\phi}{\phi_c}}{K_{HM}+\frac{4}{3}G_{HM}} + \frac{1-\frac{\phi}{\phi_c}}{K+\frac{4}{3}G_{HM}}\right]^{-1} - \frac{4}{3}G_{HM}, \\ G_{Dry} &= \left[\frac{\frac{\phi}{\phi_c}}{G_{HM}+Z} + \frac{1-\frac{\phi}{\phi_c}}{G+Z}\right]^{-1} - Z, \qquad (6.4) \\ Z &= \frac{G_{HM}}{6}\left(\frac{9K_{HM}+8G_{HM}}{K_{HM}+2G_{HM}}\right), \qquad (6.5) \end{aligned}$$

which represents the weakest possible combination of solid and critical porosity material (see Figure 6.3). For porosity above critical, K_{Dry} and G_{Dry} are calculated via the modified upper H-S bound:

$$\begin{aligned} K_{Dry} &= \left[\frac{\frac{1-\phi}{1-\phi_c}}{K_{HM}+\frac{4}{3}G_{HM}} + \frac{\frac{\phi-\phi_c}{1-\phi_c}}{\frac{4}{3}G_{HM}}\right]^{-1} - \frac{4}{3}G_{HM}, \\ G_{Dry} &= \left[\frac{\frac{1-\phi}{1-\phi_c}}{G_{HM}+Z} + \frac{\frac{\phi-\phi_c}{1-\phi_c}}{Z}\right]^{-1} - Z, \qquad (6.6) \\ Z &= \frac{G_{HM}}{6}\left(\frac{9K_{HM}+8G_{HM}}{K_{HM}+2G_{HM}}\right), \qquad (6.7) \end{aligned}$$

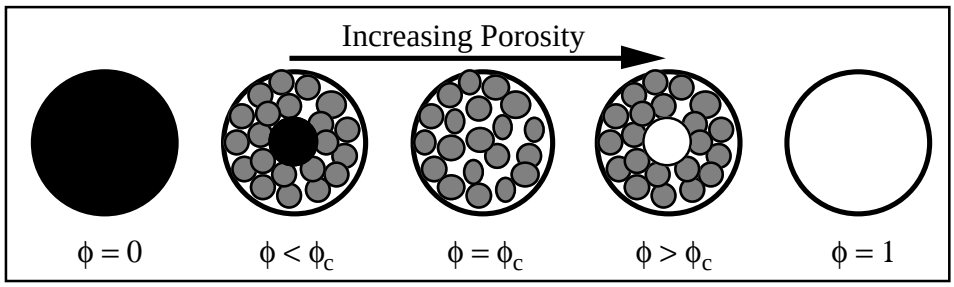

Figure 6.3: Hashin-Shtrikman arrangements of sphere pack, solid and void.

which represents the strongest possible combination of critical porosity material and void space (Figure 6.3).

If the sediment is saturated with pore fluid of bulk modulus K_f, the bulk and shear moduli of the saturated sediment (K_{sat} and G_{sat}, respectively) are calculated from Gassmann's (1951) equations as

$$K_{sat} = K\frac{\phi K_{dry} - (1-\phi)K_f K_{dry}/K + K_f}{(1-\phi)K_f + \phi K - K_f K_{dry}/K}, \tag{6.8}$$

$$G_{sat} = G_{dry}. \tag{6.9}$$

Once the elastic moduli are known, the elastic wave speeds are calculated from

$$V_P = \sqrt{\frac{K_{sat} + \frac{4}{3}G_{sat}}{\rho_b}}, \tag{6.10}$$

$$V_S = \sqrt{\frac{G_{sat}}{\rho_b}}, \tag{6.11}$$

where ρ_b is bulk density calculated from

$$\rho_b = \phi\rho_w + (1-\phi)\rho_{solid}. \tag{6.12}$$

In the common case of mixed mineralogy, the effective elastic moduli of the solid phase can be calculated from those of the individual mineral constituents using Hill's (1952) average formula:

$$K = \frac{1}{2}\left[\sum_{i=1}^{m} f_i K_i + \left(\sum_{i=1}^{m}\frac{f_i}{K_i}\right)^{-1}\right],$$

$$G = \frac{1}{2}\left[\sum_{i=1}^{m} f_i G_i + \left(\sum_{i=1}^{m}\frac{f_i}{G_i}\right)^{-1}\right], \tag{6.13}$$

where m is the number of mineral constituents; f_i is the volumetric fraction of the i-th constituent of the solid phase; and K_i and G_i are the bulk and shear moduli of the i-th constituent, respectively. The solid phase density (ρ_{solid}) is calculated as

$$\rho_{solid} = \sum_{i=1}^{m} f_i \rho_i, \tag{6.14}$$

where ρ_i is the density of the i-th constituent.

6.4 Gas Hydrate as Pore Fluid Component Model

If gas hydrate forms in the pore spaces of sediments such that it is suspended in the pore fluid, then its presence affects only the elastic moduli of the fluid and the bulk density of the sample. Therefore, the elastic moduli of the dry frame are those given by the baseline model. The volumetric concentration of gas hydrate in the pore space is given by $S_h = \frac{C_h}{\phi}$, where C_h is the volumetric concentration of the gas hydrate in the rock. ϕ is the porosity of the sediment frame without gas hydrate. If we assume that gas hydrate and water are homogeneously mixed throughout the pore space, the effective bulk modulus of the water/hydrate pore fluid mixture is the Reuss (1929) isostress average of the water and gas hydrate bulk moduli (K_f and K_h, respectively):

$$\bar{K_f} = \left[\frac{S_h}{K_h} + \frac{1 - S_h}{K_f} \right]^{-1}. \tag{6.15}$$

The bulk modulus of the saturated sediment is calculated from those of the dry frame using Equation 6.8 with $\bar{K_f}$ as the pore fluid bulk modulus. The shear modulus of the saturated sediment is that of the dry frame. The shear modulus of the pore fluid mixture is zero.

The assumption that the shear modulus of the pore filling material is zero is the limiting factor on this model. It can only be used when the pore fluid does not affect the shear modulus of the overall sediment. Therefore the model is only appropriate when the gas hydrate does not fill the entire pore space (e.g., S_h less than or approximately equal to 90%).

6.5 Gas Hydrate as Sediment Frame Component Model

If gas hydrate is instead acting as a sediment grain, in other words as a component of the load bearing sediment framework, then the original dry sediment calculations must be redone to account for the changes in composite solid phase moduli and sediment porosity. The presence of gas hydrate reduces the porosity of the original sediment (ϕ) to a new value $\bar{\phi}$ given by

$$\bar{\phi} = \phi - C_h. \tag{6.16}$$

The effective mineral modulus for the gas hydrate/sediment solid phase is calculated from Equation 6.13 where f_i is replaced by

$$\bar{f_i} = f_i \frac{1-\phi}{1-\bar{\phi}}, \tag{6.17}$$

and gas hydrate should be treated as an additional mineral component with

$$\bar{f_h} = \frac{C_h}{1-\bar{\phi}}. \tag{6.18}$$

The elastic moduli and wave speeds of the water saturated gas hydrate bearing sediments are then calculated using Equations 6.1 through 6.11 with ϕ replaced by $\bar{\phi}$. The elastic moduli of the new effective solid phase (K and G) required to use Equations 6.1 through 6.11 are calculated using Equation 6.13 by applying the new volume fractions given in Equations 6.17 and 6.18.

The gas hydrate as sediment frame component model is appropriate for any porosity and any fractional filling of the pore space by gas hydrate.

6.6 Gas Hydrate as Contact Cement Model

The third potential arrangement of gas hydrate in the pore space explored for this thesis is gas hydrate forming as an intergranular cement. The basis for this model is the contact cement theory (CCT) of Dvorkin et al. (1994), which calculates the bulk and shear moduli of a dense, random packing of identical spherical elastic grains with small amounts of elastic cement at the grain contacts. The original CCT theory was valid only for small concentrations of cement or, equivalently, residual porosities greater than approximately

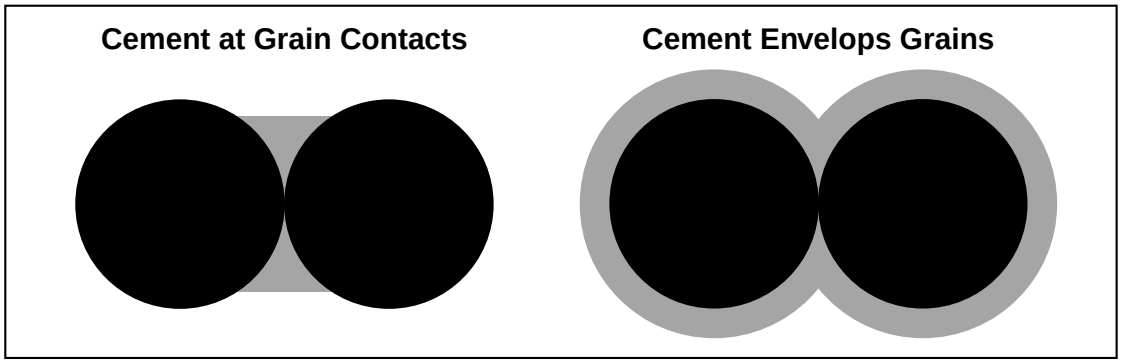

Figure 6.4: Gas hydrate cement distribution at the grain scale: scheme 1 (left) where gas hydrate is located only at the grain contacts and scheme 2 (right) where gas hydrate evenly envelops the grains.

25%. However, Dvorkin et al. (1999a) recently extended CCT to high cement concentrations (i.e., residual porosities less than 25%). This extended CCT theory provides a method for calculating the elastic moduli of sediment comprised of sand grains cemented by gas hydrate. Any remaining pore space is assumed filled with water and Gassmann's equations are used to calculate the saturated sediment's bulk and shear moduli. The cementation model depends on the porosity of the original (without gas hydrate) sediment; the amount of cement (gas hydrate); the elastic moduli of the original mineral phase; the elastic moduli of the cement (gas hydrate); and the coordination number (i.e., the average number of grain to grain contacts per grain) of the grain pack. The contact cement model is appropriate for granular sediments whose cement free porosity was approximately that of a sphere pack, namely 36 to 40%.

The CCT model can be applied to calculating the effect of two specific distributions of cement. In scheme 1, cement forms at the grain contacts. In scheme 2, cement evenly coats the grains (Figure 6.4). The arrangement represented by scheme 1 is much stiffer than that given by scheme 2 for the same amount of cement. The residual pore spaces in the two cementation schemes also have very different shapes. Scheme 1 produces roughly equidimensional residual porosity while scheme 2 is star-shaped. Modeling at high cement concentrations is greatly simplified by assuming equidimensional residual porosity (Dvorkin et al., 1999a). For this reason, only scheme 1 is used to model high gas hydrate cement concentrations (i.e., residual porosities less than 25%).

To construct the hydrate as contact cement model, I begin with the original CCT model

which describes the elastic moduli of a dense, random pack of identical elastic spheres with a small amount of gas hydrate elastic cement. The effective bulk (K_{CCT}) and shear (G_{CCT}) moduli of the dry cemented sphere pack are given by (Dvorkin et al., 1994; Dvorkin and Nur, 1996):

$$\begin{aligned} K_{CCT} &= \frac{n(1-\phi_c)}{6}\left(K_c + \frac{4}{3}G_c\right)S_n, \\ G_{CCT} &= \frac{3}{5}K_{CCT} + \frac{3n(1-\phi_c)}{20}G_c S_\tau, \end{aligned} \tag{6.19}$$

where K_c and G_c are the bulk and shear moduli of the cement; ϕ_c is the (critical) porosity of the uncemented grain pack (36 to 40%); and n is the average number of contacts per grain (8 to 9).

Parameters S_n and S_τ are the solutions to integral equations. Dvorkin and Nur (1996) supply the following approximate solutions:

$$\begin{aligned} S_n &= A_n(\Lambda_n)\alpha^2 + B_n(\Lambda_n)\alpha + C_n(\Lambda_n), \\ &\quad A_n(\Lambda_n) = -0.024153 \cdot \Lambda_n^{-1.3646}, \\ &\quad B_n(\Lambda_n) = 0.20405 \cdot \Lambda_n^{-0.89008}, \\ &\quad C_n(\Lambda_n) = 0.00024649 \cdot \Lambda_n^{-1.9864}, \\ S_\tau &= A_\tau(\Lambda_\tau,\nu)\alpha^2 + B_\tau(\Lambda_\tau,\nu)\alpha + C_\tau(\Lambda_\tau,\nu), \\ &\quad A_\tau(\Lambda_\tau,\nu) = (2.26\nu^2 + 2.0\nu + 2.3) \times 10^{-2} \cdot \Lambda_\tau^{0.079\nu^2+0.1754\nu-1.342}, \\ &\quad B_\tau(\Lambda_\tau,\nu) = (0.0573\nu^2 + 0.0937\nu + 0.202) \cdot \Lambda_\tau^{0.0274\nu^2+0.0529\nu-0.8765}, \\ &\quad C_\tau(\Lambda_\tau,\nu) = (9.654\nu^2 + 4.945\nu + 3.1) \times 10^{-4} \cdot \Lambda_\tau^{0.01867\nu^2+0.4011\nu-1.8186}, \\ &\quad \Lambda_n = \frac{2G_c}{\pi G}\frac{(1-\nu)(1-\nu_c)}{1-2\nu_c}, \\ &\quad \Lambda_\tau = \frac{G_c}{\pi G}, \end{aligned} \tag{6.20}$$

where G and ν are the shear modulus and Poisson's ratio of the grain material, and ν_c is the Poisson's ratio of the cement. Parameter α depends on the cement arrangement. For scheme 1, α is:

$$\alpha = 2\left[\frac{\phi_c - \bar{\phi}}{3n(1-\phi_c)}\right]^{\frac{1}{4}}. \tag{6.21}$$

For scheme 2, α is:

$$\alpha = \left[\frac{2(\phi_c - \bar{\phi})}{3(1-\phi_c)}\right]^{\frac{1}{2}}. \tag{6.22}$$

In Equations 6.21 and 6.22, $\bar{\phi}$ is the porosity of the cemented sphere pack.

For residual porosities $\bar{\phi}$ less than $\bar{\phi}_0$ (the porosity limit for application of the original contact cement theory) I proceed in two steps. First, I calculate the elastic moduli of the cemented sphere pack with cement distribution scheme 1 and residual porosity $\bar{\phi}_0$, and then treat this cemented sphere pack as an elastically equivalent two-phase system of voids in a homogenous matrix. I estimate the elastic moduli of this effective matrix material by applying Berryman's self consistent (SC) approximation for spherical inclusions (Berryman, 1980; Berryman, 1995):

$$\begin{aligned} 0 &= (1-\bar{\phi}_0)(K_s - K_{CCT})P_s + \bar{\phi}_0(K_{void} - K_{CCT})P_{void}, \\ 0 &= (1-\bar{\phi}_0)(G_s - G_{CCT})Q_s + \bar{\phi}_0(G_{void} - G_{CCT})Q_{void}, \end{aligned}$$

$$\begin{aligned} P_s &= \tfrac{K_{CCT}+\frac{4}{3}G_{CCT}}{K_s+\frac{4}{3}G_{CCT}}, \;\; P_{void} = \tfrac{K_{CCT}+\frac{4}{3}G_{CCT}}{K_{void}+\frac{4}{3}G_{CCT}}, \\ Q_s &= \tfrac{G_{CCT}+Z}{G_s+Z}, \;\; Q_{void} = \tfrac{G_{CCT}+Z}{G_{void}+Z}, \;\; Z = \tfrac{G_{CCT}(9K_{CCT}+8G_{CCT})}{6(K_{CCT}+2G_{CCT})}, \end{aligned} \tag{6.23}$$

where K_{CCT} and G_{CCT} are the elastic moduli of the cemented sphere pack given by CCT with scheme 1 at $\bar{\phi} = \bar{\phi}_0$; K_s and G_s are the as yet undetermined moduli of the effective matrix material; and K_{void} and G_{void} are the moduli of the material in the void space (both zero). Symbols K and G with their various subscripts stand for bulk and shear moduli, respectively. The system of equations in (6.23) can be solved analytically for K_s and G_s, giving

$$\begin{aligned} K_s &= \frac{4G_{CCT}K_{CCT}}{4G_{CCT}(1-\phi_0) - 3K_{CCT}\phi_0}, \\ G_s &= \frac{G_{CCT}(8G_{CCT} + 9K_{CCT}}{3K_{CCT}(3-5\bar{\phi}_0) + 4G_{CCT}(2-5\bar{\phi}_0)}. \end{aligned} \tag{6.24}$$

Second, I reduce the amount of void space in the effective matrix material by partially filling the remaining pore space with hydrate cement, reducing the porosity from $\bar{\phi}_0$ to the target value $\bar{\phi}$. The elastic moduli of the dry, cemented sediment (K_{eff} and G_{eff}) are

determined from the SC equations

$$0 = (1-\bar{\phi}_0)(K_s - K_{eff})P_s + (\bar{\phi}_0 - \bar{\phi})(K_c - K_{eff})P_c - \bar{\phi}K_{eff}P_{void},$$
$$0 = (1-\bar{\phi}_0)(G_s - G_{eff})Q_s + (\bar{\phi}_0 - \bar{\phi})(G_c - G_{eff})Q_c - \bar{\phi}G_{eff}Q_{void},$$

$$P_s = \frac{K_{eff}+\frac{4}{3}G_{eff}}{K_s+\frac{4}{3}G_{eff}},\ P_c = \frac{K_{eff}+\frac{4}{3}G_{eff}}{K_c+\frac{4}{3}G_{eff}},\ P_{void} = \frac{K_{eff}+\frac{4}{3}G_{eff}}{K_{void}+\frac{4}{3}G_{eff}},$$
$$Q_s = \frac{G_{eff}+Z}{G_s+Z},\ Q_c = \frac{G_{eff}+Z}{G_c+Z},\ Q_{void} = \frac{G_{eff}+Z}{G_{void}+Z},\ Z = \frac{G_{eff}(9K_{eff}+8G_{eff})}{6(K_{eff}+2G_{eff})}, \qquad (6.25)$$

where $1-\bar{\phi}_0, \bar{\phi}_0-\bar{\phi}$ and $\bar{\phi}$ are the concentrations of effective matrix material, cement-filled inclusions and empty inclusions, respectively. This system of algebraic equations (6.25) results in a sixth order polynomial expression for G_{eff} and must be solved numerically for K_{eff} and G_{eff}.

To calculate the bulk modulus of the system saturated with water, Gassmann's equations are used. The dry-frame bulk modulus is K_{eff} and the porosity is $\bar{\phi}$. The solid-phase bulk modulus is taken as the lower Hashin-Shtrikman (LHS) bound (Hashin and Shtrikman, 1963) of the mineral and gas hydrate components. The fractional amount of gas hydrate in the solid phase is $(\phi-\bar{\phi})/(1-\bar{\phi})$. The use of the LHS bound instead of the more traditional Hill's average is justified by the cemented sediment's topology in which relatively stiff grains are essentially enveloped by softer gas hydrate cement. Wave speeds are calculated from the resultant elastic moduli and the bulk density of the sample (Equations 6.10 and 6.11).

6.7 Partial Gas Saturation Models

Many natural gas hydrate deposits, although not all, are associated with free gas trapped in the sediments beneath the base of the gas hydrate stability zone. Therefore, I present here two end-member models for calculating elastic wave speeds in sediments containing free gas.

6.7.1 Homogenous Gas Saturation Model

The most commonly used model for partial gas saturation is the homogenous distribution model which assumes that free gas is evenly distributed throughout the pore space. In

this case, the composite fluid bulk modulus ($\bar{K_f}$) can be calculated as the Reuss (isostress) average of the water (K_w) and gas (K_g) bulk moduli (or equivalently the algebraic average of the water and gas compliances):

$$\bar{K_f} = \left[\frac{S_w}{K_w} + \frac{1-S_w}{K_g}\right]^{-1}, \tag{6.26}$$

where S_w is the water saturation of the pore space. This new fluid bulk modulus ($\bar{K_f}$) is used in Gassmann's equations to calculate the bulk and shear moduli of the saturated sediment. The new bulk density (ρ_b) is given by

$$\rho_b = \phi(S_w\rho_w + (1-S_w)\rho_g) + (1-\phi)\rho_{solid}, \tag{6.27}$$

where ρ_w, ρ_g and ρ_{solid} are the densities of the water, gas and solid phases, respectively. The new wave speeds are calculated from the resultant elastic moduli and bulk density using Equations 6.10 and 6.11.

In the homogenous distribution model, small amounts of free gas can have a dramatic effect on the compressibility of the composite pore fluid because the compressibility of the gas phase dominates. Essentially, any stress applied to the pore fluid is taken up by volume changes in the gas. Using the homogenous gas distribution model to analyze wave speeds produces the smallest, physically reasonable estimate of gas present in the sediment because, according to Gassmann's equation, the bulk modulus of the saturated sediment is a monotonic function of the pore-fluid bulk modulus, and the Reuss average (Equation 6.26) is the lower bound for a pore-fluid comprised of gas and water.

6.7.2 Patchy Gas Saturation Model

The patchy saturation model (Dvorkin and Nur, 1998b) produces an upper limit for the amount of gas that would produce a given wave speed in sediment (Mavko and Mukerji, 1998). The patchy distribution model assumes gas is collected in the sediment in patches which are much larger than the scale of individual pores and that these 100% gas saturated patches are surrounded by 100% water saturated sediment. For this case, the effective saturated bulk modulus is expressed by:

$$K_{sat} = \left[\frac{S_w}{K_{satW} + \frac{4}{3}G_{dry}} + \frac{1-S_w}{K_{satG} + \frac{4}{3}G_{dry}}\right]^{-1} - \frac{4}{3}G_{dry}, \tag{6.28}$$

where K_{satW} and K_{satG} are calculated from Gassmann's equations and represent the bulk moduli of the sediment fully saturated with water and gas, respectively:

$$K_{satW} = K\frac{\phi K_{dry} - \frac{(1-\phi)K_w K_{dry}}{K} + K_w}{(1-\phi)K_w + \phi K - \frac{K_w K_{dry}}{K}},$$
$$K_{satG} = K\frac{\phi K_{dry} - \frac{(1-\phi)K_g K_{dry}}{K} + K_g}{(1-\phi)K_g + \phi K - \frac{K_g K_{dry}}{K}}. \quad (6.29)$$

As in the homogenous case, the saturated shear modulus equals the dry shear modulus and the density changes according to Equation 6.27. Wave speeds are calculated from Equations 6.10 and 6.11.

6.8 Applying the Models to Idealized Sediments

In this section, the models described above are applied to idealized ocean bottom sediment and onshore sand examples. This is done to illustrate the relative effects on compressional wave speed in the sediments predicted by the different models. The idealized examples use mineralogies and porosities relevant to the real world cases which are addressed in section 6.9.

6.8.1 Idealized Ocean Bottom Sediment Setting

In the last few decades, a number of marine seismic lines have been shot by the oil industry and by research consortia such as the Ocean Drilling Project. These data and some spot drilling have shown many locations around the world where gas hydrate is inferred to be present in ocean and sea bottom sediments (Kvenvolden et al., 1993; Booth et al., 1996). These are the locations where the necessary pressure and temperature conditions are met, where sufficient volumes of methane gas are present either from shallow biogenic production or deeper thermal processes and where BSRs provide remotely sensed evidence of gas hydrate's presence. Therefore, it is relevant to estimate the effect that gas hydrate (or free gas) and its location within the pore space have on wave speeds in these high porosity, clay-rich sediments.

Table 6.1: Elastic Properties of Sediment Solid Phase Components

Sediment Constituent	Bulk Modulus (GPa)	Shear Modulus (GPa)	Density (g/cm^3)
Clay	20.9	6.85	2.58
Calcite	76.8	32.0	2.71
Quartz	36.6	45.0	2.65
Methane Hydrate	8.7	3.5	0.92

For this idealized example, I use a mineralogy which is appropriate for the specific case addressed in section 6.9.2. The solid phase of the hydrate-free sediment is assumed to be 60% clay, 35% calcite and 5% quartz. The porosity of the hypothesized sediment ranges from 40 to 70%. The critical porosity is set to 37% and the associated coordination number is 9, the theoretical values for a random, dense pack of identical spheres (Mavko et al., 1998). The effective pressure and the pore pressure are fixed at 2.5 and 32 MPa, respectively. The sediment temperature is 16°C and the pore space is saturated with brine of salinity 32,000 ppm.

The elastic moduli and densities of isotropic, polycrystalline collections of clay, calcite, quartz and methane hydrate are given in Table 6.1. The clay, calcite and quartz properties are taken from Mavko et al. (1998). The methane hydrate properties are taken from the results presented in Chapter 5. The bulk modulus and density of methane gas (0.11 GPa and 0.23 g/cm^3, respectively) were calculated at the given pressure and temperature conditions from Sychev et al. (1987). The bulk modulus and density of brine (2.5 GPa and 1.032 g/cm^3, respectively) were calculated according to Batzle and Wang (1992).

Results for the water saturated baseline model, the gas hydrate as pore fluid component model (10% bulk hydrate by volume), gas hydrate as frame component model (10% bulk hydrate by volume) and homogenous and patchy gas distribution models (1% free gas by volume) are shown in Figure 6.5 where compressional wave speed is plotted versus original sediment (i.e., hydrate-free) porosity. In this figure, it is important to note the difference between the model predictions. The gas hydrate as frame component model is approximately 40 to 70 m/s faster than the gas hydrate as pore fluid component model, and the patchy gas distribution model is approximately 100-200 m/s faster than the homogenous

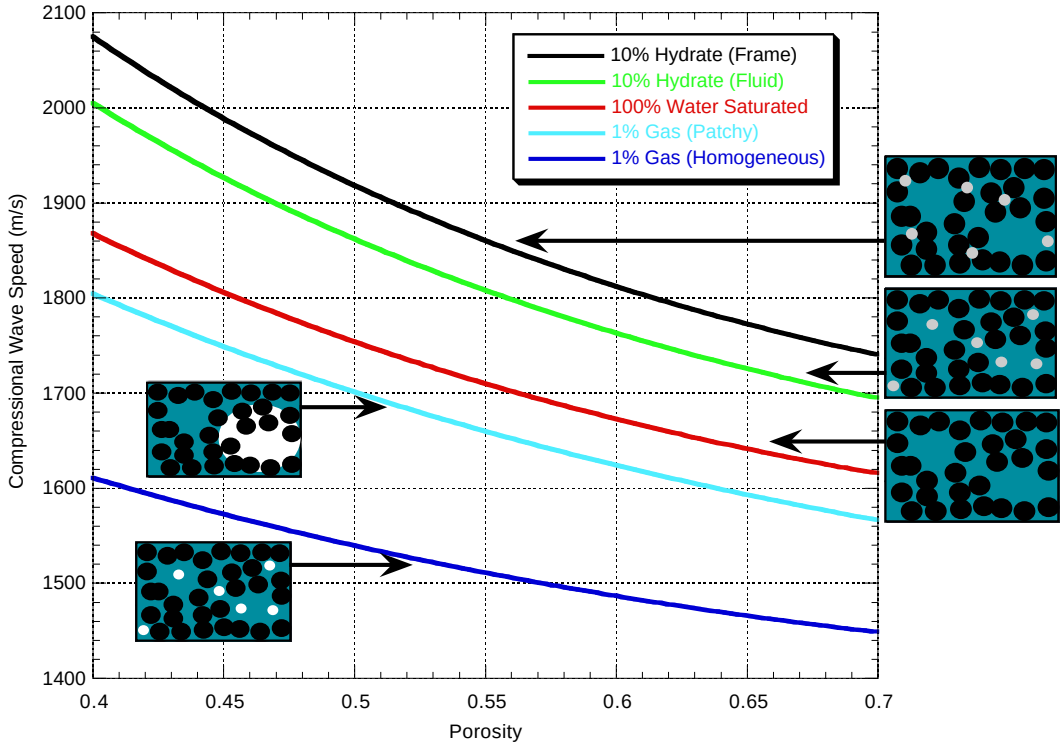

Figure 6.5: Plot showing model estimates of compressional wave speed in generalized ocean bottom sediments containing either 10% (by volume) methane hydrate or 1% (by volume) methane gas. The plot illustrates the relative difference in predicted compressional wave speeds between the individual models. The wave speed predicted by the gas hydrate as frame component model is approximately 40 to 70 m/s faster than the prediction of the gas hydrate as pore fluid component model. The compressional wave speed predicted by the patchy gas distribution model is approximately 100-200 m/s faster than the wave speed predicted by the homogenous gas distribution model.

gas distribution model. The difference in compressional wave speed predictions between the two gas-hydrate-in-sediment models is detectable using a high resolution wave speed measurement such as a well log or perhaps a vertical seismic profile (VSP), but the two models are essentially indistinguishable to conventional low resolution reflection seismic velocity analysis.

The cementation model was not used in this section because it is inappropriate for these high porosity sediments.

6.8.2 Idealized High Porosity Sand Setting

Onshore hydrate deposits in the Arctic are generally associated with coarse, high porosity sands. This is likely because these sands have the highest permeability and therefore the highest methane gas flux. If sands were present in any quantity in ocean bottom sediments, gas hydrate would likely form preferentially in sands there as well. Except for turbidite deposits, coarse grained sediments are rare in deep water settings. However, with increased exploration, deposits of this type may be found in oceanic and deep sea settings in the future.

The models presented above for the effects of gas hydrate and free gas on the elastic properties of sediment are applied to a 100% quartz sand whose properties are the same as those used to model the specific case discussed in section 6.9.1. The parameters critical porosity and coordination number are taken to be 0.4 and 8.3, respectively. The chosen critical porosity is greater than 37% because the sands discussed in section 6.9.1 are high porosity sands. However, within the range 36 to 40%, the specific value chosen for ϕ_c does not have a significant effect on the modeling results. The effective pressure and the pore pressure are taken to be 7.5 and 6.9 MPa, respectively. The temperature in the formation is 10°C and the pore space is saturated with brine of salinity 32,000 ppm. The salinity is high because the site analyzed in section 6.9.1 is on the edge of the Beaufort Sea. Choosing a brine of lower salinity should not have a significant impact on the elastic modeling results.

The elastic properties and densities used for quartz and methane hydrate are given in Table 6.1. The density and bulk modulus of the brine are calculated from Batzle and Wang (1992) as 1.024 g/cm^3 and 2.29 GPa, respectively. The density and bulk modulus of the methane gas are calculated from Sychev et al. (1987) as 0.054 g/cm^3 and 0.0097 GPa, respectively.

The results of applying the models are shown in Figure 6.6 where compressional wave speed is plotted versus hydrate saturation of the pore space. At low gas hydrate saturation, there is little difference between the compressional wave speed predicted by the gas hydrate as pore fluid and gas hydrate as sediment frame component models. However, they differ significantly from the contact-cement model results. Therefore, given porosity, compressional wave speed and gas hydrate saturation it is possible to infer whether or not gas

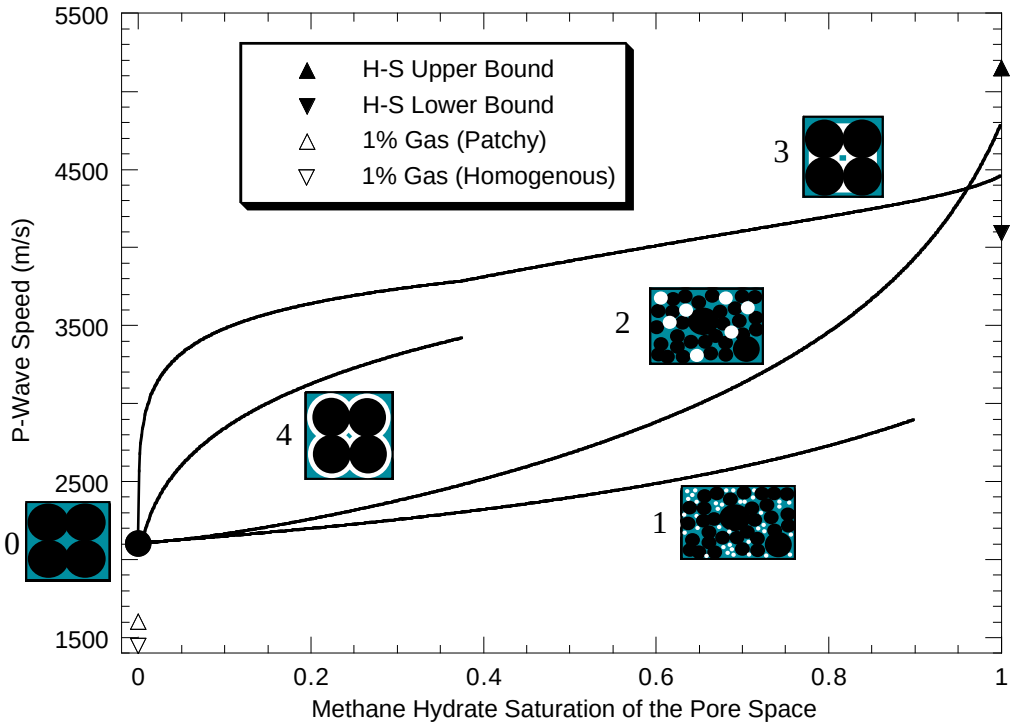

Figure 6.6: Model based compressional wave speed versus gas hydrate saturation of the pore space for 40% porosity quartz sand with brine. Cartoons show the position of gas hydrate (white) in the brine (blue) saturated pore space of the sediment (black): (0) is the baseline model; (1) is the gas hydrate as fluid component model; (2) is the gas hydrate as sediment frame component model; (3) is the contact cement model with scheme 1 cement distribution; and (4) is the contact cement model with scheme 2 cement distribution (see Figure 6.4). Curve (1) stops at 90% gas hydrate saturation because (1) is not applicable at $>$ 90% gas hydrate saturation (see text). Curve (4) stops at 37.5% gas hydrate saturation (25% porosity) because it is not applicable at higher gas hydrate saturations (see text). Filled triangles are the Hashin-Shtrikman upper and lower bounds for 40% methane hydrate and 60% quartz. Open triangles are the model predictions for 1% gas (by volume) homogeneously or patchily distributed in a hydrate-free, 40% porosity quartz sand saturated with brine.

hydrate cements the grain contacts. At higher gas hydrate concentrations, all the models produce distinctly different compressional wave speed estimates. This means that a suite of log measurements could be used to infer the location of gas hydrate at the pore scale in a well. Once that pore space location was established, the corresponding model could be used to interpret seismic velocities away from the well. This is a potential method for using seismic data for gas hydrate reservoir characterization (e.g., Ecker et al., 2000).

6.9 Applying the Models to Real World Data

Now, I turn to applying the models to real world data sets obtained on ODP Leg 164 for gas hydrates in ocean bottom sediments off the southeastern coast of the United States and Northwest Eileen State Well #2 drilled onshore in the Alaskan Arctic. Both sites have a fairly complete set of well logs. The ODP data were acquired in November and December of 1995. The Eileen data are considerably older, being acquired in 1972. Additionally, the ODP leg was specifically targeted at gas hydrate research, so a considerable amount of supplementary data is available. At the time the research for this thesis was performed, the Eileen data was the best available for a natural gas hydrate deposit located in sands. Subsequently, reports became available for a JAPEX/JNOC/GSC gas hydrate research well (Mallik 2L-38) drilled in the Mackenzie Delta (see Figure 6.1) of the Northwest Territories, Canada, in 1998 (Dallimore, Uchida and Collett, 1999). Raw data from that site were not available in time for inclusion in this thesis. Reports at national and international meetings made by others directly involved in the project suggest that conclusions from that data set are essentially the same as those described below from analyzing the Eileen data.

6.9.1 Modeling Compressional Wave Speed at Northwest Eileen State Well #2

ARCO spudded Northwest Eileen State Well #2 on March 15, 1972, onshore on the North Slope of Alaska within the Prudhoe Bay Oil Field (Figure 6.1). Gas hydrate was reportedly recovered in at least one core taken at the site (Collett, 1992; Kvenvolden and McMenamin, 1980). To determine the location of the methane hydrate in the pore space of the sediments at the well, I apply the models described above to the well log data collected at the site. The gamma ray, resistivity, neutron porosity (with sandstone correction, Schlumberger, 1989), and compressional sonic log curves are plotted versus depth in Figure 6.7. The well logs presented here were provided by Dr. Akio Sakai of JAPEX (pers. comm., 1996), except for the neutron porosity log which was digitized from Mathews (1986). The interval from 550-830 m has been previously determined to contain three methane gas hydrate bearing sand intervals (discussed in Mathews, 1986). The correlation of high compressional wave speed and high resistivity with gas shows in the mud log (Mathews, 1986) was the basis for this identification.

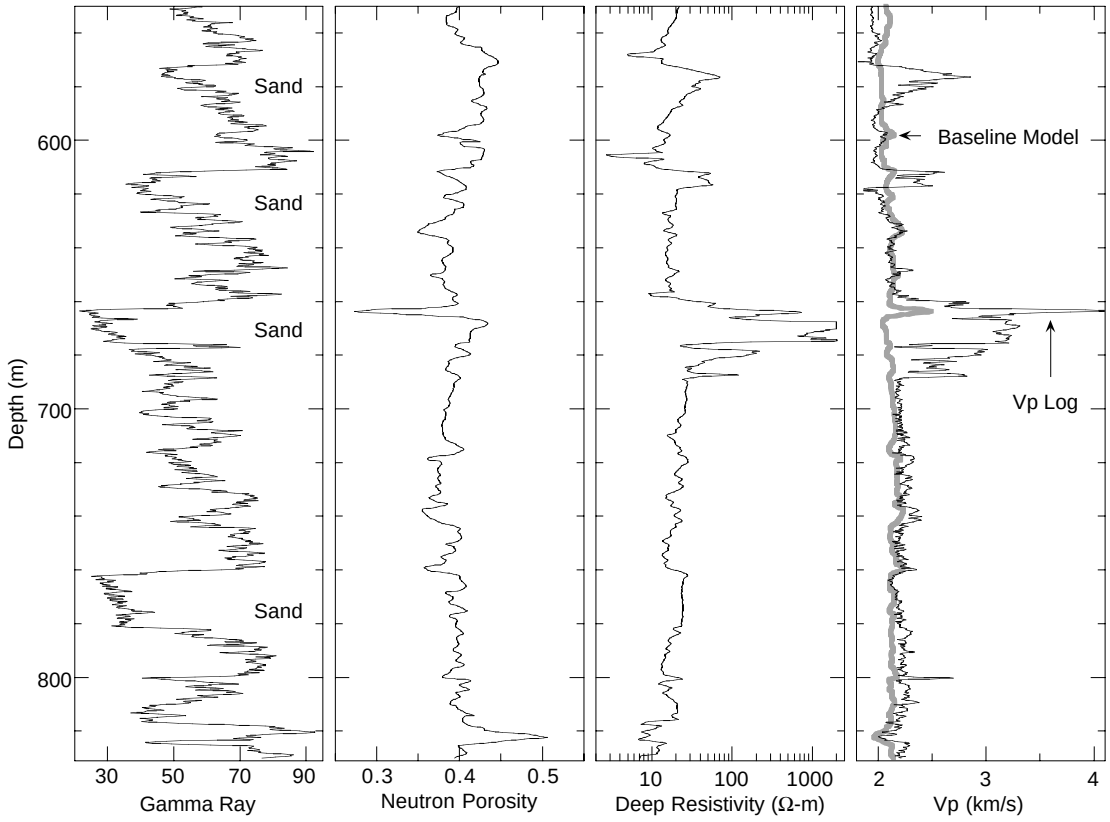

Figure 6.7: Physical property logs from Northwest Eileen State Well #2. Column one: Gamma ray versus depth. Low gamma ray value intervals identified as sands. Column two: Neutron porosity (with sandstone correction applied) versus depth. Mean value is 0.40. Column three: Deep resistivity versus depth. Note the three resistivity peaks associated with the top three sand intervals identified in the gamma ray log. Column four: Compressional wave sonic log versus depth. Note the three peaks associated with the top three sand intervals identified in the gamma ray log. Gray line is the baseline model compressional wave speed result.

In order to provide inputs for the models, I assume, for simplicity, that the mineral phase in the well is pure quartz, and the pore fluid is brine with a salinity of 32,000 ppm at an average temperature and pore pressure of 10°C and 7 MPa, respectively. The density and bulk modulus of the brine (1.024 g/cm^3 and 2.29 GPa, respectively) were calculated according to Batzle and Wang (1992) and do not vary much in the temperature and pressure regions of interest. The values for the elastic properties and density of quartz and methane hydrate are given in Table 6.1. I also assume that the porosity of the sand frame without hydrate (ϕ) is given by the corrected neutron porosity log. This assumption is based on the fact that hydrogen density in methane hydrate is essentially the same as that in liquid

water ($\sim$ 0.1 mol H/cm^3). Therefore, to first order, the neutron tool should not be able to distinguish between gas hydrate and water in the pore space. The effective pressure, 6 to 9 MPa, is calculated as the difference between the lithostatic and hydrostatic pressure where the average rock bulk density is taken as 2.12 g/cm^3 and the density of brine as 1.024 g/cm^3.

I use the physical properties listed above to calculate the compressional wave speed in the sediments at the well, assuming the pore space is fully saturated with brine and does not contain hydrate. The coordination number is fixed at 8.3 which corresponds to an average porosity of 0.4 (Mavko et al., 1998), which I use as the critical porosity at the site. The calculated 100% brine saturated compressional wave speed (column 4, Figure 6.7) closely matches the measured background compressional wave speed, justifying the choice of background model and input parameters.

To model the effect of methane hydrate on compressional wave speed in the sediment, I must estimate the amount of gas hydrate in the pore space. It is possible to calculate the non-water saturation of the pore space from the resistivity log using the "quick-look" Archie method (e.g., Collett, 1998), which is based on the equation:

$$1 - S_w = 1 - \left(\frac{R_0}{R_t}\right)^{\frac{1}{n}}, \tag{6.30}$$

where S_w is water saturation of the pore space; R_0 is the resistivity of the formation at 100% brine saturation; R_t is the formation's true (i.e., measured) resistivity; and n is an empirical constant (about 1.94, Pearson et al., 1986). It is assumed in this method that the R_0-versus-depth trend is the same as the background trend of the resistivity log. The choice of background trend is subjective. The trend is supposed to follow the data where gas hydrate is presumably absent and thus highlight the resistivity peaks.

In Figure 6.8, column one, I present three linear background fits to the resistivity data above 700 m and a single linear fit to the rest of the interval. The three trends in the upper section are meant to represent upper (3), lower (1) and "optimal" (2) fits to the background trend of the resistivity data. The corresponding non-water saturation estimates are shown in the second column of Figure 6.8. I assume that all non-water saturation shown in this plot is attributable to methane hydrate. Easily seen in this plot is the high estimated gas hydrate saturation in three of the sand intervals. Also evident is the lack

of precision ($\pm$20%) inherent in this technique. However, within the range of saturation values predicted ($\sim$20-80%), the models make easily distinguishable compressional wave speed predictions (Figure 6.6). Therefore, this lack of precision in the saturation estimate does not preclude drawing meaningful conclusions from the application of the models to the data.

To complete the modeling, I assume the hydrate saturation is given by the "optimal" (curve 2) hydrate saturation estimate in Figure 6.8. The results of applying the gas hydrate as pore fluid and gas hydrate as frame component models are shown in the third column of Figure 6.8. Both closely match the compressional wave speed data. In contrast, the contact-cement model results exceed measured compressional wave speeds by several hundred meters per second (column four, Figure 6.8). These modeling results show that in spite of the uncertainty in hydrate saturation estimates, the vastly different predictions of the models lead to the conclusion that gas hydrate does not cement grain contacts at this site.

Sakai (1999) applied a modeling approach similar to this to VSP and well log data acquired at the Mallik 2L-38 site. He concluded that gas hydrate at the Mallik site was disseminated in the pore space without any appreciable cementation at the grain boundaries. Sakai (1999) cited shear-wave data as the key to arriving at this conclusion. This result ortakned from a more modern and complete data set is consistent with the result obtained above for the sands present at Northwest Eileen State Well #2.

6.9.2 Modeling Compressional Wave Speed at ODP hole 995

ODP Leg 164 was dedicated to studying the gas hydrate deposit located beneath the Blake-Bahama Ridge, a sediment drift deposit located off the coast of the southeastern United States in a water depth of about 3000 m. Three of the holes drilled on this leg, 994, 995 and 997, had well logs, extensive core analyses and vertical seismic profiles run. In this thesis, I present a detailed analysis of the compressional wave speed data from site 995. This site has independent gas hydrate concentration estimates available from resistivity logs, chloride anomalies and methane gas volumes evolved from a pressure core sampler (PCS). Core porosity measurements and the gamma ray, resistivity and compressional wave sonic logs for site 995 are plotted versus depth in Figure 6.9. The resistivity and sonic log data shown in Figure 6.9 include both the raw data and the result of applying a 61-point median

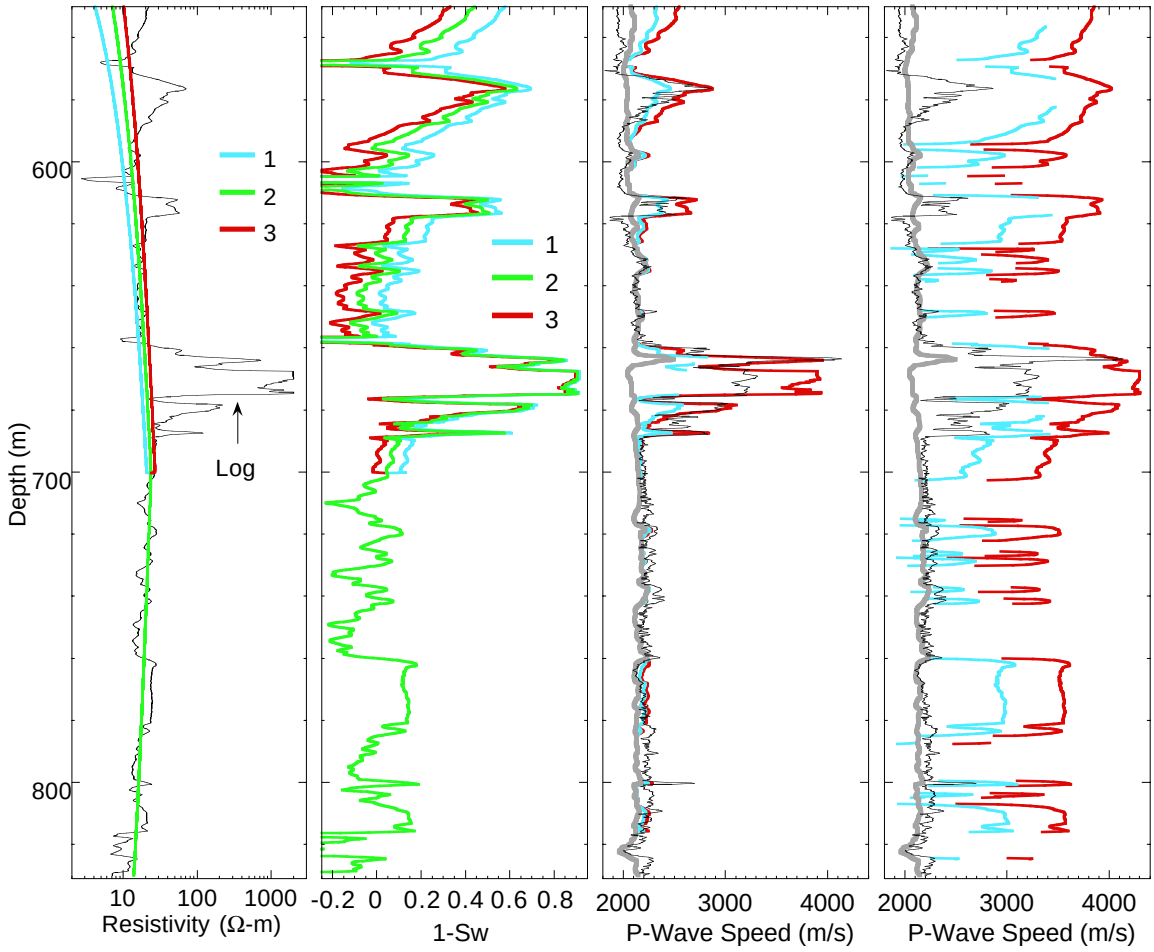

Figure 6.8: Modeling results for Northwest Eileen State Well #2. Column one: Deep resistivity log versus depth with three "quick-look" Archie background resistivity estimates (see text). Column two: Non-water pore space saturation estimates derived using the "quick-look" Archie method given the three background resistivity curves shown in column one. All non-water saturation is attributed to methane hydrate. Column three: Compressional wave speed estimates from the hydrate as fluid (blue) and hydrate as sediment frame (red) component models using the "optimal" (2) resistivity based methane hydrate saturation estimate. The black line is the compressional wave sonic log and the gray line is the baseline model result. Column four: Compressional wave speed estimates from the hydrate as contact cement model using scheme 1 (red) or scheme 2 (blue) to distribute the gas hydrate cement on the quartz grains. The amount of methane hydrate present is taken from the "optimal" (curve 2) resistivity based methane hydrate saturation estimate. The black line is the compressional wave sonic log and the gray line is the baseline model result.

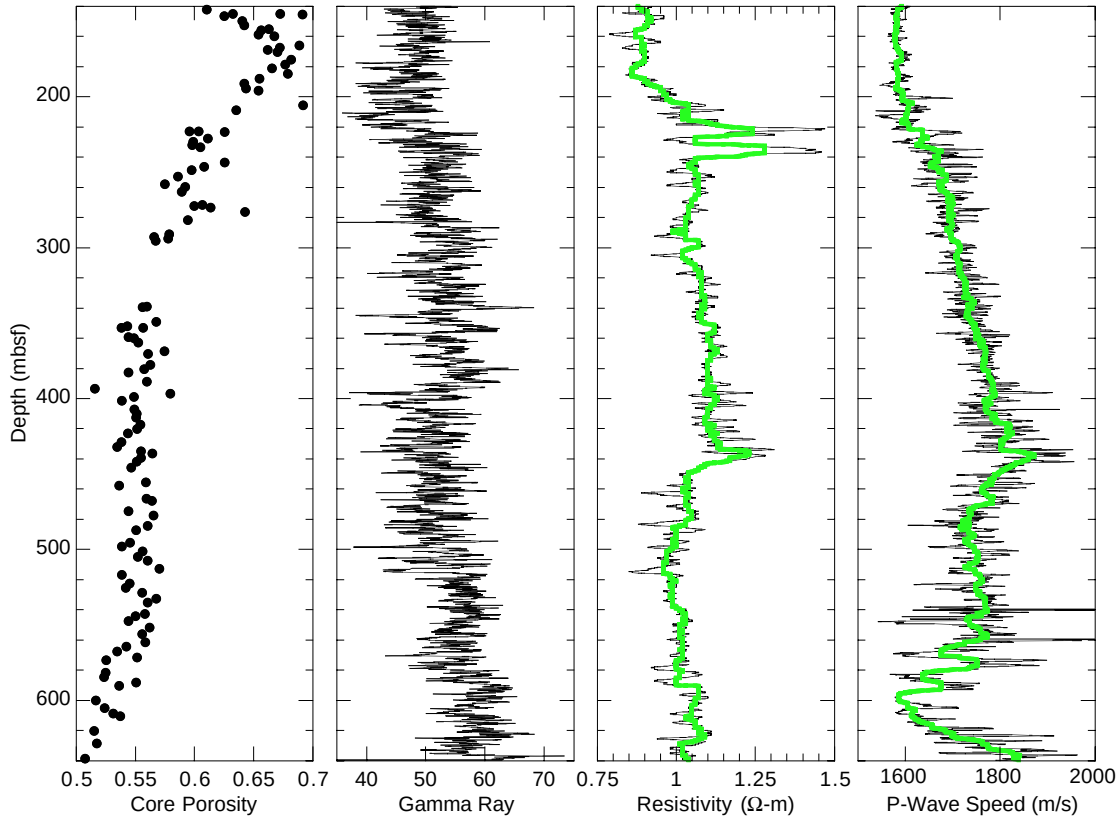

Figure 6.9: Core porosities and physical property logs for ODP site 995. Column one: Shipboard core porosity measurements versus depth. Column two: Gamma ray log versus depth. Column three: Resistivity log versus depth. Green line is the result of applying a 61-point median filter to the data. Column four: Compressional wave sonic log versus depth. Green line is the result of applying a 61-point median filter

filter to the data. The filter was applied to reduce noise. The modeling described below was done with the 61-point median filtered data.

The mineralogy at site 995 was determined from smear slides and XRD data and is reported in the Initial Reports Volume of ODP Leg 164 (Shipboard Scientific Party, 1996). The interval of interest extends from 190 meters below the sea floor (mbsf) to the bottom of the hole. This interval is lithologically uniform and predominantly comprised of clay, calcite and quartz. For the purpose of calculating the effective moduli of the solid phase, I take the solid volume percentages of clay, calcite and quartz to be 60, 35 and 5%, respectively, consistent with the mineralogy data. The elastic properties and densities used in this study for clay, calcite, quartz and methane hydrate are given in Table 6.1.

The bulk modulus and density of sea water in the formation were calculated versus depth as a function of temperature and pressure following Batzle and Wang (1992). The calculated density of the brine was essentially constant in the interval at 1.032 g/cm^3. The bulk modulus of the brine varied from 2.4 to 2.6 GPa. The bulk modulus and density of methane gas at in situ conditions were calculated from Sychev et al. (1987). The bulk modulus varied from 0.10 to 0.12 GPa and the density was essentially constant at 0.23 g/cm^3. Effective pressure was calculated as the difference between the overburden and hydrostatic pressure. Porosity was taken from shipboard core measurements. Coordination number and critical porosity were taken as 9 and 0.37, respectively, the theoretical values for a dense packing of identical spheres (Mavko et al., 1998).

Figure 6.10, column one, shows sonic log data (smoothed with a 61-point median filter) together with the calculated compressional wave speed profiles for 0% bulk hydrate (100% water saturation), as well as 2, 4, and 8% bulk hydrate by volume and 0.5 and 1% bulk gas by volume. The gas is assumed to be homogeneously distributed in the pore space and the methane hydrate is assumed to be suspended in the pore fluid. The second column in Figure 6.10 shows the modeling results using a patchy distribution for gas (1, 3, and 5%) and assuming the methane hydrate acts as a load bearing component of the sediment frame. The third column in Figure 6.10 compares hydrate concentration estimates derived from the gas hydrate as frame component model to estimates derived from the (smoothed) resistivity log at the depths where core porosity values were measured. The resistivity based estimates are derived from the "quick-look" Archie method described above.

Chloride data and PCS gas volumes suggest that hydrate is located in the interval from 190-450 mbsf (Dickens et al., 1997; Shipboard Scientific Party, 1996). The 100% brine saturation line in Figure 6.10 intersects the compressional wave speed curve at approximately these same depths, confirming the validity of the baseline model and input parameters for this site. The constant gas and gas hydrate concentration lines in Figure 6.10 are level curves for estimating bulk gas and gas hydrate percent from well log compressional wave speed. These estimates are close to independent hydrate estimates determined from resistivity (column three, Figure 6.10) and chloride (column three Figure 6.11) data. They are also consistent with the values derived from PCS evolved gas data which suggest that 0 to 9% of the pore space contains gas hydrate (Dickens et al., 1997).

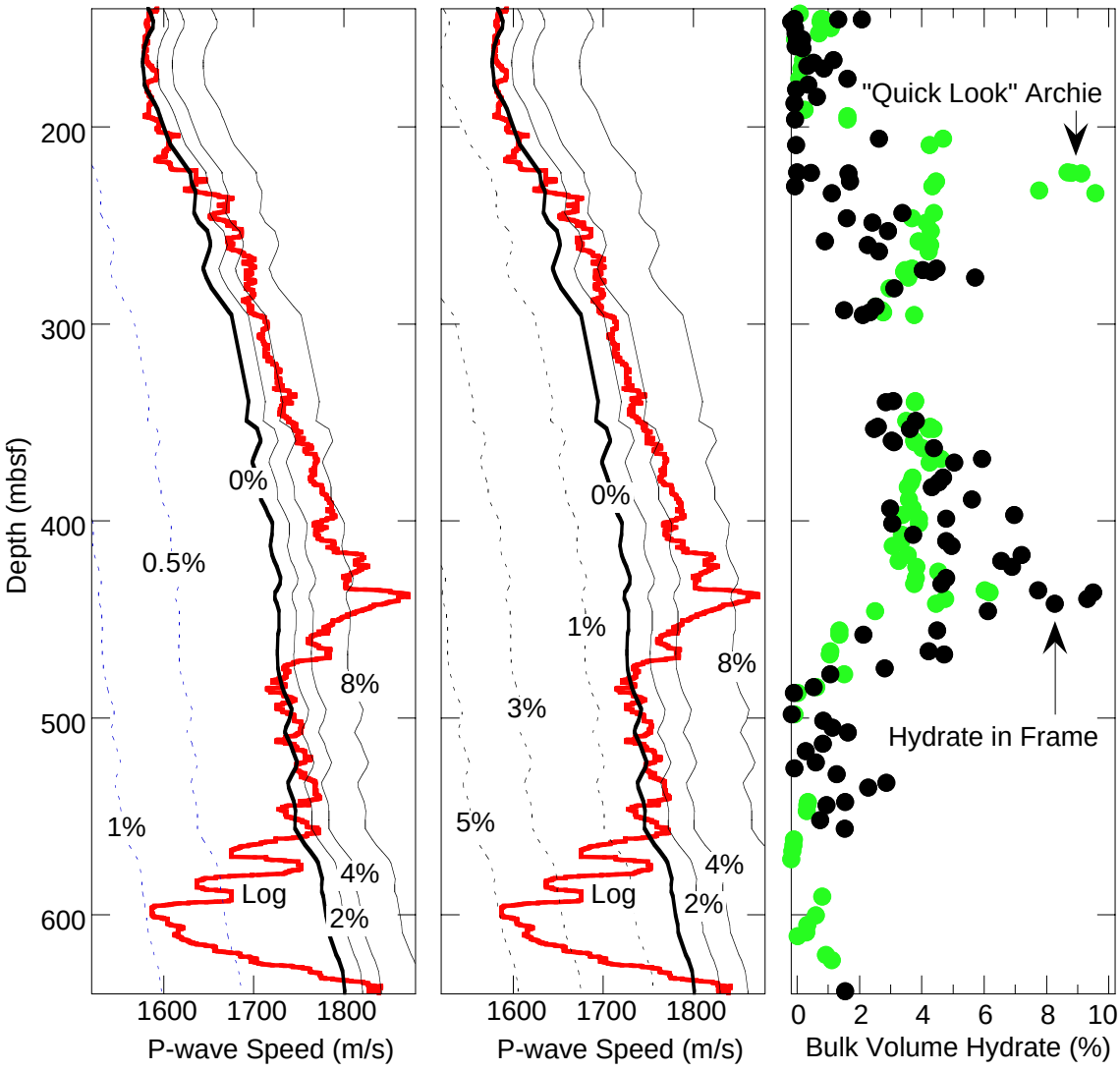

Figure 6.10: Methane hydrate concentration in the sediments at ODP site 995 from compressional wave sonic and resistivity logs. Column one: Comparison of compressional wave sonic log (red line) with model results assuming methane hydrate (solid black lines) or homogeneously distributed methane gas (dashed lines) are part of the pore fluid. Column two: Comparison with model results assuming methane hydrate is a sediment frame component (solid black lines) or methane gas is patchily distributed in the pore space (dashed lines). For both columns one and two, the model values are calculated at the core depths and the results fit with smoothed curves. Column three: Comparison of methane hydrate concentration estimates derived from the resistivity log to estimates derived from the compressional wave sonic log using the gas hydrate as sediment frame component model.

Figure 6.11 compares compressional wave speed from VSP data (Holbrook et al., 1996) to model calculations assuming the gas hydrate is either suspended in the pore fluid (column one, Figure 6.11) or a load bearing component of the sediment frame (column two, Figure 6.11). The third column in Figure 6.11 compares the gas hydrate concentration estimates derived from the latter model to those derived from pore water chlorinity data (Shipboard Scientific Party, 1996). The modeled compressional wave speeds shown in Figure 6.11 are the same as those in Figure 6.10. Differences in estimated methane hydrate concentration and distribution between Figures 6.11 and 6.10 are due solely to compressional wave speed differences detected by the two measurement techniques (sonic log and VSP).

Methane hydrate concentration estimates for ODP site 995 based on the hydrate as fluid component model are significantly higher than those derived from resistivity, chloride and evolved gas data. Gas hydrate estimates derived from the hydrate as sediment frame component model are in much better agreement with the independently derived estimates. From this I conclude that gas hydrate acts as a load bearing sediment frame component at site 995. Although there are differences in distribution and absolute amount of hydrate predicted by the different compressional wave speed data sets, the resultant hydrate concentration estimates are of the same magnitude and general distribution.

Variability between different hydrate concentration estimates prevents an exact determination of the amount of methane hydrate present at site 995, but all estimates point to a general background level of 2-4% bulk methane hydrate by volume with a peak concentration of 8-9%. Variability between methane hydrate concentration estimates reflects fundamental differences between the measurements on which the methods are based. Controlled laboratory experiments on well-characterized hydrate/sediment composites are needed to improve our understanding of the accuracy and pitfalls of the different estimation techniques.

The modeling also shows that much of the sediment beneath the gas hydrate layer contains a significant amount of free gas, perhaps as much a 5-7% by volume at some depths if the gas is collected in patches. If this result is correct and representative of the Blake-Bahama Ridge gas hydrate deposit as a whole, a significant volume of free methane gas may be trapped beneath the gas hydrate deposits.

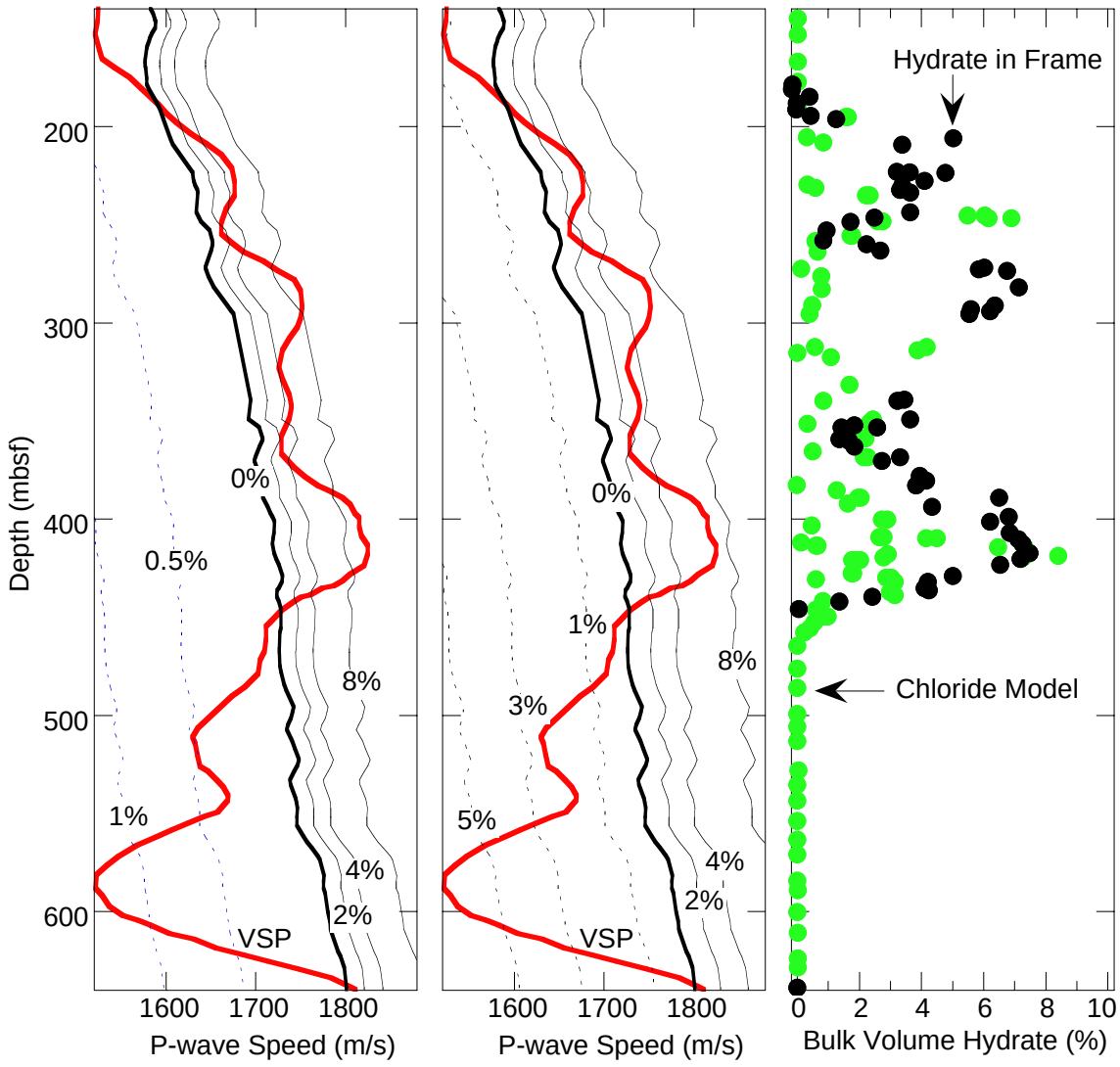

Figure 6.11: Methane hydrate concentration in the sediments at ODP site 995 from vertical seismic profile (VSP) and pore water chlorinity data. Column one: Comparison of VSP compressional wave speed (red line) with model results assuming methane hydrate (solid black lines) or homogeneously distributed methane gas (dashed lines) are part of the pore fluid. Column two: Comparison with model results assuming methane hydrate is a sediment frame component (solid black lines) or methane gas is patchily distributed in the pore space (dashed lines). For both columns one and two, the model values are calculated at the core depths and the results fit with smoothed curves. Column three: Comparison of methane hydrate concentration estimates derived from the pore water chlorinity data to estimates derived from the compressional wave VSP data using the gas hydrate as sediment frame component model.

6.10 Discussion and Summary

In this chapter I described a model for estimating the elastic properties of sediments 100% saturated with water. The model depends on solid and liquid phase elastic moduli, porosity, effective pressure and bulk density. The model was then modified to account for the presence of gas hydrate suspended in the pore fluid, included as a sediment frame component or formed as a grain contact cement. The resulting three models were applied to data acquired at sites where gas hydrate was found in sands (Northwest Eileen State Well #2) and in clay rich ocean bottom sediments (ODP Site 995).

The modeling results for the gas hydrate in sand data acquired at Northwest Eileen State Well #2 strongly suggest that gas hydrate does not cement sand grain contacts in the onshore sediments under examination there. Given the uncertainty in the gas hydrate saturation estimate, it is difficult to choose between the gas hydrate as fluid and gas hydrate as frame component models and definitively conclude whether gas hydrate is part of the pore fluid or part of the solid frame at that site. It is possible that both situations are present. Therefore, it is my recommendation that these two models be used as bounds for calculating the elastic properties from gas hydrate saturation or, conversely, estimating gas hydrate saturation from wave speed data in cases where a definitive conclusion cannot be drawn about where gas hydrate is located in the pore space.

The more detailed and complete data available at ODP site 995 make it possible to conclude that gas hydrate acts as a load bearing sediment frame component at that site. Under this conclusion, the data imply that approximately $2-4\%$ of the sediment by volume is gas hydrate in the depth interval from 190 to 450 mbsf, with peak concentrations of 8-10% present at some depths within this interval. The data also show that a significant amount of free gas may be present beneath the gas hydrate deposit.

It is clear to me after having conducted the modeling presented in this chapter that more detailed experimental work needs to be done to test and to improve the models of the elastic properties of sediments containing gas hydrate. The detailed knowledge about the sample required to improve the theoretical modelling will probably never be available from natural deposits. The resolution of data that probes pristine deposits (i.e., seismic reflection profiling) is, in general, insufficient to distinguish between the models and a ground truth

measurement is seldom available to calibrate the data. Data from boreholes are much more detailed, but the process of drilling disturbs the gas hydrate deposits to an unknown degree. Gas hydrate saturation and wave speed data from controlled experiments are what is needed to accurately distinguish which of the models is most appropriate for sands and clay rich sediments containing gas hydrate. Currently the uncertainty in estimating *in situ* gas hydrate saturation is a function of uncertainty in both the data and the models used to interpret the data. Results from laboratory work can not address the *in situ* data quality problem, but they can significantly reduce the uncertainty in the model space used to interpret that data, and in that capacity could lead to a vast improvement in our ability to estimate the amount of gas hydrate in the ground. Much more laboratory work needs to be done to adequately calibrate the various methods of estimating natural gas hydrate concentrations in sediments.

6.11 References

Batzle, M., and Z. Wang, 1992, Seismic properties of pore fluids, Geophysics, **57**, 1396–1408.

Bangs, N. L. B., D. S. Sawyer, X. Golovchenko, 1993, Free gas at the base of the gas hydrate zone in the vicinity of the Chile triple junction, Geology, **21**, 905–908.

Berryman, J.G., 1980, Long-wavelength propagation in composite elastic media, I and II, Journal of the Acoustical Society of America, **68**, 1809–1831.

Berryman, J.G., 1995, Mixture theories for rock properties, in A Handbook of Physical Constants, T. J. Ahrens, ed. American Geophysical Union, Washington, D.C., 205–228.

Booth, J. S., M. M. Rowe and K. M. Fischer, 1996, Offshore Gas Hydrate Sample Database with an Overview and Preliminary Analysis, U.S. Geol. Surv. Open-File Report 96-272, 17pp.

Collett, T. S., 1998, Well log evaluation of gas hydrate saturations, Transactions of the Society of Professional Well Log Analysts 39th Annual Logging Symposium, Paper MM.

Collett, T. S., 1992, Natural gas hydrates of the Prudhoe Bay and Kuparuk River Area, North Slope, Alaska, AAPG Bulletin, **77**, 793–812.

Dallimore, S. R., T. Uchida and T. S. Collett, eds., 1999, Scientific results from JAPEX/JNOC/GSC Mallik 2L-38 gas hydrate research well, Mackenzie Delta, Northwest Territories, Canada, GSC Bulletin 544, 403 pp.

Dickens, G.D., C.K. Paull, P. Wallace and ODP Leg 164 Science Party, 1997, Direct measurement of in situ methane quantities in a large gas hydrate reservoir, Nature, **385**, 426–428.

Dvorkin, J., J. Berryman and A. Nur, 1999a, Elastic moduli of cemented sphere packs, Mechanics of Materials, **31**, 461–469.

Dvorkin, J., and A. Nur, 1998a, Time-average equation revisited, Geophysics, **63**, 460–464.

Dvorkin, J., and A. Nur, 1998b, Acoustic signatures of patchy saturation, Int. J. Solids Structures, **35**, 4803–4810.

Dvorkin, J., and A. Nur, 1996, Elasticity of High-Porosity Sandstones: Theory for Two North Sea Datasets, Geophysics, **61**, 1363–1370.

Dvorkin, J., A. Nur and H. Yin, 1994, Effective properties of cemented granular material, Mechanics of Materials, **18**, 351–366.

Dvorkin, J., M. Prasad, A. Sakai and D. Lavoie, 1999b, Elasticity of Marine Sediments: Rock Physics Modeling, Geophysical Research Letters, **26**, 1781–1784.

Ecker, C., J. Dvorkin, and A. Nur, 2000, Estimating the amount of hydrate and free gas from surface seismic, Geophysics, **65**, 565–573.

Gassmann, F., 1951, Elasticity of porous media: Uber die elastizitat poroser medien: Vierteljahrsschrift der Naturforschenden Gesselschaft, **96**, 1–23.

Hashin, Z. and S. Shtrikman, 1963, A variational approach to the elastic behavior of multiphase materials, Journal of the Mechanics and Physics of Solids, **11**, 127–140.

Hill, R., 1952, The elastic behavior of crystalline aggregate, Proceedings of the Physical Society, London, **A65**, 349–354.

Holbrook, W. S., H. Hoskins, W. T. Wood, R. A. Stephen, D. Lizzaralde and ODP Leg 164 Science Party, 1996, Methane hydrate and free gas on the Blake Ridge from vertical seismic profiling, Science, **273**, 1840–1843.

Hyndman, R. D., and G. D. Spence, 1992, A seismic study of methane hydrate marine bottom simulating reflectors, Journal of Geophysical Research, **97**, 6683–6698.

Kvenvolden, K. A., G. D. Ginsburg and V. A. Soloviev, 1993, Worldwide distribution of subaquatic gas hydrates, **13**, 32–40.

Kvenvolden, K. A. and M. A. McMenamin, 1980, Hydrates of natural gas: A review of their geologic occurrence, United States Geological Survey Circular 825, 1–11.

Lee, M. W., D. R. Hutchinson, T. S. Collett, and W. P. Dillon, 1996, Seismic velocities for hydrate-bearing sediments using weighted equation, Journal of Geophysical Research, **101**, 20,347–20,358.

Mathews, M., 1986, Logging characteristics of methane hydrate, The Log Analyst, **27**, 26–63.

Mavko, G., T. Mukerji and J. Dvorkin, 1998, The rock physics handbook, Cambridge University Press, Cambridge, 329pp.

Mavko, G, and T. Mukerji, 1998, Bounds on low-frequency seismic velocities in partially saturated rocks, Geophysics, **63**, 918–924.

Miller, J. J., M. W. Lee, and R. von Huene, 1991, An analysis of a seismic reflection from the base of a gas hydrate zone, offshore Peru, AAPG Bulletin, **75**, 910–924.

Mindlin, R. D., 1949, Compliance of elastic bodies in contact, Journal of Applied Mechanics, **16**, 259–268.

Minshull, T. A., S. C. Singh, and G. K. Westbrook, 1994, Seismic velocity structure at a gas hydrate reflector, offshore western Colombia, from a full waveform inversion, Journal of Geophysical Research, **99**, 4715–4734.

Nur, A., G. Mavko, J. Dvorkin, and D. Galmudi, 1998, Critical porosity: A key to relating physical properties to porosity in rocks, The Leading Edge, **17**, 357–362.

Pearson, C. F., P. M. Hallek, P. L. McGuire, R. Hermes, and M. Mathews, 1983, Natural gas hydrate deposits: a review of in situ properties, Journal of Physical Chemistry, **87**, 4180–4185.

Pearson, C., J. Murphy and R. Hermes, 1986, Acoustic and Resistivity Measurements on Rock Samples Containing Tetrahydrofuran Hydrates: Laboratory Analogues to Natural Gas Hydrate Deposits, Journal of Geophysical Research, **91**, 14132–14138.

Reuss, A., 1929, Berechnung der fliessgrenzen von mischkristallen auf grund der plastizitatsbedingung fur einkristalle, Zeitschrift fur Angewandte Mathematic und Mechanik, **9**, 49–58.

Sakai, A., 1999, Velocity analysis of vertical seismic profile (VSP) survey at JAPEX/JNOC/GSC Mallik 2L-38 gas hydrate research well, and related problems for estimating gas hydrate concentration, Geological Survey of Canada, Bulletin 544, 323–340.

Schlumberger, 1989, Log interpretation, principles/applications, Schlumberger Educational Services, Houston.

Scholl, D. W., and P. E. Hart, 1993, Velocity and amplitude structures on seismic reflection profiles–possible massive gas hydrate deposits and underlying gas accumulations in the Bering Sea Basin, USGS Professional Paper **1570**, 331–351.

Shipboard Scientific Party, 1996, Site 995. In Paull, C.K., Matsumoto, R., Wallace, P.J., et al., Proc. ODP, Init. Repts., 164: College Station, TX (Ocean Drilling Program), 175–240.

Sychev, V.V., A.A. Vasserman, V.A. Zagoruchenko, A.D. Kozlov, G.A. Spiridonov, V.A. Tsymarny, 1987, Thermodynamic properties of methane, Hemisphere Publishing Corp, Washington.

Wood, A. B., 1955, A textbook of sound, The MacMillan Co., New York, 360 pp.

Wood, W. T., P. L. Stoffa, and T. H. Shipley, 1994, Quantitative detection of methane hydrate through high-resolution seismic velocity analysis, Journal of Geophysical Research, **99**, 9681–9695.

Wyllie, M. R. J., A. R. Gregory, and L. W. Gardner, 1956, Elastic wave velocities in heterogeneous and porous media, Geophysics, **21**, 41–70.